Hot Formability and Microstructural Development of Spray-Deposited Al-Li Alloy and Composite

By

Christopher Nigel Sparks, B.Eng.(Hons)

Thesis submitted for the degree of Doctor of Philosophy

Department of Engineering Materials, University of Sheffield

September 1994

Summary

Hot formability and microstructural development of
spray-deposited Al-Li alloy and composite

Christopher Nigel Sparks

The deformational and microstructural behaviour of the commercial Al-Li alloy 8090 and an 8090 based composite containing silicon carbide particulate has been investigated.

The materials were deformed at elevated temperature by the test methods of plane strain compression (PSC) and torsion to provide stress-strain data for the formulation of constitutive relationships. Torsion testing also provided high temperature ductility data. Isothermal annealing of rolled samples was carried out at the solution temperature of 530°C to investigate the recrystallisation kinetics and microstructures produced, with particular emphasis on the effect of the inclusion of reinforcement particles on the behaviour of the matrix alloy.

Hyperbolic sine forms of constitutive equation have been produced and are found to provide good agreement with the experimental data. High values of the activation energy are calculated for the deformation of both the alloy and composite from the PSC test data.

The equations obtained from the two different test methods are found to be comparable for the composite material, but a discrepancy is found for the monolithic alloy, where apparently less hardening results from torsion testing.

A distinct transition in microstructure from recrystallised equiaxed grains when deformed at low temperature to an elongated, sometimes partially recrystallised, structure for material rolled at high temperature is present in the monolithic material. This is attributed to the balance of recrystallisation driving force and the Zener pinning force exerted by the β' (Al_3Zr) phase.

The composite material exhibited greatly enhanced recrystallisation kinetics in agreement with the theory of particle stimulated nucleation (PSN) of recrystallisation.

Acknowledgements

I would like to thank Professor C.M. Sellars, as both Head of Department, and as my supervisor, for the use of the facilities of the department, and for discussions during the course of my research. I also acknowledge "Cospray" (Alcan International Ltd.) for the provision of test specimens and facilities, and the Science and Engineering Research Council for financial support.

I am grateful to the technical staff of this department, particularly Dave Manvell and Andy Marshall for initial instruction in the use of the Servotest machine and the rapid production of test specimens respectively. In addition my thanks go to John Whiteman and Gordon Richardson for many useful discussions.

I would like to express my thanks for help and an "interesting" working environment (though not in that order) to many members of the department, but mostly to my fellow Hot Workers, particularly Andy McLaren and Paul Shenton. I think, also, that the Style Police must be mentioned at this juncture, for assistance with the social side of academic life. Thanks are due to John Mawer for his help with printing of the thesis.

The following people have, in some way, been instrumental in the completion of this thesis: Alan McLelland for the somewhat extended loan of his computer, Iain Whitaker for unlimited help with the TEM, many hours of useful discussion and such generosity with his time, and Lizzy who, in one way or another, provided the motivation for me to write-up.

Finally, I would like to express my sincere gratitude to my family for their ceaseless encouragement, and many hours of listening. To Nick for making sure that I didn't starve during the last weeks of writing, and to the "Sparks Bank" and all of its members for ensuring that I never quite reached bankruptcy.

Table of Contents

1 Introduction

Materials development is of paramount importance in any engineering enterprise, and in no area does it assume greater importance than in the aerospace industry. The immense operating costs of a civil airliner, and the need for greater agility in the military sphere have dictated that the industry be driven by the need to minimise weight. The quest for military supremacy drove the development of a viable aluminium-lithium material for airframe construction. The benefits of the possible reduction in density and improvements in elastic modulii by the addition of lithium to aluminium alloys for use in commercial aircraft were easily apparent, and this led to vast expenditure on research programs world-wide to overcome some of the inherent problems, such as poor fracture toughness.

Additions of Cu, Mg, Zr to binary Al-Li alloys can enhance strength, modulus of elasticity, fatigue, corrosion and stress corrosion cracking resistance to sufficient levels to make the replacement of existing 2xxx and 7xxx aluminium alloys highly attractive. Such alloy systems are those coded 8090 and 8091.

Methods of alloy production such as spray casting have helped to alleviate some of the problems previously inherent to the aluminium-lithium group of alloys, such as extreme anisotropy of properties and poor fracture toughness, and in addition the spray casting method has allowed the production of usable low density metal matrix composites (MMC's) based on the Al-Li system. This has diminished the problem of increased density of SiC reinforcement when incorporated in conventional aluminium alloys.

When a new group of materials has been developed, then the next logical step is the acquisition of data about how that material behaves when undergoing forming operations. The forming of a metallic material generally involves some type of hot-working process, and so if the material properties are to be optimised for the end use, an extensive knowledge of the behaviour during and after hot-working is required. Laboratory tests are the preferred method of gaining such knowledge, from the time, financial and control points of view. Data from such tests are used in the formulation of constitutive relations that are capable of describing the stress behaviour during forming operations as a function of strain, strain rate and temperature. The use of these relationships enables the assessment of rolling characteristics without recourse to expensive full-scale mill trials. A full understanding of the microstructural behaviour of the material during deformation schedules and in subsequent heat treatments is also necessary for the accurate prediction of a metal's behaviour during processing.

In this project the aim was to assess the hot workability of the Al-Li- Cu-Mg-Zr alloy 8090, and of an 8090 based composite containing silicon carbide (SiC) reinforcement particles. This was undertaken by the use of plane strain compression (PSC) and torsion test methods. The data so produced were then used in the formulation of constitutive equations. The use of these test methods also enabled the materials' behaviour under different strain regimes to be investigated, and the torsion test provided ductility values for the alloys over a range of temperatures. From these results, and qualitative assessment of the edge cracking during rolling, it was found that the finishing

temperature during processing should be maintained above 400°C, especially for the composite materials.

Rolling of slabs was used to impart strain prior to recrystallisation treatments at the solution temperature (530°C). Extensive microstructural studies into the development of microstructure with time of isothermal heat treatment have been conducted, and the effect of the reinforcement particles upon the recrystallisation behaviour of the matrix alloy investigated. In the monolithic alloys, Zener drag arising from the β′ (Al_3Zr) particles appeared to be critical, and so limited transmission electron microscopy (TEM) was carried out to enable this effect to be quantified. The reinforcing SiC particles were found to have small but significant effects on the flow stress, and major effects on the recrystallisation characteristics.

2 Literature Review

2.1 Aluminium-lithium alloy development

Materials development is now considered to be the most important means of improving the performance of an aircraft (1). Throughout aviation history aluminium has proved to be vitally important in aircraft development, due to the combination of light weight, ductility, corrosion resistance and ease of fabrication.

With the advent of more advanced designs and the resultant higher speeds, alloying additions were deemed necessary to improve the strength of what is essentially a fairly weak material.

In 1909 Wilm made a significant discovery by finding that aluminium could be strengthened by the addition of Cu and Mg, resulting in the alloy known as Duralumin. This alloy remains largely unchanged as 2014 today (2). Increases in fuel costs led to studies into the cost savings possible when less dense materials were utilised in airframe construction (3). It has been estimated that a weight saving of around 16% could save up to $1million/aircraft/annum for a large airliner. This, coupled with the need for the aluminium industry to counter the very light organic matrix composites under development (4), led to research being conducted into alloy compositions outside the confines of the established systems.

Figure 2.1 illustrates the superiority of a density reduction (over similar improvements in strength, stiffness and damage tolerance) in effecting a weight saving in an aircraft. This clearly shows that a given reduction in density provides a far greater weight saving than is possible with an equivalent improvement in the other parameters, often by a factor of 3 to 5 times (5). However, specific details will vary depending upon the aircraft considered.

When the development of a new generation of aluminium aerospace alloys began in the late 1970's a reduction of 10% in the weight of an airframe was decided upon as a realistic target. Figure 2.1 clearly shows that this weight reduction is possible through a decrease in density of the same percentage. Such a reduction in density whilst still utilising an aluminium alloy is possible only with the addition of lithium as an alloying element (lithium is the least dense metal known, with a density of only $0.53g/cm^3$ compared with aluminium which possesses a density of $2.7g/cm^3$). For every 1 weight % addition of lithium (up to 4%) the density decreases by 3% and the elastic modulus increases by 6% (6).

An Al-Li development programme was established in the U.K. and certain targets were agreed by the Royal Aircraft Establishment (RAE), British Aerospace (BAe) and the British Aluminium Co. (BACo). These were (7):

- a density reduction of 10% compared with the then-current Al-Cu 2xxx series and Al-Zn-Mg-Cu 7xxx series alloys (i.e a target density of 2.52g/cm^{-3} compared with 2.8g/cm^{-3}).

- strength levels similar to conventional alloys.

- a stiffness of 80GPa (a 10% increase over 2xxx series alloys and a 15% increase over those in the 7xxx series).

The system produced by the RAE in accordance with the above was the alloy Al-2.5%Li-1.2%Cu-0.7%Mg-0.12%Zr, codenamed F92, or 8090 as it is now known. Table 2.1 shows that the commercial Al-Li alloys now all utilise the addition of Cu, Zr and usually Mg in order that the best compromise between strength and toughness can be achieved.

Studies such as those by Sankaran et al (8) clearly show that use of 8090 allows large weight savings without sacrificing other important mechanical properties. It is in fact found (7) that most of the properties of 2xxx series alloys can be reproduced by 8090 in various heat treated forms, thus potentially allowing the substitution of much conventional aluminium alloy in construction of an airframe. There are, however, disadvantages. The addition of lithium is very expensive and has a detrimental effect on certain mechanical properties, such as ductility and fracture toughness (4). Alloy 8090 has a fracture toughness that is poor in the S-T direction. This has meant that the uses of 8090 have been limited and that, when used, the alloy composition and heat treatments must be carefully controlled to allow the density and stiffness improvements to be utilised without sacrificing other properties.

That 8090 *can* exhibit acceptable standards in critical properties, such as fracture toughness and fatigue behaviour, whilst still affording its vast improvements in strength, weight and stiffness is witnessed by its inclusion in the F15 Eagle, Experimental Aircraft Program (EAP) (2) and the Westland-Agusta EH101 helicopter (9).

With regard to use in civil aviation, despite widespread predictions of the application of Al-Li alloys to most areas of conventional aluminium alloy usage, Boeing have deemed that the alloy is not sufficiently attractive to them to be incorporated in production aircraft at this time at least (10) but continue to evaluate the alloy. It is likely that the development of 8090 will continue due to the vast potential savings in aircraft operating costs, but whether the properties will be sufficiently improved to secure inclusion in a range of civil aircraft remains to be seen.

2.1.1 Physical metallurgy of 8090

The relatively high strength of 8090 is principally due to the presence of the metastable, spherical, coherent δ' (Al_3Li) precipitate phase (11). This hardening phase forms by homogeneous nucleation from the super saturated solution upon quenching from the solution treatment

temperature. The level of strengthening gained is a function of the volume fraction and size of the δ′ (12) and is a result of the resistance of the phase to shearing by slip dislocations during deformation (5).

The presence of this hardening phase is also responsible for the poor fracture toughness of many Al-Li alloys, by causing the localisation of slip. This occurs due to the fact that, once slip has begun on a given plane, then it is energetically more favourable that it continues in that slip system.

Copper and magnesium are added to 8090 to improve mechanical properties by the formation of the T_1 (Al_2CuLi) and S' (Al_2CuMg) phases. These precipitates both provide a hardening effect but also assist in decreasing the planar slip, by acting as unshearable obstacles to the movement of dislocations. These "obstacles" are able to assist in homogenising slip by causing the dislocations to bypass the particles via the Orowan mechanism (13). (It is found that S' is the more effective phase in terms of blocking planar slip due to the promotion of dislocation cross-slip (5))

Both phases nucleate heterogeneously and a strong dislocation substructure will therefore assist precipitation and ensure a more homogeneous distribution. This is normally achieved by stretching the material by around 2-7% after solution treatment and prior to ageing (14). In some material conditions (e.g. forging stock, which is unworked and aged) this stretching is not possible and so some alternative method to encourage nucleation of S' is required.

Work has shown that control of the Cu:Mg ratio controls the precipitation age hardening response, and that an increase in the Mg content can be used to optimise properties by encouraging the production of the S' phase.

Zirconium additions are made to inhibit recrystallisation via the formation of metastable, fully coherent, spherical β' (Al_3Zr) (15). This phase forms sluggishly during homogenisation and, as well as inhibiting recrystallisation, suppresses grain and subgrain growth by pinning of the boundaries (16). The presence of Zr has a significant effect on the size and distribution of δ′ as it can nucleate heterogeneously on β' (17). This leads to a so-called composite precipitate with the δ′ enveloping the β' phase. The δ′/β' particle is large (around 80nm) and is not sheared by dislocations, but is bypassed by looping. This may again assist in homogenising slip.

2.1.2 Mechanical properties

The distribution and volume fraction of precipitates (both grain boundary and matrix) have a significant effect on the properties of 8090. The ductility of this alloy is lower than that exhibited by conventional aluminium aerospace alloys and therefore needs optimising via pre-stretching and then ageing.

The unrecrystallised structure of high strength 8090 rolled plate can result in highly anisotropic mechanical properties. Peak aged commercial 8090 has, however, been found to possess superior mechanical properties in the L and L-T orientations when compared with

conventional high strength aerospace aluminium alloys (19). Similarly, the strong deformation texture in unrecrystallised products results in low ductility in the longitudinal direction (5) and anisotropy of properties is only reduced by recrystallising the material.

In addition to the precipitation processes discussed in (§ 2.1.1), reducing impurities such as iron and silicon, developing recrystallised structures and stretching of the alloy prior to ageing (5) allow the fracture toughness of 8090 to be improved to acceptable levels. Poor fracture toughness in the S-T orientation remains a problem.

2.2 Metal matrix composites (MMC's)

Metal matrix composites (MMC's) typically consist of a ceramic reinforcement in a metallic base. This group of materials is capable of providing improved strength, stiffness, wear resistance and elevated temperature properties when compared with the matrix base alloys. They can offer a designer improved structural efficiency and reliability.

The impetus behind MMC development has often been the possibility of much larger improvements in properties than were achievable through conventional alloy development. These large property "jumps" were once only achievable at considerable expense, both in terms of actual material cost and also in terms of design problems in coping with the directionality of properties that often resulted. These high costs greatly limited the commercial exploitation of this new group of materials.

Relatively recently new and less expensive reinforcements have been developed, such as SiC fibres and particulate, which have provided the possibility of commercially viable MMC products.

There are acknowledged problems in designing components using fibre reinforced materials, such as anisotropy of properties and the application of prohibitive safety factors (20). Whisker reinforced composites require that near-net shape fabrication routes are used in their processing because mechanical working of such materials inevitably leads to broken whiskers, drastically decreasing the efficiency of the reinforcement.

In contrast to the above, particulate reinforced MMC's can be processed using conventional mechanical working techniques such as rolling, forging and extrusion without adversely affecting the mechanical properties (21).

Particulate reinforced MMC's are generally fairly isotropic in their mechanical properties, and can be tested and analysed using many techniques developed for conventional alloys. This obviously confers a great advantage over other MMC's in reaching the market place.

It was stated in the previous section that a density reduction was far more effective in achieving weight savings in an airframe than was an improvement in elastic modulus or strength. The great advantage of a decrease in density as a means of weight reduction is that it allows the saving to be made without increasing the working stress level (14). This is obviously of advantage

in the case of MMC's as the fatigue strength is already adversely affected by the brittle ceramic reinforcement (22). Whilst "conventional" Al based MMC's offer huge improvements in mechanical properties when compared with those of the base alloy (23), the fact that the reinforcement is invariably of higher density than the alloy (SiC has a density of 3.2g/cm^3 compared with. 2.7g/cm^3 for pure aluminium) means that the *specific* property improvement is significantly reduced. This often leads to possible weight savings in an airframe amounting to less than those possible using an unreinforced aluminium-lithium alloy such as 8090 (i.e. around a 5% saving over 2xxx and 7xxx series alloys). Obviously great interest has centred on developing Al-Li matrix composites which will allow the weight savings to be made ***and*** provide improved properties in areas such as elastic modulus.

2.2.1 Aluminium-lithium based MMC's

Silicon carbide is, at present, deemed the most attractive of possible particulate reinforcements. What then of its effect on the properties of the aluminium-lithium series of alloys?.

Figure 2.2 shows the mechanical properties of 8090-12% SiC vs. unreinforced 8090. As can be seen, the most significant improvement is an increase in elastic modulus over the base alloy of around 25%. This is in agreement with predictions which assume very effective load transfer between matrix and particles. This improvement in modulus, when allied to the fact that the inclusion of SiC increases the density from 2.54g/cm^3 for basic 8090 to 2.62g/cm^3 for the composite, gives a specific modulus increase of around 20%. This means that 8090-SiC provides the same specific stiffness improvement over "normal" 8090 as does 8090 over conventional high strength Al alloys. As Figure 2.2 shows (14), the strengths were found to be only slightly improved over the base alloy. This has also been found to be the case in other work performed on SiC particulate reinforced Al based composites (24). In fact, lower strength matrices reinforced with high strength particles usually show a more marked improvement in strength than do relatively stronger matrices such as 8090. This is due to the fact that in weaker matrices the stress borne by the reinforcement is a larger proportion of the matrix strength.

2.3 Spray casting

The development of the spray-casting route, predominantly by Osprey Metals Ltd., is an attempt to overcome many of the problems that are inherent to conventional ingot metallurgy (IM) and powder metallurgy (PM) alloy production methods. The advantages that result from the use of the spray-casting route will be discussed, with regard to Al alloys in general, and Al-Li alloys specifically. Initially the method itself will be discussed.

2.3.1 The process

Inert gas melting and dispensing practise is used, with an ingot being melted and dispensed using a bottom pouring crucible. Gas overpressure is used to control the flow rate of metal from

the crucible into the atomiser, which is typically in the range 5-12kg/min. For the majority of aluminium alloys nitrogen is used as the atomising gas and form spray droplets of particle diameters in the range 30-80μm (25).

The atomising gas jets perform several essential functions (26):

(a) Form a spray of fine droplets from the metal stream.
(b) Propel and shape the spray
(c) Protect the atomised droplets from oxidation
(d) Transfer kinetic energy to the atomised droplets to give high density preforms
(e) Rapidly extract heat from the droplets (in flight and when deposited)

The atomised stream is collected on a substrate in the line of flight to produce a solid deposit, the shape of which can be altered by the shape and motion of the collector, and the atomising conditions. By careful control of the deposition conditions a high density preform can be formed with a microstructure unrelated to the prior particles (25). The preform can be produced from the melt at around the same rate as is possible with the direct chill (DC) IM route. Figure 2.3 shows a schematic of the plant used in this production method.

2.3.2 The deposition stage

Figure 2.4 (27) shows a schematic representation of the deposition stage of the Osprey process. Heat is rapidly extracted by the atomising gas, in a flight time of only a few milliseconds (25). At the instant of deposition the sprayed droplets will be at different temperatures and states of solidification, because of a range of particle sizes (28). Ideally, coarse particles are deposited fully molten whilst the fine particles are deposited fully solidified at a temperature around that of the atomising gas. In this way the liquid on the deposition surface is able to remelt and break-up the semi-solid deposits (29) and remelt any dendritic fragments that have occurred as a result of the impact of solid particles on the deposition surface (28).

It is important that the surface temperature is carefully controlled by the gas stream conditions. If the surface is at too low a temperature, then the individual particles will retain their own identities and microstructures. At the other extreme, too high a temperature will cause a thick layer of liquid to be built up on the surface, which may then be ejected by the impingement of the high velocity gas and the motion of the collector. Ideally, then, a layer of semi-solid/semi-liquid deposit of controlled thickness is maintained at the surface throughout the deposition. The final structure of the preform is non-dendritic as a result of the turbulence that occurs on the surface of the preform due to the impacting stream of droplets (30). It is suggested that this turbulence causes the bending and fracture of dendrite arms and enables remelting, in a manner similar to stir-casting. In addition, Leatham et al (28) state that the turbulence ensures uniform temperature and composition through the deposit, providing very rapid non-dendritic growth in a sub-surface area of the preform.

2.3.3 Problems with conventional production routes

There are many well-known problems with the usual ingot metallurgy (IM) and powder metallurgy (PM) alloy production methods. It would be useful at this stage to list where these problem areas exist, and subsequently discuss how the spray-casting route overcomes them. General problems with the manufacturing method will be given first, followed by those that have been recognised by researchers working on the production of Al-Li alloys.

2.3.3.1 Problems with the IM route

General problems with the IM route are considered to be:

- A large number of processing steps are involved because of the large amount of hot work necessary to refine the grain size.
- Material possesses a coarse and inhomogeneous grain structure due to relatively slow cooling.

When considering the IM route for the production of the Al-Li group of alloys, the following specific problems must also be included:

- The route is practically limited to Li content of < 2.5% (31)
- Very coarse second phase particles may be produced (25). This requires a substantial amount of hot working to refine, and it is therefore difficult to produce the thickness of sections often required by the aero industry. The large particles themselves may act as fatigue crack initiators, leading to poor fracture toughness behaviour.
- A high degree of anisotropy of properties results following the necessary extensive hot reduction. This is one of the major problems with DC cast 8090, giving poor ductility in the S-T and T directions (31).
- There are often problems in controlling the hydrogen content of the ingot. High levels of hydrogen have a very detrimental effect on the weldability of the Al-Li alloys.

2.3.3.2 Problems with the PM route

- Oxide films form on particles. This is the main problem with the PM route for alloy production. The oxide layers mean that, to a certain extent, the prior particle boundaries are retained in the product, and consequently lead to poor ductility and toughness. Studies on 7075 (32) have shown that the oxide particles and fine microstructure lead to high tensile strengths in the longitudinal direction, but the brittle nature of the oxide stringers decreases the tensile properties in the transverse extrusion direction.
- The process is expensive. A large number of consolidation steps are required in order to break-up some of the oxide particle layers.

- The large number of consolidation steps (and degassing to limit oxidation) mean that large sections are not easily produced (33).

- High hydrogen levels may result from the hydrated nature of the oxide films (31).

2.3.4 Advantages of spray-casting

The rapidly solidified (RS) nature of this process results from convective cooling by the low temperature atomising gas (28), and leads to deposits of a fine uniform grain structure without macrosegregation (irrespective of the thickness of the preform).

It also means that novel alloy compositions can be produced that cannot be conventionally cast, (31,33) and that any subsequent processing steps can be performed without prolonged soaking times and/or large deformation ratios due to the fine grained, segregation free and non-dendritic structures (26,34). Spray-casting therefore carries with it some similar benefits to those obtained via conventional PM routes. However, it also has other advantages which will be discussed below (33):

- Because of the use of inert gas atomisation, and the fact that the alloy being processed only exists in particulate form for a few milliseconds, the oxygen pickup is very low, typically 50ppm as opposed to around 2000ppm in PM processes (25). The fact that much of the hydrogen pick-up comes from the hydrated oxide layer means that the spray-casting route can also significantly reduce hydrogen levels.

- No degassing step is required, and therefore no limit on product size results.

- As there are no oxide films or prior particle boundaries to break-up, less hot working steps are required. This again leads to the possibility of thicker sections of material and obviously reduces costs. In fact spray formed billets have been found to be capable of being directly HIPped without previous hot work (35).

- Direct extrusion of spray formed billets is possible without surface machining, due to the small variations possible in billet diameter (33).

- Powder handling and safety problems are reduced.

Because of the refinement of grain size and primary phase distribution, significant improvements in damage tolerance have been reported in standard 2000 and 7000 series alloys. Figure 2.5 shows a 25% improvement in toughness of spray-cast 7075 over the conventionally DC cast material.

2.3.5 Advantages of spray-casting aluminium-lithium alloys

Many of the general advantages given previously have far-reaching consequences in the production of the Al-Li series of alloys, with which there are acknowledged problems using conventional casting methods. The most significant of these advantages will be discussed below.

Spray casting provides a marked improvement in the ductility and toughness of 8090, attributed to the refinement of grain size and second phase particles (36), low hydrogen and sodium levels, a reduction in the amount of grain boundary phases, and the homogenisation of slip due to the fine grain size (37). Ductility in the S-T and T directions has been found to be increased from 4% in the DC cast material to 8% by the method of spray casting (33). The volume fraction of second phase has also been found to be reduced when comparing the as-produced microstructures of spray cast and DC cast material. In fact the amount of second phase in the spray cast sample was found to be reduced to a level comparable to that of the DC cast material *after homogenisation*, and where it was present it was uniformly distributed as fine precipitates within the grains (36). The fact that Lockheed have been successful in directly HIPping spray cast 8090 billets is attributed to this lack of segregation in the as-cast state. In this way one of the biggest problems in the 8090 system - anisotropy of properties - is removed, and has resulted in enhanced ductility and fracture toughness whilst maintaining thick section material.

Decreases in alkali metal and hydrogen contents have been realised through development of the process by Alcan International (38). This has been found to lead to improvements in general mechanical properties, and to have a significant and favourable effect upon the corrosion resistance and weldability of 8090. Up to a two-fold improvement in corrosion resistance has been found by some workers (33).

By use of the spray casting route, the lithium content can be increased up to a practical maximum of 4%, to produce the alloy designated UL40 (31). With a density of 2.4g/cm^3 it is capable of providing the greatest possible weight saving of any aluminium alloy. Coupled with good corrosion resistance this means that there many potential applications in the aerospace and marine fields for this unique alloy. If the Li content is increased to just 3% by spray casting, and the Zr to 0.3% (compared with 2.5 and 0.12 respectively for 8090) then the alloy designated UL30 is produced. As strengthening in this alloy is primarily due to β' (Al_3Zr) and δ' (Al_3Li), which form without prior cold work, (plus Cu and Mg in solid solution) then the stretching which is used in the production of full strength 8090 can be abandoned. This opens the way for the production of near-net shape forgings (34). Neither of the above mentioned alloys could be successfully produced by a conventional ingot metallurgy route.

The grain size refinement resulting from the rapid solidification nature of the spray casting process provides an equiaxed grain structure which is considerably smaller than that produced from conventional IM routes (e.g. a size of around 40-50μm compared with around 300μm for DC cast 8090 (31)).

2.3.6 MMC production

MMC production by spray deposition simply involves the co-deposition of the reinforcement particles with the atomised alloy stream. Particulate reinforcement (up to 30 volume %) (39) is introduced to the atomised stream at the top of the spraying chamber (see Figure 2.3).

The advantages of spray casting monolithic alloys are also valid in the production of MMC's by the process. Some additional advantages result from this method of particulate introduction, and these are discussed below.

The integrity of the matrix-particulate interface is obviously of importance to the mechanical properties of the resulting composite material. TEM studies have shown that precipitation at the interfaces in spray cast material is negligible in direct contrast to that which can occur in other MMC production routes (40). The amount of reaction and precipitation that occurs can be related directly to the contact time between molten metal and the SiC reinforcement; in the case of squeeze casting it is of the order of minutes, with spray casting, seconds.

Problems in SiC distribution can arise from many of the established particulate MMC manufacturing routes, such as mechanical alloying and melt stirring. PM routes can, however, produce homogeneous distributions of reinforcement (and are not subject to the problem of reaction products at the particulate-matrix interface), ***but*** the material is subject to the oxide layer problems discussed previously.

In summary, PM routes may incorporate oxide particles, and molten metal routes can be susceptible to the problem of reaction between the matrix material and the reinforcement particles. Spray co-deposition has shown itself, as a process, to be relatively free from these problems. The advantages of the process are achieved at reasonable overall operating costs due to a decrease in the number of subsequent processing steps.

2.4 Modelling stress-strain behaviour

The aim of this section is only to give the background to the formulation of equations describing the stress-strain behaviour of metals and alloys under hot-working conditions. Original papers such as (41) should be consulted for more detail.

2.4.1 Review

It is generally agreed that an equation of the form:

$$\dot{\varepsilon} = f(\sigma)\exp\left\{-\frac{Q_{def}}{RT}\right\} \tag{2.1}$$

describes the relationship between strain rate ($\dot{\varepsilon}$), temperature (T) and stress (σ), where Q_{def} is the activation energy of deformation, and R is the gas constant. The stress function $f(\sigma)$ can take several forms, depending upon the stress level experienced during deformation. These equation forms, together with approximate ranges of stress for which they are valid for aluminium, are given below:

Power law

$$f(\sigma) = A_1\sigma^n \tag{2.2}$$

valid for $\sigma < 20\text{N/mm}^2$

Exponential law

$$f(\sigma) = A_2 \exp(\beta\sigma) \tag{2.3}$$

valid for $\sigma > 20\text{N/mm}^2$

Hyperbolic sine law,

$$f(\sigma) = A_3\{\sinh(\alpha\sigma)\}^{n'} \tag{2.4}$$

valid over all ranges
where $A_1, A_2, A_3, n, \beta, \alpha$ and n' are material constants that are independent of temperature, and

$$\alpha = \frac{\beta}{n'} \tag{2.5}$$

where $n' \approx n$.

Equation 2.4 was proposed after similarities between the steady-state creep regime and that of hot-working were noted (41), and is capable of describing the flow stress behaviour over the whole range of stresses due to the fact that at low stress levels ($\alpha\sigma < 0.8$) it reduces to Equation 2.2, and at high levels of stress ($\alpha\sigma > 1.2$) will take the form of Equation 2.3. Combination of the stress function that best fits the data (i.e. Equations 2.2, 2.3 or 2.4) with Equation 2.1, leads to the equations:

$$Z = A_1\sigma^n \tag{2.6}$$

$$Z = A_2 \exp(\beta\sigma) \tag{2.7}$$

$$Z = A_3(\sinh \alpha\sigma)^{n'} \tag{2.8}$$

The above forms of equation are restricted in application to data produced under deformation conditions similar to those used in the formulation of the original equations (41). In order that the stress-strain behaviour of a metal or alloy undergoing deformation in any temperature and strain rate regime in the hot-working range can be described, it is necessary for algebraic functions to be fitted to stress-strain data obtained under constant conditions. Equations of the forms:

$$\sigma = k\varepsilon^m \tag{2.9}$$

$$\sigma = \sigma_0 + k\varepsilon^m \tag{2.10}$$

$$\sigma = A(B + \varepsilon)^m \tag{2.11}$$

where k, σ, A, B, and m are constants dependent on temperature and strain rate, have been proposed (42) to model the stress-strain behaviour of aluminium alloys, but only up to the point at which a steady-state stress is achieved (41). To model the complete stress-strain data of an aluminium alloy, an equation that is capable of describing the steady-state regime is also necessary.

It has been found (43,44) that the following equation forms are able to describe the stress-strain behaviour at these higher strains:

$$\sigma = A(A - B)\exp(-C\varepsilon) \tag{2.12}$$

$$\sigma = \sigma_0 + B\{1 - \exp(-C\varepsilon)\}^m \tag{2.13}$$

$$\sigma = A\{1 - \exp(-C\varepsilon^{mn})\}^{\frac{1}{n}} \tag{2.14}$$

where: σ_0 is the initial flow stress, m is the work hardening coefficient and C is a constant defining the curvature of the first part of the curve.

For aluminium alloys, for which flow stress usually rises to a steady state (due to work hardening and concurrent dynamic recovery), Equation 2.13 is frequently used, and is known as the Voce equation. Use of this equation allows extrapolation of test data to define the flow stress of a material at any given strain. The equation form is fixed, and by altering the constants, can be made to define the shape of experimental stress-strain curves for different materials. The constants themselves are dependent on the stresses at certain characteristic values of strain.

Appendix 2 describes the procedures necessary for the production of Voce-type flow stress equations from the experimental stress-strain data.

2.5 Recovery and recrystallisation

Processing of metals and alloys in the hot working regime (i.e. strain rates of between 10^{-1} and 10^{3} s^{-1} and at $T > 0.6\ T_m$, where T_m is the absolute melting temperature) permits the operation of restorative processes both during ("dynamic") and after ("static") deformation. The study of this subject area is of great industrial relevance as the processes which operate allow large deformations to be undertaken using relatively small applied stresses. Many comprehensive reviews have been conducted in this area (see, for example, (45,46,47 and 48) and, as many of the ideas are very well established, only a brief review of the fundamentals will be presented here.

A result of plastic deformation is work hardening of the material due to the movement of dislocations being hindered by other dislocations, grain boundaries and second phase particles (45). This results in the mechanism of dislocation multiplication, with the dislocation density rising from 10^{10} - 10^{11} m^{-2} in an annealed metal to around 10^{14} - 10^{15} m^{-2} in a heavily worked sample (46). The presence of these extra defects means that the material is in a thermally unstable state. Rearrangement and annihilation of these "extra" dislocations at elevated temperature (either during deformation or upon subsequent annealing) allows the material to be restored to its condition prior to working by a lowering of free energy. The processes by which this lowering of energy generally occurs in aluminium alloys are dynamic and static recovery (DREC and SREC respectively) and static recrystallisation (SRX), and will be outlined in the following sections.

2.5.1 Dynamic recovery (DREC)

Metallic materials vary in their ease of dynamic and static recovery and recrystallisation and can roughly be divided into two groups, depending upon the ease of their formation of stacking faults. Stacking faults are regions in the crystal lattice in which the atoms are imperfectly ordered. High stacking fault energy (HSFE) metals, e.g. aluminium and ferritic steels, have the partial dislocations of the fault closely spaced. When held at high temperatures this allows relatively easy recombination to produce mobile dislocations. HSFE metals therefore present easy dynamic recovery (DREC) at any strain, by means of dislocation cross-slip and climb, to produce a lower energy distribution (16).
Low stacking fault energy (LSFE) metals, where the partials are widely spaced, allow only limited DREC, and at a critical strain undergo dynamic recrystallisation (DRX).

2.5.1.1 The stress-strain curve

In the case of HSFE metals and alloys, work hardening causes an initially rapid rise in stress as dislocation movement becomes hindered. As strain, and therefore the dislocation density, increase, so the rate of DREC also increases. This leads to softening by the annihilation of some dislocations, and the rearrangement of others to form regular cellular arrays, known as subgrains. Eventually, at the strain to steady state, ε_{ss}, the hardening and softening effects balance. No further change in stress with strain occurs, and thus a steady state stress region results.

The level of the stress-strain curve and the onset of steady state deformation are sensitive to both strain rate and temperature. An increase in the severity of the deformation conditions (i.e. higher strain rate and lower temperatures) will reduce the number of recovery events per unit strain, due to lower dislocation diffusion rate. This will lead to an increase in the amount of dislocation generation per unit strain, thus causing annihilation to lag behind generation until higher strains are reached. In this way severe deformation conditions increase the stress level and delay the onset of steady state.

The cellular arrays mentioned above are an attempt to lower the energy of the dislocation arrangements. In the HSFE metals this substructure is well developed. During steady state, the method of "repolygonisation" (46) allows the subgrains to maintain a constant *mean* size, as the concurrent actions of work hardening and recovery constantly produce new substructure. The constant mean size of these subgrains occurs in spite of the normal elongation of the high angle grain boundaries during deformation. The perfection, dimensions and misorientation of the subgrains so formed are indicative of the stage of deformation reached.

2.5.1.2 Static recovery (SREC)

For SRX to occur after hot-working a critical strain of around 0.1 must be exceeded. Where no nuclei have been formed during the deformation (i.e. no dynamic recrystallisation (DRX) has occurred) then a period of incubation will be necessary (of a duration which is dependent on the deformation conditions). Static recovery will always take place in this incubation period but is difficult to follow experimentally. Even if the critical strain for SRX were not reached then SREC could not provide total softening of the material.

2.5.1.3 Static recrystallisation (SRX)

Goncalves (16) states that nucleation of recrystallisation defines a process whereby dislocations are rearranged into a more stable condition, in the production of high angle boundaries which can subsequently grow. Favoured methods of nucleation, such as subgrain coarsening and the bulging mechanism (49) are capable of accounting for the fact that nucleation is frequently observed to be heterogeneous, occurring at particular features such as grain boundaries, where high stored energies exist.

Once a nucleus has formed, static recrystallisation (SRX) can occur if the material is held at high temperature. The areas of low dislocation density will grow into areas of high density, thus replacing strained grains with new strain-free ones. SRX may therefore have a profound effect on the final structure and strength of a metal during hot rolling, depending on whether the interpass times are of sufficient length to allow the processes to occur. SRX can be a useful aid to achieving the required properties of a material, and for increasing the ductility in the majority of processing routes.

The kinetics of primary SRX obey an equation of the Avrami form:

$$X = 1 - \exp -C\left(\frac{t_x}{t_f}\right)^k \qquad (2.15)$$

where:

t_x is the time for fraction X to recrystallise, t_f is the time for a characteristic fraction f to recrystallise and k is the Avrami constant.

C is a constant given by

$$C = -\ln(1 - f) \qquad (2.16)$$

As strain increases so the time to a given recrystallised fraction is reduced. The reasons for this are two-fold:

(i) The stored energy (in terms of unstable dislocation arrangements) is increased.

(ii) Greater strain causes elongation of the original grains thus providing more grain boundary area per unit volume. This provides more nucleation sites per unit volume for a given nucleation density on the grain boundaries.

Because of this last point the original grain size will exert an influence on the recrystallisation kinetics and limit the size to which nuclei can grow before impingement. Point (i) will be significantly affected should SREC occur between deformation and annealing. If the disordered dislocation density is reduced by SREC then the time to recrystallisation will be increased.

2.6 The effect of particles on recrystallisation

Research into the role of non-deformable particles in microstructural development is of great commercial interest. As mentioned in § 2.2 the presence of particles can affect the yield and flow stresses, work hardening behaviour and ductility of a metal, many of these parameters being greatly affected by the occurrence of particle influenced recrystallisation effects.

If processing routes are to be optimised it is vital that a full understanding of a materials behaviour be gained under the conditions which it is processed. It is therefore surprising to find that most of the studies conducted in the field of particle effects on recrystallisation have consisted of cold-working the material before subsequent annealing. Whilst valuable information can be gained from these studies, it is obvious that the energy introduced to the material during deformation will be far greater than if the material was hot-worked. A review of the relevant literature, with regard to large and small particles' effects on the behaviour of aluminium alloy matrices, has been carried out.

2.6.1 Particle stimulated nucleation

It is well established that the presence of non-deformable particles of diameter > 1μm may assist in the nucleation of recrystallisation (50, 51). This phenomenon is termed particle stimulated nucleation (PSN) and may occur because the presence of particles can fulfil parameters essential to the nucleation of recrystallisation, namely:

- high dislocation density
- large orientation gradients

It is suggested by Humphreys and Kalu (52) that there are two possible scenarios during the deformation of a particle hardened alloy, dependent upon the severity of the deformation conditions:

(i) **Elevated temperature and low strain rate**

The rate of dislocation arrival (by glide) at a particle is less than the possible rate of climb around the same particle, and no accumulation results. The subsequent deformational behaviour corresponds to that of a comparable single phase alloy.

(ii) **Low temperature and/or high strain rate**

Dislocations arrive at the particle at a greater rate than they are removed at by climb. Accumulation of dislocations at the particles results because of incompatibility between the deforming matrix and the deformable particle.

The above was proposed after a transition in microstructure was observed in the Al-Si system when progressing to more severe deformation conditions. In case (ii) above, TEM examination of the deformed structures showed that the subgrains near to the particles were smaller and more highly misoriented with respect to those in the matrix. The microstructures produced during the less severe deformation conditions, however, were rarely related to the particles (52).

This transition in behaviour means that a critical strain rate exists for the build-up of dislocations at particles, and this has been expressed as (53):

$$\dot{\varepsilon}_c = \frac{KD}{Td^3} \tag{2.17}$$

where: $\dot{\varepsilon}_c$ is the strain rate at which the transition occurs, K is a constant (equal to 7E-3$m^3s^{-1}K$ in the quoted work), D is a temperature dependent diffusivity term, T is the deformation temperature in degrees K, and d is the critical particle diameter (μm) for PSN at elevated temperature.

The small highly misoriented sub grains arising from type (ii) deformation are a result of local rotation of the lattice in an attempt to accommodate the local elastic stresses caused by the presence of the undeformed particle. The formation of lattice rotations allows the particle to retain, or regain, its original shape (54), and is shown schematically in Figure 2.6. Rotation of the particle and the adjacent matrix allows the relaxation of stresses at the particle, and on further straining the debris from this movement forms an "impenetrable zone" to glide dislocations that may approach. This allows further relaxation in both the particle and the surrounding zone (51). For a detailed discussion of these relaxation mechanisms see, for example, (54).

These areas of locally rotated structures constitute what are known as deformation zones (shown schematically in Figure 2.7), and are vitally important in the stimulation of nucleation (52). The growth phase of recrystallisation may also depend on the presence of these zones, as growth of nuclei has been found to cease when the deformation zone has been consumed.

The model given above is supported by work on the Al-Si system (55), where TEM investigation of the areas near to the Si particles showed highly misoriented subgrains (up to 15°). These were, however, observed never to grow larger than other subgrains in the specimen. This shows that although the nuclei are provided during deformation, the driving force out of the deformation zone is too low for dynamic recrystallisation to occur.

Nes suggests that a nucleation mechanism, based only on the growth of nuclei from local misorientations cannot account for development of different preferred orientations during recrystallisation of some commercial aluminium alloys. It is claimed that nucleation of recrystallisation will occur preferentially at the particles located on grain boundary / transition band type heterogeneities (56). This suggests that the particles act merely as "catalysts" providing the deformation zones in which the heterogeneity-induced nuclei can favourably grow.

Sandstrom was able to reproduce Humphreys' results for the Al-Si system thereby arriving at a similar model for PSN (57). Three stages of growth were observed, and are shown graphically in Figure 2.8. The slow growth rate in stage III is attributable to the lower dislocation density in the matrix compared with that in the deformation zone, whereas stage II shows a significantly accelerated rate of growth in the deformation zone due to the formation of more mobile high angle grain boundaries.

Sandstrom proposed the following criteria for nucleation at particles:

- The nucleus must obtain high angle boundaries in the deformation zone, with a maximum misorientation across the zone in excess of 10°.
- The critical size of the nucleus must be smaller than the size of the deformation zone to enable the nucleus to withstand growing into the matrix.

2.6.2 Critical particle size

It can easily be seen from Equation 2.17 that the critical particle size for nucleation will increase as the strain rate is increased. A reworked version of Equation 2.17 is proposed to describe the critical transitional strain rate for both large and small particles, over a range of temperature (52). This is given below:

$$\dot{\varepsilon}_c = \frac{K_1 \exp\left(-\frac{Q_v}{RT}\right)}{Td^2} + \frac{K_2 \exp\left(-\frac{Q_b}{RT}\right)}{Td^3} \qquad (2.18)$$

where: Q_v and Q_b are the activation energies for bulk and surface diffusion respectively, and K_1 and K_2 are constants, of values $1712 m^2 s^{-1} K$ and $3E\text{-}10 m^3 s^{-1} K$ respectively, from the quoted authors' work on Al-Si alloys.

It is also well established that the number of recrystallisation nuclei per particle is a function of particle size. See, for example (58) where particles were often found to provide a PSN efficiency in excess of 1, i.e. more than one nucleus is produced per particle. This is so because the size of the deformation zone is related to the size of the reinforcement particles. The larger the particle, the larger is the deformation zone, and the greater the amount the nucleus can grow before undertaking the critical step of growth out of the deformation zone and into the matrix.

2.6.2.1 Particle spacing

The spacing of the particles is important in determining the effect on recrystallisation behaviour. Large particles present in clusters provide very strong nucleation sites, and nucleation can be observed at clusters of particles which are individually smaller that the calculated critical size (59). This enhancement arises because of the fact that the deformation zones of several particles may overlap, thus developing very high dislocation density in the area around the cluster. In effect this then provides a larger deformation zone in which the nuclei can grow.

2.6.2.2 Pinning by reinforcement particles

Pinning of newly formed high angle grain boundaries will effectively inhibit the recrystallisation process. Boundaries being pinned by reinforcement particles have been observed in many works (see, for example, (60,61). The ratio:

$$\frac{f}{r} \qquad (2.19)$$

where f is the volume fraction of particles present and r is the particle radius, has been found to be significant in deciding the effect of particles on the recrystallisation behaviour of particle containing metals. If Equation 2.19 is approximately equal to $0.2\mu m^{-1}$ then inhibition of recrystallisation is likely (60).

In work conducted by Humphreys (62) on the hot rolling of powder metallurgy Al-SiC a notable effect of the volume fraction of reinforcement on the extent of recrystallisation was observed and is illustrated in Figure 2.9. It can be seen that for intermediate volume fractions no recrystallisation occurs.

Whilst the f/r value is only about 1/10th of that required to inhibit recrystallisation after cold working it should be borne in mind how much lower the stored energy of hot working is. The authors felt this justified attributing the pinning effect to the SiC reinforcement particles.

2.6.2.3 Pinning effect of small particles

As the recrystallisation process consists of a nucleation and ***growth*** mechanism, the effect of pinning on grain and subgrain boundaries is of primary importance. This section will deal, in brief, with the effect exerted by small particles on the possible movement of a boundary.

The phenomenon of pinning (generally referred to as "Zener drag") was first described by Zener and Smith (63). The situation is considered where a moving boundary comes into contact with a particle. The presence of the particle at the boundary means that a "gap" then exists, with the result that the grain boundary energy is reduced. For the continued motion of the boundary past the particle, an energy greater than this decrease in grain boundary energy must be input to the system. If it is not then "pinning" of the boundary will result. The detailed mathematics of the problem can be found in a number of references (e.g. 16,49,63).

The total pinning force (P_z) in a matrix containing a random distribution of particles is usually represented (e.g. 49) as:

$$P_z = \frac{3f\sigma}{2r} \tag{2.20}$$

where: σ is the grain boundary energy (J/m^2)
and f and r have their meanings as defined for Equation 2.19.

Changes proposed by various workers to this original equation form have, in the majority of cases, been found not to significantly affect the value of pinning force (64), and Nes et al conclude that the approximations inherent to the calculations, and the lack of experimental data with which to validate them, means that the assessment of the "best" equation is very difficult.

At this point attention should be brought to the work of Goncalves (16), where it was found that the Zener equation failed to accurately describe the recrystallisation behaviour of the alloys 8090 and 8091. This will be discussed in § 2.9.4, where the specific case of β' (Al_3Zr) pinning in aluminium-lithium alloys is considered.

2.6.2.4 Bimodal particle distribution

It is well established that alloys containing large (>1μm) and small particles experience a decreased recrystallisation rate compared with that found if just large particles are present. (e.g 65). It is frequently found that materials produced by the PM route are more resistant to recrystallisation than spray cast material due to the presence of small oxide dispersoids resulting from the break-up of oxide skins on the original powder particles (64,66). In studies such as those by Shahani (67) on SiC reinforced aluminium alloy, the oxide powder on the Al is broken up by the extrusion process into stringers. These stringers are found to delineate prior grain boundaries and restrict the movement of new grain boundaries. For this reason recrystallisation is found to occur between the original grain boundaries and result in an elongated recrystallised grain structure.

It is generally agreed that the critical particle diameter required for the nucleation of a recrystallising grain is larger when both large and small particles are present, instead of just large particles. There are, however, conflicting views on just why this is so. Zaidi and Wert (68) state that the recrystallisation rate is due to the small particles lowering the net driving pressure for nucleation of recrystallising grains. Baker et al (69) suggested that the rate is retarded by the homogenisation of the microstructure by the small particles presence. The argument used is that the pinning effect of the small particles on boundaries prevents the highly misoriented regions being formed around the large particles, and so the driving force for recrystallisation nucleation is diminished. This is in contradiction to the work of Chan and Humphreys (65) where Al-Si alloys were produced with varying distributions of particle size. Alloys with large (L), small (S) and bimodal (B) size distributions were produced, and the recrystallisation behaviour compared. It was observed that nucleation occurred at the large particles in both the L and B samples, but that the growth rate was a factor of around ten times slower for the B alloy. From this it was concluded that the main effect of the fine dispersion is to severely slow down the growth stage of the new grains nucleated at large particles.

The model proposed by Nes (70), as discussed in § 2.6.2.2, predicts that as the ratio f/r increases so the critical particle size increases, and the recrystallised grain size increases. Chan and Humphreys (65) suggest that the f/r model is incorrect because it uses the thermodynamics of particle pinning to explain the decreases in recrystallisation rate, whereas the authors felt that it is the *kinetics* of recrystallisation that determines the rate. This implies that the large particles are still viable nucleation sites as the ratio f/r of the fine dispersion is increased, but that the growth of the nucleated grains is retarded.

Experimental support comes from the work of Morris and Ball (71) where the grain size was actually found to decrease with increasing f/r of the disperoids, as the pinning became sufficient to prevent the rapid growth of any grains.

The pinning effect of the small particles is again apparent in the work of Chan and Humphreys (65) where the alloy containing just large particles presented an equiaxed recrystallised grain structure, whereas the alloy which possessed a bimodal particle size distribution was seen to produce a large range of recrystallised grain size, with ragged grain boundaries where pinning of certain areas has occurred. "Island grains" were found to exist in

the bimodal alloy, and were thought to be the result of the more rapid growth of some relatively unpinned grains around heavily pinned grains. The proposed reason for the small grains not shrinking totally is that the shrinkage force, due to the possible decrease in grain boundary energy, is counteracted by the Zener pinning force.

The usually inhomogeneous distribution of dispersoids capable of pinning grain boundaries means that their effect is very difficult to accurately model (64). It is, however, necessary to model the combined effects of small and large particles as most commercial alloys contain both. It is only in this way that the thermomechanical processing schedules can be designed to produce the optimum microstructures.

2.7 Test methods

The assessment of a material's hot-workability is most often investigated by use of laboratory test methods. These methods confer advantages over industrial trials in terms of cost and control of the deformation parameters. The strong effect of strain rate and temperature on the flow stress behaviour of metallic materials means that accurate control and measurement of these parameters are of prime importance if the results are to be useful to industrial metal-formers. The two test methods used in the current research will be briefly reviewed here.

2.7.1 Compression

Compression testing allows reasonably high strains of around 2.5 to be achieved. The use of uniaxial compression tests can lead to barrelling of the specimen at strains in excess of 0.7 (72), which can lead to problems in subsequent stress-strain analysis.

Kapellner et al (73) deemed that it was necessary that "the testing procedure for investigating the hot shaping process resembles the technical process as closely as possible", otherwise it was felt that the results may no longer be open to simple metallurgical interpretation. It was for this reason that the authors decided that hot PSC testing on a laboratory scale was preferred for investigating the hot rolling and forging processes.

Because of the difference in stress systems between uniaxial and plane strain compression tests, the stresses obtained from PSC must be multiplied by a factor of $\sqrt{\frac{3}{2}}$ and plane strains by $\frac{2}{\sqrt{3}}$ to give equivalent uniaxial results. More details of the PSC test method and subsequent analysis are given in Chapter 3 and Appendix 1.

2.7.2 Torsion

The hot torsion test provides a simple means of producing a constant strain rate test up to high strains (possibly up to 20 without significant plastic instability (74)) and is considered to provide a reasonable measure of a material's hot ductility (75). The specimen should be axially constrained if possible, as the constancy of dimensions thus afforded means that the strain rate is truly constant. This constraint will have no effect on the shearing stress, but may affect the fracture process. It

is generally neglected in the production of equivalent stress-strain curves (76). Barraclough also makes the point that identical results can be obtained for fixed and free end tests for small strains.

Regarding the analysis of the torque-twist data resulting from torsion test, the conventional Fields and Backofen approach (see (77)) has the disadvantage that m (strain rate sensitivity) and n (strain hardening coefficient) must be accurately known. Barraclough et al proposed an *"effective radius"* as a way of dealing with this. A full mathematical description is given elsewhere (77), and only a brief outline of the method will be given here. It is considered that at the "effective radius" m = n = 0. Use of this radius for the purposes of analysis simplifies the problems that often result from the pronounced gradients of these parameters through the specimen. It is therefore advantageous to calculate stress, strain and strain rate at this point rather than at the surface, which is usual. For solid specimens Barraclough found that this effective radius always occurred at 0.724a, where "a" is the outside diameter of the specimen (77).

The equivalent stress, strain and strain rate are derived by applying either the Tresca-Mohr or von Mises criteria. Von Mises is generally accepted as the more satisfactory and can be applied to axially constrained specimens without significant errors arising from the longitudinal stresses generated (42). It was, however, thought possible that this axial stress could have a detrimental effect on the strain to failure (76).

As regards the effect of deformational heating, Barraclough (76) makes the point that at lower strain rates the deformational heat is often balanced by the loss of heat by radiation from the specimen surface and conduction to the ends of the specimen and grips, leading to approximately isothermal conditions.

2.8 Deformational behaviour of Al-Li alloys

This section will review the available literature on the behaviour of the aluminium-lithium group of materials when deformed at elevated temperatures.

2.8.1 Description of the stress-strain behaviour

Many of the studies conducted have used torsion as the means of deforming the material. Studies by Smith et al (78) and Oh (79) on the alloy 8090 exhibit some similarities, such as the exaggerated increase in strength at the lowest testing temperatures used (300°C and 320°C respectively), and the tendency for a large amount of softening to occur following the peak stress. The curves of Oh et al, however, exhibit distinctly less softening at the lower deformation temperatures (380-500°C) whilst the curves for deformation carried out at 400 and 500°C by Smith et al still present stress-strain curves with a marked peak.

Whilst a peak in the stress-strain curve is generally associated with dynamic recrystallisation, Smith et al found only elongated grains containing a substructure in the tested and quenched specimens, indicating that only dynamic recovery had occurred. Neither was it felt that the decrease in stress level could be attributed to deformational heating effects, as only a 5 C rise was detected in the higher stress tests.

In Smith et al's study (78), both solution heat treated (SHT) and aged materials were tested.

The fact that at the test temperature of 300°C the SHT material was much stronger, whilst at 400 and 500°C little difference in the materials was evident, suggested to the authors that the peak and subsequent softening was due to excess solute in the SHT material leading to dynamic precipitation, and subsequent coarsening respectively. The presence of a peak and significant softening in elevated temperature stress-strain curves has been observed for other aluminium alloys, e.g. Al-Cu-Mg in a study by Wouters et al (80), and in this case was also attributed to dynamic precipitation processes.

The fact that the curves of 8090 deformed at temperatures in excess of 380°C have been observed by Oh et al (79) to possess no peak does not fit in with the study described above, as all of the specimens in Oh's study were cooled from the SHT temperature, and thus would be expected to have sufficient solute available for dynamic precipitation to occur. Peaks *are* present at all deformation temperatures down to 300°C in the work on 8090 by Smith et al (78).

Niikura et al's work on an Al-Li-Cu-Mg-Zr alloy again found peaks occurred in the stress-strain curve (81). In keeping with the other works mentioned in this section, evidence was only found for a dynamically recovered grain structure. The authors dismissed deformational heating as the cause of the softening (there was no similar peak effect observed in non-Li containing alloys deformed at a similar stress level) and the authors attributed the peak stress behaviour to a solute drag effect by lithium on dislocations during deformation. All of the material tested by Niikura et al had been solution heat treated at 550°C prior to deformation, and so the argument of Smith et al (78) regarding dynamic precipitation of excess solute could feasibly be applied. The effect of %Li on the stress-strain curve shape found by Niikura et al (81) is shown in Figure 2.10. The absence of any appreciable peaks in the case of deformation of the 0%Li alloy is worthy of note. Further evidence for the importance of excess Li in solution to the peak effect is presented in Figure 2.11, where the effect of lowering the solution heat treatment (SHT) temperature is shown. It can be seen that the peaks are virtually non-existent in the case of the deformation of material that has undergone SHT at just 400°C. It is not only the absence of peaks under certain conditions that is of interest from this study. Figure 2.12 illustrates the point that the difference in strength at steady state between alloys of a fixed composition is greater between data gained from tests carried out at 10^{-1} and $10s^{-1}$ than would be expected from the comparison of data from tests at 10^{-3} and 10^{-1} s^{-1}.

Goncalves' study into 8090 using PSC as the means of deformation produced curves of the usual form for aluminium alloys. A feature in common with the other studies, however, was the rapid attainment of steady state, with even the material deformed at 300°C achieving steady state by a strain of 0.3.

2.8.2 Constitutive relations

The first stage in the formulation of a constitutive relation to describe a material's behaviour must be the calculation of a suitable activation energy of deformation, Q_{def}. (See Appendix 2). In the literature surveyed, a wide range of values of Q_{def} has been reported. The values obtained by various workers are presented in Table 2.2, along with the compositions of the alloys used.

It is suggested by Smith et al (78) that the very high peak stresses observed when the solution

treated material is deformed at 300°C may indicate the necessity for either an overall higher activation energy, or the use of two activation energies, to describe differing mechanisms for low and high temperature deformation. It is suggested that the possibility of dynamic precipitation may prevent sub grain formation, and thus lead to a higher stress level. Whilst Smith et al (78) used the hyperbolic sine form of equation to describe the high temperature deformation behaviour. the studies by Oh et al (79) and Goncalves (82) found that the exponential law was sufficient to describe the material behaviour. The relevant constants are listed in Table 2.2. Oh et al highlight what appears to be very different behaviour of the 8090 alloy at different deformation temperatures. Both power and exponential laws show that at 500°C the material strength is virtually independent of strain rate. The constants from these analyses are provided in Table 2.3. It should be borne in mind that although the β values (i.e. the slope) from the $\ln \dot{\varepsilon}$ vs. σ plots are very similar for all of the other deformation temperatures considered, the lines for the 320°C deformations are very much displaced on the stress axis, because of the higher stress levels experienced. An example of such a plot from Oh et al's work (79) is given in Figure 2.13, where the exponential law to describe the behaviour at steady state is shown. Despite the difference in behaviour at the extremes of deformation temperature, one equation is suggested to describe the behaviour of 8090 deformed at elevated temperature. The constants resulting from this analysis and the other equations reviewed here are given in Table 2.2.

Whilst a different microstructural behaviour of 8090 was noted by Goncalves (16) after deformation at low and high temperatures, it was not found to be necessary to use two different values of Q_{def} to describe the behaviour, and a value in agreement with "conventional" aluminium alloys was used satisfactorily.

It has been noted (78) that considerable scatter in experimental data points could occur as a result of the sensitivity of 8090 to small variations in the reheating procedure.

2.8.3 Ductility

The work on torsion testing of 8090 by Oh et al (79) provides data of strains to failure (ε_f) over a comprehensive range of temperature and strain rate. These values are given in Table 2.4. The high values of ε_f should be noted. For comparative purposes the values of ε_f found by Smith et al (78) are also included.

Goncalves (83) states that high ductility values are expected from unrecrystallised material, and found this to be the case in his work on alloys 8090 and 8091. Tensile tests on rolled material showed there to be very little difference in the properties of 8090 with respect to the temperature at which the material had been rolled. 8091 did, however, show a marked increase in the % elongation for the specimens produced from material rolled at the higher temperatures. This was presumably due to the amount of dynamic recovery that had occurred. The observed positive effect of unrecrystallised structures on ductility is in agreement with work by Takahashi et al (84) and has been attributed to a high energy absorbing transgranular fracture mode (85). The change from intergranular to transgranular fracture mode has also been used to explain the observed increase in ductility with strain rate during a study conducted using torsion testing of a Al-2.76Li binary alloy (86).

2.9 Recrystallisation of Al-Li alloys

This section will attempt to provide a view of the most important aspects of the recrystallisation behaviour of the Al-Li group of alloys. Considering that the recrystallisation behaviour following hot deformation is of major significance in deciding the final properties of the processed material, relatively little research has been conducted on grain structure development of some of the more important commercial alloys, e.g. 8090. This is, perhaps, an indication of the level of complexity of such a study involving these alloy systems. Before discussing patterns and mechanisms of recrystallisation it is important to decide what is a desirable microstructure for processed material. The answer to this question depends upon what end use the material is to be put to. It is certain, however, that the partially recrystallised state is to be avoided due to the resulting inhomogenenous microstructure. The relative advantages and disadvantages of unrecrystallised and recrystallised structures will be discussed below.

2.9.1 Unrecrystallised structures

Whilst the unrecrystallised state leads to anisotropy of structure and properties, it is still necessary when considering certain applications. For high strength plate, the presence of a substructure leads to higher strengths than are possible with recrystallised material (87,88), so much so that for alloy 8090 Miller et al (89) state that the contribution to strengthening from grain and sub-grain boundaries could be equal to as much 56% of the contribution from the main strengthening phase, δ' (Al_3Li).

Whilst anisotropy of mechanical properties does exist (due to the highly textured nature of unrecrystallised 8090) (88), the coarse laminar structure can help to improve the fracture toughness of 8090 in the L and T directions by providing reduced sensitivity to crack nucleation. In addition, high values of elongation in the L and T directions have been found for unrecrystallised material compared with that which is recrystallised (84). The poorer values in the S-T direction must of course be taken into account in design. The tendency to recrystallisation is reduced during processing by using as high a finishing temperature as possible, in combination with short solution heat treatment times (90).

2.9.2 Recrystallised structures

An important application of conventionally recrystallised Al-Li alloys (predominantly 8090) is that of damage tolerant sheet for the aerospace industry (91) - it is now felt that 8090 can produce damage tolerance superior to that of the alloys that it was originally intended to replace (88).

The planar slip inherent to alloys of the Al-Li system makes them susceptible to strain localisation and microbanding. A recrystallised structure after solution heat treatment is therefore advantageous in that it initially provides a random selection of slip systems. This delays the formation of localised slip until higher strains are reached (92), and thus provides improved homogeneity in ductility and fracture toughness.

Recrystallisation can be achieved by decreasing the Zr, Mg and Li contents, utilising optimised roll pass schedules and inter-anneals, and by the utilisation of salt baths to increase the heating rate during the final solution heat treatment (88). Modified chemistry versions of alloys still tend to exhibit anisotropic behaviour and so modified thermomechanical treatments are viewed as more favourable (91).

2.9.2.1 Applicability for super-plastic forming (SPF)

A very fine grain structure is required of a material if superplasticity is to result, and the material is usually recrystallised to produce the necessary fine structure. Because of the difficulty in recrystallising many commercial Al-Li's, strain assisted continuous recrystallisation is used by some manufacturers (93), with the fine microstructure being produced dynamically during the early stages of deformation. An alternative is given by Wadsworth et al (94) where the material is solution heat treated, aged and then rolled to a high strain at a low temperature prior to SRX at the superplastic forming temperature.

2.9.3 Elements/mechanisms used in controlling recrystallisation

The elements Cr, Mn, and Zr have all been utilised in the control of the grain structure of Al-Li alloys. Zr is the most powerful of these (via the formation of the coherent β′ phase, Al_3Zr), and this is reflected in the fact that it is used for grain structure control in all of the commercial Al-Li base alloys (95).

The planar slip effects inherent to the Al-Li alloys are minimised by the addition of Zr, both by means of promoting grain refinement (and therefore reduction of slip line length) and by the promotion of substructure (via boundary pinning), that inhibits dislocation movement (87). It is the inhibition of grain boundary movement that often results in processed material having highly elongated unrecrystallised grain structures with pronounced crystallographic texture.

Many studies have been conducted into the recrystallisation behaviour of the Al-Li-Cu-Mg system where the Zr content has been systematically varied in the range around 0.01-0.16 weight % (e.g. 92,96,97). The results usually suggest that there is a minimum % of Zr necessary to begin to control recrystallisation, and this has been found by one group of workers to be fairly independent of the extrusion parameters used in the study, and of the Mg and Cu content (97). It is usually found that the lower limit of % Zr is around 0.04%. Above this value, the alloy tends to show progressively increased resistance to recrystallisation. Below 0.04%, a fully recrystallised and equiaxed grain structure usually results from solution heat treatment (92). Relatively high Zr contents (around 0.05%) are sometimes used in the production of superplastic material, allowing continuous recrystallisation during the initial straining, and then stabilisation of the final grain size (98).

The most likely reason for the ease with which the Zr additions (as β′ (Al_3Zr)) retard the grain boundary migration is thought to be the requirement for the β′ particles to transform from coherent to incoherent if a boundary passes (95,99).

TEM investigations have shown that the β′ particles provide preferential nucleation sites

for the δ′ (Al_3Li) phase (17) - the main strengthening phase in the commercial Al-Li systems. Provided that the β′ phase is distributed uniformly, this can help to homogenise the distribution of δ′ (100).

The formation of recrystallised layers at the surfaces of Al-Li alloys solution heat treated for long times at high temperatures is well known (e.g. 101,102). Two possible theories are suggested for this phenomenon. Makin and Stobbs (102), in work on the ternary Al-3Li-0.12Zr system, suggested that a sizeable proportion of the pinning effect is the result of solute drag from Li on the boundaries. As the time of solution heat treatment continues so the Li depleted region (caused by the diffusion of Li to the surface and the formation of oxide) grows. The grain boundaries, then free from the drag effect of Li, are free to migrate thus allowing recrystallisation. Secondly, TEM studies of the surface and centre of heat treated alloy have shown that the supposed "synergistic" effect between Li and Zr appears to be correct (97). This work by Collier et al has shown that the β′ distribution agrees with that for δ′, therefore as the Li at the surface is lost by oxidation, the stability of β′ appears to decrease and eventually the β′ particles begin to dissolve, thus allowing recrystallisation to proceed.

2.9.4 Pinning due to β′ (Al_3Zr)

Goncalves' work on 8090 and 8091 (16,99) has shown that, in some instances, the Zener pinning model (see § 2.6.2.3) is not as applicable as was at first thought. Moving boundaries were found to envelope the precipitates rather than cut them, and a significant pinning effect was observed, when the balance of recrystallisation driving force (F_R) and Zener pinning force would suggest that none existed (90).

The Rios model (103) has been found to better describe the situation with these alloys. The model (as developed by Goncalves (99)) will be described briefly below.

Considering the growth stage of the recrystallisation process:

for a volume fraction, f, of spherical precipitates of radius, r ,the critical radius for grain growth, R_c, is:

$$R_c = \frac{r}{6f} \tag{2.21}$$

From the classical theory of grain growth (104), the driving force for grain growth, F_g, is given as:

$$F_g = \frac{2\sigma_s}{R} \tag{2.21}$$

where σ_s represents the grain boundary energy and R is the radius of the growing grain. When grain growth ceases, $R = R_c$, and the driving force, F_g, is balanced by the pinning force, F_p. The combination of Equations 2.21 and 2.22 then leads to the expression:

$$F_p = \frac{12\sigma_s f}{r} \tag{2.23}$$

For the values used by Goncalves:

f (equal to the volume fraction of Zr) = 0.00145 for 8090 (99)
r (β' (Al_3Zr) particle radius) = 33E-9 for 8090 (99)
$\sigma_s = 0.324 J/m^2$ (105)

it was found that the driving and pinning forces counter-balance each other when the start-rolling temperature is in the range 400-450°C. Therefore at rolling temperatures greater than 450°C $F_p > F_R$ (where F_R is the driving force due to recrystallisation) and this results in an elongated recrystallised structure, whereas for rolling temperatures less than 400°C, $F_p < F_R$ and an equiaxed recrystallised structure results.

2.9.5 Patterns of recrystallisation

As seen in § 2.9.3, the Zr content critically affects the fraction recrystallised in these materials. Studies have shown that limited (or no) recrystallisation occurs unless severe strains are imposed (87). The planar slip often present in Al-Li alloys is frequently found to lead to a pattern of recrystallised grains on the preferred slip planes, and the strong effect of Zr on boundary mobility is found to be responsible for the commonly observed move from laminar recrystallised structures to equiaxed grain structure as the deformation conditions become more severe (83,99). The next section will describe some of these patterns in recrystallisation behaviour that have been observed.

2.9.5.1 Problems in recrystallising Zr-containing Al-Li alloys

The difficulty in achieving recrystallised structures in this class of alloys is well known. Extruded structures have frequently been found to exhibit recrystallised surface layers, but virtually no recrystallisation at the core (105,106). In these same studies, the alloys (including 8090) were found to show very great resistance to SRX thereafter, with the extruded structure remaining unchanged through subsequent solution heat treatments; even the sub-grain structure was found to be stable (105). Mukhopadhyay et al (106) have shown that further annealing in excess of 5 hour at 530°C merely caused grain growth in some pre-existing fine grains, so stable was the structure. In all cases the core was found still to be unrecrystallised. Whilst the recrystallised layers commonly found at the surface of worked Al-Li material are frequently

attributed to the loss of Li through diffusion and oxidation (and a consequent decrease in solute drag (102), Mukhopadhyay et al found that the recrystallised layer extended to a depth that was greater than could be accounted for by this mechanism, and therefore attributed the phenomenon to severe surface strains (and therefore high driving force for recrystallisation) resulting from the extrusion process (106). A study by Sheppard and Tan (107) on 2090 (extruded at ratios between 10 and 50:1, at temperatures of 350-525°C and then solution heat treated for 40 minutes at 530°C before ageing) found that the extrudates did recrystallise. At the highest deformation temperatures there was a very considerable increase in the fraction recrystallised, which was attributed to DRX. Upon further solution heat treatment additional recrystallisation was found to occur, and in this case the relatively low Zr content of 0.07% was thought to be partially responsible for the recrystallisation behaviour.

Makin and Stobbs (102) have found very limited recrystallisation after a solution heat treatment of 16 hours at the high temperature of 580°C. A "limit of softening" was attained, with hardness decreasing from around 95 VPN as-cold-worked to 60+/-5VPN within a few minutes of solution heat treatment. This was found not to be due to recrystallisation, and was attributed by the authors to a "low activation energy for recovery processes".

2.9.5.2 Mechanisms of recrystallisation in the Al-Li alloys.

Having discussed patterns of recrystallisation that have been observed, it is important that the processes by which these patterns arise are reviewed. § 2.5 has reviewed the general recovery/recrystallisation literature and therefore this section will concentrate only on the mechanisms observed in the Al-Li system.

Many workers have investigated the reasons for two of the most commonly observed phenomenon in the recrystallisation behaviour of this group of alloys:

(i) The structures are often banded in the deformation direction

(ii) There is generally a transition from elongated to equiaxed recrystallised grain structures at some critical condition of deformation.

The original grain boundaries are found to play a very large part in the formation of both of these features. High angle grain boundaries have been found to be important sites for the nucleation of recrystallisation in Al-Li alloys by many workers, and the nucleation is often found to occur by a rotation and coalescence mechanism of enlarged subgrains associated with high angle grain boundaries (e.g. 87,107). The same mechanism has been found to occur at deformation bands (108).

Goncalves (16) suggests the following as a reason for the transition in observed aspect ratio of the recrystallised grain structures:

If subgrain coalescence is assumed as the nucleation mechanism then at high deformation temperatures the large subgrains that result mean that there is not enough room across a deformed grain to allow sufficient misorientation for the production of a high angle grain boundary. The coalescence therefore continues by engulfing subgrains in the longitudinal direction. However, at low deformation temperatures small subgrains are formed during deformation. Sufficient of these are able to coalesce, across a grain, to produce a nucleus without meeting the barrier of a high angle grain boundary. This leads to smaller equiaxed nuclei. Goncalves proposes the fact that 8091 (which possesses a finer grain substructure for given deformation conditions) produces a more equiaxed grain structure as evidence. The nucleation of new grains at the original grain boundaries has been used by other authors to explain the banded nature of the recrystallised structures under many conditions (105).

Bulging of boundaries into others, driven by dislocation density differences across the boundaries, has been observed in Al-Li alloys (102,108), and in the former study was found to be promoted by the use of higher reheating rates. The observed increase in the rate and extent of recrystallisation resulting from the use of a higher reheating rate is attributed to the suppression of recovery permitting a greater driving force for the recrystallisation processes to proceed. The difficulty experienced in recrystallising the ternary Al-3Li-0.12Zr alloy studied by Makin and Stobbs (102) was attributed to the pinning forces exerted on the substructure by the presence of the β' (Al_3Zr) particles in the following way: In an alloy such as Al-Li-Zr, it is considered likely that recrystallisation nuclei may be formed adjacent to high angle grain boundaries (as was observed) via a subgrain coalescence mechanism. Doherty and Cahn have developed a strain induced boundary migration (SIBM) model (109) whereby the necessary bowing of a section of high angle grain boundary into a grain of higher stored energy is possible because of subgrain coalescence processes occurring adjacent to that boundary during annealing. (As stated above this bowing of boundaries was also observed in the study discussed here). If, as is generally agreed, β' particles pin the subgrain boundaries, then the resistance of the structure to this process would be increased, and nucleation by this mechanism would be very difficult. The authors conclude that the combined effects of the pinning β' particles, slow reheating rates and solute drag on high angle grain boundaries due to Li lead to extensive recovery prior to nucleation and are jointly responsible for the suppression of recrystallisation in this alloy. Their studies into the binary Al-Li and Al-Zr alloys indicate that, in isolation, none of these effects are sufficient to prevent recrystallisation occurring.

3 Experimental Details

3.1 Introduction

The aim of the experimental work performed within this research project is to provide a description of the elevated temperature behaviour of the materials studied. The use of plane strain compression (PSC) testing allows the accumulation of accurate stress-strain data which can then be isothermally corrected and used for the formulation of constitutive equations. Use of torsion testing, and comparison of the resulting stress-strain data, provides an insight into the materials' behaviour under different strain regimes and information about the material's ductility. An attempt is made to give a rounded view of the hot-workability of these materials through a study into the restoration processes that occur at the solution temperature after hot rolling.

3.2 Materials used

The materials under investigation have, as their base, alloys from within the 8090 system, the compositional limits of which are shown in Table 3.1. All material tested has been produced by Alcan Laboratories, Banbury, by means of the Osprey spray-deposition process. Both of the materials investigated were provided in two different conditions. The actual materials used, therefore, are:

(i) **ASC**. 8090 monolithic alloy, spray-cast and homogenised.

(ii) **AMMP**. 8090-16% SiC, spray-cast and homogenised.

(iii) **MONO**. 8090 monolithic alloy, spray-cast, homogenised and extruded at a ratio of 22:1 to rectangular bar of cross-section 63x25mm.

(iv) **MMC**. A composite consisting of 8090 matrix alloy plus around 17 volume % of 12μm silicon carbide (SiC), in the same condition as the above.

The extruded condition was investigated because of its obvious commercial importance (all "Cospray" material was extruded after spraying to close up porosity) and the as-cast material for a study into the material behaviour without any prior deformation.

Grain sizes of the as-supplied extruded material proved difficult to ascertain because of problems in satisfactorily anodising samples of non heat-treated material, but are around 6μm for the monolithic alloy, with aspect ratios of up to 60. The as-supplied extruded composite material proved impossible to grain size with any degree of accuracy. The microstructure is depicted in Figure 4.58, and can be seen to exhibit lower aspect ratios than its monolithic counterpart. The

as-supplied spray-cast and homogenised materials initially have equiaxed grain structures and are more easily examined. Initial grain sizes of around 40-50μm for both the monolithic 8090 and composite material have been measured.

The exact compositions of the materials used for each series of experiments are shown in Tables 3.1 and 3.2.

3.3 Experimental conditions

3.3.1 Plane strain compression

Plane strain compression testing was carried out on a computer controlled servo-hydraulic machine, described in detail elsewhere (110). Use of this test apparatus allows accurate constant strain rate tests to be performed under nominally isothermal conditions in the strain rate range of $0.05s^{-1}$ to $50s^{-1}$, and over a range of temperatures from room temperature to 1100°C. The position of the hydraulic ram and the load are recorded, and these data allow strain, strain rate and stress to be calculated. The machine is shown in Figure 3.1 and again in schematic form in Figure 3.2. A 1.5mm K-type chromel-alumel thermocouple inserted to the centre of the deformation zone permits the temperature history from re-heat to post-quench to be recorded. By performing tests at a range of different temperatures and strain rates the stress-strain behaviour can then be fully investigated.

The thin slab specimens of dimensions 50x30x10mm (shown in Figure 3.3) are mounted on the arms of a trolley system (see Figure 3.4) and heated in the pre-heat furnace for a period of time equivalent to 40 minutes isothermal treatment at 530°C. The specimen is transferred from the pre-heat furnace to the test furnace by means of this trolley system, and is then soaked at the test temperature for a period of three minutes, in order that any temperature gradients produced in the specimen during transit may be removed.

The deformation schedule used in this series of experiments consisted of constant strain rate isothermal tests to a strain of 1.5. Equivalent tensile strains are used throughout, converted from the near plane strain conditions using the conversion factor F given below:

$$\varepsilon = F \ln\left(\frac{h_{f(test\,T)}}{h_{0(test\,T)}}\right) \tag{3.1}$$

given that:

$$F = \frac{1.155(b - w) + w}{b} \tag{3.2}$$

where:

$$b = b_0\left(1 + C - \left(C\sqrt{\frac{h}{h_0}}\right)\right) \qquad (3.3)$$

and: b_0, b are initial and final specimen breadths

h_0, h are initial and final specimen thicknesses

w is the tool width and

C is the spread coefficient (described in more detail in Appendix 1).

The temperatures used were 300, 400 and 500°C in combination with strain rates of 0.05, 1 and $10s^{-1}$ to provide a matrix of conditions suitable for the formulation of the constitutive equations.

The extruded specimens were all tested unlubricated because of initial concerns that the SiC particles in the composite material might "cut" through any lubricant applied during the later stages of deformation (when the lubricant film is thin), thus leading to different friction conditions for the MMC and monolithic materials. The use of unlubricated tests was therefore an attempt to provide the same interfacial conditions for both materials. It was then assumed that full sticking friction was operating during the tests. Pressure-displacement curves are particularly sensitive to the value of friction coefficient (μ) in the range $0<\mu<0.1$ (the normal range covering lubricated tests). The curves are, however, less sensitive in the range covering unlubricated tests, i.e. $0.3<\mu<0.6$. This means that any variation in μ due to the presence of SiC should have a less significant effect on the stress-strain behaviour when tests are performed unlubricated.

The as-spray-cast materials were tested in the lubricated condition after problems were encountered with the apparent breakdown of the full sticking friction regime mentioned above. As the graphite lubricant used is only stable up to 500°C, the severity of the re-heat period would mean that the lubricant would degrade prior to the test being performed. To avoid this problem the reheat was carried out without the graphite, and it was then applied in the period of air cooling down to the test temperature.

After the test has been performed a raw data file is produced consisting of displacement, load, temperature in mV, and command signal for the duration of the test. This file is input into the "Turtle" analysis program which provides easily interpreted values of displacement, load, temperature in degrees Celsius, stress in MPa, strain, and Z, the temperature compensated strain rate, or Zener-Hollomon parameter).

More comprehensive details of the testing machine, its operation and analysis of the resulting data are given in Appendix 1.

Appendix 2 lists the procedures necessary to produce isothermally corrected curves and the analysis of the data required for the formulation of the final constitutive equations.

3.3.2 Torsion

Hot-torsion testing was performed only on the extruded grades of material, in an attempt to study the hot ductility of the commercially available material. The stress-strain curves produced also enable the testing methods of torsion and plane strain compression to be compared.

Solid specimens of both the monolithic and MMC materials have been torsion tested using the facility at Alcan International, Banbury, utilising specimens of the dimensions shown in Figure 3.4. The testing machine is shown in Figure 3.5 and schematically in Figure 3.6. A detailed description of the testing equipment is given below.

3.3.2.1 The torsion machine

The machine is driven by a 6kW 3-phase motor giving a torque capacity of 29.8 Nm. Infinitely variable output speeds of 50-1200rpm are available, the torque being applied to the test-piece through an electromagnetic clutch with an engagement time of around 0.02s. A heavy flywheel, together with the aforementioned clutch, ensure that at speeds < 580rpm the rate of twist applied to the specimen is maintained constant from the instant that the test is started.

The specimen is held in a pair of grips, one affixed to the driving chuck and the other to the stationary shaft. Deformation is carried out to a pre-determined number of revolutions set via an electronic counter controlling the clutch and brake systems.

The torque transmitted by the specimen during the test is measured by strain gauges attached to a cantilever beam on the stationary shaft. This system is calibrated by hanging standard weights on a lever attached to this beam. It has been found previously (111) that the torque values measured are accurate to +/-2%. A photo source shining through a disc slotted at 90° intervals generates pulse signals which are detected by a photo-electric cell and enable the number of twists (and in turn the twisting rate) to be monitored. Outputs from the strain gauges and the photo-electric cell are converted to D.C. voltage signals and logged on a 3-channel H.P 7090A recorder.

The raw torque-twist data were saved to disk and subsequently analysed using the method outlined in Appendix 3.

All specimens were heated in the R.F. induction coil to 530°C, at a rate of around 200°C/minute. The temperature was sensed by a 1mm diameter K-type chromel-alumel thermocouple inserted axially into the specimen to a position at the edge of the shoulder (see Figure 3.4). This temperature was then maintained for a period to give 40 minutes equivalent time at 530°C prior to testing. After air-cooling to the test temperatures of 300, 350, 400, 450 and 500°C all specimens were tested to failure at one equivalent tensile strain rate of $1s^{-1}$, at the surface. This provides an equivalent strain rate of $0.73s^{-1}$ at the "effective radius", described in Appendix 3. They were subsequently water-quenched within around 5s.

Tests were mostly performed "free-end" (the stationary grip is not axially constrained) with some tests being performed as "fixed-end" when it became apparent that this type of test could be performed using the existing test facilities. Fixed-end tests allow the specimen geometry to be maintained constant through the deformation and thus provide more easily interpreted results. As the majority of tests in this series were performed free-end, the stress-strain curves have been corrected to reflect the behaviour under fixed-end conditions. The correction method is described in more detail in § 4.2.

3.3.3 Rolling

Slabs of dimensions 100x40x20mm (cut from extruded bar for materials (i) and (ii) above and from billet for materials (iii) and (iv)) were hot-rolled after pre-heating to 530°C in a resistive element furnace. The duration of the re-heat was equivalent to 40 minutes isothermal treatment at this temperature, calculated from the heating curve T_i vs t_i according to the equation:

$$t_{equivalent} = \Sigma t_i \exp \frac{\left(-\frac{Q}{RT_i}\right)}{\left(-\frac{Q}{RT_{anneal}}\right)} \tag{3.4}$$

using an activation energy, Q, of 230kJ/mol.

The rolling was performed on a 2-high reversible Hille mill, of roll diameter 137mm, at a roll speed of 0.2ms^{-1}. Prior to rolling the slabs were air cooled to the start rolling temperatures of 480, 400 and 300°C for the monolithic materials, and to 480 and 400°C for the composite materials. Lack of ductility at the lowest temperature prevented its use with the composite materials. The temperature was monitored in all cases by a 1.5mm diameter chromel-alumel thermocouple inserted to the centre of each slab and connected to a PC based data-logging system. The slabs were subjected to a 3 pass reduction schedule of 20%, 30% and 30% to provide a total reduction in thickness of 60%. The loads during each pass were recorded, via the two 27 tonne load cells of the mill, on a calibrated U.V. chart recorder. After the schedule was completed the specimens were cold water quenched in around 5s.

This pass schedule was used so as to mimic as closely as possible the conditions used in previous work on D.C. cast 8090 (16) so that comparisons in the materials' behaviour may be drawn. At the time of the aforementioned research, (1986-1989), this reduction schedule was used in industrial practice. The rolling temperatures were selected because it had previously been concluded that for the pass reductions given they were the most useful in illustrating the behaviour of 8090.

3.3.4 Heat treatments

Specimens of dimensions 20x10x20mm were cut from the rolled and quenched slabs from the positions shown in Figure 3.7. These were subsequently heat treated, at the solution

temperature of 530°C, for several intervals in the range 1/2 to 336 hours for the monolithic alloys and 30 seconds to 8 hours for the composite materials. All times of heat treatments are given as equivalent isothermal times at 530°C, calculated according to Equation 3.4. Heat treatments were performed in an electric resistive element furnace.

3.4 Methods of analysis

3.4.1 Analysis of PSC load-displacement data

The raw data from the servo-hydraulic machine are analysed using software developed in this department (112). Once the basic stress-strain curve has been produced it is necessary to correct the data for the effects of a number of variables, namely friction, spread of test specimens, temperature rises due to deformational heating. A discussion of the need for such corrections is given here, and the methods used are given in Appendix 1.

3.4.1.1 Spread correction

During plane strain testing there is invariably some spread in the 2 direction (shown in Figure 3.8). This will decrease the stress level calculated by the computer, as the load-bearing area will increase as the test progresses. For calculation of accurate flow stresses the instantaneous contact area throughout the deformation is therefore needed. The use of a "spread coefficient" enables this area to be calculated.

3.4.1.2 Friction correction

Friction between the tools and specimen leads to an increase in the load during a test, as the material under test is constrained in the deformation zone rather than flowing outwards. High frictional forces can also lead to large amounts of "redundant" work being done due to the test material shearing rather than slipping out of the deformation zone. This can mean that the specimen experiences a far higher strain rate than is indicated by the test data. The use of too high a coefficient obviously leads to an artificially low stress level, as it leads to the "assumption" by the analysis program that a greater proportion of the work done is redundant due to shearing of the specimen than is actually so. The reverse of this is also true.

Determination of the effective coefficient of friction, μ, involves testing specimens of different initial thicknesses (usually 10mm, 6mm and 4mm), to a constant strain, and over the range of test temperatures used. Deformation of the thinner specimens will involve more redundant work and the stress-strain curves will therefore migrate upwards towards the end of the deformation. When the correct friction coefficient is found (by the method given in Appendix 2) then stress-strain curves from different thickness specimens can be superposed upon one another.

3.4.2 Constitutive equation formulation

The methods of isothermally correcting the stress-strain data from the PSC test schedule, and the formulation of the constitutive equations to describe this stress-strain behaviour are dealt with in Appendix 2.

3.4.3 Analysis of torque-twist data from torsion tests

The analysis of the raw torque-twist data to produce true stress-strain curves is dealt with in detail in Appendix 3.

3.4.4 Microscopical methods and quantitative metallography

Heat treated rolled specimens were sectioned longitudinally, using a diamond slitting wheel, and mounted in slow set resin. The samples were prepared using a standard grinding and polishing regime of 120, 400, 800 and 1200 grit SiC papers followed by 6μm diamond. At this stage the composite was subjected to a further 1μm diamond polish, with both types of material receiving a final polish using colloidal silica. All samples for metallographic examination were subsequently anodised using an applied voltage of 20V for 120 seconds, in Barkers etch (a 2% HBF_4 solution in water). The anodised samples were examined under crossed polars, with a variable wavelength plate filter being used to provide the colour contrast. It was not viable to quantify fractions recrystallised for the series of heat treated samples, for reasons outlined in § 4.3.3.

3.4.5 Other analytical techniques

In this section, other techniques which have been used during the course of this research will be briefly described.

3.4.5.1 Hardness testing

Problems were encountered when attempting to quantify fractions recrystallised from the rolling series, when using the usual point counting methods. It was therefore decided to undertake a series of experiments which involved hardness testing of freshly heat treated specimens. It was of importance that the specimens had been solution treated recently with respect to the hardness tests being performed, because of the marked natural ageing of the materials studied. Specimens were quenched immediately after their heat treatment times and were then ground plane and polished to a 6μm diamond finish prior to hardness testing. Measurements were taken at 1/4 depth from the surface.

3.4.5.2 Scanning electron microscopy

Back scattered electron imaging was used in an attempt to distinguish between recrystallised and unrecrystallised and/or recovered grains. Samples of the monolithic alloys were mounted in conducting Bakelite and subsequently ground and polished to a colloidal silica finish. The samples were electropolished using a 10% solution of perchloric acid in methanol at a temperature of -35°C at a potential difference of 25V. The time of etching recommended (113) produced significant scarring of the specimen surface. A time of 15s was found to have less of a detrimental effect on the surface quality. In the scanning electron microscope (SEM) a working distance of 5-10mm was used, with a working voltage of 5kV. No useful image was produced by this method.

The method of EBSP (electron back scattered patterns) was also attempted. This method necessitates use of the same working conditions described above, but involves using the clarity of the diffraction patterns that can be produced as a means of detecting whether a grain is recrystallised or not. If a grain is recrystallised then a clear pattern is produced. This method also provided no useful results.

3.4.5.3 Transmission electron microscopy

Thin foils of the monolithic materials were produced and viewed in a Philips EM420 transmission electron microscope (TEM) at a working voltage of 120kV. This work was carried out for three reasons:

(i) To ascertain whether certain structures were recovered or recrystallised, judged on whether a well defined substructure could be imaged.

(ii) To ascertain if any difference existed in the size of the pinning β′ (Al_3Zr) phase between samples rolled at different temperatures.

(iii) To investigate whether any coarsening of the β′ phase occurred at long solution treatment times.

The foils viewed were taken from the following material conditions:

ASC, as-rolled at 300°C
ASC, as-rolled at 400°C
ASC, rolled at 300°C and subsequently heat treated for 30 minutes
ASC, rolled at 400°C and subsequently heat treated for 14 days
MONO, as-rolled at 400°C.

The above materials were investigated because it was felt that they would provide the most useful insight into the behaviour of the material without undue complications.

4 Results

4.1 Plane strain compression tests

Nominally isothermal tests were performed at 300, 400 and 500°C and at strain rates of 0.05, 1 and $10s^{-1}$ using conditions given in Chapter 3. The raw data have been analysed using the methods given in Appendix 2.

4.1.1 Friction coefficient

A friction coefficient of value 0.1 was found to provide the best fit to experimental data for the graphite lubricated tests. For the unlubricated series a coefficient of value 0.6 was used, to provide the analysis program with conditions of full sticking friction.

4.1.2 Spread coefficient

A spread coefficient specific to each test specimen has been calculated for the materials studied and the values are given in Tables 4.1-4.4. There appears to be more variation between the lubricated and unlubricated tests for the monolithic materials than for the equivalent conditions in the composite materials.

4.1.3 Shape of the stress-strain curves

Excepting a few cases the form of the curves is not that expected for aluminium alloys. It can, however, be seen that all of the materials exhibit the usual behaviour for high temperature deformation of an increase in flow stress with increasing strain rate, and decreasing temperature.

4.1.3.1 Uncorrected curves

The uncorrected stress-strain behaviour is depicted in Figures 4.1-4.12. For all four materials it is noted that the effect of work hardening decreases with decreasing strain rate and increasing temperature. When subjected to deformation conditions less severe than 400°C and $10s^{-1}$ no appreciable curvature due to strain dependence is noted for any of the materials studied. Work hardening is much less pronounced in the case of the MMC series under the more severe deformation conditions.

The usual effect of softening due to deformational heating is seen under the most severe deformation conditions. In the case of the AMMP series the effect is so pronounced that the curves from deformation at all temperatures, at 1 and $10s^{-1}$, meet. This effect is shown in Figures

4.7-4.9. A similar effect is observed in the case of the MMC material deformed at 300 and 400°C and for the MONO material when deformed at 400°C. This behaviour is depicted in Figures 4.10, 4.11 and 4.5 respectively.

4.1.3.2 Z corrected curves

The aforementioned stress-strain curves were corrected to constant Z curves (using the equations to be presented in § 4.2.2) in order that the effect of strain rate and temperature on the stress-strain behaviour may be more easily observed. The curves so produced are presented in Figures 4.13-4.24. The magnitude of the correction (mostly due to deformational heating) should be noted by comparison with the relevant curves from Figures 4.1-4.12.

A further feature which becomes clear from examination of these figures is that, after correction to the nominal Z, some softening with strain is observed in the cases of the composite MMC and AMMP series. This is obviously due to some effect other than temperature rise, as it is the corrected curves that are now being considered. It is not attributable to lubricant breakdown, as this would cause the curves to move upwards, and the MMC tests were performed unlubricated.

4.1.4 Steady state flow stress

Table 4.5 contains the steady state flow stress levels achieved for all of the materials presented, under all test conditions used, from the corrected Z stress-strain curves. From examination of this table a number of points become evident. These are:

(i) A dynamic process appears to cause softening of the MMC and AMMP materials during testing under the most severe conditions.

(ii) The flow stresses of the as-cast materials (ASC and AMMP) are higher than those of the extruded monolithic materials (MONO and MMC).

(iii) The flow stress of the extruded monolithic material (MONO) is very similar to that of the extruded composite (MMC) when deformed at the highest temperatures and lowest strain rates.

(iv) The behaviour described in (iii) above is ***not*** repeated in the case of the as-cast materials. In this case the composite material ***always*** exhibits a flow stress greater than that of the monolithic material.

4.1.5 Comparison of lubricated and unlubricated tests

No effect of lubricant on the subsequent stress-strain behaviour has been observed in this study. This is considered to justify including both lubricated and unlubricated tests together in the subsequent analyses. An example plot of lubricated and unlubricated tests performed under the same conditions of 400°C and $1s^{-1}$ is given for the MONO series in Figure 4.25.

4.1.6 Reproducibilty

The range of scatter for three identical tests on each material has been assessed and is presented in Table 4.6. The stress-strain curves of these tests are presented in Figs 4.26 to 4.29.

The percentage scatter is around that considered as average for this type of testing and analysis. The scatter appears no worse for the as-cast materials than for the extruded materials.

The similarity between the ASC and MONO series under these conditions is highlighted.

4.1.7 Evaluation of the activation energy of deformation (Q_{def})

Values of Q_{def} have been evaluated for all materials using the method given in Appendix 2.:

ASC 165kJ/mol
MONO 185kJ/mol
AMMP 181kJ/mol
MMC 187kJ/mol

Of the above, only the ASC material displays a value of Q_{def} that is within the range expected for aluminium alloys.

A value of 185kJ/mol was used in the analysis of the stress-strain behaviour of the MONO, AMMP and MMC series of materials. This value is within the range of experimental scatter of the other values and the use of a common value of Q_{def} aids comparison.

4.1.8 Stress function equations

With the exception of the as-cast monolithic material, the values of Q_{def} given above provide higher values of Z (the Zener-Holomon parameter) than usual for aluminium alloys. The equations presented in this section utilise values read from ***uncorrected*** stress-strain curves and ***instantaneous*** Z values.

4.1.8.1 Exponential law

The plots of the exponential type law (see Equation 2.7 for form) at the characteristic strains of 0.02, 0.1, 0.5, and 1.0 are given in Figures 4.30-4.33 for the four materials investigated. Deviation from the exponential law can be observed at low stress levels. In accordance with the criterion in Appendix 2, data for tests where $\sigma_{ss} < 5x10^{-4}E$ (where E is Youngs modulus in GPa) have not been included in the regression analyses. They do, however appear on the plots.

The values of β showed a systematic decrease with strain for the ASC, MONO, and AMMP series, but none was observed for the MMC series. The constants from the formulation of these equations are given in Table 4.7(a)-(d).

4.1.8.2 Hyperbolic sine law

The plots of the sinh type law (see Equation 2.8 for form) are given at the same strains as for the exponential law. These appear in Figs 4.34-4.37. The constants for each value of strain are again given in Table 4.7(a)-(d). It can be easily seen that use of the sinh law gives a superior fit at the low stress levels. The similarity of the equations at the higher strains means that, for each of the materials, the points from equations formulated at strains of 0.5 and 1.0 are able to be combined into one plot. The fact that no systematic shift is evident can be seen in Figure 4.38.

In all but the case of the MMC series the sinh law plots for strains of 0.02, 0.1, 0.5 and 1.0 are found not to cross and so are able to be extrapolated to cover conditions below and beyond those investigated here.

4.1.8.3 Comparison of the equation types

Values of the coefficient of determination (R^2) calculated during the formulation of the above equations appear in Table 4.8. Using these values as a means of comparison of the different types of equation shows that the sinh equations generally provide a better fit with a very good correlation of experimental data points.. It should be remembered that the R^2 values for the exponential laws discount the points where $\sigma_{ss} < 5x10^{-4}E$. If all points are included then the coefficients of determination are obviously much lower.

Experimental scatter worsens at higher strains for both types of equation, this can be seen from the R^2 values and from examination of the stress function plots given in Figures 4.30-4.37.

4.1.8.4 Comparison of equations and experimental results

The sinh equations were used to produce stress values at the nominal test values of Z, at the strains used in the equation formulation. These values have been added to the Z-corrected experimental stress-strain curves that appear in Figures 4.33-4.37. It can be seen that, whilst the fit at the lowest value of strain is not very satisfactory in some cases, the equations show good agreement at the higher values of strain.

4.1.8.5 Voce equations

Considering the shape of the curves presented by all of the materials studied here, fitting of a Voce type equation was deemed unnecessary.

4.2 Torsion tests

Tests have been performed at 300, 400 and 500°C and at the equivalent true strain rate of $0.73s^{-1}$, calculated at the effective radius. The raw data have been analysed using the methods given

in Appendix 3. The data from the MONO series free-end tests have been converted to equivalent values for fixed-end tests, utilising the final specimen geometry (measured from failed specimens fitted together) and the assumption that the specimen radius decreases, and length increases, linearly during deformation. A plot of final specimen length vs. strain, given in Figure 4.39, shows that this assumption is reasonable. The agreement of the level of the corresponding fixed-end stress-strain curves in Figures 4.40 and 4.45 also suggests that this assumption is valid. No change in dimensions was found to occur during deformation of the MMC material, thus no correction was made.

4.2.1 Shape of the stress-strain curves

Two sets of stress-strain curves are presented. Those in Figures 4.40 and 4.42 show the stress behaviour only to a strain of 1, for ease of comparison with the results presented for the PSC series of tests. The set of curves featured in Figures 4.41 and 4.43 show the stress-strain behaviour to failure.

Both materials show the usual effect of an increase in flow stress with a decrease in temperature. It was felt that it was unnecessary to correct the stress-strain curves for the effect of deformational heating, as the curves from the MONO series show no decrease in stress level (up to an equivalent strain of 1) that could be attributed to deformational heating. Some decrease in stress level is observed in the case of the test carried out at the temperatures of 450 and 500°C, but this is unlikely to be a heating effect when it is not present at the lower deformation temperatures. The MMC series curves display a decrease in stress level at the lowest deformation temperatures. This is unlikely to be caused by deformational heating as the same decrease was observed in the Z corrected PSC curves (see § 4.1.3.2).

It should be noted that, in the case of the MONO material, detectable work hardening occurs up to strains of 0.5 at temperatures above 400°C, whereas there is no systematic trend within the MMC series. Both series exhibit very rapid initial work hardening, in agreement with the results from the PSC test schedule.

Comparison of corresponding curves in Figures 4.40 and 4.42 shows that whilst the flow stress level is considerably higher at the low deformation temperatures for the MMC series compared with the MONO series, at 450 and 500°C the stress levels are very similar. Table 4.9 summarises the steady state flow stresses for both materials under the deformation conditions used. Where no true steady state stress is attained values are given at a strain of 0.5.

4.2.2 Stress function equations

A value of Q_{def} of 185kJ/mol has been used, established from the PSC series of tests and nominal values of temperature have been used in the evaluation of Z because, as stated in § 4.2, it was felt that the temperature rise at such low strain rates and strains could be considered negligible. The procedure given in Appendix 2 was used to provide optimised equations for both materials. These equations are described in the following sections.

4.2.2.1 Exponential law

The exponential law plots for the MONO series appear in Figure 4.46(a)-(c). As with the PSC analysis, data for tests where $\sigma_{ss} < 5x10^{-4}E$ (where E is Young's modulus) have not been included in the regression analysis, but do appear in the plots. The values of β show no systematic variation with strain. The exponential law plots for the MMC series are given in Figure 4.47(a)-(b). The constants from the regression fitting of these equations are given in Table 4.10(a) and (b) for the MONO and MMC materials respectively.

4.2.2.2 Hyperbolic sine law

The plots of the sinh type law for the MONO series, utilising the β values derived from the torsion data are presented in Figure 4.48(a)-(c). The sinh equations for the MMC material are depicted in Figure 4.49(a)-(b). The constants from the formulation of these equations are again given in Table 4.10(a)-(b).

4.2.3 Comparison of equation types

Values of the coefficient of determination (R^2) resulting from the formulation of the above equations appear in Table 4.11, and show no difference in the quality of fit of the two types of equation. As was the case with the PSC formulated equations, it is important to note that the $\sigma_{ss} < 5x10^{-4}E$ criterion used for the applicability of the exponential law means that only a limited stress range has been used in the formulation of the exponential laws. If all points were included then the R^2 values of the exponential equations would be less good.

4.2.4 Strains to failure

The strains to failure, ε_f, were read from Figures 4.41 and 4.43 and plotted in Figure 4.50. From examination of this figure a number of significant points become evident. These are:

(i) The MONO series exhibits ε_f values which are greater than those of the MMC series by a factor of approximately 2.5, at all but the highest deformation temperature.

(ii) The ductility of both materials increases with deformation temperature (until 450°C for the MONO material and 400°C for the MMC material) and then exhibits a decrease at 500°C.

(iii) Whilst the correction of free-end data to fixed-end conditions allows the formulation of stress function equations with no systematic variation in the data between types of test, from the limited data available there is a definite shift in the ε_f values to lower equivalent true strains.

(iv) The failure strains for the fixed-end tests appear to have no significant dependence upon temperature.

4.3 Rolling experiments

Hot rolling was carried out at the temperatures of 300, 400 and 480°C for the monolithic materials (ASC and MONO series) and at 400 and 480°C for the composite materials (AMMP and MMC series). The temperatures given above are start-rolling values. The workpiece is subject to cooling in air and by contact with the rolls, and to a rise in temperature during each pass as a result of deformational heating. The full temperature histories for the rolling schedules performed are presented for the ASC, MONO, AMMP and MMC series in Figures 4.51-4.54 respectively.

The loads resulting from the rolling passes are given in Table 4.12 for the as-spray-cast materials, and in Table 4.13 for the extruded materials. From examination of the values in these tables two interesting points become apparent, both of them contrary to the results found from the PSC test schedules. These are:

(i) The composite materials exhibit, without exception, higher loads than the monolithic materials for equivalent deformation.

(ii) There is no systematic variation in relative strengths of the as-spray-cast and extruded materials.

Examination of the slabs after rolling allowed an assessment of the extent of edge cracking at the different rolling temperatures. As stated in Chapter 3, the use of a rolling temperature below 400°C was not possible in the case of the composite materials, due to excessive cracking. The extent of edge cracking diminished with an increase in temperature for composites. In the case of the monolithic materials, an overall improvement in ductility was evident with respect to the composites. Edge cracking decreased between 300°C and 400°C, but then worsened at the rolling temperature of 480°C.

4.3.1 Microstructural development

This section will concentrate on observations noted from the optical microscopical examination of rolled and heat treated samples, subsequently anodised and viewed under polarised light. All samples were rolled to the same reduction of 60% and heat treated at the same temperature. In this set of experiments only the deformation temperature has been altered. Unless otherwise stated the sections viewed are at 1/4 depth from the surface of the rolled slab.

When viewing the optical micrographs it should be borne in mind that many heat treatments have been performed in addition to those depicted here. Where a large discontinuity occurs in solution heat treatment times between micrographs it indicates that no difference was observed in the interim period.

During examination of the micrographs presented it became obvious that several trends existed which were common to more than one of the materials investigated. These will be summarised after a separate discussion of points of interest noted for the individual materials.

A photomicrograph of each of the as-supplied materials is shown in Figures 4.55-4.58. The elongated nature of the extruded materials is diminished during the reheat period prior to rolling, as can be seen in Figures 4.59 and 4.60. After holding at 530°C for the duration of the reheat both

materials present very serrated grain boundaries. It is surprising to note that the effect of the reheat period on the grain structure seems to be more pronounced for the MONO material than for the reinforced MMC material.

4.3.1.1 ASC series

Figures 4.61(a)-(f), 4.62(a)-(f) and 4.63(a)-(f) illustrate the microstructural evolution of the ASC material, rolled at 480, 400 and 300°C respectively, upon subsequent solution heat treatment.

It is easily observed that, in the cases of the material deformed at 480 and 400°C, very low fractions recrystallised are present, even after 14 days solution treatment (see Figures 4.61(f) and 4.62(f)). Transition banding is observed at both of these deformation temperatures, being more intense at the lower deformation temperature. These bands become more evident as the time of solution treatment increases, especially when deformed at 400°C, where new grains appear to be forming on these bands (see Figure 4.62(c)). The presence of serrated grain boundaries becomes increasingly common as the solution treatment time is increased.

A further feature common to the microstructure of the ASC material when deformed at 400 and 480°C is the formation of significant numbers of small, approximately equiaxed grains as the solution treatment time exceeds 7 days. This feature is obvious from Figures 4.61(e),(f) and 4.62 (e),(f).

The number of grains formed is larger in the case of the 400°C rolled material, and in this case several large, approximately equiaxed, grains are also seen to exist. It should be noted that the microstructures appear much clearer after relatively short solution treatment times, but they still have a "mottled" appearance.

When the deformation temperature is decreased to 300°C, the pattern of microstructural evolution is completely different from that at the higher deformation temperatures. It is obvious from Figure 4.63(a) that the as-rolled state is very heavily worked. Figure 4.63(b) shows the formation of some equiaxed grains after just 5 minutes solution treatment. After 10 minutes solution treatment much of the structure consists of new grains of low aspect ratio, that are considered to be recrystallised. Some transition banding is still visible in the structure with, in some instances, new grains forming at these heterogeneities (see "A" on Figure 4.63(c)). Progressing to a 20 minutes solution treatment time, virtually all of the structure could be considered recrystallised. Some doubt remains about areas which still present a mottled appearance to the grain interiors.

The clarity of the grain interiors and well defined boundaries should be noted from Figure 4.63(e) where the sample has been heat treated for 30 minutes. Very few grains now exist that are not approximately equiaxed in form. The relatively large size of certain grains should be noted, and will be discussed in a later section of these results with respect to errors of observation that may arise as a result of the use of anodised structures.

4.3.1.2 MONO series

Figures 4.64(a)-(e), 4.65(a)-(e) and 4.66(a)-(e) depict the microstructural evolution of the MONO material from the as-rolled condition to solution treated for up to 14 days, after deformation at temperatures of 480, 400 and 300°C respectively. As with the ASC series, the MONO material presents very similar microstructures after being deformed at the temperatures 400 and 480°C. Comparison of Figures 4.64(e) and 4.65(e) shows that even after 14 days solution treatment (the condition that showed the most significant difference in the ASC material deformed at 400 and 480°C) there is very little to distinguish the microstructures resulting from the different rolling temperatures. The 400°C case possibly exhibits a slightly more coarse structure after this prolonged period of heating. Both of the highest deformation temperatures result in a very low fraction recrystallised, at any solution treatment time up to and including 14 days.

The 300°C case also appears to behave similarly until 4 hours solution treatment time is reached. Figure 4.66(c) shows that at this time of heat treatment many small grains appear to form from within the original elongated structure. It can be observed from Figure 4.66(d) that these grains appear to coarsen when the time of heat treatment is increased to 48 hours. After 14 days heat treatment (see Fig.16(e)) the structure has very significantly coarsened with many approximately equiaxed grains present amongst a coarse elongated structure. The specimen appears to have a significant fraction recrystallised, and the clarity of many grain interiors and boundaries should be noted.

4.3.1.3 AMMP series

The evolution of the microstructure after hot rolling is shown in Figure 4.67(a)-(d) and Figure 4.68(a)-(d) for the as-cast composite material, rolled at 480 and 400°C respectively.

Both of these deformation temperatures lead to very little of what could be termed progressive recrystallisation behaviour; after 7 hours solution treatment the 480°C rolled material has a microstructure that bears a very close resemblance to that of the as-rolled state (see Figures 4.67(c) and (a) respectively), yet Figure 4.67(d) shows that after 8 hours treatment the structure is fully recrystallised.

The 400°C rolled material presents more "clearing" of the grain interiors after a short period at the solution temperature, which it retains up until around 7 hours. At this point the 400 and 480°C rolled materials differ because the former begins to exhibit the formation of some small grains of a size similar to the SiC reinforcement. Many of these small grains are, in fact, associated with the reinforcement particles.

After 8 hours solution treatment (see Figure 4.68(d) the 400°C case is again seen to be fully recrystallised, to a grain size very similar to that of the 480°C case.

In common with the as-cast monolithic material (ASC series) the structure exhibits serrated grain boundaries at intermediate heat treatment times (see, for example, Figure 4.67(b)) and there is evidence of transition banding. Both of these features, in contradiction to the results

from the ASC series, are more commonly observed in the case of the material rolled at the higher temperature. It is interesting to note the difficulty in establishing the location of certain grain boundaries in the fully recrystallised state (see Figures 4.67(d) and 4.68(d)).

4.3.1.4 MMC series

Figures 4.69(a)-(e) and 4.70(a)-(e) illustrate the behaviour of the MMC series microstructure when solution heat treated for up to 8 hrs after being rolled at the temperatures of 480 and 400°C respectively.

Unlike any of the previous series there is a definite difference in behaviour dependent upon the deformation temperature. Considering the 480°C case first, the microstructure changes with duration of solution treatment from a very fine elongated structure in the as-rolled condition (Figure 4.69(a)) to a fine, mostly equiaxed structure after 8 hours heat treatment (see Figure 4.69(e)). Whilst this may indicate that recrystallisation has occurred, it possibly shows only that the process has been nucleated, and not completed. This is suggested by comparison of the 400 and 480°C microstructures. The 400°C case, heat treated for 8 hours, presents many larger grains with very clear interiors. These grains are very much larger than the rest of the structure in which they reside, and they are of a similar size to the grains seen in the fully recrystallised AMMP material. Very few of these grains are present in the samples from the material rolled at 480°C; two examples of grains that are present are marked as A and B in Figure 4.69(b).
A significant number of these larger, apparently recrystallised, grains are present in the 400°C rolled material after only 1 minute solution treatment. Their number does not seem to increase significantly through the longer heat treatment times, but the surrounding grain structure (as with the 480°C rolled material) does alter from a fine elongated type structure to a fine mostly equiaxed type grain structure.

This presence of recrystallised grains at shorter heat treatment times for material deformed at lower temperatures is in agreement with usual theory.

4.3.2 Trends through series'

As mentioned earlier, several trends were observed that were common to more than one of the series investigated. These are summarised below.

(i) Both monolithic materials rolled at 300°C behaved differently from those rolled at the higher temperatures. The difference was far more marked in the case of the as-cast material (ASC series).

(ii) Very low fractions recrystallised were found in the monolithic materials, even at very long solution treatment times, when deformed at temperatures of 400°C and greater.

(iii) The 400 and 480°C rolling temperatures produced very little difference in the microstructures of the ASC, MONO and AMMP series.

(iv) Serrated grain boundaries were observed in the ASC and MONO series, occurring at shorter times for the MONO material. This effect also occurred in the AMMP material in areas

of low particle density. The scale of the microstructure in the case of the MMC material makes examination difficult. This effect appears, however, not to be present.

(v) "Clearing" of the grain interiors to a mottled effect is observed after relatively short solution treatment times for all series.

4.3.3 Quantifying fractions recrystallised

Point counting to quantify the effects of deformation temperature and length of solution treatment has not been performed for a number of reasons stated below.

(i) When viewing anodised structures, a popular criterion used in deciding whether a grain is recrystallised is the "clarity" of the grain interior. As is shown, for example, in Figure 4.62(f) it is perfectly possible to have an elongated grain structure that appears, according to the "clarity" criterion, to be recrystallised. This study has raised doubts about the validity of the use of this criterion in point counting. The reasons for this will be discussed more fully in Chapter 5.

(ii) The materials which exhibit large fractions recrystallised in this study (i.e ASC, AMMP) recrystallise so rapidly that it has proven impossible to follow a gradual change of fraction recrystallised.

(iii) There is great difficulty associated with resolving microstructures which are as fine as those presented by the MONO and MMC series. The magnification used in this study was as high as was possible before the contrast effect from the anodised surface was lost.

4.3.4 Methods attempted to quantify fraction recrystallised

As examination of the anodised samples did not provide a definite answer as to whether a sample was partially recrystallised or not, several other techniques were tested. The outcome of these will be discussed briefly below.

4.3.4.1 Hardness testing

Having ascertained that the materials exhibited significant natural ageing, several samples from each of the materials tested were solution treated and then immediately sectioned, ground and tested using a Vickers hardness indenter. The results from this series of experiments again proved inconclusive. All materials presented a decrease in hardness value after a short solution treatment time of 30 minutes that did not then alter with further heating, even up to 14 days. The ASC sample was heated for a shorter period of 5 minutes (because of its relatively rapid recrystallisation) and again showed the same effect. It was in fact found that the monolithic materials studied presented a hardness of between 58-65 VPN after only a few minutes of solution heat treatment, regardless of the deformation temperature used. This value did not change with further heat treatment.

4.3.4.2 Back Scattered Electron Imaging

Samples of the ASC and MONO materials were prepared according to the procedure given earlier in Chapter 3 and then placed in the SEM. It was hoped that if subgrains were present (and hence recrystallisation had not occurred in that grain) then they would be visible by this method. This proved not to be the case. The use of electron back scattered patterns (EBSP) (details were given previously in the Chapter 3) to distinguish between recrystallised and unrecrystallised grains also proved unsuitable.

4.3.5 Transmission electron microscopy

A very limited amount of work has been performed using this technique, mostly on the ASC series. Its use has shown that the pinning of boundaries and sub-boundaries by the β′ (Al_3Zr) phase is relatively common. An example image of this phenomenon is shown in Figure 4.71 for a foil prepared from ASC material rolled at 400°C and solution heat treated at 530°C for 14 days. Figure 4.72 shows a lower magnification electron micrograph of the same specimen depicting the substructure that has resulted from widespread recovery. The presence of dislocation loops around the β′ particles in the sample depicted in Figure 4.73 is evidence for recrystallisation having occurred in this sample (ASC material, rolled at 300°C and SHT for 30 minutes); the loops are formed as a boundary by-passes the particle. The presence of segregation in the as-cast materials is suggested by the preferential thinning of certain areas of the foil shown in Figure 4.74. For comparative purposes Figures 4.75 and 4.76 show micrographs of an extruded monolithic sample. The very small scale of the microstructure (obvious from examination of Figure 4.65) is illustrated by the fact that many high angle grain boundaries are evident at such high magnification in Figure 4.75. Whilst no significant difference was observed in the size of the β′ in the as-rolled samples of ASC and MONO materials, comparison of Figures 4.71 and 4.76 suggests that the sample heat treated for a prolonged period of time (14 days) exhibits fewer but larger particles. From the limited number of particle measurements that have been performed, the average particle size is around 40nm. During these investigations, no evidence was found to suggest that the mechanism of dynamic recrystallisation had occurred.

5 Discussion

This section will discuss the results gained in the three series of experiments performed. Initially areas of interest in the individual testing series will be discussed separately. The majority of this section will, however, involve comparing and contrasting the results from the present study, both from within this study, and within the context of other work that has been carried out in associated areas.

5.1 Deformation behaviour

Flow stress data have been obtained from both the PSC and torsion testing methods, and further indications of the materials' behaviour has been provided from loads obtained during the series of rolling experiments. Any points specific to one particular type of testing will be discussed initially, and the behaviour of the alloys and composites under the different strain regimes will then be discussed.

5.1.1 Spread coefficient

Comparison of the spread coefficients resulting from the measurement of the tested PSC specimens in Tables 4.1-4.4 reveals less variation between lubricated and unlubricated test coefficients for the composite materials than is present for the monolithic materials. This seems to justify the idea that the SiC particles may somehow "cut" through the lubricant, altering the coefficient of friction for both the lubricated and unlubricated tests. As stated in § 3.3.1, this was the original thinking behind testing all of the samples in the unlubricated condition. This hypothesis was, however, impossible to verify experimentally, and the same values of μ were therefore used in the analysis of the composite and monolithic materials, i.e. $\mu = 0.1$ for lubricated tests and $\mu = 0.6$ ("sticking friction") for unlubricated tests. This possibility that μ may be variable, and too high a value may contribute to the downwards trend of some of the MMC stress-strain curves must be considered. The downward trend only occurs when a test is performed at high Z, and it could be imagined that the greater force needed for material flow to occur could contribute to the SiC particles "cutting" through the lubricant layer. Whilst this possibility cannot be ruled out, examination of the relevant curves in Figures 4.10-4.12 illustrates the large decrease in stress level that exists. This decrease is considered too large to be accounted for solely by an incorrect coefficient of friction.

5.1.2 PSC stress-strain behaviour

This section will concentrate on the form of the curves produced during deformation under plane strain conditions. Where necessary, results from the other forms of experiment performed within this project will be commented upon, and reference will be made to other published works.

Figures 4.10-4.24 form the basis of the results discussed here, and whilst many other analyses have been performed and will be discussed here, the basic stress-strain curve provides the data from which these further results are formed. It is therefore obvious that reproducible data from each deformation is essential to a meaningful discussion of a material's behaviour. Examination of the Figures 4.26-4.29 highlights the generally excellent reproducibility found in this method of testing.

5.1.2.1 Curve shape

The stress-strain curves obtained as a part of this research are not generally of the form resulting from the deformation of aluminium alloys. The very rapid attainment of a steady state stress level, and the occurrence of perceptible work hardening only under the most severe deformation conditions is not readily explicable in terms of the material condition prior to testing, as both extruded and as spray cast materials exhibit the same behaviour. In the case of the simple plateaus formed by the deformation of all four materials under conditions less severe than 300°C and $1s^{-1}$ a similar form of curve was found by Oh et al (79) when deforming 8090 at 380°C and 500°C in torsion. The work of Goncalves (16) on 8090 and 8091 alloys, although exhibiting low strains to steady state, produced a more usual curve for aluminium alloy deformation.

As stated in § 4.1.3.1, all four materials exhibit a decrease in the amount of work hardening as the deformation temperature increases and the strain rate decreases. This is in agreement with general recovery theory, which states that under severe deformation conditions the number of recovery events per unit strain will be decreased, and so dislocation annihilation will lag behind dislocation generation until higher strains are reached. In this way the onset of steady state is delayed. For a more detailed explanation see § 2.5.1.1.

5.1.2.2 Comparison of as-cast and extruded materials

Essentially similar curve forms are presented by the as-cast and extruded grades of material after correction to constant Z. As stated in § 4.1.4, and shown in Table 4.5, the as-cast materials generally present flow stresses greater than or equal to those of the corresponding extruded grades of material. The use of a different activation energy of deformation, Q_{def}, in the analysis of the ASC material (see § 4.1.7) could be thought of as having some effect upon the level of the corrected Z curves presented for the ASC material, when comparing the as-cast and extruded monolithic materials', but the fact that the ASC material is still stronger when the raw data curves of Figure 4.1-4.3 are consulted, and that the AMMP and MMC material are both analysed using the same value of Q_{def} suggests that this is a real effect. This effect is not expected, as neither of the extruded materials recrystallise significantly in the rolling reheat and, therefore, retain the extrusion strain. This is expected to increase the strength due to the higher dislocation density present. It is also unlikely that a grain size effect is responsible as, by conventional thinking, the very much smaller grain size of the extruded material in the thickness of the test piece would

be expected to afford higher strength to that material. When considering the loads from the rolling experiments, there is no systematic difference in the loads of as-cast and extruded monolithic and composite materials.

5.1.2.3 Comparison of monolithic and composite materials

From comparison of the relevant curves in Figures 4.13-4.24 it can readily be seen that whilst the composites generally exhibit higher strengths than their monolithic counterparts, under the test conditions of 500°C/0.05s^{-1}, 500°C/1s^{-1} and 400°C/0.05s^{-1} (i.e. the least severe conditions used) the flow stresses of composite and monolithic materials of both grades are very similar. This is in accordance with the elevated temperature and low strain rate scenario proposed by Kalu and Humphreys discussed in § 2.6.1. Here the rate of dislocation climb is sufficient to ensure that no accumulation occurs at the reinforcement particles, and the subsequent deformational behaviour conforms to that of a comparable single phase material (52). A similar effect is exhibited by the torsion test stress-strain curves (shown in Figure 4,40-4.43) for tests carried out at temperatures of 450°C and above, and, for the MONO and MMC materials, from the rolling passes at 480°C. The fact that the ASC and AMMP materials rolling loads are not comparable at 480°C is not understood.

5.1.3 Activation energy of deformation

Comparison of the activation energies of deformation Q_{def} calculated during the current research (see § 4.1.7) with those from the literature (see Table 2.2) shows that they are very consistent with a number of studies (78,81), and with the work of Oh et al (79) to a lesser extent, in that both provide Q_{def} values that are significantly higher than is normal for aluminium alloys. The value of around 156kJ/mol, that is normally associated with the deformation of aluminium alloys, is based on the activation energy for self-diffusion in pure aluminium, implying that the rate controlling step during deformation is dislocation climb. This figure was found to be consistent with the experimental data gained by Goncalves in his study on the hot working of D.C. cast 8090 (16). The high values obtained in the present research, and other studies noted in Table 2.2, indicate that processes other than the above occur during the deformation. As the previous section of this Chapter has highlighted, this indeed seems likely. The different behaviour of solution heat treated 8090 deformed at 300°C, discussed earlier in Chapter 2, was felt by Smith et al (78) to indicate that maybe two activation energies were required to describe the differing mechanisms; his value of 185kJ/mol is calculated for aged material. However, the generally excellent fit of the stress function equations of the present work (shown graphically in Figures 4.30-4.37 and via the coefficient of determination values in Table 4.8) suggests that the use of one suitable value of Q_{def} is perfectly adequate to describe the materials' behaviour.

5.1.4 General stress-strain behaviour, and comparison of torsion and PSC test data

Most of the studies carried out on the deformation characteristics of 8090 have been performed using torsion testing. As the resulting data have invariably been converted to equivalent tensile stresses and strains, then comparison of those results with the present PSC study is possible, in addition to comparison with the torsion results from the present research.

A feature of the PSC test results is an exaggeratedly high flow stress for tests performed at 300°C. This behaviour has been noted in other works on this alloy system (78,79). In the former of these studies, Oh et al found that deformation at 380°C and above resulted in the sort of simple plateau that is found under conditions of PSC in the present work. In the study of Smith et al (78), solution heat treated material exhibited pronounced peaks and subsequent softening, attributed to dynamic precipitation and subsequent coarsening, respectively. Peaks have also been noted by Oh et al (79), and Niikura et al (81). Whilst none of the reviewed studies appeared to correct data for the effects of deformational heating, this is dismissed as a possible cause of the post-peak softening (78,81). In the present work, when the data have been corrected to constant Z only the MMC material exhibits appreciable softening, and this occurs only under the most severe conditions. It should be noted that dynamic recrystallisation (DRX) promoted by the presence of reinforcement particles is not suspected as the cause of the softening in this case, as no such softening was observed in the corresponding AMMP case. In the limited TEM study of the monolithic materials, no evidence was found for the occurrence of DRX. Figure 4.75 shows a transmission electron micrograph of 400°C as-rolled MONO material, and shows only a dynamically recovered substructure. This is in agreement with several works that have been reviewed (78,79,81), but not with the work of Goncalves (16) where the presence of small dynamically recrystallised nuclei was claimed. Lack of success in the preparation of usable thin foils of the composite materials have precluded an investigation of the possibility of particle nucleated DRX by TEM.

The present study under torsional conditions *does* show the peak and softening behaviour reported in the literature, for all test temperatures in the case of the MONO material, and for test temperatures less than 450°C in the case of the MMC. Comparisons of the relative stresses under PSC and torsion are presented for the MONO and MMC materials in Figures 5.1 and 5.2 respectively. It should be noted that the more pronounced softening under PSC is due to the greater deformational heating effect in this test method, as is easily observed when the PSC curves corrected to constant Z in Figures 4.16 and 4.22 are consulted.

Comparison of the relevant curves in Figures 4.16-4.18 with Figure 4.40, and Figures 4.22-4.24 with Figure 4.42 shows the higher flow stress of the materials tested under PSC. Because of the lack of torsion test data for the as-cast materials, it is not possible to say if this effect would occur with the as-cast systems, or whether it could be some effect of the different grain structures of as-cast and extruded material. By way of explaining this phenomenon, and that of the formation of peaks in the torsion curves, it is useful to consider what possible precipitation and solute effects occur within the alloy during deformation.

5.1.5 Consideration of the high flow stress at 300°C

From the literature it is found that the high flow stress that results when 8090 is deformed at 300°C is present only in material that has been solution heat treated (SHT) at high temperature (i.e. > 500°C) (78,81). Figure 2.11 shows that as the SHT temperature is decreased, so the exaggerated peak flow stress behaviour decreases, as it does when the test temperature is high. Work by the same authors (81) has shown that the effect of lithium content on the peak behaviour is just as pronounced, and this is shown in Figure 2.10.

Whilst the same basic cause of the peaks is given by both of the above mentioned researchers (78,81) (that of excess solute being available in SHT material) the former study suggests dynamic precipitation from this solute as the reason for the high flow stresses, and the latter that a solute drag effect of lithium on dislocations is responsible.

It was initially thought that the higher flow stress in PSC tests, compared with those from torsion tests, in the present study could be due, at least in part, to the slightly different heating schedules to which the specimens were subjected prior to testing. Both PSC and torsion testing schedules utilised a common scheme of heating to 530°C, holding at this temperature for 40 minutes and then air cooling to the test temperature. At this point the schedules for PSC and torsion vary. Transient temperature gradients that are caused by the transferral of the PSC specimen into the test furnace necessitate the specimen being allowed to soak for a period of 3 minutes in the test furnace, at the test temperature. The torsion specimens, being in the test position permanently, were tested immediately. Consultation of Figure 5.3 (114) shows that at around 340°C the phase S' nucleates. This phase has been claimed to be capable of providing considerable hardening effect (115), and holding at the temperature of 300°C will provide the opportunity for greater precipitation of this phase prior to deformation. This would not appear, however, to explain the importance of the %Li found by Niikura et al (81), as the S' phase does not contain lithium (it has the stoichiometric formula Al_2CuMg). An effect of an Li-containing phase on the precipitation characteristics of other phases (as is the case with δ' (Al_3Li) and β' (Al_3Zr), mentioned in § 2.9.3) could be considered a possiblity. The formation of equilibrium δ (AlLi) could be considered but, in work by Silcock (116) on the Al-Li-Cu system, it was found that this phase did not afford significant hardening anyway. In this case, then, it could not have a sufficiently large effect on the deformation behaviour to explain the observed features in the stress-strain curve.

It seems reasonable that the presence of lithium may be responsible for the different stress-strain behaviour of the studied materials at low temperature, either via a solute drag effect (at low temperature more solute may segregate to grain boundaries) or by precipitation of excess solute to the grain boundaries, thereby hindering dislocation movement and increasing the flow stress. The fact that peaks are present in deformation at all temperatures in the work of Smith et al (78) suggests that the precipitation of a phase at low temperature is at least not the whole reason for this behaviour. As regards the possibility of a lithium solute drag effect, a similar effect of lithium in preventing recrystallisation by the hindrance of grain boundary movement has been

proposed by Makin and Stobbs (102), and is mentioned later in this Chapter. The post-peak softening effect that is observed both in the present work and in the literature can presumably be attributed to a critical stress for the dislocations to become "unpinned" from the lithium solute. The lack of peaks in the present PSC study is unexplained.

5.1.6 Constitutive equations

The constants generated for constitutive relations from other worker's studies on Al-Li alloys are presented in Table 2.2. Comparison of the β values with those from the present work (given in Tables 4.7 (a)-(d)) shows reasonable agreement with all but those of Smith et al (78). This is possibly due to his inclusion of solution heat treated and aged material data in the same plots. Comparison of the n and α values (again given in Table 2.2) with the present work, and amongst the literature values, shows virtually no consistency.

Figures 4.13-4.24 illustrate the good agreement of data and constitutive equations from the PSC study. The relatively poor agreement at the lowest strains is due to the variation in the work hardening behaviour of these materials that has been highlighted earlier in this Chapter. The agreement of experimental data points with individual equation lines is shown in Figures 4.30-4.37 for both the exponential and hyperbolic sine laws. The superiority of the sinh type law in describing the deformation behaviour over all ranges of stress is immediately obvious when corresponding exponential and sinh plots are compared. This is because of the approximation of the sinh law to a power law at low stress values, and to an exponential law at higher stress levels. Details of this were given in § 2.4.1.

Figure 5.4 illustrates the hyperbolic sine form of equation at a strain of 0.5 for all of the materials tested, deformed under PSC conditions. The excellent agreement with experimental data is immediately obvious. Apart from the displacement of the ASC line to the right (because of the use of a lower activation energy of deformation in analysis) it is feasible that, within experimental error, all of the AMMP, MONO and MMC data could be reasonably well described by one equation. A slight variation in the values of α may account for some of the lateral displacement of the lines. This comparison of as-cast (unconsolidated) and extruded (consolidated) material is valid because, certainly when a low strain (of around 0.1 (117)) has been exceeded, one would expect any effect of the material not having been consolidated (e.g. porosity) to have been removed. In addition to this, Figure 4.38 shows that, once beyond a strain of 0.5, one hyperbolic sine equation for each material can quite satisfactorily describe the stress behaviour. It was for this reason that Voce type equations were not fitted to the data; the simple plateau type stress-strain curves do not require Voce equations for a full description of the deformation behaviour.

5.1.6.1 Comparison of PSC and torsion equations

It is usual that data from different test methods may be compared when converted to equivalent stresses and strains, and it is evident from examination of Figures 4.31 and 4.46 that if the PSC or torsion test method had been used in isolation, then a self-consistent set of equations would have been produced for the MONO material. These may then have been applied to data gained from other test methods.

Comparison of the results gained from both of the test methods, however, is shown in Figures 5.5 (a)-(c) and 5.6 (a)-(c); the disagreement between the data obtained from the two test methods is obvious. The MONO torsion/PSC comparison of the exponential laws given in Figure 5.5 (a)-(c) shows that the data from both test types agree at low values of Z, but not at the higher values, apparently indicating that less hardening occurs in the extruded monolithic material when tested under torsional conditions. The possibility of the deformational heating being greater than was at first thought must be considered, thus leading to softening of the specimen under severe deformation conditions.

In considering the effect of possible temperature rises during the test, even if adiabatic heating conditions prevailed, an approximation of the temperature rise is given by:

$$\Delta T = \frac{1}{c\rho}\sigma d\varepsilon \qquad (5.1)$$

where: ΔT is the adiabatic temperature rise in °C, c is the specific heat capacity of the material ($JK^{-1}kg^{-1}$), ρ is the density (kg/m^3), σ is the stress level (MPa) and $d\varepsilon$ is the strain increment over which the temperature rise occurs.

Under the most severe test conditions used in the present study the adiabatic temperature rise calculated in this manner would be equal to 37°C. It can safely be assumed that the heating conditions that exist are very much less than adiabatic (Barraclough (76) makes the point that heat losses to the grips often mean that approximately isothermal conditions exist, and Smith et al (78) found that in their work on 8090 heat rises of only 5°C existed under the most severe deformation conditions). Therefore, although correction for a temperature rise would move the MONO torsion data closer towards the PSC equation, the magnitude of correction that is likely would be far from making one equation fit both sets of data. Further justification for assuming negligible temperature rises during the torsion tests comes from examination of Figure 5.5 (a)-(c), from which it is obvious that the magnitude of the disagreement between the PSC and torsion equations is essentially the same at strains of 0.1 and 1.0. This would certainly not be the case if a temperature rise were responsible for the discrepancy, as the temperature rise would be very different at these two strains. Neither is the disagreement a result of the torsion machine running at too low a speed when the test commenced as the machine was running for a period of two minutes to stabilise the speed prior to the tests being performed. Again, the fact that the disagreement is the same at high and low strain negates the possibility of this being responsible.

It is thought that the unusual work hardening behaviour of this group of materials when deformed at high Z under plane strain compression is responsible for the disagreement of the PSC and torsion data for the MONO material. Evidence for this comes from consultation of Figures 5.7 (a)-(b) and 5.8 (a)-(b). Here, for the MMC material, the agreement between the PSC and torsion derived equations is actually very good. When Figure 4.22 is examined and compared with the corresponding MONO curve in Figure 4.16, it is immediately obvious that the work hardening effect is far less pronounced in the case of the composite material. It is therefore concluded that the mechanisms by which the flow stress of the MONO material is raised, at high Z under PSC test conditions, (discussed in § 5.1.5 of this Chapter) are responsible for the disagreement between the test methods. The hyperbolic sine analysis of the data is shown in Figure 5.6 (a)-(c). This shows the lines for the torsion curves to be displaced to the right, but parallel to, the PSC equation lines at all strains. As the values of Q_{def} calculated from the PSC test schedule have been used in the subsequent analysis of torsion stress-strain data, this could indicate the necessity for a different activation energy to describe the situation under torsional deformation, or at least because of the variation in heating schedule mentioned earlier in this Chapter.

5.1.7 Strains to failure

Limited information has been obtained in the present work on the ductility of the extruded monolithic (MONO) and composite (MMC) materials. This is in the form of strains to failure (ε_f) over the range of temperatures 300-500°C and at the strain rate of $0.73s^{-1}$. These data are presented in Figure 4.50. A significant peak in ductility in the MONO material is shown at the temperature of 450°C. No such significant peak is seen for the MMC material, with only a slight increase in $\varepsilon_f$being apparent at 400°C. The above observations are in agreement with those made on edgecracking during rolling of the MONO material, but do not show agreement with the observation of more edgecracking in the composite slabs rolled at 400°C. The equipment used did not allow examination of the fracture surface after the specimen had broken, as a pre-determined number of revolutions were performed in each test, and the fracture surfaces of the specimen invariably rubbed before the test terminated. It is possible that a change of fracture mode could be responsible for the poorer ductility in the MONO material at 500°C, but without fracture surfaces to examine this is merely conjecture.

Most of the studies carried out into the ductility of 8090 seem to have been concerned with the room temperature (118) or "warm" (i.e. up to around 200°C) properties (119). There are, therefore, few studies available for comparison. Table 2.4 lists the values of ε_f obtained from the two studies found that examine the hot ductility of 8090 under torsion (78,79). The value of ε_f of Smith et al (79) from solution heat treated material tested at 300°C is comparable with the strains obtained in the present study. From comparison of their other failure strains, the material condition (e.g. solution heat treated or aged) seems to have a far more profound effect upon the ductility than does the strain rate at which the test is performed.

The study of Oh et al (79) provides ε_f data over a range of temperature and strain rate. From

these data it is apparent that a slight increase in ductility is consistently present at the test temperature of 380°C, which is comparable to that in the present study. The strains to failure are, however, around a factor of two greater than those of the present study and those of Smith et al (78).

The decrease in ductility of the MMC when compared with the MONO material is as expected when relatively brittle reinforcement particles are introduced to an aluminium alloy matrix, and is confirmed by the fact that rolling of the composite materials was found not to be possible below 400°C because of excessive edge cracking. For the MONO material, comparison of the effect of rolling temperature on the tendency to edge cracking, and the ductility data from torsion tests shows good agreement of the trends in ductility.

5.1.7.1 Fixed end tests

A series of fixed end test was only performed for the MMC due to material constraints. The MMC series free end specimens showed no increase in measured length after testing and so would be expected to show the same failure strains as the fixed end tests. Figure 4.50, however, shows this not to be the case, with the fixed end tests displaying fairly constant and low strains to failure. It could be considered that, because of the method of measurement, some slight increase in length did occur, leading to an axial force being created. If this is the case, then the axial force, however small, appears to have a detrimental effect upon the ductility of the composite. This is in agreement with some work by Barraclough, (76) where it was suggested that the existence of an axial force in fixed end tests would not significantly affect the stress level experienced but could possibly influence the fracture behaviour of the specimen.

5.2 Recrystallisation behaviour

The recrystallisation behaviour of as-cast and extruded monolithic and composite materials has been investigated via the optical and microstructural examination of rolled and solution heat treated (SHT) samples. The results from these investigations are described in § 4.3 of this thesis, and the resulting microstructures are depicted in Figures 4.55-4.76.

Because of the large differences in recrystallisation behaviour of the monolithic and composite materials, the two groups will be discussed separately. Any points common to both will be discussed subsequently.

5.2.1 Monolithic materials

The ASC material is felt to illustrate the behaviour of the monolithic alloys most concisely, and will therefore be considered first.

It is obvious that very different behaviour occurs during SHT after rolling at 300°C rather than 400 and 480°C. The production of a large, mostly equiaxed grain structure in as little as 20 minutes (see Figure 4.63(d)) is greatly at odds with the structures resulting from the rolling temperatures of 400 and 480°C, where predominantly elongated grains are evident, and it is

thought that full recrystallisation has not resulted even after 14 days SHT. Evidence for this will be presented shortly. Deformation at a relatively low temperature results in a high dislocation density, and therefore greater driving force for recrystallisation than does the same deformation at a higher temperature. The reluctance of the materials deformed at higher temperature to recrystallise is indicative that a "pinning" process is operating on the grain boundaries. The consequent reduction in grain boundary mobility means that recrystallisation will not occur unless the energy input (from the deformation) is high enough to allow the grain boundaries to "break-free" from the particles or solute that is pinning them.

5.2.1.1 The competition between pinning and recrystallisation

The effect of Zr, in the form β′ (Al_3Zr), on grain boundary mobility is beyond doubt, and has been discussed in § 2.9.3. Makin and Stobbs (102) also suggest a significant effect of Li solute in limiting boundary motion. The slower recrystallisation kinetics of Al-Li alloys when compared with conventional aluminium alloys are attributed to the fact that the drag of Li on the boundaries allows extensive recovery to occur. This has been found to diminish the energy available for recrystallisation (120).

The pinning of boundaries and subgrain boundaries has frequently been observed in the TEM part of this study (such a feature is shown in Figure 4.71) and is assumed to be the dominant mechanism in controlling the rate and extent of recrystallisation. It is therefore of importance, when considering which deformation conditions are likely to result in recrystallisation upon subsequent SHT, to perform a calculation of the actual recrystallisation driving forces and pinning forces that exist. As discussed in § 2.94, Goncalves found that the equation of Zener (Equation 2.20) resulted in too low a value of pinning force to adequately describe the experimental observations in his work on DC cast 8090 (16). The Rios model (104) has been used here to calculate the pinning force that is present due to the β′ particles.

The driving force for recrystallisation can be given as:

$$F_R = Gb^2(\rho_1 - \rho_2) \tag{5.2}$$

where:
G is the shear modulus
b is the burgers vector
ρ_1 is the dislocation density of the deformed grains
ρ_2 is the dislocation density of the recrystallised grains, and $\rho_1 \gg \rho_2$.

From Goncalves' measurements of the dislocation density of 8090 grain interiors (ρ_i), and his calculation of the subgrain boundary contribution (ρ_{sb}), the total dislocation density was calculated from:

$$\rho_1 = \rho_i + \rho_{sb} \tag{5.3}$$

and placed in Equation 5.2 to provide driving forces for recrystallisation. These values are shown in Table 5.1, along with the finish-rolling temperatures for the ASC and MONO materials. As dislocation densities of the samples were not measured in the present research, and the deformation conditions here are very similar to those of Goncalves, the values of recrystallisation driving force given in Table 5.1 will be used for the purposes of this discussion.

The Rios model (Equation 2.23) has been used to calculate the pinning force due to β′ (Al_3Zr) in the ASC and MONO materials, using a radius of 20nm, and a volume fraction of 0.0014, calculated according to the method given in Appendix 4. This pinning force (F_P) has been found to be equal to 2.72E+5 Nm^{-2}. Comparison with the values of F_R given in Table 5.1 shows that $F_R = F_P$ when the start rolling temperature is between 400 and 480°C. Consultation of the rolling temperature profiles in Figures 4.51 and 4.52 shows that this corresponds to finish-rolling temperatures of between 370 and 410°C for the ASC material, and between 350 and 395°C for the MONO material.

Figure 5.9 shows Goncalves' plot linking recrystallisation force with finish-rolling temperature and pinning force (16), with lines added from the present calculations for ASC and MONO material, using the experimentally determined finish rolling temperature. It should be noted that the pinning force line shows total agreement with that originally calculated for the alloy 8091. The F_R line for ASC material possesses a steeper gradient, and is between Goncalves 8090 and 8091 lines. The MONO line agrees totally with the previous line for DC cast 8090. It is probable that the MONO line should be shifted to higher temperatures in Figure 5.9 due to the higher dislocation density that may well result from this material having been extruded and rolled without recrystallising in the interim period. As in the deformational behaviour, however, the presence of these "extra" dislocations has not made itself easily noticeable.

The shifting of the F_P line upwards, and the new position of the ASC line moves the $F_R = F_P$ point to higher temperatures. For the MONO material the $F_R = F_P$ intersection is shifted to lower temperatures. These movements of the balance points of recrystallisation and pinning forces would be expected to mean that the 300°C deformed ASC material has a much higher actual driving force available for recrystallisation than would be predicted by the original 8090 F_R line proposed by Goncalves. By the same reasoning, the MONO material might be expected to show decreased recrystallisation kinetics as the balance point of driving and pinning forces is moved towards the lowest temperature of deformation used.

The above ideas appear to be supported when micrographs from the present and referenced study (16) are compared - the ASC material presents an equiaxed grain structure at 300°C, similar to the behaviour of 8091, whilst the MONO material displays sluggish recrystallisation behaviour, and produces an elongated (i.e. pinned) grain structure.

From the limited number of measurements performed on the TEM micrographs, no systematic difference was found in the β′(Al_3Zr) particle sizes in ASC and MONO foils produced from the same condition material. Difference in pinning phase size is therefore not believed to be responsible for the difference in recrystallisation behaviour of the materials. It is possible that the process of extrusion followed by rolling, and the resulting grain width, means that most

of the β′ is aligned and present on grain boundaries. Certainly in the TEM study, the MONO sample appeared to exhibit larger numbers of particles involved in pinning. As in the case of the ASC material, the 300°C rolled MONO material behaves differently compared with that rolled at 400 and 480°C, this difference becoming noticeable only after around 4 hours SHT when many small grains appear to form. Problems arise in the interpretation of these fine anodised structures, and will be discussed later in this section.

The cause of β′ inhibiting recrystallisation so effectively is discussed in § 2.9.5.2, and can be attributed to pinning of subgrain boundaries thus preventing nucleation by subgrain coalescence processes (102,109). The pinning of high angle grain boundaries has also been proposed by (16) as the reason for the observation of elongated recrystallised structures: when a large subgrain size exists, there is not sufficient distance *across* a grain to allow sufficient misorientation for the production of a high angle grain boundary. The coalescence process therefore continues in the longitudinal direction. The very fine grain structure in the MONO material studied here could well enhance this effect. Whilst some doubt exists about which structures of the MONO material are recrystallised (see § 5.2.3., it seems likely from examination of Figure 4.66(e) that an elongated structure does exist at the higher rolling temperatures. This is not thought to be the case with the ASC material. With both the 400 and 480°C rolled material, as SHT proceeds, and the anodised structures "clear" (thought to be due to recovery) it is obvious that bulging provides a serrated appearance to many of the high angle boundaries. This is apparent particularly at times of 7 days SHT and above, and is evidence for the favoured recrystallisation nucleation mechanism of subgrain coalescence linked with boundary bulging (102,108,109).

The fact that this effect appears when no increase in energy input is provided suggests that an alteration of the pinning force has occurred. The long SHT times required for this effect to become apparent hint that coarsening of the pinning β′ may be responsible for this change in the F_R and F_P balance. Additional evidence for the hypothesis of β′ coarsening exists in the fact that, for the ASC material, the production of some equiaxed grains has occurred at SHT times of 7 days, and after 14 days several large equiaxed grains are apparent. Whilst it is known that the loss of Li through oxidation can result in abnormal grain growth (due to its effect on the behaviour of β′ (97)), it is considered unlikely that this is responsible for the observed behaviour. This is because the effect is not widespread, as is frequently seen at the surface of heat treated samples, and the loss of lithium is unlikely to have occurred to the 1/4 depth even in 14 days of SHT.

5.2.1.2 β′ (Al_3Zr) coarsening

From the Lifshitz and Slyozov and Wagner (LSW) theory (122) the diffusion controlled coarsening of spherical particles will proceed according to:

$$\overline{r}^3 - \overline{r_0}^3 = k(t - t_0) \qquad (5.4)$$

where:

$\bar{r}$ is the average particle radius at time t,

$\bar{r}_0$ is the average particle radius at time t_0 and

k is represented by

$$k = \frac{8\sigma C_0 V_m^2 D_0 \exp\left\{-\frac{Q}{RT}\right\}}{9\nu RT} \tag{5.5}$$

where:

k is the coarsening rate constant

Q is the effective activation energy for Zr diffusion in the matrix (222kJmol^{-1})

D_0 is the diffusivity of the rate controlling solute (5.4E-3m^{2}s^{-1})

C_0 is the solubility limit of that component in the matrix (43moles Zr m^{-3})

ν is the stoichiometry factor (=1)

V_m is the molar volume of dispersed phase (4.13E-5m^{3}mol^{-1})

σ is the interfacial energy (4Jm^{-2})

T is the temperature of SHT (803K).

The above equations and values were proposed after studies were performed on the Al-Zr and Al-Zr-V systems (122), and their use here is intended only to provide an insight into the possible magnitude of coarsening effect that could occur in the 8090 system.

From the use of t_0 as 2400s (the time of the rolling reheat) and an initial particle radius of 20nm, Equation 5.5 suggests that β′ particle diameters of up to 200nm may result from the SHT of a sample for 14 days at 530°C. Whilst no particles quite as large as this were observed in the TEM, comparison of the β′ particle sizes in Figures 4.71 and 4.76 does suggest that some coarsening has occurred, and it should be noted that some particles in Figure 4.71 appear to approach around 80-100nm in size. Therefore, placing a realistic particle radius of 50nm in Equation 2.23 will predict the pinning force that exists if the particles do coarsen to the size observed (i.e. half that predicted). When this is done a pinning force of around 1.1E+5 is calculated. Comparison of this value with the F_R values in Table 5.1 suggests that recrystallisation would be unlikely in the material rolled at 480°C, but is likely to have started in the 400°C rolled material where the coarsened particles are present. This very closely describes the experimental observations in the ASC material.

The presence of these large and equiaxed recrystallised grains for material deformed at high temperature (and therefore at relatively low driving force for recrystallisation) suggests that the occurrence of some so-called recrystallised elongated grains may be a product of the difficulty in interpreting the appearance of anodised specimens, and that instead of recrystallisation merely extensive recovery has occurred (see § 5.2.3).

5.2.2 Composite materials

Both AMMP and MMC composite materials were found to display extensive recrystallisation at much shorter times of SHT than their monolithic counterparts. The size and distribution of β′ (Al_3Zr), and its behaviour during SHT, could not be studied for the composite materials, due to lack of success in producing usable thin foils.

The enhanced recrystallisation kinetics of the composite materials is in agreement with the theory of particle stimulated nucleation (PSN) (e.g.51), and this will be discussed more fully in the next section.

The agreement of the observed microstructural features and predicted β′ particle size suggests that coarsening of this phase may be a significant feature at very long times of solution heat treatment (i.e. 7 days or greater). It is, however, of no significance industrially, because of the timescale involved.

5.2.2.1 Particle stimulated nucleation

The mean strain rate for each pass of the rolling schedule has been calculated from the relation:

$$\bar{\dot{\varepsilon}} = \frac{\varepsilon v}{\sqrt{R\Delta h}} \tag{5.6}$$

where:

$\bar{\dot{\varepsilon}}$ is the mean strain rate (s^{-1})

v is the roll velocity (ms^{-1})

R is the roll radius (m)

Δh is the reduction in height of the workpiece (m)

These strain rates, and the measured finish rolling temperatures are given in Table 5.2, and when substituted into Equation 2.18:

$$\dot{\varepsilon}_c = \frac{K_1 \exp\left(-\frac{Q_v}{RT}\right)}{Td^2} + \frac{K_2 \exp\left(-\frac{Q_b}{RT}\right)}{Td^3}$$

with the interfacial energy assumed to be approximately equal to grain boundary energy (123), $Q_b \approx 10RT_m$ (124) and the Td^3 term neglected at high temperature, provides a critical particle diameter for PSN of between 1.5 and 3μm for the 3rd pass of the 400 and 480°C rolling schedules respectively. The fact that the less severe first pass conditions provide critical particle diameters of 3.5 and 12μm (and the composite materials contain 12μm SiC) suggests that, even allowing

for error in applying the Al-Si derived equations directly to the present system, most of the reinforcement particles are likely to be able to provide nuclei for recrystallisation, and that PSN is of importance when heat treatment schedules are devised for composite materials.

5.2.2.2 General recrystallisation behaviour

The presence of the undeformable SiC particles provided the expected increase in rolling loads, as can be seen from Tables 4.12 and 4.13. The higher dislocation densities that will result mean that the driving force for recrystallisation will be significantly higher for all deformation temperatures. Thus the enhanced kinetics may be attributed to both enhanced nucleation via PSN, and an overall increased dislocation density.

The sudden change from what essentially appears an unrecrystallised structure at 7 hours for the AMMP rolled samples to fully recrystallise for both the 400 and 480°C material at 8 hours suggests, in common with the ASC material at long SHT times, that the grain boundaries have suddenly become unpinned, albeit to a greater extent. However, the likelihood of coarsening of β′ at such short times is very low, and so the reason for this behaviour is unknown.

The scale of the extruded composite's microstructure makes resolving specific features very difficult. It is apparent, however, that recrystallised grains are very definitely associated with the SiC particles, as can be seen in Figure 4.70(b) where many larger grains are observed at the reinforcement particles. The MMC material appears to exhibit a more gradual change towards a recrystallised structure than the as-cast composite material. Whilst both materials have nominally been homogenised, a possible reason for the described differences in behaviour of AMMP and MMC materials is that grain boundary segregation exists in the AMMP material, and relatively protracted SHT times are required to homogenise the sample and "unpin" the grain boundaries in order that recrystallisation may occur. Evidence for some as-cast structure remaining after rolling is shown in Figure 4.74, where a transmission electron micrograph shows preferentially thinned foil areas, indicative of segregation (125). During the TEM study areas at grain boundaries in the as-cast samples were found to exist where segregation appeared likely.

5.2.3 Quantifying fractions recrystallised

Use of hardness testing as a means of following recrystallisation in aluminium alloys is a well established technique. In this study, however, it proved impossible, from hardness measurements, to distinguish between material that was obviously recrystallised and that which was not (e.g. ASC material after 30 minutes and 5 minutes respectively). The value of hardness decreased from the as-rolled state to a value of around 60 VPN in a few minutes of SHT, regardless of initial rolling temperature, or material examined. The value of hardness, and the fact that no perceptible change occurred as the length of SHT was increased, is in exact agreement with the work of Makin and Stobbs (102), and a similar lack of success in following recrystallisation by this method prevented its use in the study by Goncalves (16). The sudden drop to a stable value was attributed by Makin and Stobbs to a "low activation energy for recovery processes", and this would fit well with the behaviour of the monolithic materials studied here, when rolled at

temperatures of 400°C and above.

It does not, however, explain the case of the solution treated ASC material, after rolling at 300°C. Here the material recrystallises to an appreciable extent in a relatively short time, indicating that recovery has not significantly decreased the energy available for recrystallisation by widespread rearrangement of the dislocations. It is difficult, however, to speculate as to what other phenomenon could lead to the effect.

The quantification of fractions recrystallised is further complicated by the problems that became apparent during the extensive investigation of anodised specimens during the course of this research. These are summarised in § 4.3.3. There is a problem in establishing just what criterion is to be used for deciding whether a grain is recrystallised or not. From the "clarity" criterion that is sometimes used, where the cleanness of the anodised grain interior under cross-polars is used as the decisive factor (clean interiors being indicative of recrystallisation) one would assume that the ASC material rolled at 400°C and SHT for 14 days was recrystallised. The onset of grain boundary bulging and the formation of equiaxed grains that has been reported, however, show that the driving force for recrystallisation still exists, and that the microstructure is most likely just recovered. Evidence is available for this in the form of Figure 4.72, where a transmission electron micrograph of an area of the solution heat treated ASC material discussed above is seen to exhibit only a well *recovered* substructure. A further problem discovered with the use of anodised specimens in quantifying fractions recrystallised is that, depending upon the orientation of the specimen with respect to the cross-polars, different grains came into view. The effect is shown in Figure 5.10(a)-(c). For the sake of clarity, abnormally large surface grains are shown, but the same effect is also prominent in "normal" interior grains, as can be seen from comparison of Figure 5.11 (which shows a MONO sample, solution heat treated for 14 days) with Figure 4.66.

This last micrograph shows that the problem is not just one of grain size, but of apparent fractions recrystallised. The specimen of Figure 5.10 exhibits areas of very small equiaxed grain structure, and the position of these areas shifts as the specimen is rotated with respect to the cross-polars. This poses the question: how is it possible to see all of the grains in an anodised specimen?.

This research has not answered this question, but does suggest, at least, that many grain size measurements performed using this etching and viewing technique may be open to question.

5.3 Industrial implications

As this project was originally devised in order that the hot workability of the studied materials be assessed in an industrial context, it is important that the salient points are now noted.

The comparison of monolithic and composite materials has been made in order that the viability of processing the latter by conventional methods be investigated. The elevated temperature strength of the composite materials is only slightly higher than that of the monolithic alloys, and should not therefore present any problems in industrial forming processes. The importance of finishing the deformation process at a sufficiently high temperature is evident from both a ductility and microstructural point of view. The torsion ductility study and examination of edge cracking in rolled slabs has suggested that rolling and forging of these composite materials are possible, but, especially in the case of the MONO material, the temperature should be carefully controlled to ensure that the maximum ductility is utilised. As stated earlier, the very poor ductility of the composite materials precluded rolling at less than 400°C. Some cracking was evident in the composite PSC samples, but the effect was not so pronounced. Overall, if the finish-deformation temperature is maintained above 400°C then the processing of the composite materials by conventional methods appears viable. In addition to corresponding with peak ductility, the importance of 400°C as a lower limit of finishing temperature is evident from the fact that the recrystallisation kinetics of the ASC material are enhanced to such an extent when the deformation is finished at around 300°C, that the possibility of partially recrystallised grain structures arises. As stated in § 2.9, these structures are to be avoided, because of the inhomogeneous properties that may arise. Figures 4.69(b) and 4.70(b) show that the introduction of reinforcement particles may lead to the presence of some recrystallised grains at very short times of SHT. This suggests that it is not viable for a fully unrecrystallised structure to be produced in these materials.

6 Conclusions

• Constitutive equations of the hyperbolic sine type, formulated from plane strain compression data, are found to provide excellent agreement with experimental value of stress.

• High activation energies of deformation (of around 185kJ/mol) are found for the MONO, AMMP and MMC materials tested under plane strain compression. The ASC material possesses an activation energy only slightly higher than is usual for aluminium alloys, at 165kJ/mol.

• Unusually high stress levels result from deformation in plane strain compression at 300°C.

• Constitutive equations formulated from torsion test data agree with those formed from PSC test data for the MMC material. However for the MONO material the two test methods lead to different equation constants when the experimental data is to be accurately described. Less hardening of the MONO material seems to result from the use of torsion testing compared with the use of PSC. Equations from each test type are, however, self-consistent.

• The strengths of the composite materials (AMMP and MMC) are very similar to their monolithic counterparts when tested at high temperature and low strain rates under conditions of plane strain. This indicates that no accumulation of dislocations occurs under these conditions. This is in agreement with general theory.

• From torsion test data, the ductility of the MONO material peaks at 450 °C and subsequently decreases at 500°C. The MMC material does not exhibit a large ductility change with the test temperature, and exhibits failure strains that are a factor of around 2.5x lower than those of the MONO material.

• Anodised samples viewed under cross-polars may present different apparent fractions recrystallised and recrystallised grain sizes, depending upon the orientation of the specimen relative to the analyser. For this reason, and the general resistance of the alloys to recrystallisation, quantifying fractions recrystallised has not been possible. Samples which, according to a criterion of recrystallised grains appearing "clear" under the microscope, would be considered recrystallised, have been shown in a TEM study to have undergone extensive ***recovery***.

• In the ASC material there is a very prominent transition in the solution heat treated microstructure from a recrystallised equiaxed structure arising from material rolled at 300°C to a partially recrystallised elongated structure in material rolled at 400 and 480°C. The 300°C rolled material is fully recrystallised within 20 minutes, whereas the material rolled at higher temperatures is unrecrystallised even after 14 days of solution heat treatment at 530°C.

• Particle stimulated nucleation is found as a viable mechanism for a large enhancement of the recrystallisation kinetics of solution heat treated rolled slabs, when the composite materials are compared with the monolithic alloy. The occurrence of PSN under the deformation conditions used is in agreement with prediction.

• Evidence has been found from a limited TEM investigation that the β' (Al_3Zr) pinning phase coarsens at very long solution heat treatment times. This evidence is in the form of serrated grain boundaries and equiaxed grains being formed at these SHT times. The occurrence of coarsening is in agreement with prediction.

Overall, it is concluded that the incorporation of reinforcement particles has a small but significant effect on the hot strength of the matrix alloy, but a very significant effect on the recrystallisation kinetics. It is recommended that the deformation temperature be maintained above 400°C.

7 Suggestions for further work

• A detailed study of β′ (Al_3Zr) coarsening kinetics in these spray cast materials would enable accurate particle size data to be established. In combination with measured dislocation densities this would allow the accurate determination of the point at which the recrystallisation driving force and pinning force due to β′ balance. This balance point could then be experimentally verified with a series of carefully controlled rolling and heat treatment experiments.

• A TEM study of specimens of the monolithic alloy deformed at 300°C and quenched at various points in the deformation would enable the precipitates at certain strains to be characterised. From this it would be possible to determine whether dynamic precipitation and solute effects are responsible for the high stress levels and peak behaviour that occur in the monolithic alloy.

• Examination of thin foils of the composite materials would allow assessment of the extent of particle stimulated nucleation and also whether dynamic recrystallisation could be responsible for the drop in stress level apparent when the MMC material is deformed in PSC.

• A method of terminating the torsion tests at the point of fracture (i.e. a mechanism that stops the test when the load tends to zero) would allow the fracture surfaces to be examined, and aid investigation of why the ductility of the MONO material decreases when deformed at a temperature greater than 450°C.

8 Appendices

8.1 Appendix 1. Use of the servo-hydraulic plane strain compression machine

8.1.1 Introduction

There is a need to optimise and standardise the testing procedures used with this piece of apparatus in order that each stress-strain data set may be directly compared with other similar tests. This report will discuss the factors that need to be considered when setting up a test, and deal with the necessary calibration of the machine. The discussion will be limited to the use of constant strain rate tests, of the type used in the present research. The basic details of machine operation are catalogued elsewhere (1-1) and will not be dealt with here.

8.1.2 Calibration of the machine prior to testing

8.1.2.1 Zeroing of the tools

Re-zeroing of the tools must be performed each time the tools are changed and/or the temperature of the test furnace is altered (the latter due to the effect of thermal expansion). It ensures that a test is started from the optimum pre-test tool position (see § 8.1.2.5). The tools zero position is set assuming a specimen thickness of 10mm, and variations in thickness due to machining, lubricant and thermal expansion are taken into account with the command given to the computer and the setting of the wedge prior to a test being performed (see § 8.1.2.5).

The procedure used is as follows:

1/ Unlock the crosshead and put the machine into load control.
2/ Apply a 5kN load.
3/ Use the "displacement set zero" dial to set the displacement reading to 10.00.
4/ Remove the load.
5/ Move the crosshead up by 1 brief push of the crosshead "up" control button (located on the panel mounted on the machine frame).
6/ Reapply the 5kN load. If a load is registered then push the crosshead button "up" once. Repeat until no load is registered.
7/ At this point bring the crosshead down (one push of the "down" button at a time) until a 5kN load is again registered.
8/ Lock the crosshead.
9/ With a 5kN load applied set the displacement readout to a value of 10.00 using the "displacement set zero" control.
10/ Move the ram up and bring in the wedge using the setting dial until a reading of 4.5 is attained.

11/ Raise the ram and squash the wedge sharply.
12/ Raise the ram up to 10mm above the wedge and allow it to drift slowly back down onto the wedge.
13/ Check the displacement reading. If it does not read 0.00 then repeat the above procedure after bringing in the wedge to a value of 4.55. Again check the displacement reading and repeat this procedure until the reading of 0.00 is obtained.

From the above procedure, the final position of the wedge used to obtain a displacement reading of 0.00 is known as the "wedge zero position".

8.1.2.2 Load-elongation compensation

The load-elongation compensation device electronically compensates for the elasticity of the machine frame that will occur during testing. To illustrate the point, a check performed with the tools touching and the load elongation device set correctly for compensation would produce a horizontal line on the x-axis of a load vs. displacement plot.

The setting of the device needs to be calibrated prior to a test being performed. The method of calibration is outlined below:

1/ The test furnace should be stable at the desired test temperature.
2/ Withdraw the wedge and bring the tools into contact, in load control. load the tools to ensure that any minor surface imperfections are removed.
3/ A 5kN load should be applied to ensure full tool contact and the displacement readout set to a reading of 10.00.
4/ The load should be increased in 5kN steps initially to 50kN and 10Kn steps thereafter. The displacement corresponding to each increment of load should be noted. The variation in displacement readings between increments of load should not exceed 0.02mm. It is only necessary to load up to the maximum stress level of interest in the planned testing schedule.
5/ If the amount of compensation is incorrect reduce the load to 5kN and alter the device setting on the pot located in the back of the middle electronics cabinet.
6/ Repeat the above procedure until the compensation is correct.

8.1.2.3 Tests performed using zero load elongation compensation

When tests are performed using the load-elongation compensation device (L.E.) set to zero a proportion of the initial displacement of the ram is effectively "lost" to the frame of the machine due to the machine's frame having a finite stiffness. The amount of displacement "lost" obviously depends upon the load at a certain point in the test, which in turn will depend upon the temperature of test. The loss of displacement to the machine means that the strain rate experienced by the specimen is initially too low, even though the raw ram displacement readings

indicate that the strain rate is equal to that set. If the basic raw data file is used in the "Turtle" program then the strain rates calculated for the initial loading part of the deformation will be incorrect.

To correct the data file the "elastic modulus" of the machine frame must first be ascertained by the procedure below:

1/ The same loading procedure listed above should be used, but with the L.E. set to 0. This must be carried out for each test temperature used.

2/ The readings of displacement for each increment of load should be noted

3/ Load vs. displacement readings should be plotted and the modulus for each test temperature calculated from the slope.

4/ Each load reading in the raw data file must be multiplied by this modulus value. This gives a value of displacement which must be subtracted from the corresponding raw displacement reading.

5/ The raw displacement readings must then be replaced by the corrected readings, and the corrected raw file analysed using "Turtle".

8.1.2.4 Velocity compensation

This device allows the time lag between the command signal and the actual displacement of the ram to be reduced. Optimum values are found by performing "dummy" tests (i.e. tests with the machine running but no specimen) at several strain rates, and observing which setting of the compensation device reduces the discrepancy of displacement behind the control signal. A value of < 0.1mm for the variation is deemed acceptable.

When the correct value has been found it should be entered in the relevant potentiometer, which is located in the side of the first electronics cabinet. **NOTE: at present, (September 1994) the machine behaviour is optimised by the use of a velocity compensation setting of 3.**

8.1.2.5 Setting of the pre-test tool position

It is important that the test begins from the optimum position of the tools just contacting the specimen. To achieve this the actual thickness of the specimen must be input into the computer prior to testing. This must take into account a number of factors which may cause the actual thickness to vary from the perfect 10.00mm that the machine tools have been set for:

1 Variation in the machined thickness of the specimen.

2 Residual lubricant.

3 Thermal expansion of the specimen at the test temperature.

Failure to correct for 1/ and 3/ above will mean that the tools contact the specimen before they the test is intended to begin, thus increasing the actual amount of deformation incurred by the specimen, compared with that requested.

The value of hot initial specimen thickness that should be input to the computer is given by:

$$h_0 = h_{(Room\,Temp.)}(1 + \alpha\Delta T) + 2l_f \qquad (A1-1)$$

where: l_f is the residual lubricant thickness (see below) and α is the linear thermal expansion coefficient.

As regards 2/, if the position of the tools is not set correctly then the squeezing out of any excess lubricant will appear on the positive side of the strain axis (see Figure A1) and the total strain to the specimen will be less than requested. The value for residual thickness of lubricant l_f that should be entered into Equation A1-1 (1) above is 0.1mm (1).

8.1.2.6 Wedge position

The wedge is a mechanical means of ensuring that the desired end-point of a test is not exceeded. The normal wedge setting for a nominally 10mm thick specimen can be calculated from:

((Actual specimen thickness-10)x0.436)+ wedge zero position

where the "actual specimen thickness" is that calculated from § 8.1.2.4 above.

8.1.3 Processing the raw data

8.1.3.1 Spread correction

A spread coefficient unique to each specimen, C, is calculated from the equation:

$$C = \frac{\frac{b}{b_0} - 1}{1 - \sqrt{\frac{h}{h_0}}} \qquad (A1-2)$$

where: b_0 and b are initial and final breadths

h_0 and h are initial and final thicknesses.

This value is used in the "Turtle" analysis program to enable the stress calculation to be performed using instantaneous contact area.

8.1.3.2 Origin correction

When the final PSC stress-strain curves are presented then they should depict only the plastic behaviour of the test specimen. Therefore the elastic behaviour of the specimen and a number of sources of error need to be removed from the raw data produced by the machine.

Assuming that the zero position of the tools has been accurately determined (see § 8.1.2.1) then as the tools first impinge upon the sample there will be a number of events that do not affect the plastic deformation of the specimen. The first of these is that the lubricant (if used) will be squeezed from between the tools and the specimen, down to a thickness that is assumed to be 0.1mm. As the lubricant reaches its final thickness, than any small misalignment of the two tools will be rectified as the load increases. This first part of the deformation will contain an elastic contribution from the specimen and, in certain circumstances (i.e. if the load-elongation compensation device is switched out of the operating circuit - see § 8.1.2.2), an elastic component due to expansion of the machine frame itself. All of the effects mentioned above have the effect of decreasing the gradient of the load-displacement curve. They are all corrected out of the raw data by means of the "origin correction" in the "Turtle" analysis program.

8.1.3.3 Friction correction

Friction between the tools and specimen leads to an increase in the load during a test, as the material under test is constrained in the deformation zone rather than flowing outwards. High frictional forces can also lead to large amounts of "redundant" work being done due to the test material shearing rather than slipping out of the deformation zone. This can mean that the specimen experiences a far higher strain rate than is indicated by the test data. The use of too high a coefficient obviously leads to an artificially low stress level, as it leads to the "assumption" by the analysis program that a greater proportion of the work done is redundant due to shearing of the specimen than is actually so. The reverse of this is also true.

Determination of the effective coefficient of friction involves testing specimens of different thicknesses (usually 10mm, 6mm and 4mm), to a constant strain, and over the range of test temperatures used.

To calculate the coefficient of friction at the different temperatures, a graph of (stress to strain of 0.5) vs (friction coefficient) is plotted for the analysed data. The value of coefficient is then found from the point of intersection of the lines for each data set.

8.1.4 Use of the "Turtle" analysis program

This section will provide a basic guide to the contents (and order of use) of the Turtle program.

Enter the Turtle program.

A: read source file.

B: modify test characteristics.

This section allows the following test parameters to be altered prior to analysis being carried out:

- test number (for use with multiple deformation tests)
- initial thickness (should be corrected for temperature)
- final thickness (should be corrected for temperature)
- breadth of sample (should be corrected for temperature)
- width of tools (should be corrected for temperature)
- spread coefficient (use the coefficient specific to the specimen analysed)
- friction coefficient

D: change material characteristics

Here the activation energy for deformation can be input so as to enable the correct Z to be calculated by the program.

G: Temperature adjustment

A value (usually negative) can be **added** to the recorded temperature values if they are different from those given by the hand-held thermometer. The recorded temperature is ascertained by running a dummy test (without the pump running) with the thermocouple between the tools. A print out of the data ("P" on the main Servotest menu) will give a mV reading corresponding to the temperature. This can be converted to degrees Celsius by the use of a look-up table.

H: Origin correction.

Here two points are selected on the slope of the first part of the load-displacement curve. It is important that the points are selected only on the first **linear** and most vertical part of the curve. To facilitate this the program allows the axes to be expanded. Usually expansion to a scale from -1 to 1.5 will allow the curve to be viewed in sufficient detail. The details of the operations performed in the origin correction are included in a separate report.

J: Friction correction

Performed by the program using the previously entered value of friction coefficient.

K: Strain rate calculation

Performed by the program.

W: write a result file

V: values for a given deformation

This allows values of stress, strain rate, temperature and Z to be displayed for an input value of strain.

After plotting of the results the strain given should be checked on the specimen using the formula:

$$\varepsilon = F \ln\left(\frac{h_{f(test\,T)}}{h_{0(test\,T)}}\right) \qquad (AI-3)$$

and comparing with the value of final strain given by the computer. F is a conversion factor which allows for the effect of specimen breadth on the condition of plane strain, and is expressed as:

$$F = \frac{1.155(b-w)+w}{b} \qquad (AI-4)$$

where:

$$b = b_o\left(1 + c - \left(c\sqrt{\frac{h}{h_o}}\right)\right) \qquad (AI-5)$$

rearranged from Equation A1-2.

and b_o is the initial specimen breadth

h_o is the initial specimen thickness

h is the instantaneous (final) thickness

w is the tool width

c is the spread coefficient

Appendix 1 References

(1-1) Servotest users guide, D.R.Manvell, University of Sheffield.

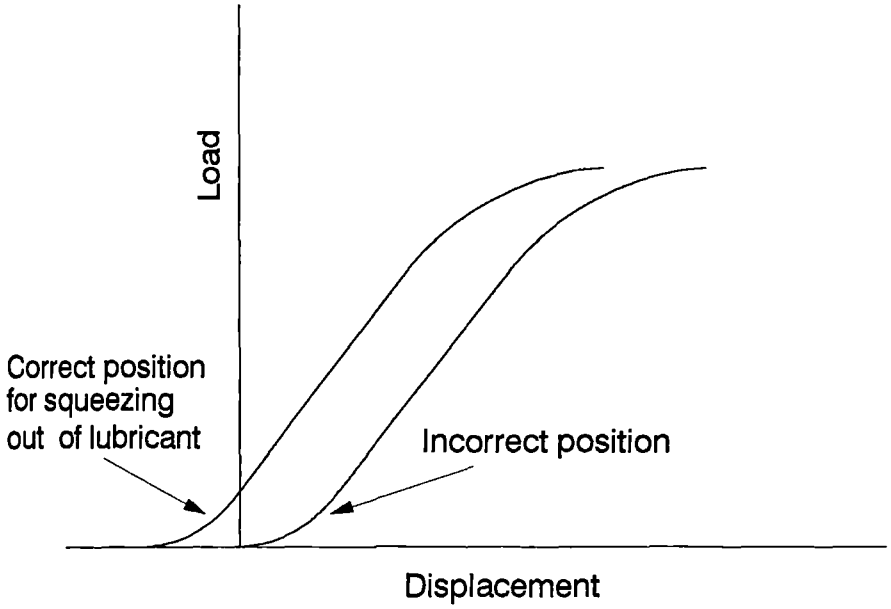

Figure A1 The result of incorrect positioning of the tools

8.2 Appendix 2. Production of flow stress equations from raw stress-strain data

1 It is necessary to possess data from tests performed over a range of temperatures and strain rates. Analyse this raw data from the PSC tests using the "Turtle" programme.

2/ Plot all stress-strain curves from the testing matrix and read values of characteristic stresses from them. These are the stresses at strains that are capable of describing the shape of the curves (e.g. $\sigma_0, \sigma_{01} \sigma_y, \sigma_{peak}, \sigma_{ss}$).

3/ Plot instantaneous Z values vs. $f(\sigma)$ at each of the characteristic strains (Z is calculated using the Q_{def} value determined by the method given in § 8.2.1). The graphs that need to be plotted for each stress function are given below:

Power law: lnZ vs $\ln \sigma$

Exponential law: lnZ vs σ

Hyperbolic sine law: lnZ vs $\ln(\sinh \alpha\sigma)$

Values of n and B are found from the plots of power law and exponential law respectively, and α is initially found from the relation:

$$\alpha = \frac{\beta}{n'}$$

where $n' \approx n$ applies. Where few data points exist at sufficiently low stresses for accurate plotting of a power law relation, n can be assumed to be equal to 5.

4/ A line is placed through the points in each of the plots by means of linear regression. The coefficient of determination (R^2) can be used as an indication of which stress function best fits the experimental data.

5/ Having decided upon the best-fit stress function, the constants should be calculated from the straight line plots for each characteristic strain. Placing these constants in the relevant Equation (2.6 to 2.8) provides a relation between temperature compensated strain rate and stress.

6/ The experimental stress-strain data can now be corrected for the effects of deformational heating using the stress function formulated in 5/ above. As an example, for the exponential law, under constant strain rate conditions, σ_2, the temperature corrected stress, is given by:

$$\sigma_2 = \sigma_1 + \frac{Q_{def}}{\beta R}\left(\frac{1}{T_2} - \frac{1}{T_1}\right) \qquad (A2-1)$$

where: σ_1 is the experimental stress reading, T_2 is the initial specimen temperature, and T_1 is the temperature to which the data are to be corrected. Alternatively the data can be corrected to constant Z, for example using the exponential law given in Equation 2.7.

The corrected stress-strain curve is now in its final form.

7/ To account for the strain dependence of the stress data use of the Voce form of equation (given as Equation 2.13) is necessary.

By use of the expansion of e^{-x}, at low strains Equation 2.13 reduces to:

$$\sigma = \sigma_0 + BC^m\varepsilon^m \qquad (A2-2)$$

and at high strains reduces to:

$$\sigma_{ss} = \sigma_0 + B \qquad (A2-3)$$

where σ_{ss} represents steady state stress.

8/ Combination of Equation 2.13 and the preferred form from Equations 2.6 to 2.8 allows the flow stress for any strain, strain rate and temperature to be calculated.

Example:

Assume the use of Equation 2.7 (the exponential stress function). This allows σ_{ss} and σ_0 to be expressed as follows:

$$\sigma_{ss} = \frac{1}{\beta_{ss}}\ln\frac{Z}{A_{2(ss)}} \qquad (A2-4)$$

$$\sigma_0 = \frac{1}{\beta_0}\ln\frac{Z}{A_{2(0)}} \qquad (A2-5)$$

Placing the above expressions in Equation 2.13 allows the constant B to be simply expressed.

9 To determine the constants C and m:

(a) C is determined as a function of Z by manipulation of Equation 2.13 and is given the form:

$$C = \frac{1}{-\varepsilon}\ln\{1 - (\frac{\sigma - \sigma_0}{B})^{\frac{1}{m}}\} \qquad (A2-6)$$

(b) From Equation (A2-2),$(\sigma - \sigma_0)\alpha\varepsilon^m$ then a plot of $\ln(\sigma - \sigma_0)$ vs $\ln\varepsilon$ provides the value of m. Generally m is ≈ 0.5.

10/ An alternative method is available for fitting the constant C (2-1). This involves defining the strain at the onset of steady state, ε_{ss}, as the strain when:

$$(\sigma - \sigma_0) = 0.98(\sigma_{ss} - \sigma_0) \qquad (A2-7)$$

This removes some of the ambiguity in deciding where εss occurs. εss is then determined as a function of Z and with the value of m fixed at 0.5, C can then be expressed as:

$$C = \frac{3.23}{\varepsilon_{ss}} \qquad (A2-8)$$

The value σ_0 from Equation 2.13 is then fitted so that the correct curvature results. An equation is then fitted to the resultant σ_0 values in order that a full description of a stress-strain curve can be made from knowledge of the deformation conditions only.

8.2.1 Calculation of the activation energy of deformation

Activation energies of deformation (Q_{def}) are often assumed to be equal to those given in the literature. This can lead to problems in the fitting of stress function equations.

The method given below (2-2) enables the Q_{def} value to be calculated from plain strain compression data.

- For each material to be considered plot $\log_{10}\dot{\varepsilon}$ vs. flow stress. The strain rate for a constant flow stress can then be read from this curve.

- These strain rate values are now plotted vs. 1/T (where T is in degrees Kelvin). If the activation energy does not show any systematic variation with temperature then the slope of the lines is constant and is equal to:

$$\frac{Q}{\log_e 10.R} \qquad (A2-9)$$

The actual value of Q_{def} is then simply calculated from this expression and the slope of the line.

Appendix 2 References

(2-1) C.M.Sellars, "Microstructural Modelling of Thermomechanical Processing", Third International Conference on Aluminium Alloys, their Physical and Mechanical Properties, Eds. L.Amberg, O.Lohne, E.Nes and N.Ryum, NTH/SINTEF, Trondheim, Norway. 1992, Vol III, pp.89-105.

(2-2) G.J.Richardson, D.N. Hawkins and C.M.Sellars, in "Worked Examples in Metalworking" Institute of Metals, 1985 p.27

8.3 Appendix 3. Analysis of torsion data to produce true stress-strain curves

8.3.1 Introduction

Two possible methods are available for the conversion of data produced by torsion testing to provide true stress-true strain curves. The first method requires a matrix of different strain (twisting) rate tests to be performed in order that the strain rate sensitivity, m, and the strain hardening coefficient, n, may be ascertained. The second method uses the concept of the "effective radius" (3-1) and means that the conversion from shear stress and strain data to effective true stress and strain data can be made when tests at only one strain rate have been performed.

The effective radius is a point in the specimen at which the effects of m and n can be considered to be balanced and, as such, effectively ignored.

This concept is merely a way of describing the strength of the material at a point in the specimen; the real geometry of the specimen is still dealt with in the calculations of strain and true stress. The exception to the use of external dimensions in the calculations performed is in the use of the effective radius in ascertaining the true strain rate of the test. A specimen tested in torsion has an inherent strain rate gradient running from centre to surface. The strain rate cited for a test should obviously be indicative of the actual strain rate at the point at which the flow stress is quoted, i.e. at the effective radius. Fortunately the calculations are made simple by the fact that in solid cylindrical specimens the effective radius a^* always coincides with a distance $0.724a$, where a is the actual specimen radius (3-1).

This method of calculation of true stress-true strain curves has been shown to produce results with errors which are always < 2.5%, and are therefore generally within the range of experimental reproducibility (3-2). This method has also been found to be comparable in accuracy with the method involving determination of the work hardening coefficient and strain rate sensitivity.

8.3.2 Analysis of raw data

Use of the effective radius concept provides the following equations:

$$\tau_{a^*} = \frac{3\Gamma}{2\Pi a^3} \qquad (A3-1)$$

$$\gamma_{a^*} = \frac{a^*\theta}{l} \qquad (A3-2)$$

$$\dot{\gamma}_{a^*} = \frac{a^* \dot{\theta}}{l} \qquad (A3-3)$$

where τ is shear stress, Γ is torque, γ is shear strain, θ is angle of twist (radians), l is specimen gauge length, $\dot{\gamma}$ is shear strain rate and $\dot{\theta}$ is twisting speed (radians/s). The subscript a^* denotes that the parameter in question is that at the effective radius.

The von Mises criterion is used as the means of converting shear stresses and shear strains to equivalent true stresses and true strains. This criterion enables the following equations to be formulated:

$$\sigma_{a^*} = \sqrt{3}\,\tau_{a^*} \qquad (A3-4)$$

$$\varepsilon_{a^*} = \frac{\gamma_{a^*}}{\sqrt{3}} \qquad (A3-5)$$

$$\dot{\varepsilon}_{a^*} = \frac{\dot{\gamma}_{a^*}}{\sqrt{3}} \qquad (A3-6)$$

where σ is true stress, ε is true strain, $\dot{\varepsilon}$ is true strain rate and other terms have their meanings as above.

The actual calculation method used for production of true stress-true strain data from the raw torque-twist data utilises a spreadsheet package and is outlined below:

1/ From the combination of Equations (A3-1) and (A3-4):

$$\sigma_{a^*} = \frac{3\sqrt{3}\,\Gamma}{2\Pi a^3} \qquad (A3-7)$$

where σ is in N/mm^2 and Γ is in Nm.

2/ Combination of equations (A3-2) and (A3-5), using $a = 0.724a^*$ gives the equivalent true strain at the effective radius:

$$\varepsilon_{a^*} = \frac{0.724a\theta}{\sqrt{3}\,l} \qquad (A3-8)$$

which leads to:

$$\varepsilon_{a^*} = \frac{0.724ax2\Pi xNo.revs}{\sqrt{3}l} \qquad (A3-9)$$

3 Similarly, for calculation of true strain rate, combination of equations (A3-3) and (A3-6) gives:

$$\dot{\varepsilon}_{a^*} = \frac{0.724a\dot{\theta}}{\sqrt{3}l} \qquad (A3-10)$$

leading to the equation:

$$\dot{\varepsilon}_{a^*} = \frac{0.724ax2\Pi xrpm}{\sqrt{3}lx60} \qquad (A3-11)$$

4/ Once all of the above values are calculated the true stress-true strain curve can be produced using a graph plotting package.

Appendix 3 References

(3-1) Barraclough, D.R., Whittaker, H.J., Nair, K.D. and Sellars, C.M.
"Effect of specimen geometry on hot torsion test results for solid and tubular specimens"
Journal of testing and evaluation Vol1 No.3 May 1973 pp.220-226.

(3-2) G.J.Richardson, D.N. Hawkins and C.M.Sellars, in:
"Worked Examples in Metalworking" Institute of Metals, 1985 p.27

8.4 Appendix 4. Calculation of the volume fraction of β′ (Al_3Zr)

In both ASC and MONO material 0.12wt% of Zr is present. Therefore, considering 1kg of alloy, 1.2g of Zr is available.
The number of moles of Zr available in 1kg of alloy is given by

$$No.ofmoles = \frac{mass\,of Zr\,per\,1kg}{Relative\,atomic\,mass\,of Zr} \qquad (A4-1)$$

= 0.013 moles

Because of the stoichiometry of the β′ phase, this is equal to the number of moles of Al_3Zr that may be formed.
Therefore, the mass of Al_3Zr in 1kg of alloy is given by:

$$Relative\,molecular\,mass \times No.ofmoles\,of Zr \qquad (A4-2)$$

which in the present case = 2.24g of Al_3Zr per kg of 8090.
The volume of Al_3Zr is then given by:

$$\frac{mass\,of Al_3Zr}{density\,of Al_3Zr} = 0.55cm^3\,of Al_3Zr\,per\,1kg\,of Alloy \qquad (A4-3)$$

where the density is given as 4.1gcm^{-3} [**4.1**]
To calculate the volume fraction of β′, the aluminium tied up in Al_3Zr is neglected, and the volume of 1kg of alloy must be calculated from

$$Volume = \frac{Mass}{density} \qquad (A4-4)$$

The density of 8090 is taken as 2.54gcm^{-3}. From equation (A4-5), the volume of 1kg of alloy = 393.7cm^3. The volume fraction of Al_3Zr is then equal to

$$\frac{volume\,Al_3Zr\,per\,1kg}{volume\,of\,1kg\,alloy} \qquad (A4-5)$$

= 0.0014 for both monolithic alloys.

Appendix 4 References

[4.1] Mondolfo, C.F.,
"Aluminium Alloys: Structure and Properties", Pub. Butterworth & Co., 1976.

9 References

(1) Grimes, R.,Cornish, A.J., Miller, W.S. and Reynolds, M.A.
Metals and Materials June 1985 pp.357-363.

(2) Stubbington, C.A.
Metals and Materials, July 1988 pp.424-431.

(3) Sakata, I.F.
NASA report CR 165820 January 1982.

(4) Quist,W.E., Narayanan, G.H. and Wingert, A.L.
Aluminium-Lithium Alloys II, Eds. Starke Jr., E.A., Sanders Jr., T.H. TMS-AIME, Monterey, California, 1983, pp.313-334.

(5) Quist, W.E. and Narayanan, G.H.
Treatise on Mat. Sci. and Tech., Vol.31, Academic Press, 1989, pp.219-254.

(6) Sankaran, K.K. and Grant, N.J.
in Al-Li alloys I, Eds. Sanders, Jr, T.H. and Starke, Jr, E.A., Atlanta, USA, May 1980, pp.205-227.

(7) Peel, C.J., Evans, B. and McDarmaid, D.S.
Metals and Materials, August 1987, pp.449-455.

(8) Sankaran, K.K., Vasey-Glandon, V.M. and Iugel, E.J.
in Aluminium-Lithium Alloys V, Vol.I, Eds. Sanders Jr, T.H., Starke Jr, E.A.,
Williamsburg, Virginia, March 1989, pp.1625-1634.

(9) Smith, A.F.
Metals and Materials, August 1987 pp.438-444.

(10) Hyatt, M.V. and Axter, S.E.
Proc Conf.RASELM '91 Eds. Hiruna, K. et al pp.273-280.

(11) Williams, D.B. and Howell,P.R.
in Treatise on Materials Science and Technology, Vol. 31, pp.365-388.

(12) Jensrud, O.
in Aluminium-Lithium Alloys III, Eds. Baker, C., Gregson, P.J., Harris, S.J. and Peel, C.J., Inst. of Metals, London, 1986 pp.411-419.

(13) Hull, D. and Bacon, D.J.
"Introduction to dislocations" International series on Materials Science and Technology, Vol.37, Pergamon Press, 1986.

(14) White, J., Palmer, I.G., Hughes, I.R. and Court, S.A.
in Aluminium-Lithium Alloys V, Vol.III, Eds. Sanders Jr, T.H., Starke Jr, E.A., Williamsburg, Virginia, March 1989, pp.1635-1645.

(15) Ryum, N.,
Acta Met.,(1969) 17 p.269.

(16) Goncalves, M.
Ph.D thesis, University of Sheffield, April 1989.

(17) Gayle, F.W. and Vander Sande, J.B.
Scripta Met. Vol 18, 1984, pp.473-478.

(18) Miller, W.S., Thomas, M.P., Lloyd, D.J. and Creber, D.
Mat. Sci and Tech. Vol.2, part 2, 1986 pp. 1210-1216.

(19) Venkateswara Rao, K.T., and Ritchie, R.O.
Mat. Sci and Tech. Vol.5, part 2, 1989, pp. 882-895.

(20) Peel, C.J., Moreton, R. and Flitcroft, S.M.
in MMC's - property optisation and applications (extended abstracts)
Inst. of Metals, London 1989 p.4.1.

(21) Trumper, R.L.
Metals and Materials, November 1987, pp.662-667.

(22) King, J.E.
Metals and Materials, December 1989 pp.720-726.

(23) Pritchett, T.R.
Proc. Conf Aluminium Technology '86, Ed. Sheppard, T., Inst. of Mets., March 1986, London. pp.51-57.

(24) Friend, C.M.
Journal of Material Science 1987 **22**, pp.3005-3010.

(25) Elias, L.G., Ogilvy, A.J.W., Leatham, A.G. and Kahl,W.
Proc Conf. "International Conference on P.M. Aerospace Materials, Nov. 4-6 1991, Lausanne, Switzerland, p.10.

(26) Estrada, J.L. and Duszczyk, J.
J Mat Sci (25) 1990 pp.1381-1391.

(27) Willis, T.C.
Metals and Materials, Aug 1988 pp.485-488.

(28) Leatham, A., Ogilvy, A., Chesney, P. and Wood, J.V.
Metals and Materials, March 1989 pp.140-143.

(29) Ogilvy, A.
Seminar at the University of Sheffield, February 1990.

(30) Doherty, R.D., Lee, H. and Feest, E.A.
Mat. Sci Eng. 1984 (65) p.181.

(31) Palmer, I.G., Chellman, D.J. and White, J.
International Conference on Spray Forming 2, Ed Wood, J.V. 13-15 September 1993, Swansea, U.K. pp.385-394.

(32) Duszczyk, J., Estrada, J.L., de Haan, T.L.J., Leatham, A.G. and Ogilvy, A.J.W.
Proc. Conf. "International Conference on Powder Metallurgy for Aerospace Materials" 1987 pp.26.1-26.13.

(33) Leatham, A.G., Ogilvy, A. and Elias, L.
Proc Conf. "P.M. in Aerospace, Defence and Demanding Applications
San Diego, Feb.7-10 1993 MPIF, pp.165-175.

(34) White, J., Mingard, K., Hughes, I.R. and Palmer, I.G.
International Conference on Spray Forming 2, Ed Wood, J.V. 13-15 September 1993, Swansea, U.K. pp.355-361.

(35) Lewis, R.L
Proc. Conf. PM in Aerospace and Defence Technologies, MPIF, pp.185-192.

(36) Kojima, K.A., Lewis, R.E. and Kaufman, M.J.
in Aluminium-Lithium Alloys V, Vol.I, Eds. Sanders Jr, T.H., Starke Jr, E.A.,
Williamsburg, Virginia, March 1989, pp.85-94.

(37) Hughes, I.R., Palmer, I.G., White, J., Willis, T.C., Becker, J., Fisher, G., Lewis, R.E. and Willner, E.
in Aluminium-Lithium Alloys VI, Vol.II, Eds. Peters, M. and Winkler, P.J., Garmisch Partenkirchen (FRG), 1991, pp.1347-1352.

(38) Leatham, A.F., Elias, L. and Ogilvy, A.
Met Powder Rep. Oct. 1991, 46, (10) pp.38-41.

(39) Singer, A.R.E. and Ozbech, S.
Powder Met. Vol 28, No.2, 1985, pp.72-78.

(40) Willis, T.C., White, J., Jordan, R.M. and Hughes, I.R.
Proc. Conf. Solidification Processing 1987, Inst. of Mets., Sheffield, U.K.pp.476-478.

(41) Sellars, C.M., and McG.Tegart, W.J.
Int. Met Rev. (1972) 17, pp.1-24.

(42) Hockett, J.E.
Trans. Met. Soc., AIME, 1967, 239, pp.969-976.

(43) Voce, E.
J. Inst. Mets. 1948, 74, 536, pp.760-771.

(44) Glover, G.
Ph.D thesis, University of Sheffield, 1969

(45) Roberts, W.
Deformation, processing and structure, ASM Metals Science Seminar, 1982,
Ed. Kraus, G., ASM Metals Park, Ohio 1984, pp.109-134.

(46) McQueen, H.J. and Jonas, J.J.
"Plastic deformation of materials", Ed. Arsenault, R.J., Academic Press, New York, (1975), pp.393-493.

(47) Sellars, C.M.
Phil. Trans., Royal Soc. London, 1978, A288, pp.147-158.

(48) Jonas, J.J., Sellars, C.M. and Tegart, W.J.McG.
Met. Rev., 14 (1969), pp.1-24.

(49) Haessner, F.
"Systematic survey and basic problems of recrystallisation"
Recrystallisation of metallic materials, Ed. Haessner, F. Riederer-Verlag, Stuttgart 1978.

(50) Humphreys, F.J.
Acta Met. Vol.25, 1977, pp.1323-1344.

(51) Humphreys, F.J.
Recrystallisation '90 Ed. Chandra, T. The Minerals, Metals and Materials Soc., Wollongong, Australia, 1990, pp.113-122.

(52) Humphreys, F.J. and Kalu, P.N.
Acta Met. (1977) Vol.35, 12, pp.2815-2829.

(53) Kalu, P.N. and Humphreys, F.J.
in Aluminium Technology '86, Ed. Sheppard,T., Inst. of Mets., March 1986, London. pp.197-203.

(54) Humphreys, F.J.
Proc. Conf. 4th Riso Int. Symp. on Metallurgy and Materials Science, Ed. Bilde-Sorenson, J.B., 1983, pp.41-52.

(55) Kalu, P.N. and Humphreys, F.J.
Proc Conf 7th Riso Int. Symp. on Metallurgy and Materials Science, Eds. Hansen, N., Juul Jensen, D., Leffers, T. and Ralph, B., 1986 pp.385-390.

(56) Nes, E.
Proc Conf 1st Riso Int. Symp. on Metallurgy and Materials Science, Eds. Hansen, N., Jones, A.R. and Leffers, T., 1980, pp.85-96.

(57) Sandstrom, R.
Proc Conf 1st Riso Int. Symp. on Metallurgy and Materials Science, Roskilde, Denmark, Eds. Hansen, N., Jones, A.R. and Leffers, T. 1980 pp.45-50.

(58) Bay, B. and Hansen, N.
Met. Trans. A, Vol.10A March 1979 pp.279-288.

(59) Gawne, D.T. and Higgins, G.T.
J. Mat. Sci. 1971. 6, p.403-412.

(60) Humphreys, F.J.
Metal Science Vol.13, 1979 pp.136-145.

(61) Liu, Y.L., Hansen, N. and Juul Jensen, D.

Met. Trans. A Vol.20A Sept. 1989. pp.1743-1753.

(62) Humphreys, F.J., Miller, W.S. and Djazeb, M.R.
Mat. Sci. and Tech. Nov. 1990, Vol.6 pp.1157-1166.

(63) Smith, C.S.
Trans. AIME, 175, 1948, p.15.

(64) Nes, E., Ryum, N. and Hunderi, O.
Acta Metall. Vol.33, No.1, 1985, pp.11-22.

(65) Chan, H.M., and Humphreys, F.J.
Acta Met. Vol.32, 2, 1984 pp.235-243.

(66) Hansen, N. and Bay, B.
Acta Met. Vol.29, 1981, pp.65-77.

(67) Shahani, R.A.
Ph.D. thesis, University of Cambridge, 1991.

(68) Zaidi, M.A. and Wert, J.A.
Treatise on Materials Science and Technology. Vol.31, Academic Press, 1989, p.159.

(69) Baker, I., Martin, J.W.
J. Mat. Sci., 15, 1980, p.1533-1538.

(70) Nes, E.
Acta Met. 1976, 24, p.391-398.

(71) Morris, P.L. and Ball, M.D.
Proc Conf 1st Riso Int. Symp. on Metallurgy and Materials Science, Roskilde, Denmark, Eds. Hansen, N., Jones, A.R. and Leffers, T. 1980 pp.97-102.

(72) Beynon, J.H.
Ph.D thesis, University of Sheffield, 1979.

(73) Kapellner, W., Kaspar, R. and Pawelski, O.
Steel Res., 1987, 57, (6) pp.256-261.

(74) McQueen, H.J.
Journal of metals, 20, 1968, pp.31-38.

(75) McQueen, H.J. and Jonas, J.J.
in: AIME Fall meeting, "The relation between theory and practise in metal forming", Cleveland, Oct. 1970, quoted in ref (79)

(76) Barraclough, D.R.
Ph.D thesis, University of Sheffield, 1974.

(77) Barraclough, D.R., Whittaker, H.J., Nair, K.D. and Sellars, C.M.
Journal of testing and evaluation, Vol 1, No.3, May 1973, pp.220-226.

(78) Smith, I.C., Avramovic-Cingara, G. and McQueen, H.J.
in Aluminium-Lithium Alloys V, Vol.I, Eds. Sanders Jr, T.H., Starke Jr, E.A., Williamsburg, Virginia, March 1989, pp.223-232.

(79) Oh, B.M. and Yoo, Y.C.
J. of Korean Inst. of Metals, Vol.28, No.4, 1990 pp.367-375.

(80) Wouters, P., Verlinden, B, McQueen, H.J., Aernouldt, E., Delaey,L. and Cauwenberg,S.
Mat. Sci Eng. A, Vol. A123, No.2, Feb. 1990, pp.239-246.

(81) Niikura, M., Takahashi, K. and Ouchi,C.
in Aluminium-Lithium Alloys III, Eds. Baker, C., Gregson, P.J., Harris, S.J. and Peel, C.J., Inst. of Metals, London, 1986 pp.213-221.

(82) Goncalves, M.
in Aluminium-Lithium VI, Eds. Peters, M. and Winkler, P.J., Garmisch Partenkirchen (FRG), 1991, pp.457-461.

(83) Goncalves, M. and Sellars, C.M.
in Aluminium-Lithium Alloys V, Vol.I, Eds. Sanders Jr, T.H., Starke Jr, E.A., Williamsburg, Virginia, March 1989, pp.305-311.

(84) Takahashi, K., Minakawa, K. and Ouchi, C.
in Aluminium-Lithium IV, Eds. Champier,G., Dubost, B., Miannay, D. and Sabetay, L., Journal de Physique, 48, Colloque C3 pp.163-170.

(85) Starke Jr., E.A. and Lin, F.J.
Met Trans 13A (1982) p.2259-2269.

(86) Dodd, B. and Kobayashi, H.
Mat Sci. and Tech. May 1990, Vol. 6 pp.447-452.

(87) Miller, W.S., White, J., Reynolds, M.A., McDarmaid, D.S. and Starr, G.M.
in Aluminium-Lithium IV, Eds. Champier,G., Dubost, B., Miannay, D. and Sabetay, L., Journal de Physique, 48, Colloque C3 pp.151-162.

(88) Gatenby, K.M., Reynolds, M.A., White, J. and Palmer, I.G.
in Aluminium-Lithium Alloys V, Vol.I, Eds. Sanders Jr, T.H., Starke Jr, E.A., Williamsburg, Virginia, March 1989, Vol.II p.909-919.

(89) Miller, W.S., White, J. and Lloyd, D.J.
"International Conference on Aluminium Alloys", Charlottesville, V.A.,
Pub. EMAC, 1986, Vol3. p.1799.

(90) Goncalves, M. and Sellars, C.M.
in Aluminium-Lithium IV, Eds. Champier,G., Dubost, B., Miannay, D. and Sabetay, L., Journal de Physique, 48, Colloque C3 pp.171-177.

(91) Schelb, W., Haszler, A., Jager, H., Welpmann, K. and Peters, M.
in 6th Int. Al-Li Conf. Eds. Peters,M., Winkler,P.J.
Garmisch-Partenkirchen (FRG) 1991, pp.315-320.

(92) Palmer, I.G., Miller, W.S., LLoyd, D.J. and Bull, M.J.
Proc Conf. Aluminium-Lithium Alloys III, Eds. Baker, C., Gregson, P.J., Harris, S.J. and Peel, C.J.
Inst. of Metals, London, 1986 pp.565-575.

(93) Ricks, R.A., Mahon, G.J. and Court, S.A.
in 6th Int. Al-Li Conf. Eds. Peters,M., Winkler,P.J.
Garmisch-Partenkirchen (FRG) 1991, pp.1151-1156.

(94) Wadsworth, J., Palmer, I.G., Crooks, D.D. and Lewis, R.E.
in Aluminium-Lithium II, Eds. Starke Jr., E.A., Sanders Jr.,T.H.
Monterey, California April 1983, pp.111-135.

(95) Miller, W.S., White, J. and Lloyd, D.J.
in Aluminium-Lithium IV, Eds. Champier,G., Dubost, B., Miannay, D. and Sabetay, L., Journal de Physique, 48, Colloque C3 pp.139-149.

(96) Weiyong, H., Guozhang, G., Jizhi, C. and Jinghi, L.
in 6th Int. Al-Li Conf. Eds. Peters,M., Winkler,P.J.
Garmisch-Partenkirchen (FRG) 1991, Vol. I, pp.173-178.

(97) Collier, L.S., Ranganathan, K. and Sanders Jr.,T.H.
Proc. Conf. "Light alloys for Aerospace Applications II"
Eds. Lee, E.W., Kim, N.J. The Minerals, Metals and Materials Society, 1991. pp.141-155.

(98) Nes, E.
Journal of Mat. Sci. Letters (13) 1978, pp.2052-2055.

(99) Goncalves, M.
Scripta Met. et Mater. Vol 25, 1991, pp.835-840.

(100) Jianping, K., Yuan, L., Xiaodong, Z. and Guansen, Y.
in "Al-alloys 1990, their physical and mechanical properties"
Eds.Chen, C.Q., Starke Jr, E.A., Beijing, China, Oct. 9-13, 1990, pp.37-39.

(101) Starke Jr, E.A., Sanders Jr, T.H. and Palmer, I.G.
Journal of Metals, 33, 1981, pp.24-33.

(102) Makin, P,L and Stobbs, W.
in Aluminium-Lithium IV, Eds. Champier,G., Dubost, B., Miannay, D. and Sabetay, L., Journal de Physique, 48, Colloque C3 pp.392-401.

(103) Rios, P.R.
Acta Met. Vol. 35, No. 12, 1987, pp.2805-2814.

(104) Porter, D.A. and Easterling, K.E.
"Phase transformations in metals and alloys"
Van Nostrand Reinhold, U.K., 1984, p.139.

(105) Parson, N.C. and Sheppard, T.
Aluminium-Lithium Alloys III, Eds. Baker, C., Gregson, P.J., Harris, S.J. and Peel, C.J., Inst. of Metals, London, 1986, pp.222-232.

(106) Mukhopadhyay, A.K., Flower, H.M. and Sheppard, T.
Mat. Sci. and Tech. May 1990, Vol.6 pp.461-468.

(107) Sheppard, T. and Tan, M.J.
in Aluminium-Lithium Alloys V, Vol I, Eds. Sanders Jr, T.H., Starke Jr, E.A., Williamsburg, Virginia, March 1989, pp.233-260.

(108) Chen, R.T. and Starke Jr., E.A.
Mat. Sci and Eng. 67, 1984, pp.229-245.

(109) Doherty, R.D. and Cahn, R.W.

Journal of Less Common Metals, 28, 1972, p.279.

(110) Sellars, C.M., Sah, J.P., Beynon, J.H. and Foster, S.R.
"PSC testing at elevated temperature" Report on research work supported by SRC grant No. B/R6/1481.

(111) Yiu, H.
"High temperature torsion testing and its relationship to the extrudabilityof Al alloys", Alcan Int. Ltd., research report BCR-85/05/.

(112) Stoltz, L.
University of Sheffield 1st year research report, Aug. 1991.

(113) Vernon-Parry, K., private communication.

(114) Luo, A., Lloyd, D.J., Gupta, A. and Youdelis, W.V.
Acta metall. mater., 41, 1993, p.769.

(115) Silcock, J.M.
J. Inst. Metals, 89 1960-1961, p.203.

(116) Silcock, J.M.
J. Inst. Metals, 88 1959-1960, p.357.

(117) Sellars, C.M., private communication.

(118) Srivatsen, T.S., Place, T.A. and Sudershan, T.S.
Aluminium, May 19991, 67 5, pp.474-478.

(119) Liu, Y.L., Zhang, Y., Hu, Z.Q. and Shi, C.X.
Z. Metallkd, Jan. 1992, 83, 1, pp.47-51.

(120) Dimitrov, O. Fromageau, R. and Dimitrov, C.
reference as (50), p.155.

(121) Koster, U.
Met. Sci. 8, 1974, p.157.

(122) Zedalis, M.S. and Fine, M.E.
Met Trans A, vol. 17A, 1986, pp.2187-2198.

(123) Greenwood, G.W., private communication.

(124) Ashby, M.F. and Jones, R.H.
"Engineering Materials 1", International Series on Materials Science and Technology, Vol.34., Pergamon Press.

(125) Whitaker, I.R., private communication.

Element[a]	Alloy						
	2090	2091	8090	8090A	8091	X8092	X8192
	Aloca August 6, 1984	C. Pechiney April 8, 1985	Alcan and C. Pechiney May 1985	Alcoa Late 1985	Alcan March 29, 1985	Alcoa May 1985	Alcoa August 1985
Si	0.10	0.20	0.20	0.10	0.30	0.10	0.10
Fe	0.12	0.30	0.30	0.15	0.50	0.15	0.15
Cu	2.4–3.0	1.8–2.5	1.0–1.6	1.1–1.6	1.8–2.2	0.5–0.8	0.4–0.7
Mn	0.05	0.10	0.10	0.05	0.10	0.05	0.05
Mg	0.25	1.1–1.9	0.6–1.3	0.8–1.4	0.5–1.2	0.9–1.4	0.9–1.4
Cr	0.05	0.10	0.10	0.05	0.10	0.05	0.05
Ni	—	—	—	—	—	—	—
Zn	0.10	0.25	0.25	0.10	0.25	0.10	0.10
Ti	0.15	0.10	0.10	0.15	0.10	0.15	0.15
Li	1.9–2.6	1.7–2.3	2.2–2.7	2.1–2.7	2.4–2.8	2.1–2.7	2.3–2.9
Zr	0.08–0.15	0.04–0.16	0.04–0.16	0.08–0.15	0.08–0.16	0.08–1.5	0.08–1.5
Other: each	0.05	0.05	0.05	0.05	0.05	0.05	0.05
total	0.15	0.15	0.15	0.15	0.15	0.15	0.15

[a] Numbers shown are either maximums or ranges.

Table 2.1 The chemical composition of Al-Li type alloys registered with the Aluminium Association as of March 1988. (5)

Alloy Designation	Workers	Li	Cu	Mg	Zr	Fe	β	n	α	Q_{def}
8090	Smith et al (78)	2.5	1.4	0.6	0.1	0.08	0.161*	3.1	0.052	185
8091	Smith et al (78)	2.8	1.8	0.8	0.12	0.08	0.182*	3.5	0.052	209
-	Niikura et al (81)	2.2	1.3	1.2	0.14	0.03	-	4.8	-	183
-	Parson & Sheppard (105)	2.4	0.9	3.5	0.15	0.12	0.057*	2.28	0.025	153
-	Parson & Sheppard (105)	2.2	-	3.6	0.15	0.11	0.071*	2.15	0.033	168
8090	Goncalves (16)	2.42	1.23	0.6	0.11	-	0.071	-	-	153
8091	Goncalves (16)	2.52	1.86	0.81	0.15	-	0.071	-	-	153
8090	Oh et al (79)	2.34	1.27	0.95	0.11	-	0.076	-	-	207

* denotes that β values have been calculated according to Equation2.5

Table 2.2 Survey of constants obtained from hot-working experiments.

	Temperature of Deformation/°C			
Stress law/ constant	320	380	440	500
Power law, peak stress; n	19.22	3.87	5.78	11.18
Exponential law, peak stress; ß	0.487	0.073	0.077	0.076
Power law, steady state; n	15.04	3.87	6.38	12.41
Exponential law, steady state; ß	0.425	0.072	0.087	0.089

Table 2.3 Constants resulting from the analysis of data from torsion testing of 8090 by Oh et al .(79)

Worker	Temperature of deformation/°C	Strain Rate/s^{-1}	Strain to failure
Oh et al (79)	500	6.13E-1	5.5
"	380	"	7.2
"	320	"	5.5
"	500	1.03	5.8
"	380	"	6.6
"	320	"	5
"	500	2.07	6.4
"	380	"	6.9
"	320	"	4.5
Smith et al (78)	300 (SHT)	4	1.75
"	300 (Aged)	4	2.5
"	300 (SHT)	1	2.25
"	500 (Aged)	4	3.75

Table 2.4 Failure strains resulting from analysis of hot torsion test data on 8090. The material condition is given in parentheses for the results of Smith et al (78). (SHT) is solution heat treated at 550°C.

Element	Minimum	Maximum
Li	2.3	2.60
Cu	1.00	1.60
Mg	0.50	1.00
Zr	0.08	0.16
Fe	-	0.30
Si	-	0.20
Zn	-	0.25

Table 3.1 Compositional range of alloy 8090 (in weight percent).

Element	Extruded monolithic	Extruded composite	As-sprayed monolithic	As-sprayed composite
Thesis code	MONO	MMC	ASC	AMMP
Code number	*D80NG 170D	*D80SG 252	D80NG 769	D80SG 737
Li	2.42	2.3	2.33	2.57
Cu	1.16	1.14	1.06	1.25
Mg	0.73	0.83	0.87	0.91
Zr	0.11	0.12	0.12	0.13
Fe	0.04	0.04	0.04	0.05
Si	0.02	0.06	0.06	0.08
Zn	0.01	0.01	0.03	0.03
SiC	-	15.9	-	15.85

Table 3.2 Compositions of materials used in the plane strain compression series and (*) in the torsion series. All values are given as weight percent.

Element	Extruded monolithic	Extruded composite	As-sprayed monolithic	As-sprayed composite
Thesis code	MONO	MMC	ASC	AMMP
Code number	D80NG 431	D80SG 253	D80NG 769	D80SG 737
Li	2.51	2.25	2.33	2.57
Cu	1.19	1.2	1.06	1.25
Mg	0.91	0.68	0.87	0.91
Zr	0.12	0.11	0.12	0.13
Fe	0.06	0.05	0.04	0.05
Si	0.03	0.03	0.06	0.08
Zn	0.01	0.02	0.03	0.03
SiC	-	17.05	-	15.85

Table 3.3 Compositions of materials used in the rolling series . All values are given as weight percent.

Spec. No.	Deform. Temp.	Strain Rate	h_0	b_0	h_f	b_f	C
ASC10	300	0.05	10.04	30	2.49	40	0.66
ASC8	300	1	10.01	30.05	2.52	39.65	0.64
ASC18	300	10	10.02	29.95	2.2	41.25	0.71
ASC22	300	10	10.04	29.95	2.27	39.13	0.58
ASC2	400	0.05	10.02	29.95	2.55	39.74	0.66
ASC21	400	1	10.02	29.95	2.01	39.99	0.61
ASC1	400	1	10.07	29.9	2.62	38.28	0.57
ASC3	400	1	10.03	29.95	2.55	39.16	0.62
ASC12	400	1	10	30	2.37	39.24	0.6
ASC14	400	1	10.03	29.95	2.28	40.08	0.65
ASC17	400	10	10.02	29.95	3	41.2	0.83
ASC23	400	10	10.04	30	2.08	39.8	0.6
ASC7	500	0.05	10.04	30.05	2.14	41.8	0.73
ASC4	500	1	10.03	30	2.36	40.45	0.68
ASC20	500	10	10.02	30	2.3	40.13	0.65

Table 4.1 Specimen dimensions and spread coefficients for the as-spray-cast PSC test series.

Spec. No.	Deform. Temp.	Strain Rate	h_0	b_0	h_f	b_f	C
SC6	300	0.05	10	29.7	2.51	38.5	0.59
17D10	300	1	10	30	2.98	35.7	0.42
SC22	300	1	10.04	30	3.07	37.35	0.55
SC11	300	1	10.01	29.8	2.08	40.5	0.66
SC9	300	10	9.97	30.45	2.53	37.59	0.47
SC35	400	0.05	10.03	29.9	2.08	37.85	0.49
17D8	400	0.05	10	29.99	2.84	37.14	0.51
SC31	400	1	9.97	29.85	2.05	39.28	0.58
17D7	400	1	9.98	30	2.86	36.18	0.44
SC3 *	400	1	10.03	29.65	2.08	40.68	0.68
SC7 *	400	1	9.98	30.5	2.28	39.91	0.59
SC8 *	400	1	10.03	29.65	2.34	39.51	0.64
17D6	400	10	10	29.99	2.87	35.16	0.37
17D29	500	0.05	10.02	30	2.24	39.88	0.63
17D28	500	1	10.07	30	2.84	37.85	0.56
17D15	500	10	10.01	29.99	2.88	36.26	0.45
SC34	500	10	9.97	29.9	2.17	37.25	0.46

(Graphite lubricated tests are marked *)

Table 4.2 Specimen dimensions and spread coefficients for the extruded monolithic PSC test series.

Spec. No.	Deform. Temp.	Strain Rate	h_0	b_0	h_f	b_f	C
AMMP 10	300	0.05	10.03	29.95	2.48	40.66	0.71
AMMP 8	300	1	10.04	29.95	2.65	41.54	0.8
AMMP 9	300	1	10.02	29.9	2.65	40.74	0.75
AMMP 19	300	10	10.01	29.9	2.08	42.06	0.75
AMMP 2	400	0.05	10.01	30	2.59	40.83	0.73
AMMP 16	400	1	10.04	29.9	2.08	42.3	0.76
AMMP 1	400	1	10.03	30	2.61	40.85	0.74
AMMP 14	400	1	10.02	30	2.53	42.55	0.84
AMMP 23	400	10	10.04	29.9	2.1	41.6	0.72
AMMP 7	500	0.05	10.03	29.92	2.25	41.94	0.76
AMMP 4	500	1	10.03	29.9	2.46	41.29	0.75
AMMP 6	500	10	9.97	29.99	2.35	42.51	0.81
AMMP 21	500	10	10.02	29.99	2.12	42.59	0.79

(All tests performed lubricated)

Table 4.3 Specimen dimensions and spread coefficients for the as-spray-cast AMMP PSC test series.

Spec. No.	Deform. Temp.	Strain Rate	h_0	b_0	h_f	b_f	C
M2_12	300	0.05	10.01	29.99	2.49	39.76	0.65
MMC31	300	1	10.07	29.95	2.27	42.11	0.77
M2_16	300	1	10.01	29.99	2.64	39.3	0.64
M2_3	300	10	10	30	3.04	37.79	0.58
MMC32	300	10	10.03	29.85	2.1	42.6	0.79
MMC30	400	0.05	9.99	29.9	3.05	41.5	0.87
M2_30	400	0.05	9.98	29.99	2.65	38.71	0.6
MMC33	400	1	9.99	29.8	2.1	41.09	0.7
MMC35 *	400	1	10.08	29.8	2.06	41.76	0.73
M2_27 *	400	1	10.01	29.99	2.13	41.58	0.72
M2_28 *	400	1	9.94	29.99	2.28	40.35	0.66
M2_29 *	400	1	10	30	2.3	40.25	0.66
M2_15	400	10	10.01	29.99	2.53	39.58	0.64
M2_13	500	0.05	10.01	30	2.86	40.5	0.75
M2_22	500	0.05	9.98	29.99	3.25	41.48	0.89
M2_24	500	1	9.99	30	2.58	39.34	0.63
M2_25	500	1	10	30	2.21	40.4	0.65
M2_14	500	10	10.01	30	2.8	38.49	0.6
MMC3	500	10	10.03	29.9	2.18	44.1	0.89
MMC4	500	10	10.02	29.85	2.24	43.8	0.87

(Lubricated tests are marked *)

Table 4.4 Specimen dimensions and spread coefficients for the extruded MMC PSC test series.

Strain Rate	Material	300	400	500
0.05	ASC	135	55	20
0.05	MONO	105	50	20
0.05	AMMP	*	50	35
0.05	MMC	*	50	25
1	ASC	185	85	45
1	MONO	165	75	45
1	AMMP	*	*	55
1	MMC	*	*	40
10	ASC	215	110	70
10	MONO	210	105	65
10	AMMP	250	*	75
10	MMC	*	*	70

(* indicates that no steady state stress is attained)

Table 4.5 Steady state stress levels from PSC testing (corrected to constant Z)

Series	Range/MPa	% Scatter
ASC	75-82	8.5
MONO	78-83	6
AMMP	102-110	7.3
MMC	90-95	5.3

Table 4.6 Scatter in PSC reproducibility study.

	Strain			
Constant	0.02	0.1	0.5	1
A_2	3.4E+9	1.5E+10	3.2E+10	3.5E+10
β	0.084	0.068	0.059	0.059
A_3	2.7E+11	9.8E+11	2.3E+12	2.3E+12
α	0.0168	0.0136	0.0118	0.0118
n'	4.4	4.51	4.42	4.4

Table 4.7(a) ASC series constants for exponential and sinh equations formulated from PSC test data.

	Strain			
Constant	0.02	0.1	0.5	1
A_2	2.0E+11	7.8E+11	1.2E+11	2.1E+12
β	0.093	0.077	0.068	0.061
A_3	8.2E+12	4.1E+13	7.2E+13	1.2E+14
α	0.0186	0.0154	0.0136	0.0122
n'	4.93	4.75	4.66	4.92

Table 4.7(b) MONO series constants for exponential and sinh equations formulated from PSC test data.

	Strain			
Constant	0.02	0.1	0.5	1
A_2	1.1E+11	4E+11	7.5E+11	1.1E+12
β	0.068	0.058	0.055	0.053
A_3	6.8E+12	2.7E+13	5.2E+13	6.4E+13
α	0.0136	0.0116	0.011	0.0106
n'	4.67	4.62	4.58	4.84

Table 4.7(c) AMMP series constants for exponential and sinh equations formulated from PSC test data.

	Strain			
Constant	0.02	0.1	0.5	1
A_2	3.1E+10	1.1E+11	1.8E+11	2.4E+11
β	0.095	0.085	0.085	0.085
A_3	2.9E+12	7.8E+12	9.8E+12	6.8E+12
α	0.019	0.017	0.017	0.017
n'	4.42	4.62	4.94	6.04

Table 4.7(d) MMC series constants for exponential and sinh equations formulated from PSC test data.

Series	Equation Form	Eqn @ strain 0.02	Eqn @ strain 0.1	Eqn @ strain 0.5	Eqn @ strain 1.0
ASC	Exp	0.92	0.96	0.95	0.9
	Sinh	0.97	0.98	0.98	0.97
MONO	Exp	0.98	0.95	0.96	0.89
	Sinh	0.99	0.99	0.99	0.95
AMMP	Exp	0.97	0.98	0.97	0.95
	Sinh	0.98	0.99	0.98	0.95
MMC	Exp	0.97	0.97	0.95	0.83
	Sinh	0.98	0.98	0.98	0.97

Table 4.8 Coefficients of determination from the fitting of stress of stress functions to PSC test data.

Temperature	MONO	MMC
300	114	* 142
350	89	* 102
400	71	* 94
450	* 51	50
500	* 47	36

(* indicates that no true steady state stress is attained, values are then given at a strain of 0.5)

Table 4.9 Steady state stress levels (MPa) from torsion tests.

	Strain		
Constant	0.1	0.5	1
A_2	9.5E+10	1.5E+10	2.8E+10
β	0.122	0.133	0.128
A_3	8.2E+12	4.3E+11	1.5E+12
α	0.0244	0.0266	0.0256
n'	4.45	5.06	4.74

Table 4.10(a) MONO series constants for exponential and sinh equations formulated from torsion test data.

	Strain	
Constant	0.1	0.5
A_2	5.8E+10	8.0E+10
β	0.099	0.094
A_3	1.1E+13	8.9E+12
α	0.0198	0.0188
n'	3.97	4.31

Table 4.10(b) MMC series constants for exponential and sinh equations formulated from torsion test data.

Series	Equation Form	Eqn @ strain 0.1	Eqn @ strain 0.5	Eqn @ strain 1.0
MONO	Exp	0.99	0.99	0.99
	Sinh	0.99	0.99	0.99
MMC	Exp	0.96	0.97	-
	Sinh	0.96	0.98	-

Table 4.11 Coefficients of determination from the fitting of stress function equations to torsion test data.

Material	Initial rolling Temp./ °C	Pass 1 Load, kN	Pass 2 Load, kN	Pass 3 Load, kN
ASC	480	51	95	115
AMMP		76	132	163
ASC	400	88	137	149
AMMP		101	152	182
ASC	300	106	200	214

Table 4.12 Loads resulting from the rolling of as-sprayed material.

Material	Initial rolling Temp./ °C	Pass 1 Load, kN	Pass 2 Load, kN	Pass 3 Load, kN
MONO	480	62	106	132
MMC		68	111	145
MONO	400	96	130	156
MMC		117	188	183
MONO	300	135	192	205

Table 4.13 Loads resulting from the rolling of extruded material.

Nominal rolling temperature/°C	ASC finish rolling Temp.(°C)	MONO finish rolling Temp.(°C)	DC cast 8090 finish rolling Temp.(°C)	DC cast 8090 F_R (Nm^2) (16)
480	410	395	410	1.15E+5
400	370	350	360	4.24E+5
300	315	290	290	1.67E+6

Table 5.1 Finish rolling temperatures and recrystallisation driving forces (F_R) for ASC and MONO series', plus data from DC cast 8090 (16).

	Pass 1	Pass2	Pass 3
Pass reduction (mm)	4.0	4.8	3.36
True strain	0.26	0.36	0.36
True strain rate (s^{-1})	3.15	3.99	4.76
Roll velocity (v) = 0.2ms^{-1}, roll radius = 0.068m			

Table 5.2 Deformation conditions for the rolling experiments.

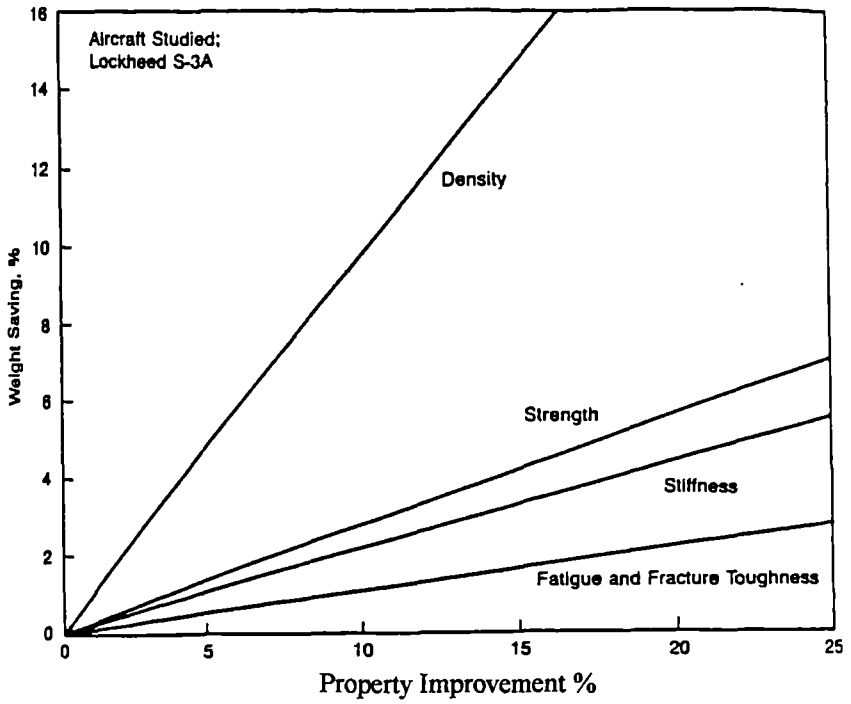

Figure 2.1 The relative effect of various material properties on reducing structural weight in a Lockheed S-3A aircraft. (5)

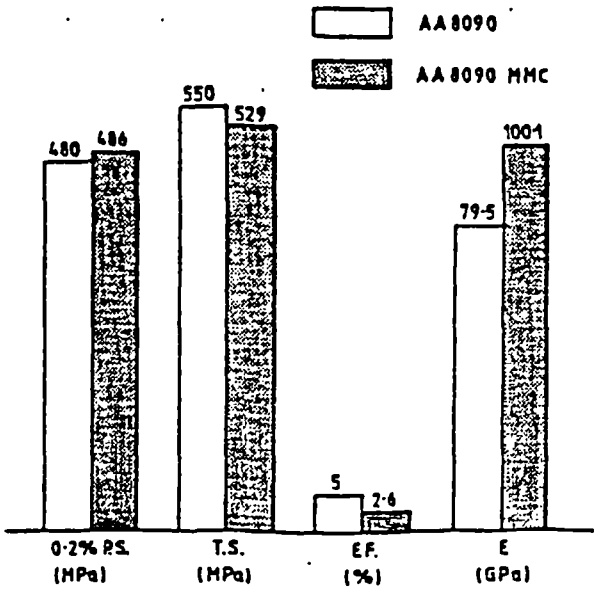

Figure 2.2 Tensile properties of 8090-12% SiC compared with 8090 (14).

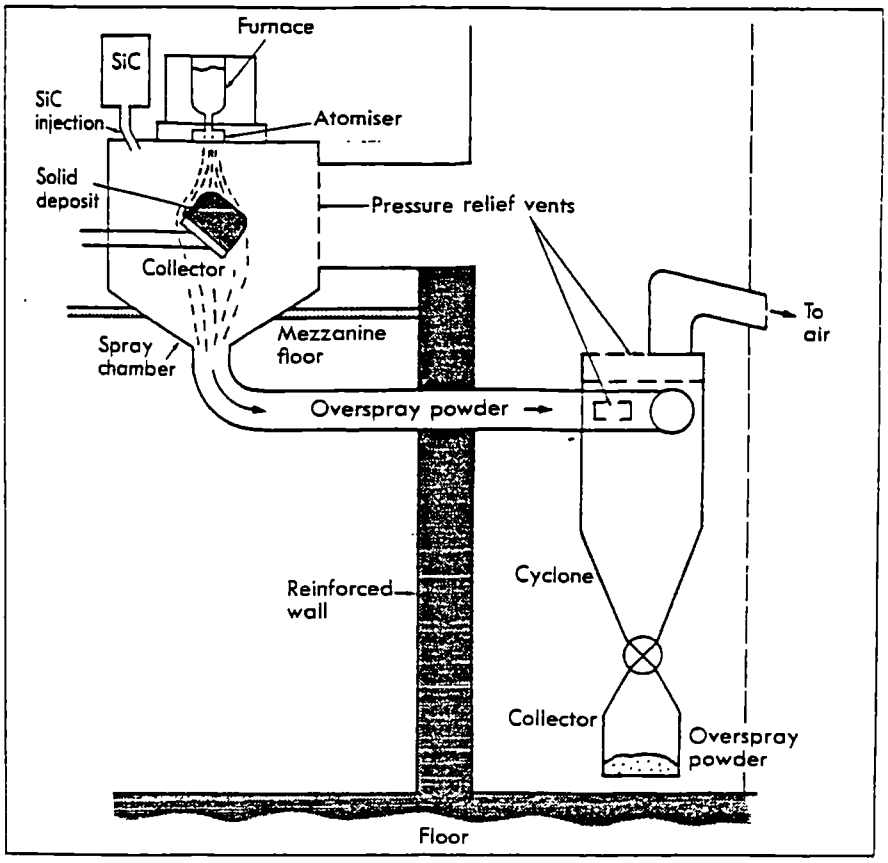

Figure 2.3 Schematic of plant used in the Osprey process (27).

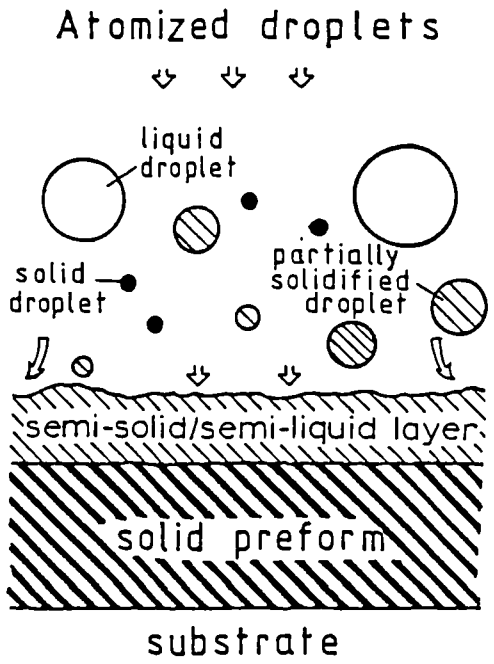

Figure 2.4 Schematic representation of the deposition stage of the Osprey process (26).

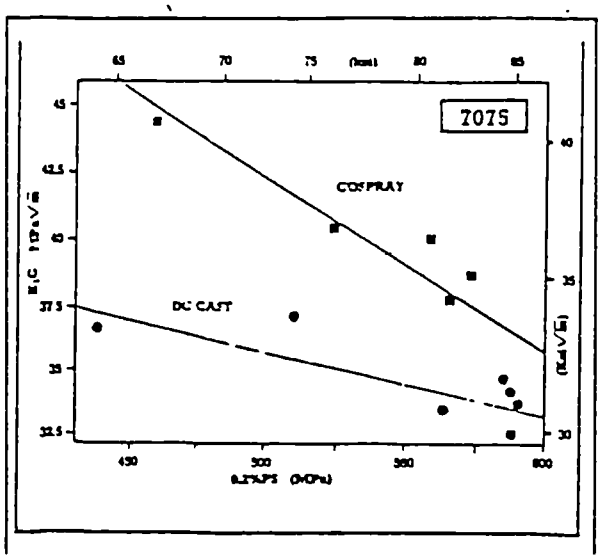

Figure 2.5 Improvement in fracture toughness possible with the spray-casting production method (illustrated for 7075) (35).

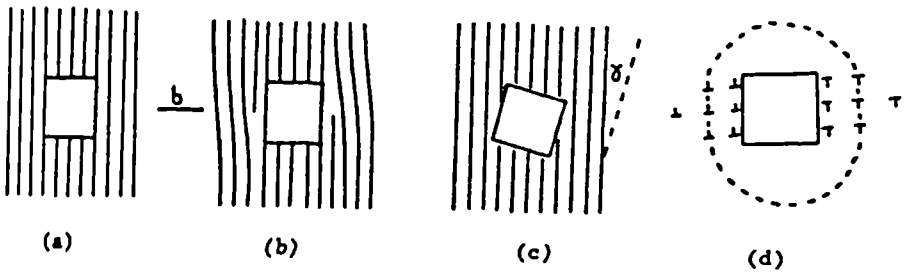

Figure 2.6 Schematic of plastic relaxation at a large particle.
(a) Undeformed .(b) Unrelaxed. (c) Relaxation by rotation
(d) Formation of impenetrable zone at high strain (51).

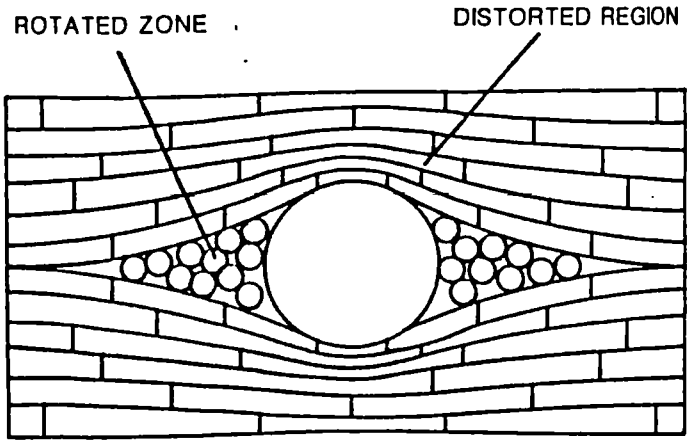

Figure 2.7 Schematic diagram of a deformation zone formed at a large equiaxed particle (62).

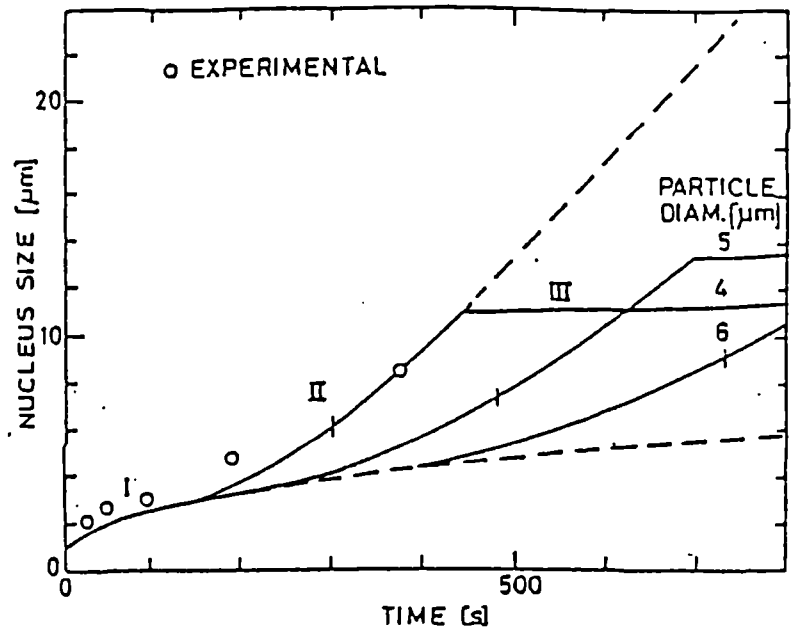

Figure 2.8 Diameter of recrystallisation nucleus vs. time for 4, 5 and 6mm particles. The three different growth stages, I, II and III are shown (57).

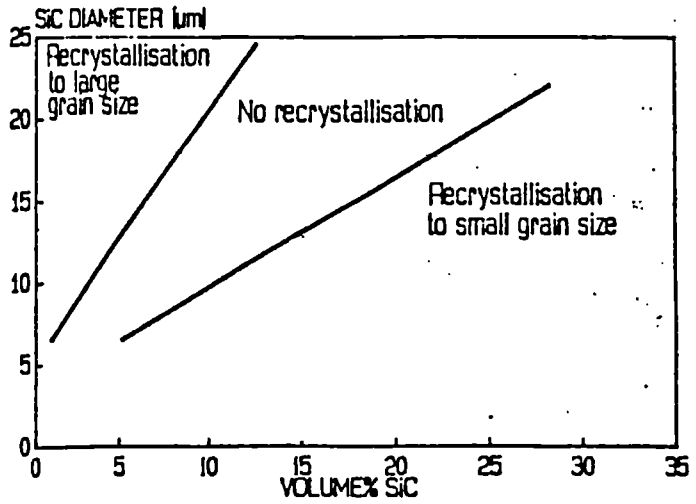

Figure 2.9 The effect of volume fraction and size of SiC reinforcement particles on the extent of recrystallisation (62).

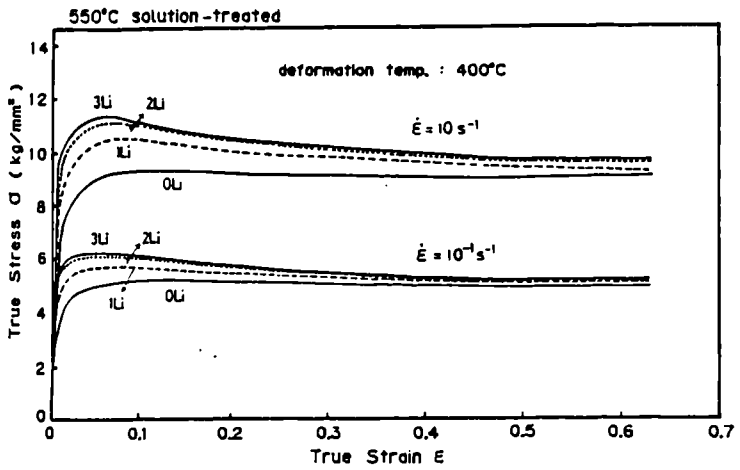

Figure 2.10 The effect of %Li on the true stress-strain curves of an Al-Li-Cu-Mg-Zr alloy deformed at 400°C after solution treatment at 550°C (81).

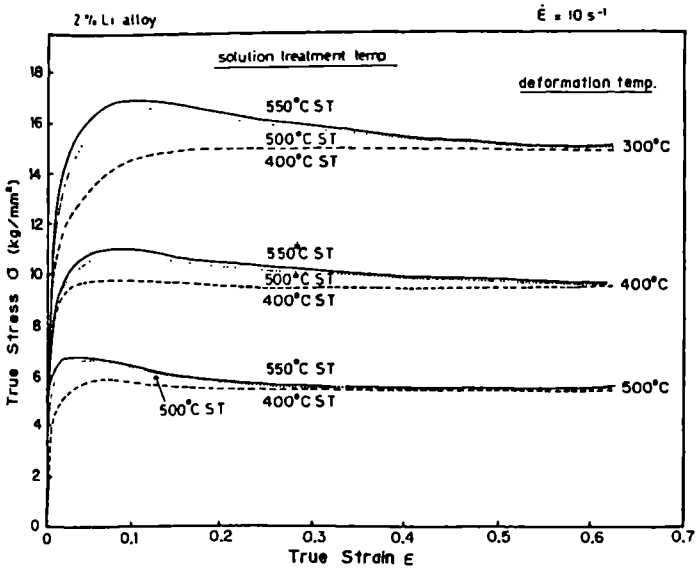

Figure 2.11 The effect of different SHT temperatures on the true stress-strain curves from the deformation of a 2%Li Al-Li-Cu-Mg-Zr alloy (81).

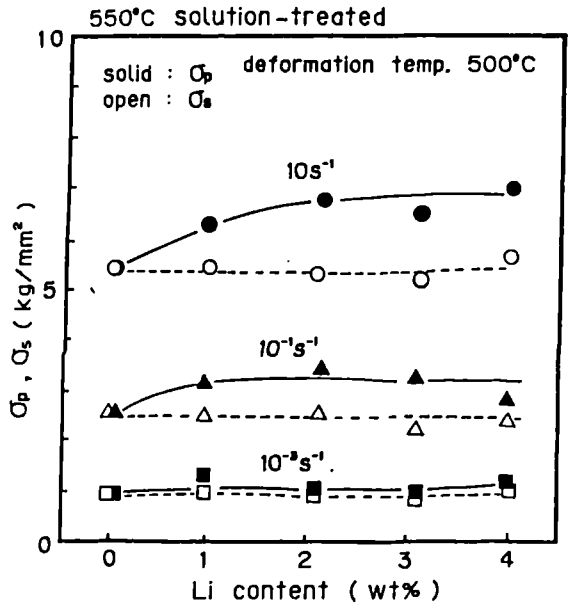

Figure 2.12 The dependence of peak and steady state stresses on the Li content of an Al-Li-Cu-Mg-Zr alloy (81).

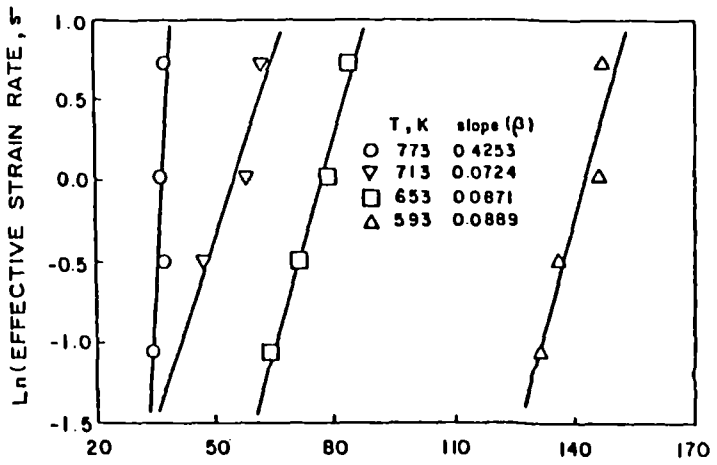

Figure 2.13 Dependence of flow stress on strain rate through an exponential law, at steady state stress, for alloy 8090 (79).

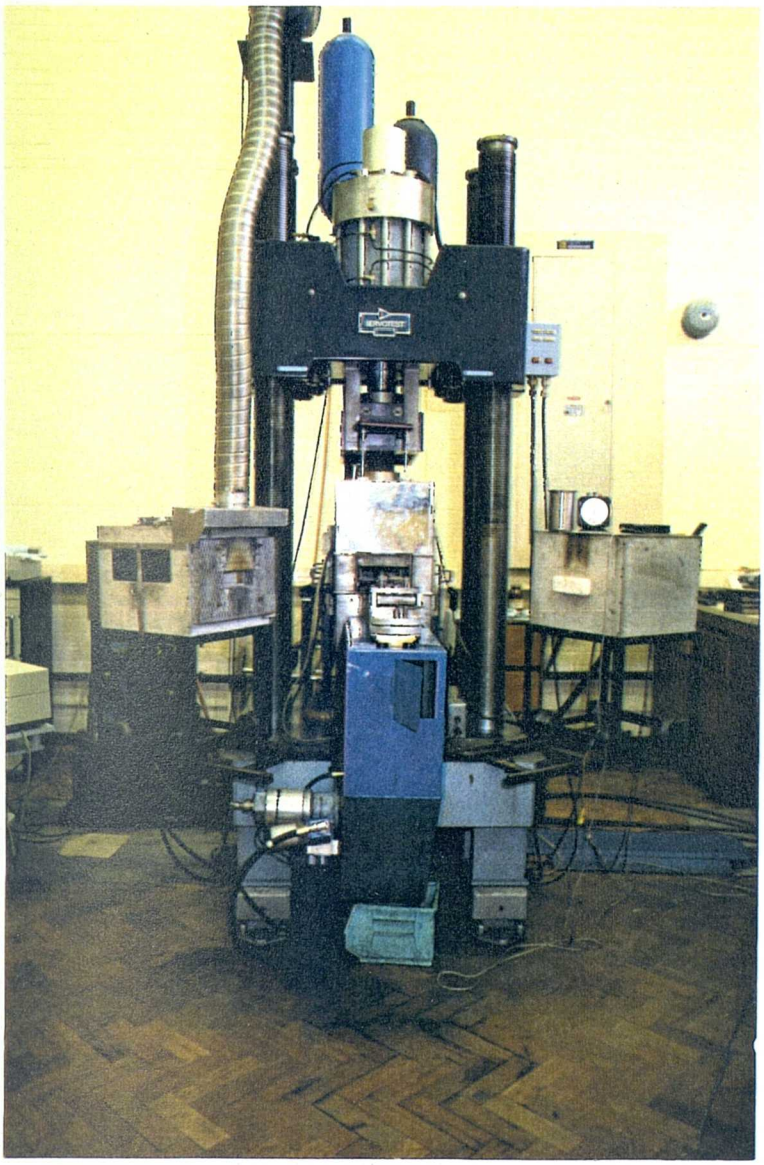

Figure 3.1 Photograph of the servohydraulic plane strain compression testing machine.

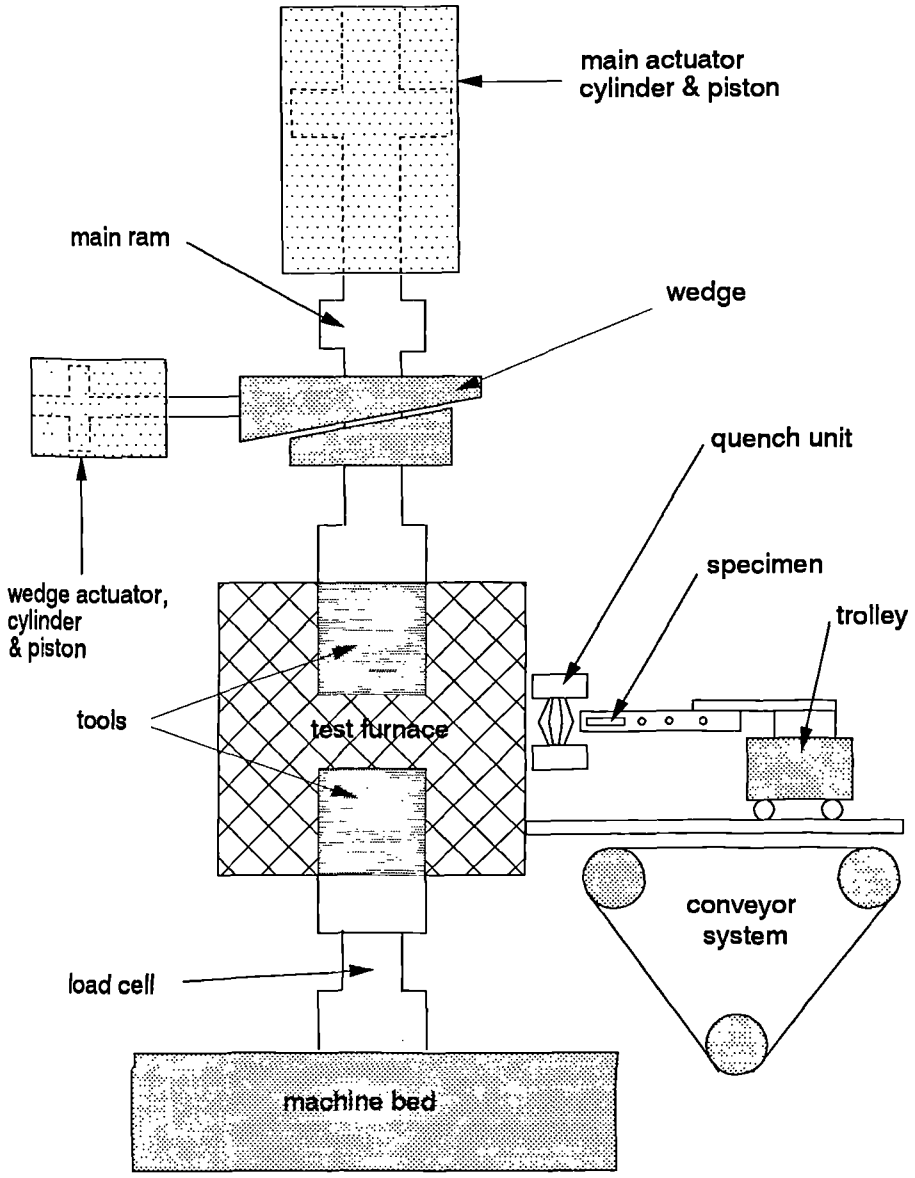

Figure 3.2 Schematic diagram of the PSC testing machine.

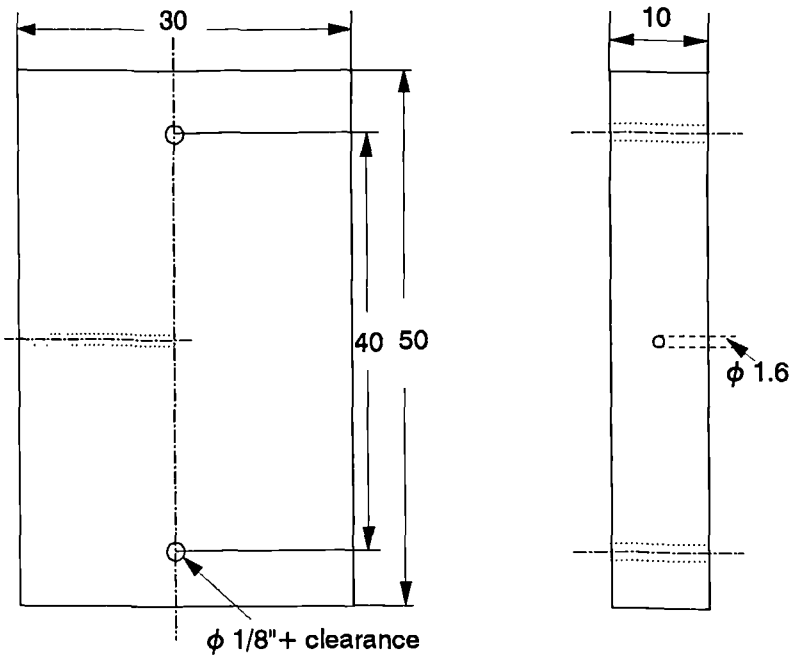

Figure 3.3 Plane strain compression (PSC) specimen geometry.

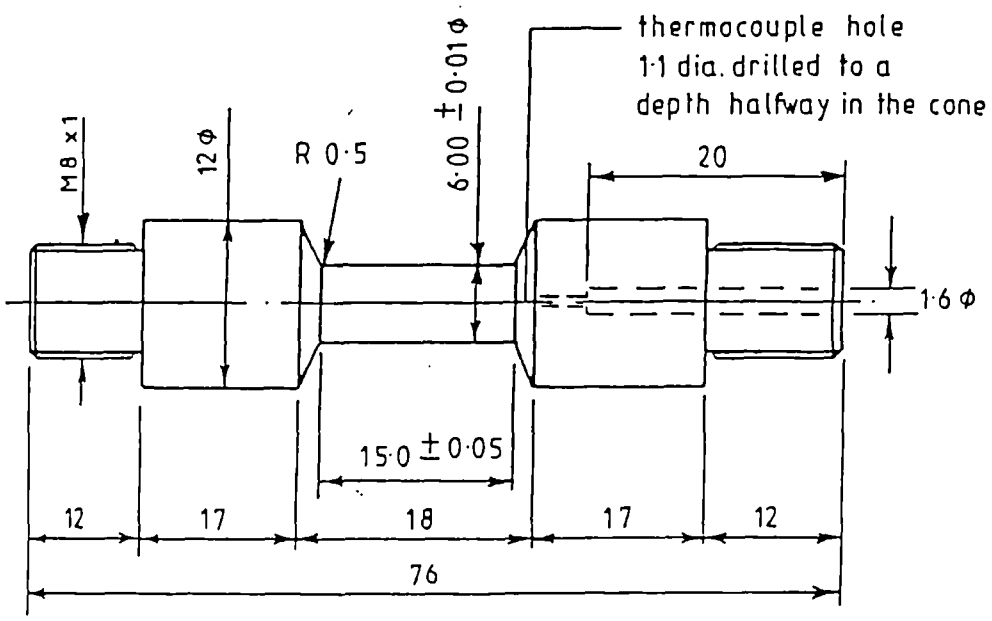

Figure 3.4 Geometry of the torsion testpiece.

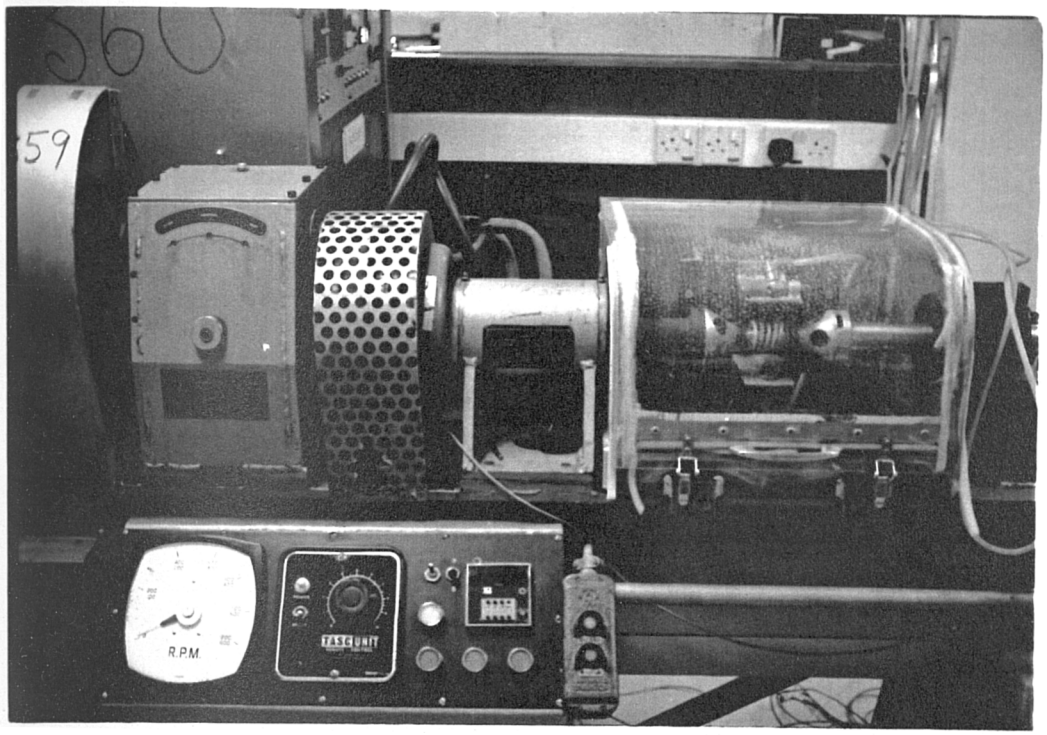

Figure 3.5 Photograph of the torsion testing machine.

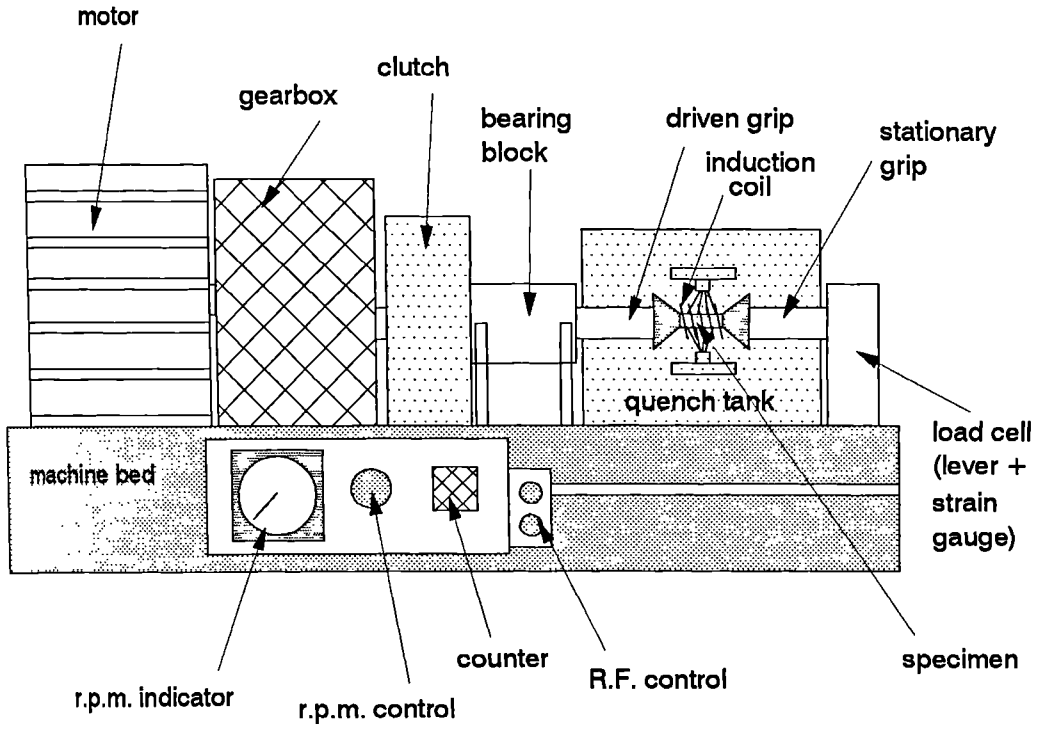

Figure 3.6 Schematic diagram of the torsion testing machine.

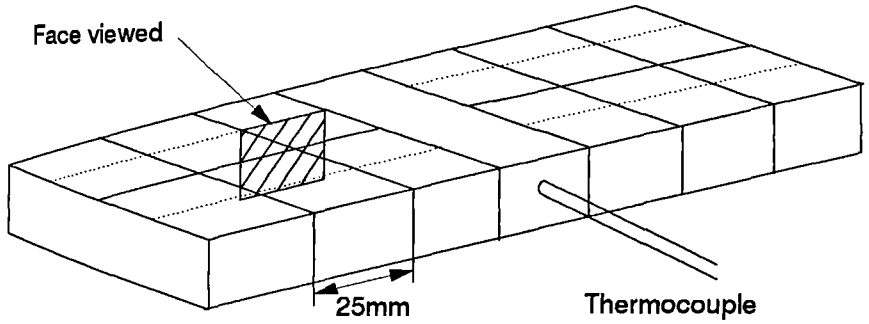

Figure 3.7 Method of sectioning rolling slabs for metallography.

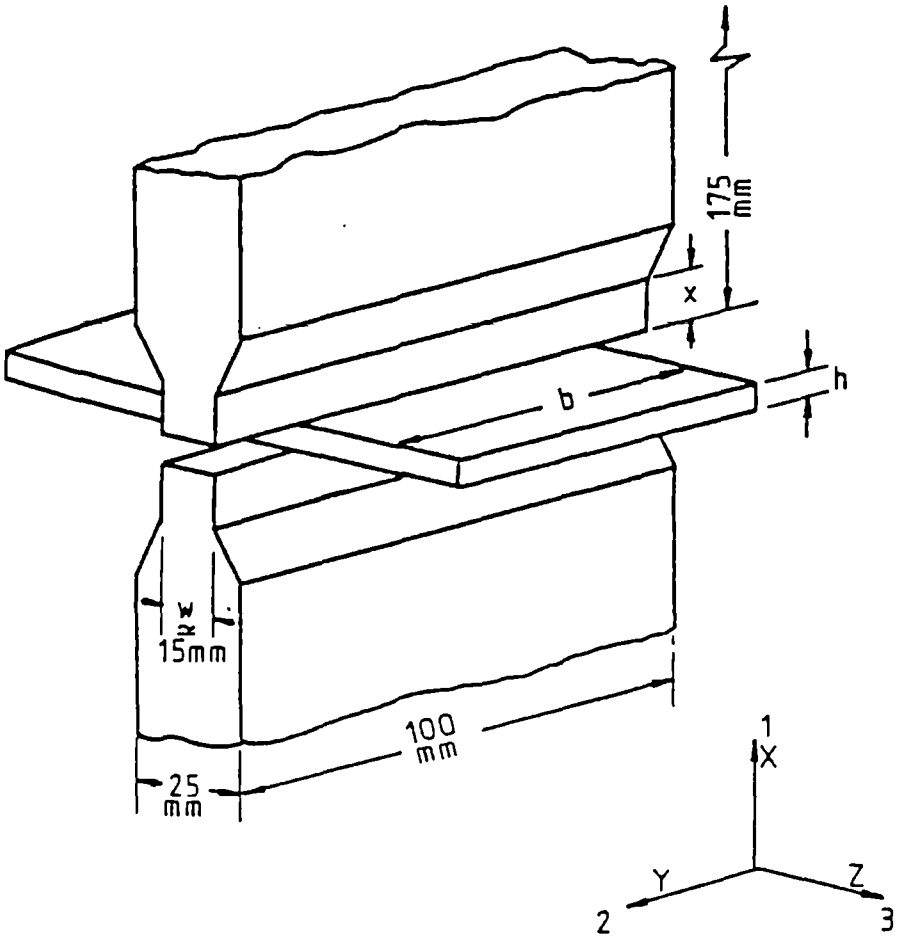

Figure 3.8 Geometry of the plane strain compression test apparatus.

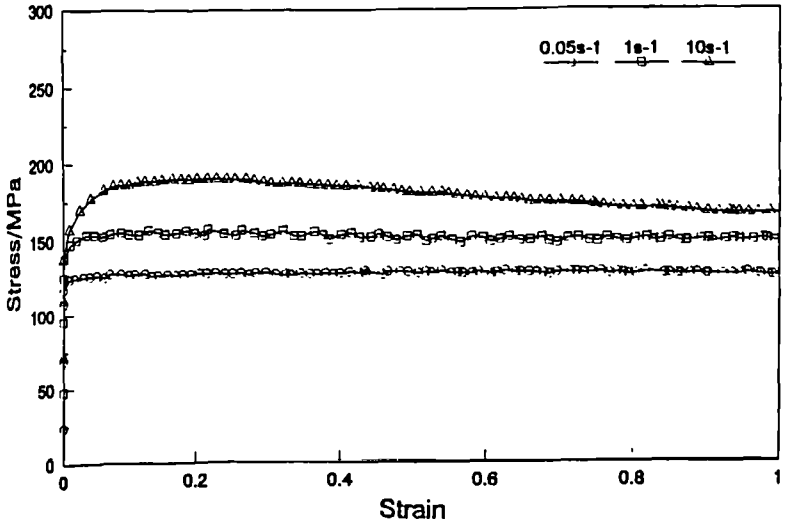

Figure 4.1 ASC series uncorrected stress-strain curves from PSC tests performed at 300°C.

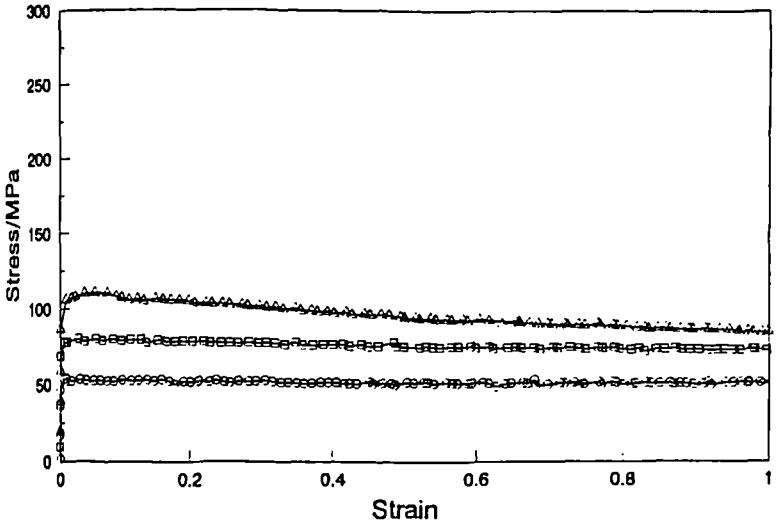

Figure 4.2 ASC series uncorrected stress-strain curves from PSC tests performed at 400°C.

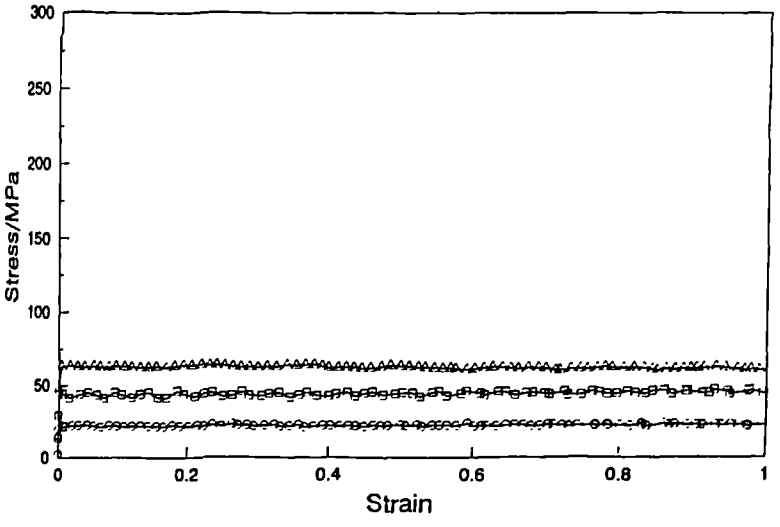

Figure 4.3 ASC series uncorrected stress-strain curves from PSC tests performed at 500°C.

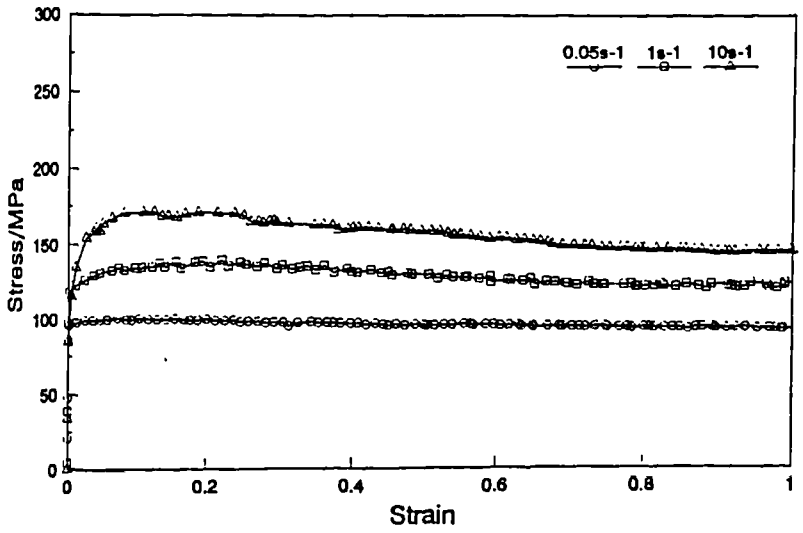

Figure 4.4 MONO series uncorrected stress-strain curves from PSC tests performed at 300°C.

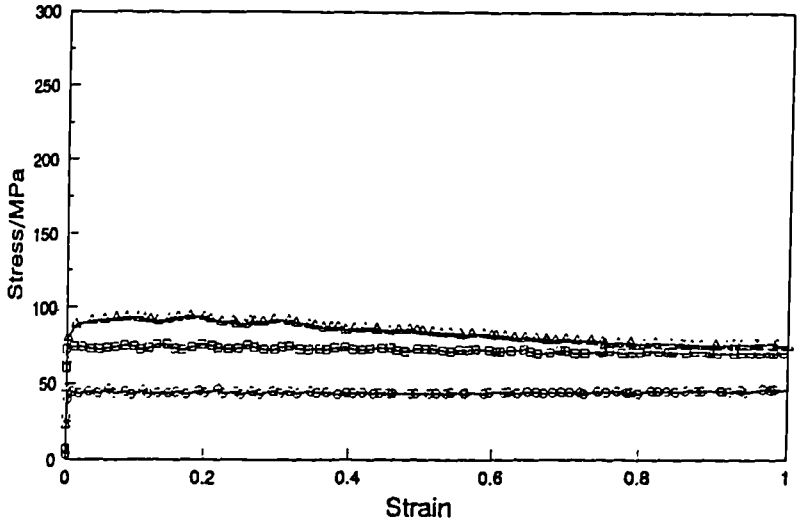

Figure 4.5 MONO series uncorrected stress-strain curves from PSC tests performed at 400°C.

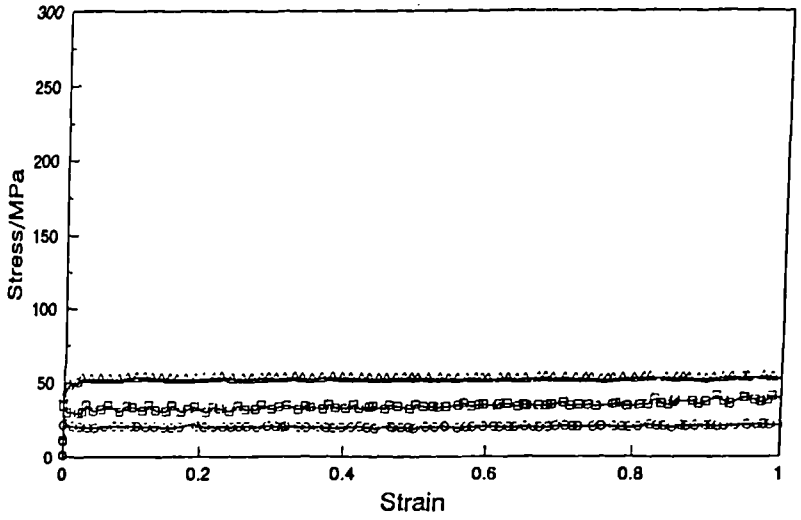

Figure 4.6 MONO series uncorrected stress-strain curves from PSC tests performed at 500°C.

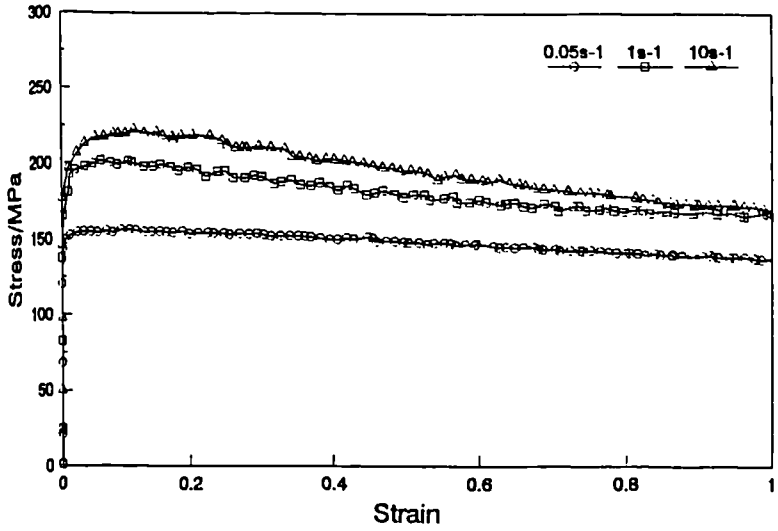

Figure 4.7 AMMP series uncorrected stress-strain curves from PSC tests performed at 300°C.

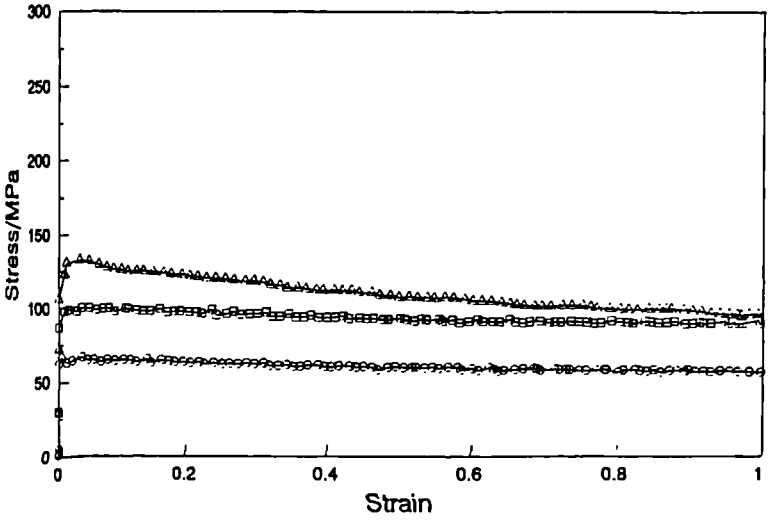

Figure 4.8 AMMP series uncorrected stress-strain curves from PSC tests performed at 400°C.

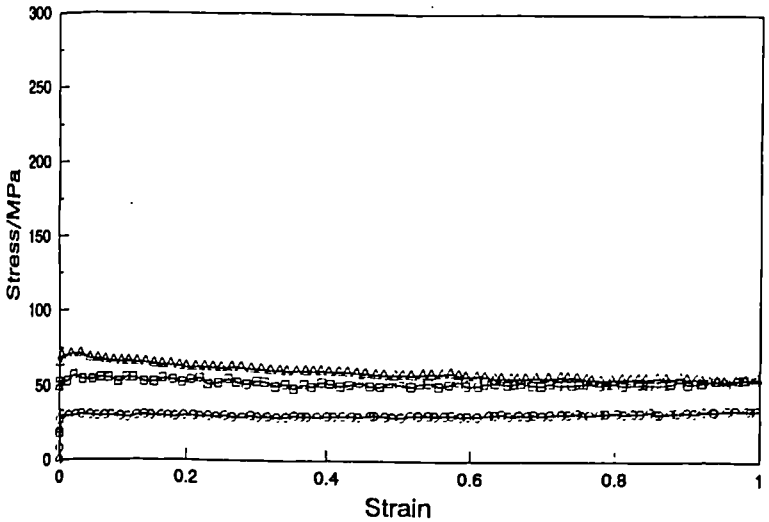

Figure 4.9 AMMP series uncorrected stress-strain curves from PSC tests performed at 500°C.

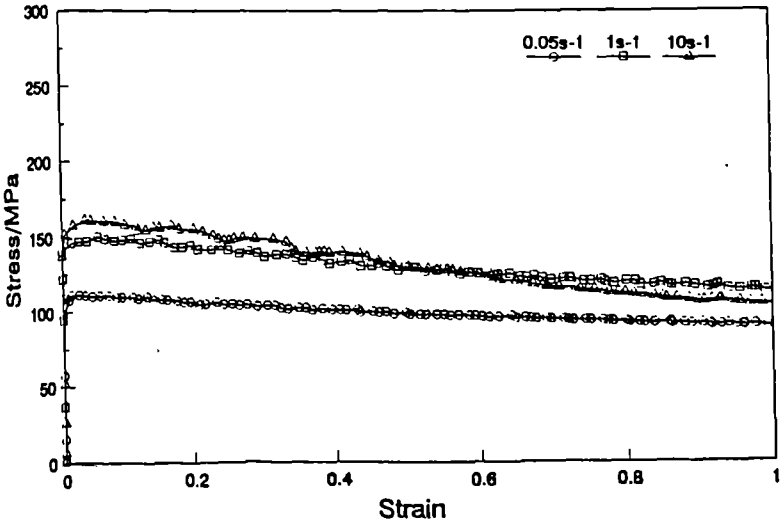

Figure 4.10 MMC series uncorrected stress-strain curves from PSC tests performed at 300°C.

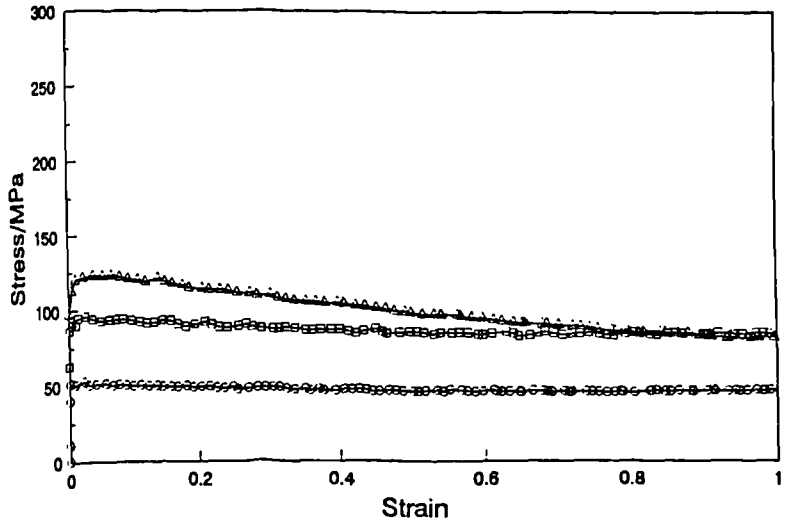

Figure 4.11 MMC series uncorrected stress-strain curves from PSC tests performed at 400°C.

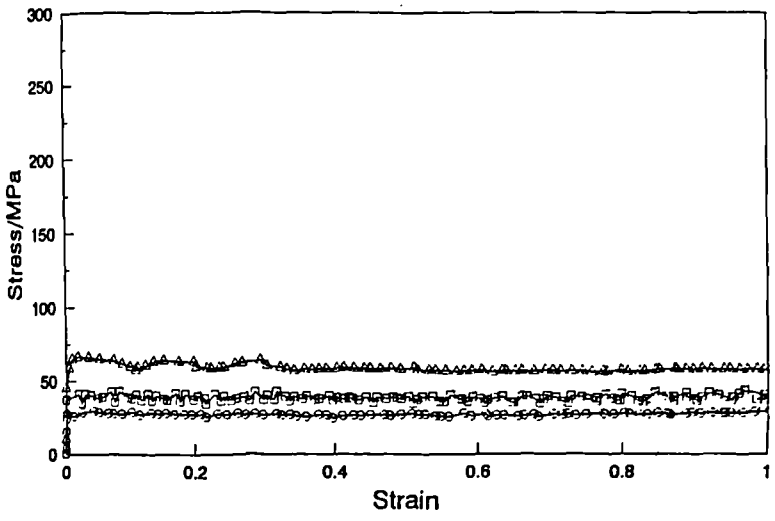

Figure 4.12 MMC series uncorrected stress-strain curves from PSC tests performed at 500°C.

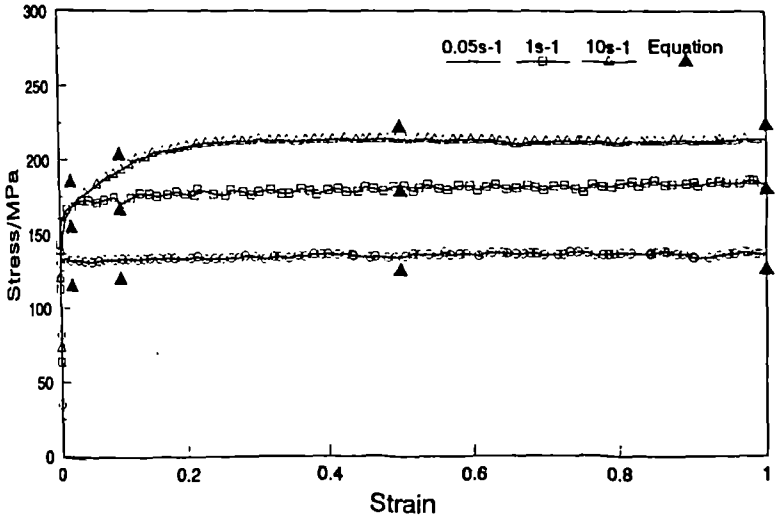

Figure 4.13 ASC series stress-strain curves from PSC tests performed at 300°C, corrected to nominal Z. Comparison with equation shown.

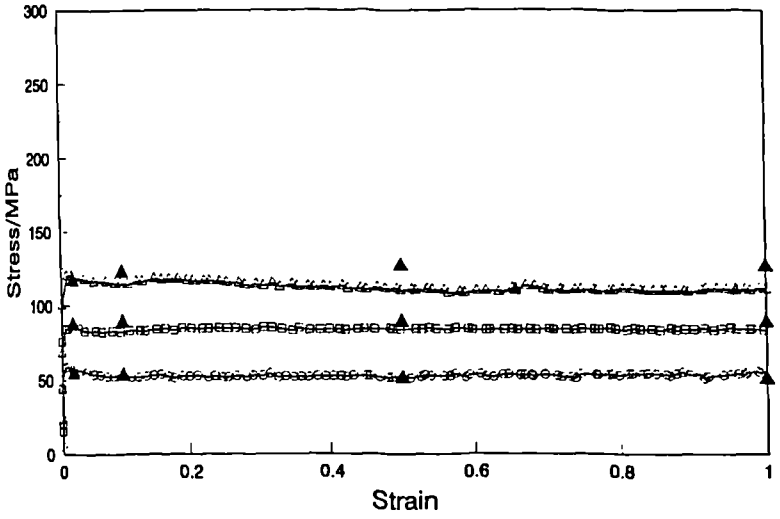

Figure 4.14 ASC series stress-strain curves from PSC tests performed at 400°C, corrected to nominal Z. Comparison with equation shown.

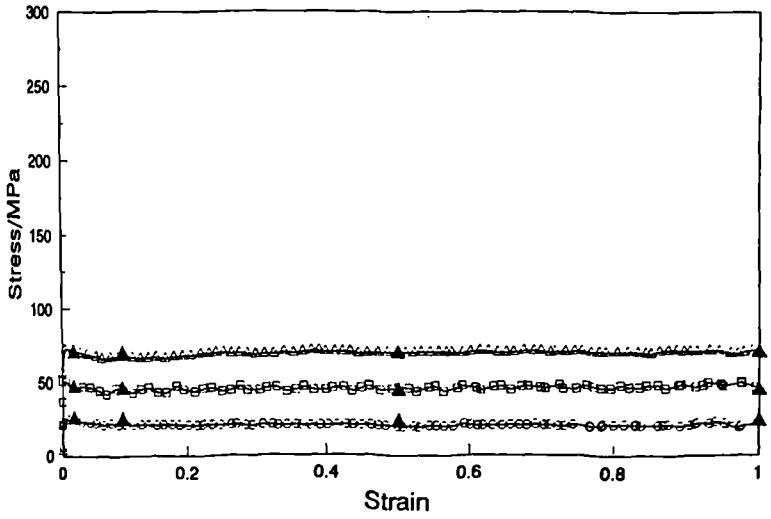

Figure 4.15 ASC series stress-strain curves from PSC tests performed at 500°C, corrected to nominal Z. Comparison with equation shown.

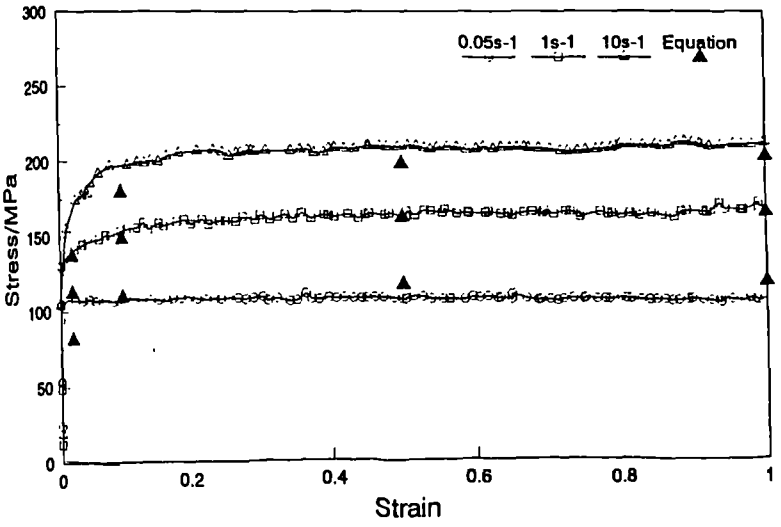

Figure 4.16 MONO series stress-strain curves from PSC tests performed at 300°C, corrected to nominal Z. Comparison with equation shown.

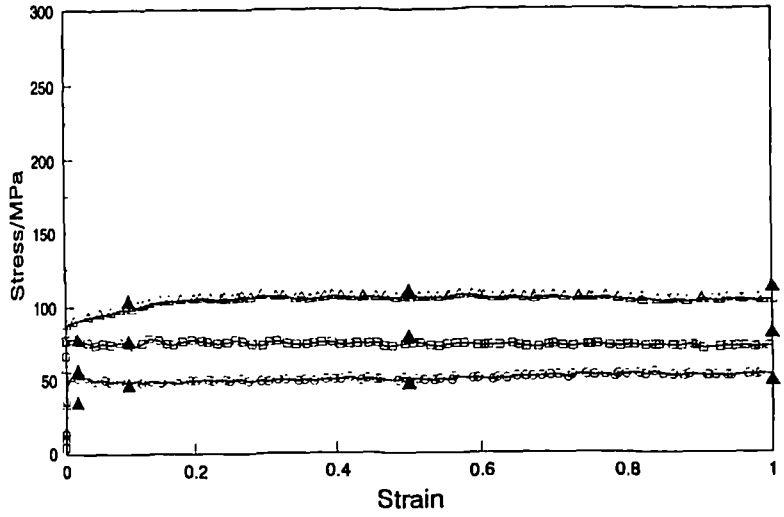

Figure 4.17 MONO series stress-strain curves from PSC tests performed at 400°C, corrected to nominal Z. Comparison with equation shown.

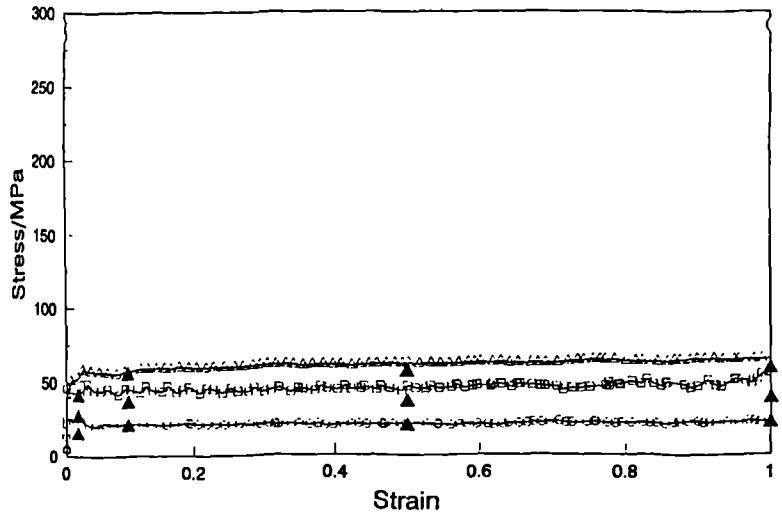

Figure 4.18 MONO series stress-strain curves from PSC tests performed at 500°C, corrected to nominal Z. Comparison with equation shown.

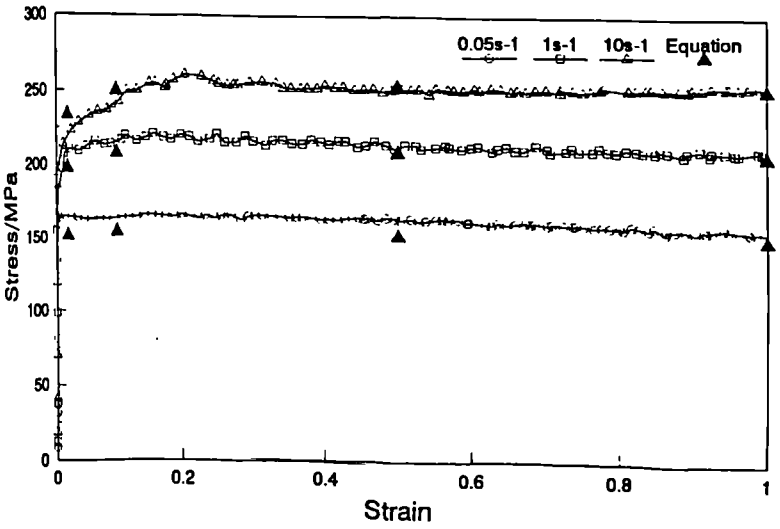

Figure 4.19 AMMP series stress-strain curves from PSC tests performed at 300°C, corrected to nominal Z. Comparison with equation shown.

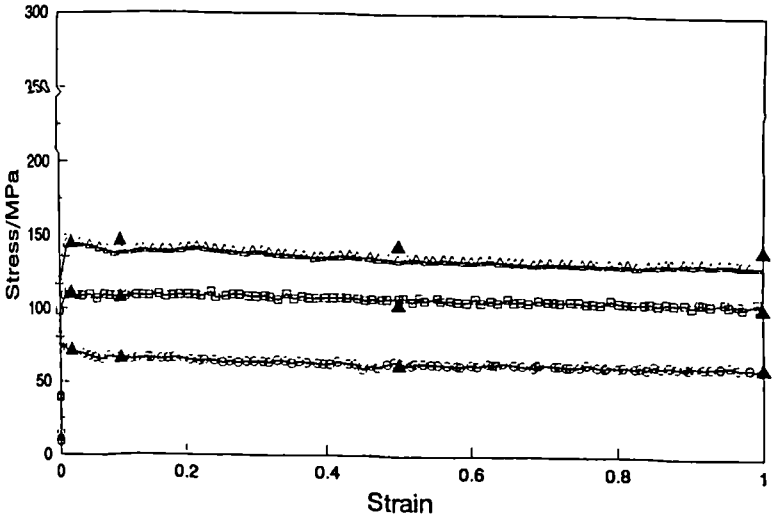

Figure 4.20 AMMP series stress-strain curves from PSC tests performed at 400°C, corrected to nominal Z. Comparison with equation shown.

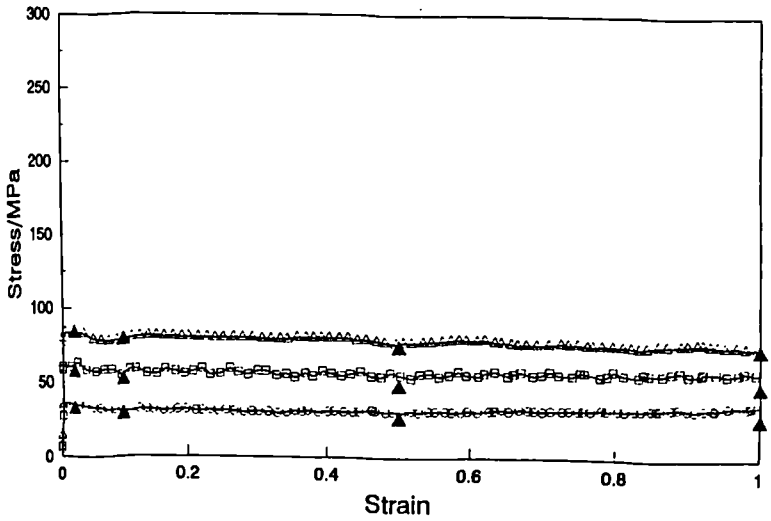

Figure 4.21 AMMP series stress-strain curves from PSC tests performed at 500°C, corrected to nominal Z. Comparison with equation shown.

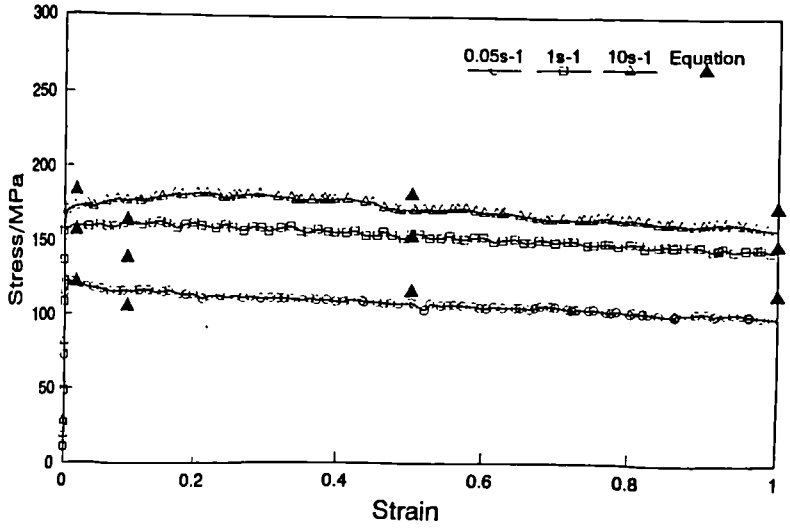

Figure 4.22 MMC series stress-strain curves from PSC tests performed at 300°C, corrected to nominal Z. Comparison with equation shown.

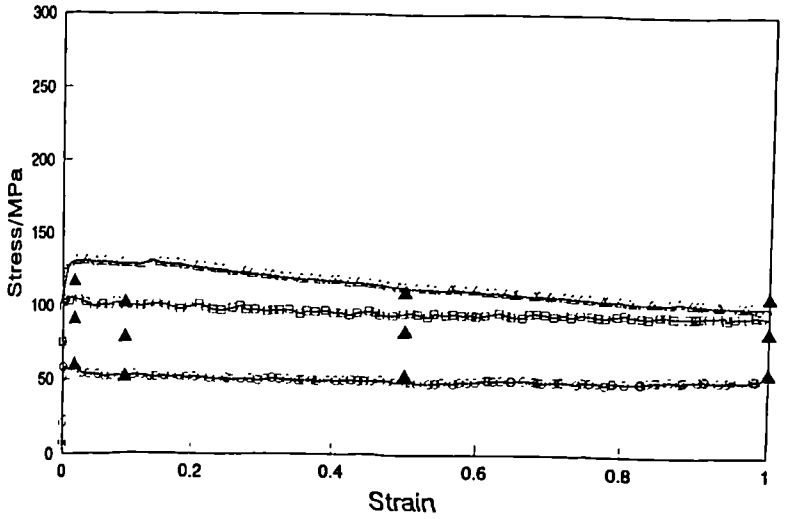

Figure 4.23 MMC series stress-strain curves from PSC tests performed at 400°C, corrected to nominal Z. Comparison with equation shown.

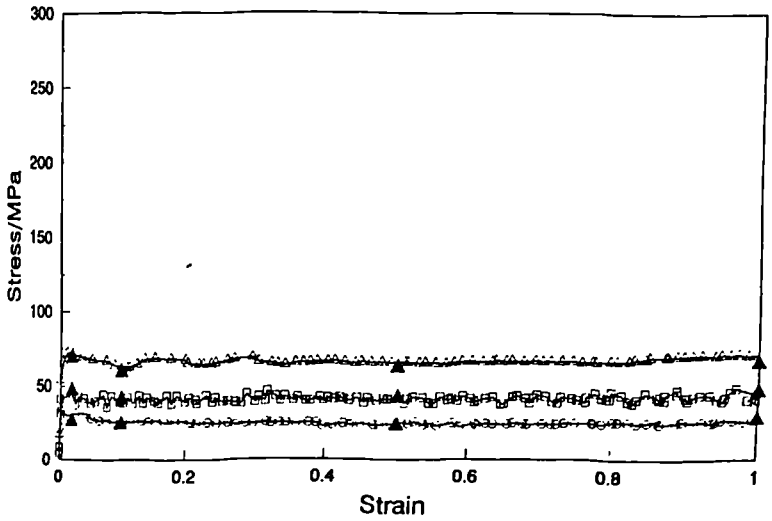

Figure 4.24 MMC series stress-strain curves from PSC tests performed at 500°C, corrected to nominal Z. Comparison with equation shown.

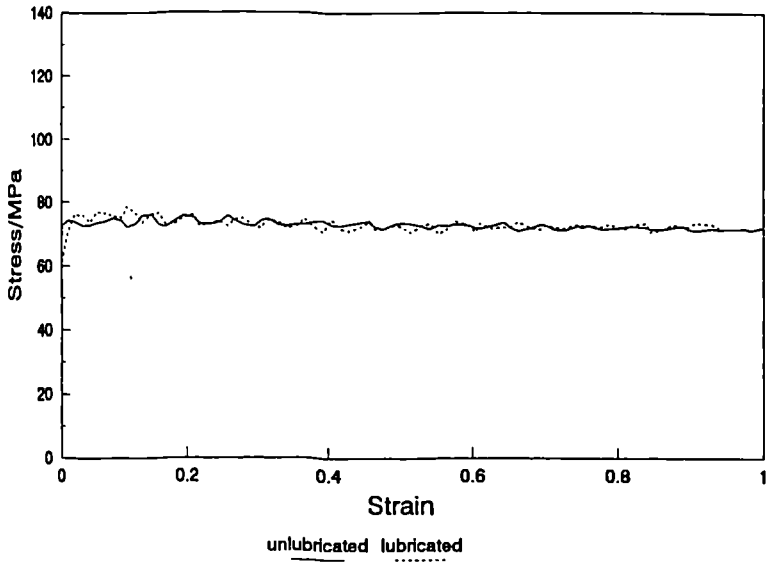

Figure 4.25 Comparison of MONO series stress-strain curves for lubricated and unlubricated PSC tests performed at 400°C and $1s^{-1}$. Corrected to nominal Z.

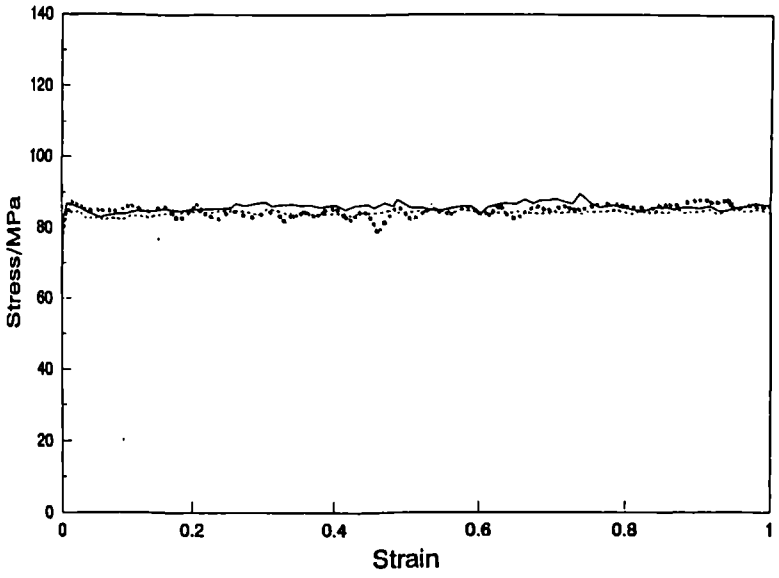

Figure 4.26 ASC series reproducibility study for PSC tests performed at 400°C and 1s-1. Curves are corrected to nominal Z.

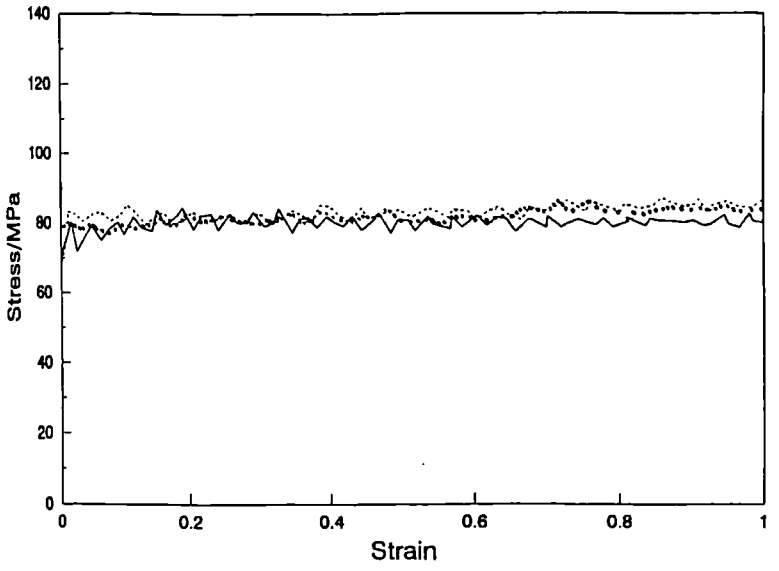

Figure 4.27 MONO series reproducibility study for PSC tests performed at 400°C and 1s-1. Curves are corrected to nominal Z.

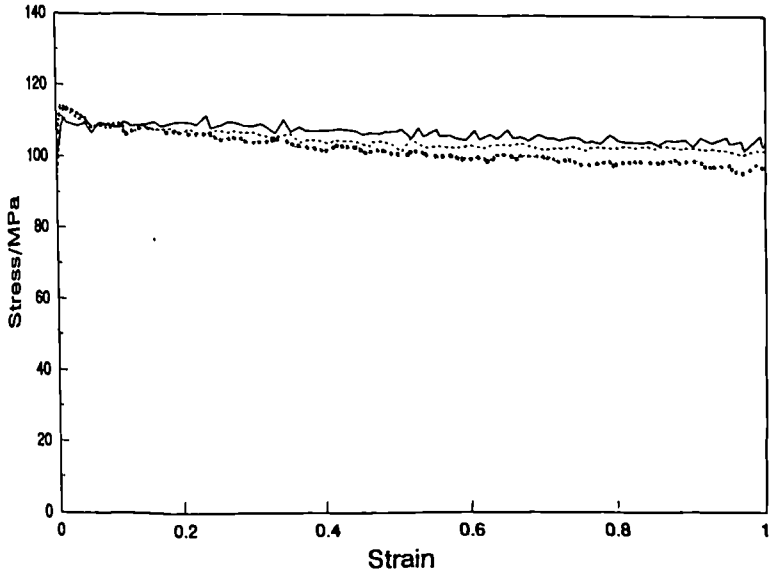

Figure 4.28 AMMP series reproducibility study for PSC tests performed at 400°C and 1s-1. Curves are corrected to nominal Z.

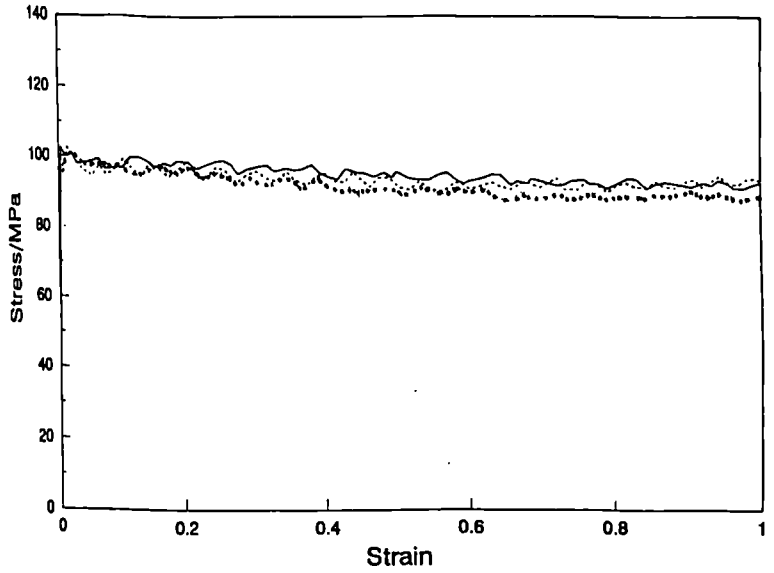

Figure 4.29 MMC series reproducibility study for PSC tests performed at 400°C and 1s-1. Curves are corrected to nominal Z.

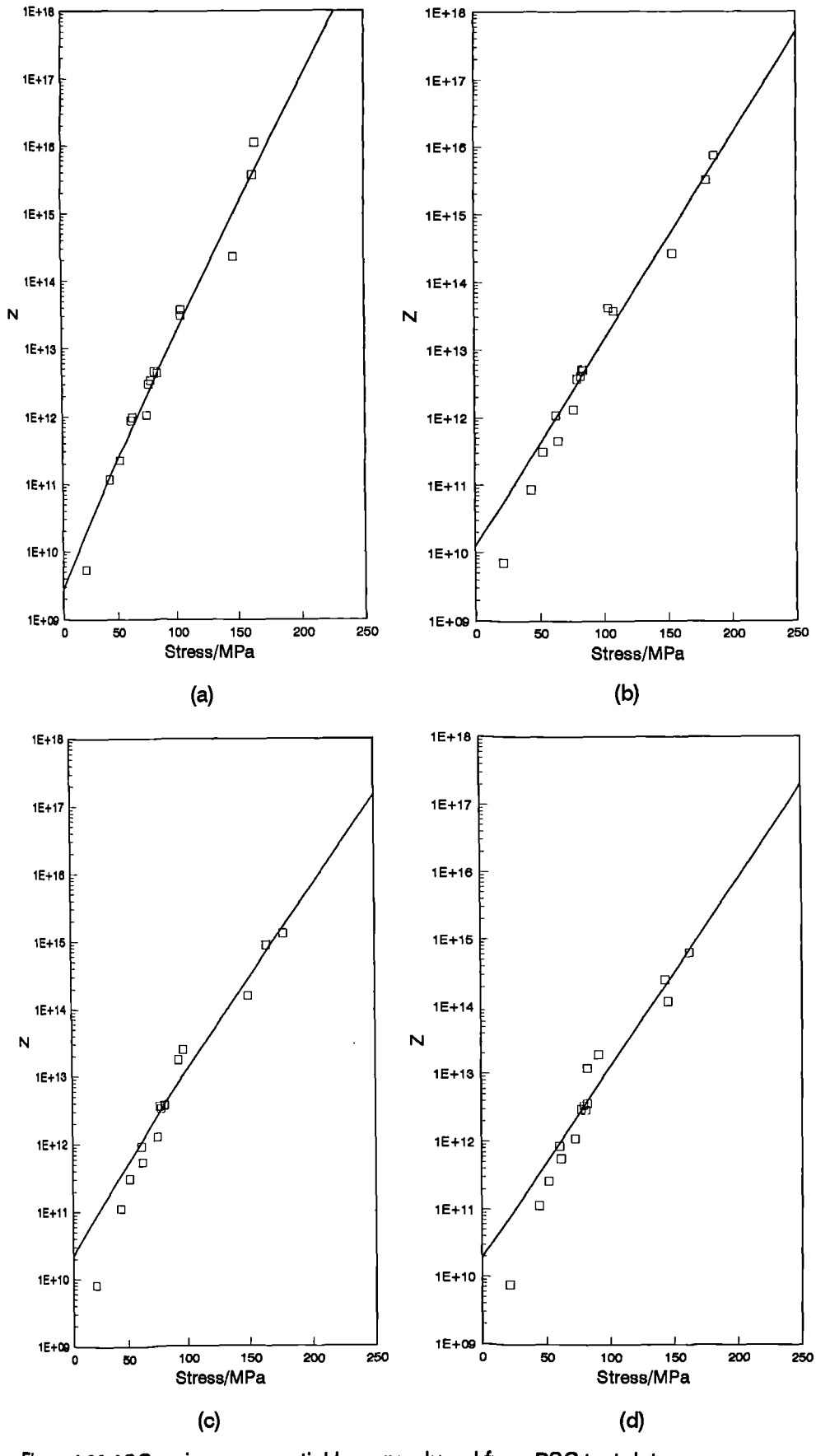

Figure 4.30 ASC series exponential laws produced from PSC test data at strains of: (a) 0.02 (b) 0.1 (c) 0.5 (d) 1.0

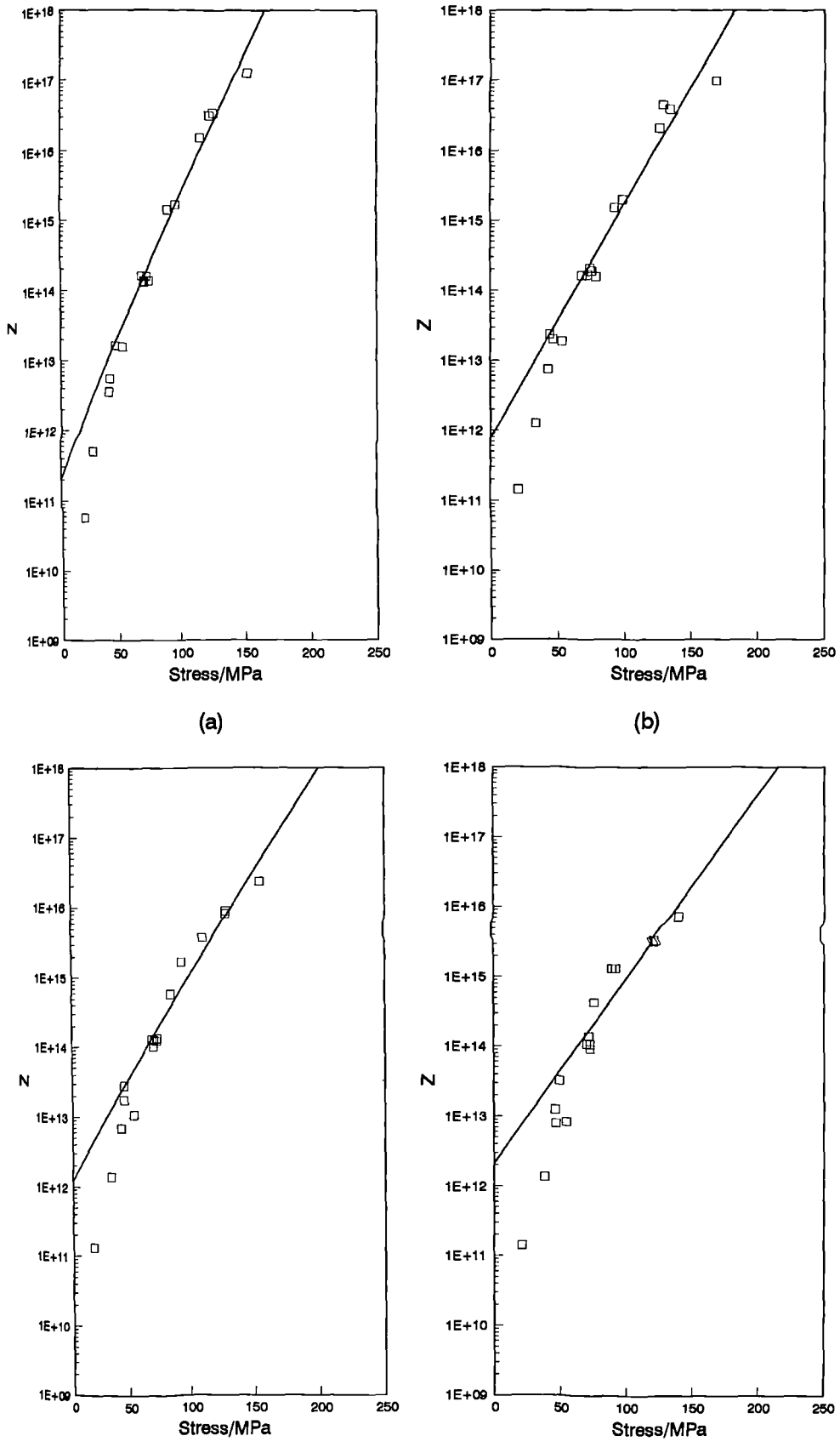

Figure 4.31 MONO series exponential laws produced from PSC test data at strains of: (a) 0.02 (b) 0.1 (c) 0.5 (d) 1.0

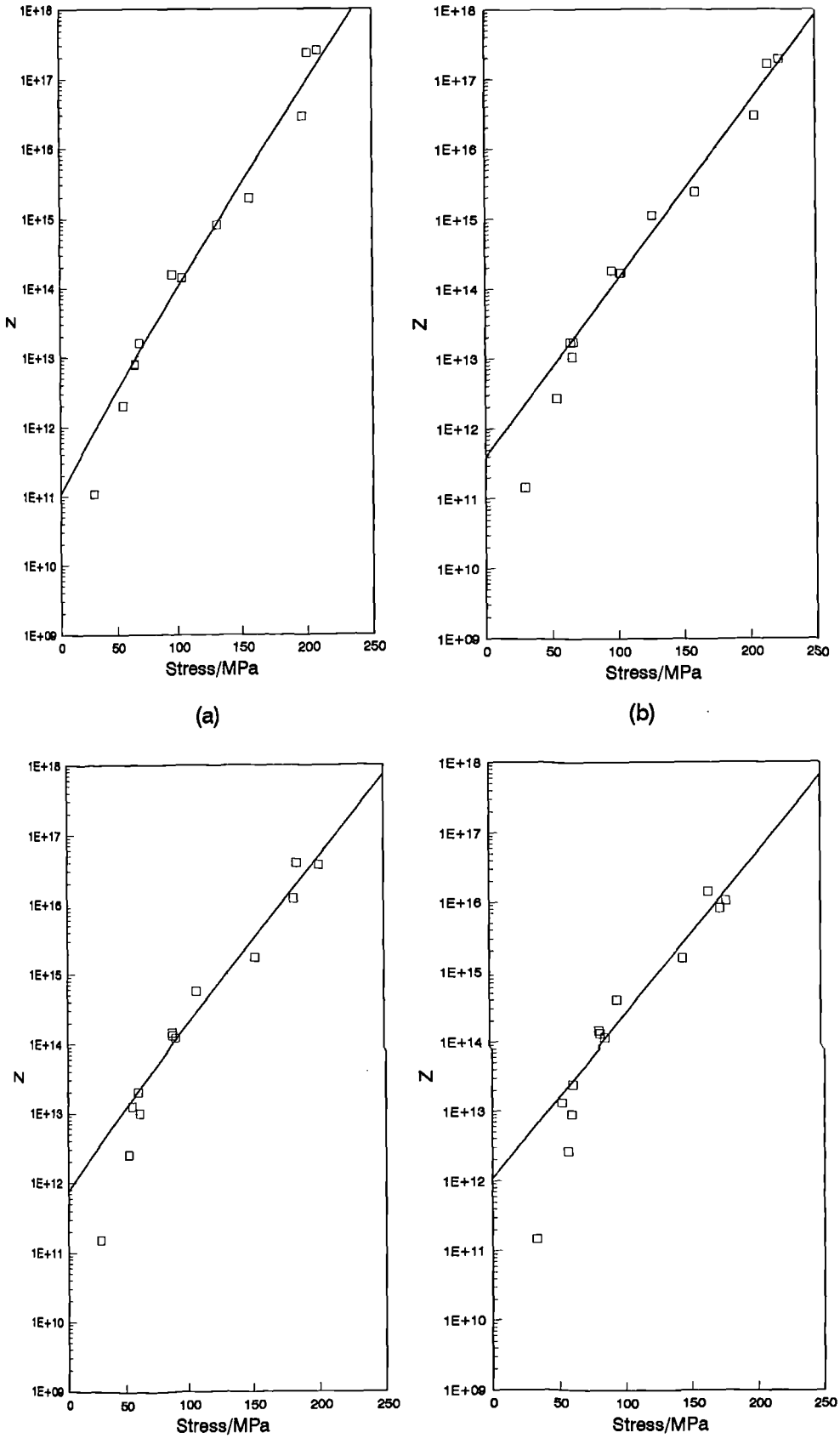

Figure 4.32 AMMP series exponential laws produced from PSC test data at strains of: (a) 0.02 (b) 0.1 (c) 0.5 (d) 1.0

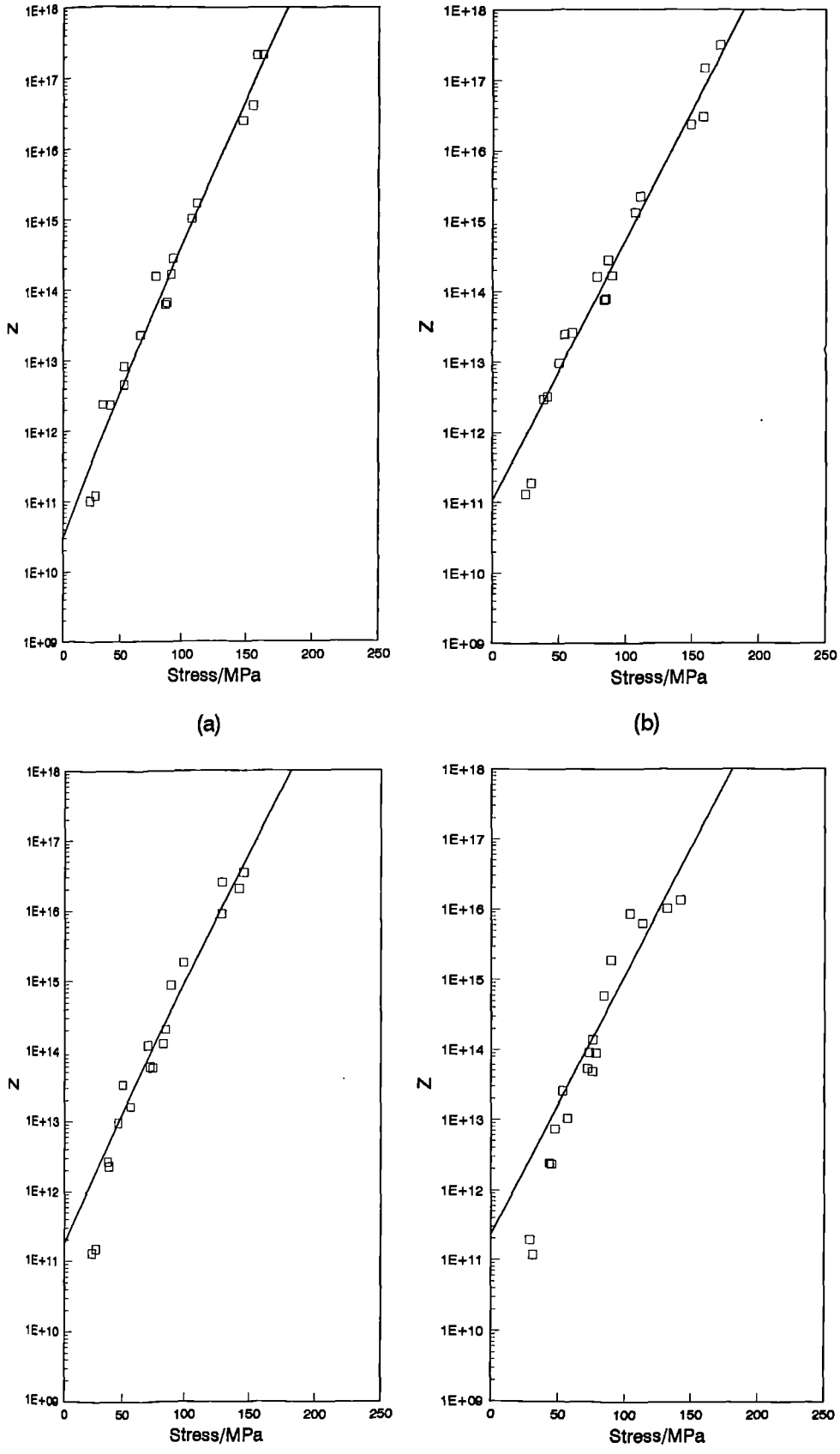

Figure 4.33 MMC series exponential laws produced from PSC test data at strains of: (a) 0.02 (b) 0.1 (c) 0.5 (d) 1.0

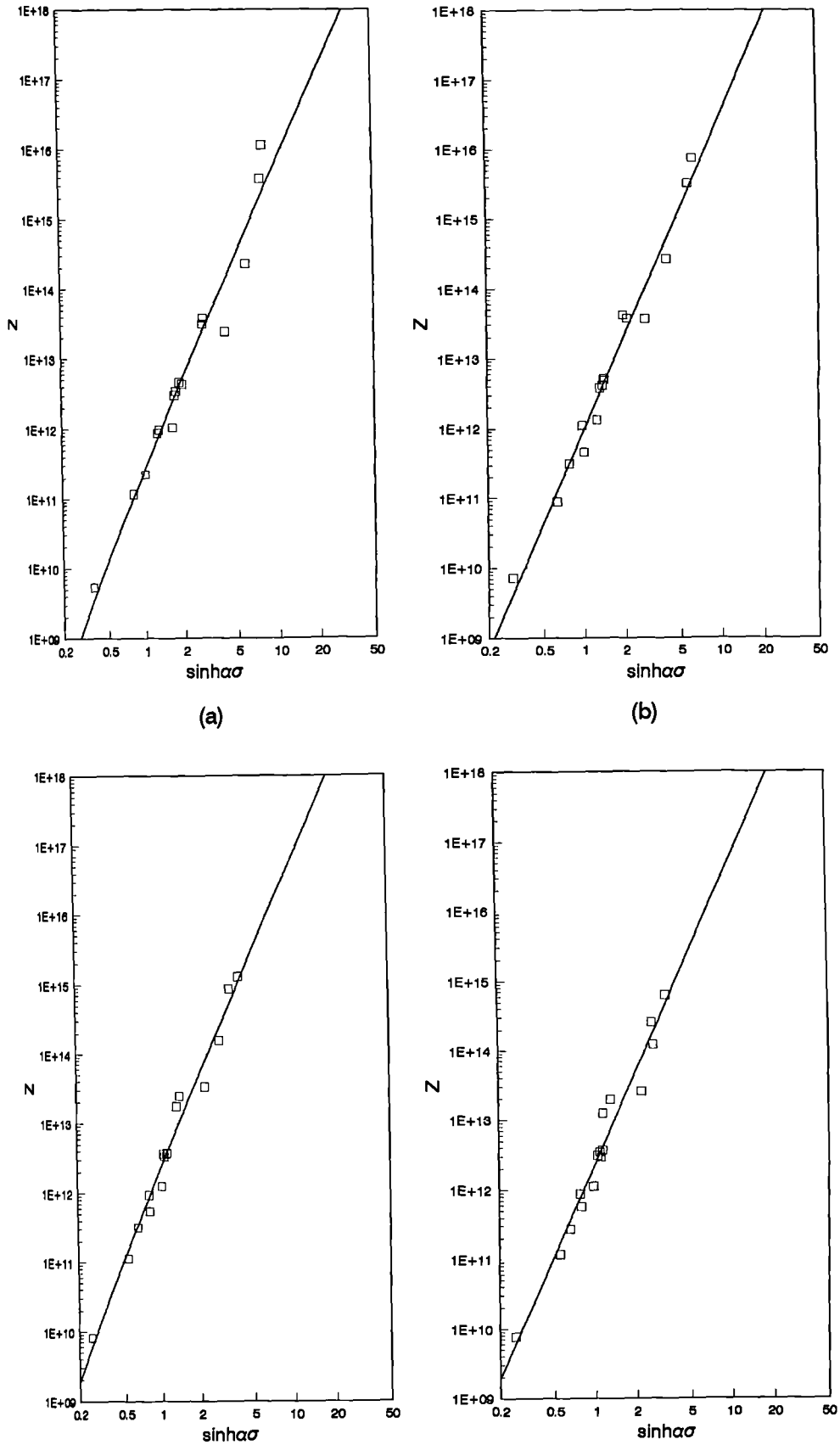

Figure 4.34 ASC series hyperbolic sine laws produced from PSC test data at strains of: (a) 0.02 (b) 0.1 (c) 0.5 (d) 1.0

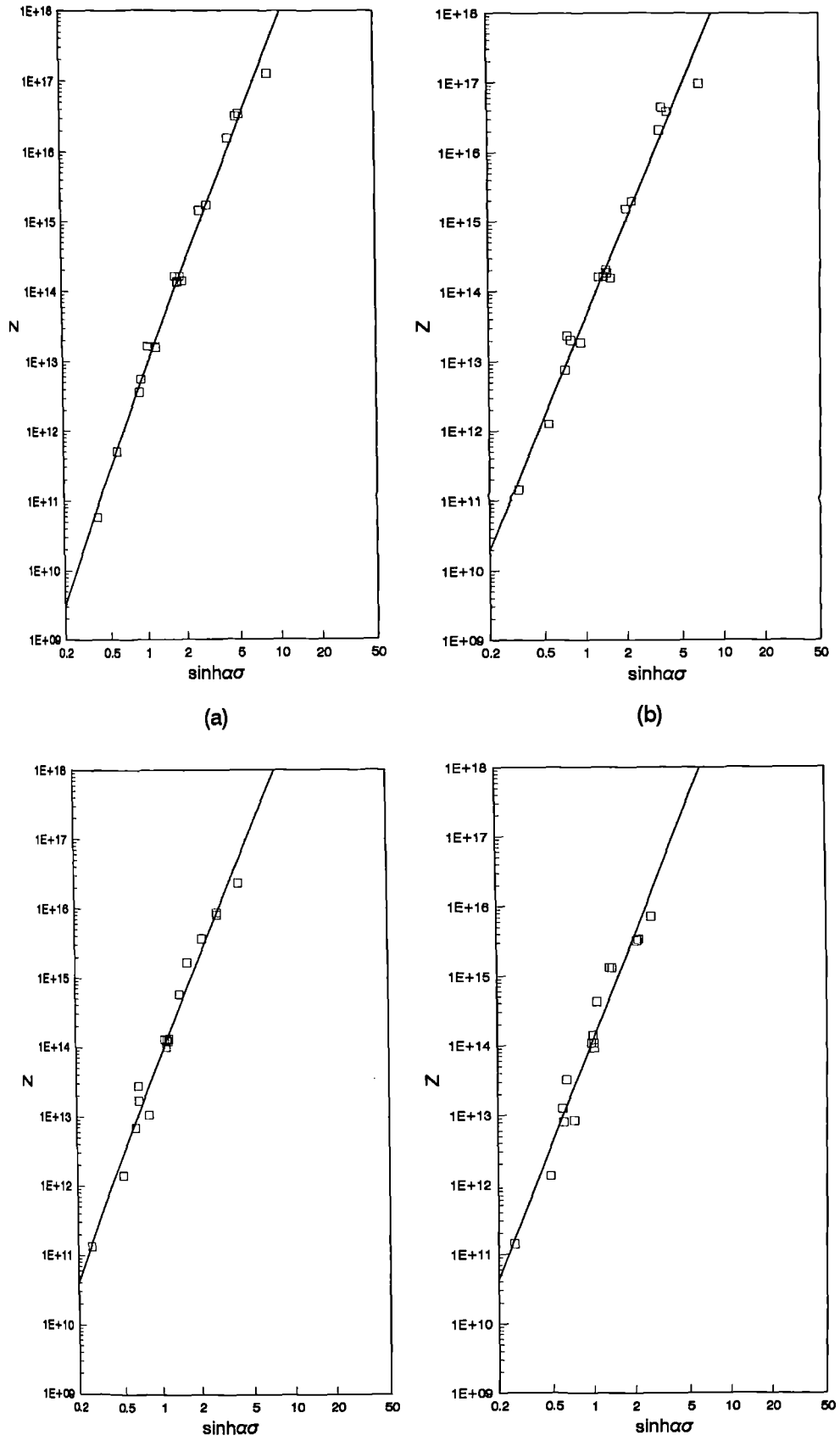

Figure 4.35 MONO series hyperbolic sine laws produced from PSC test data at strains of: (a) 0.02 (b) 0.1 (c) 0.5 (d) 1.0

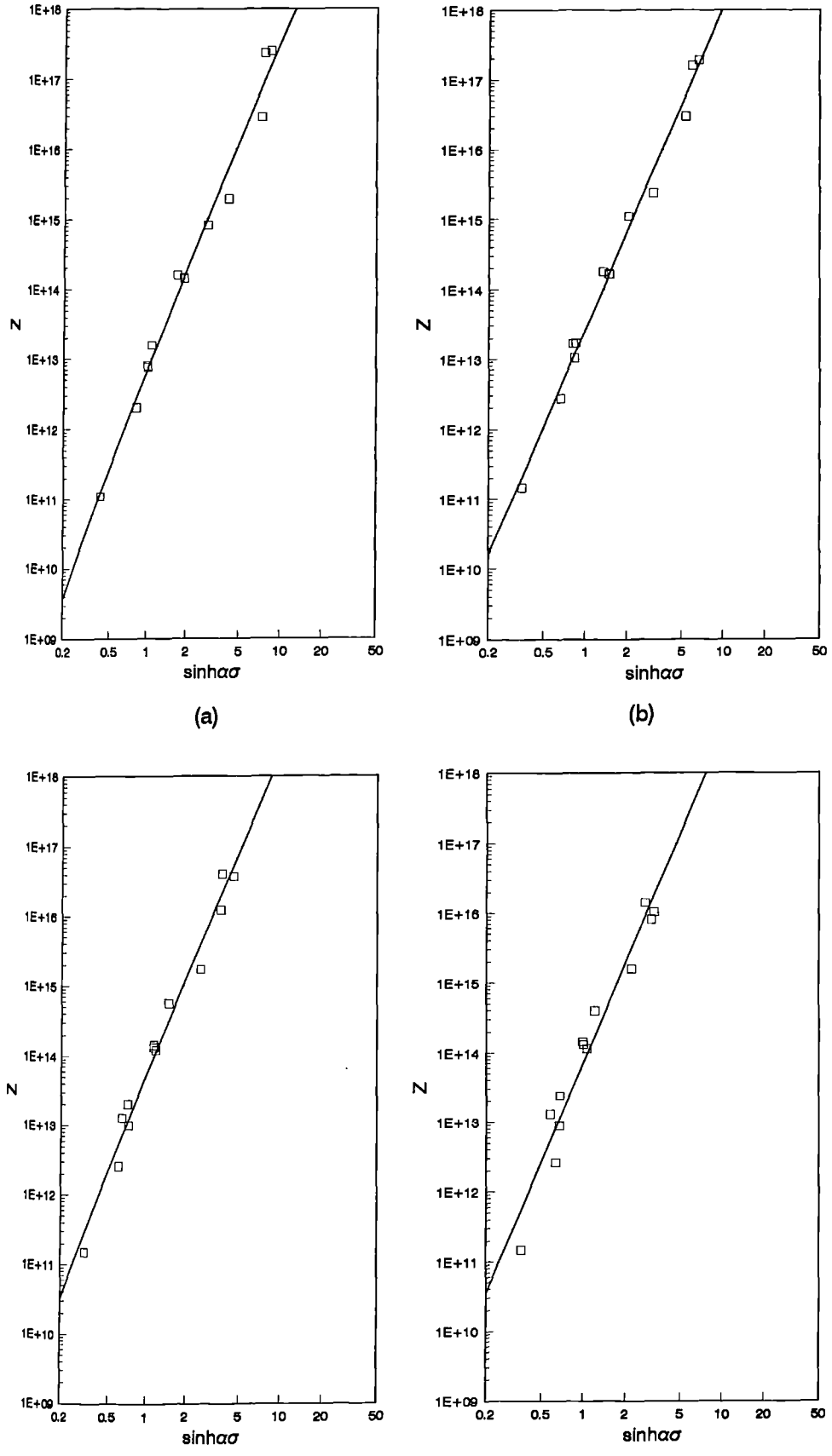

Figure 4.36 AMMP series hyperbolic sine laws produced from PSC test data at strains of: (a) 0.02 (b) 0.1 (c) 0.5 (d) 1.0

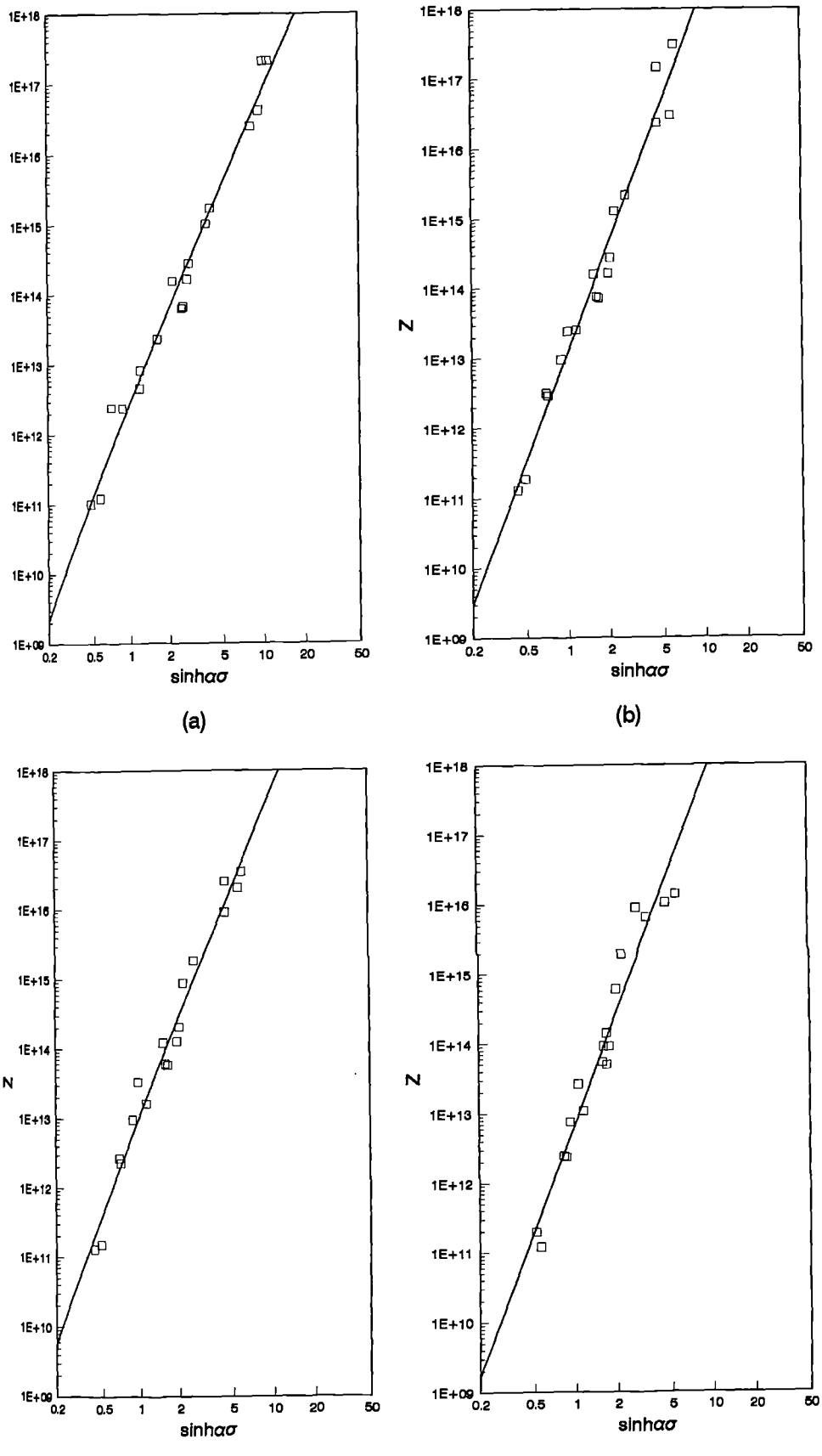

Figure 4.37 MMC series hyperbolic sine laws produced from PSC test data at strains of: (a) 0.02 (b) 0.1 (c) 0.5 (d) 1.0

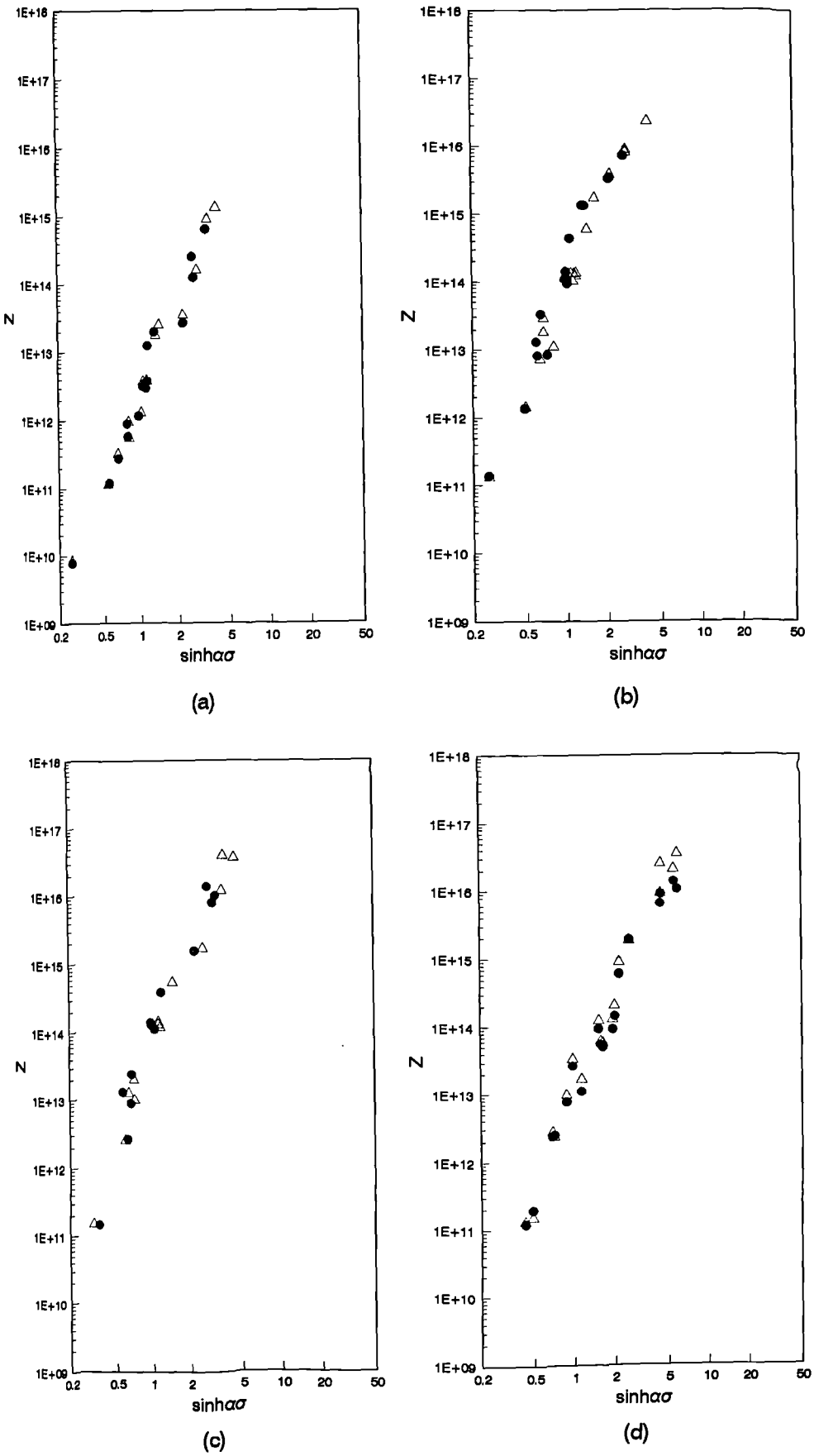

Figure 4.38 Combination of hyperbolic sine laws at strains of 0.5 and 1.0 for (a) ASC series (b) MONO series (c) AMMP series (d) MMC series

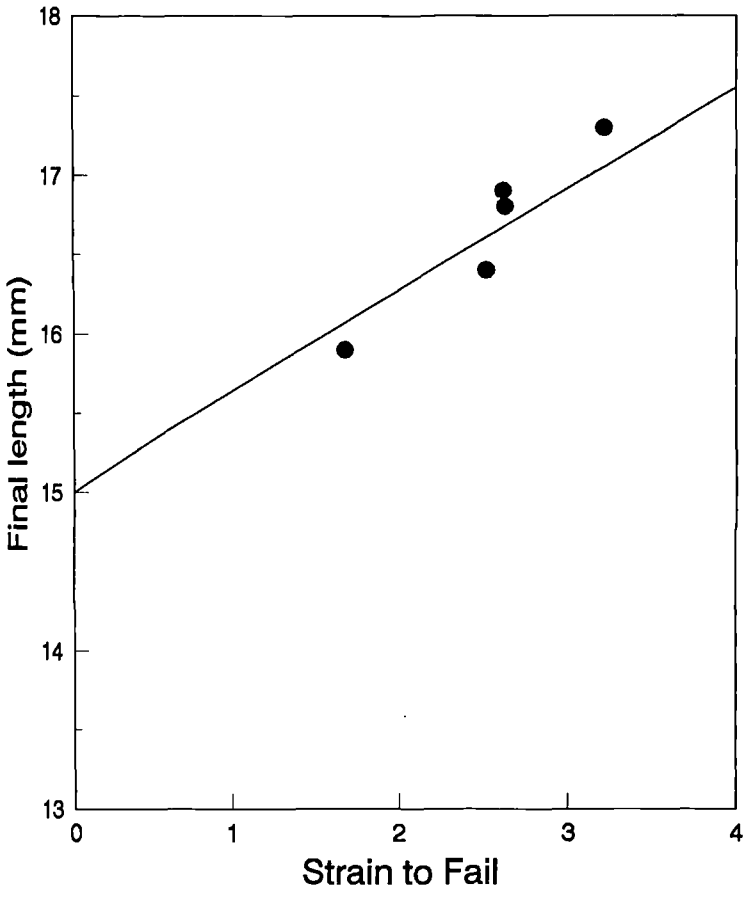

Figure 4.39 Final length vs. Failure strain for MONO series torsion tests.

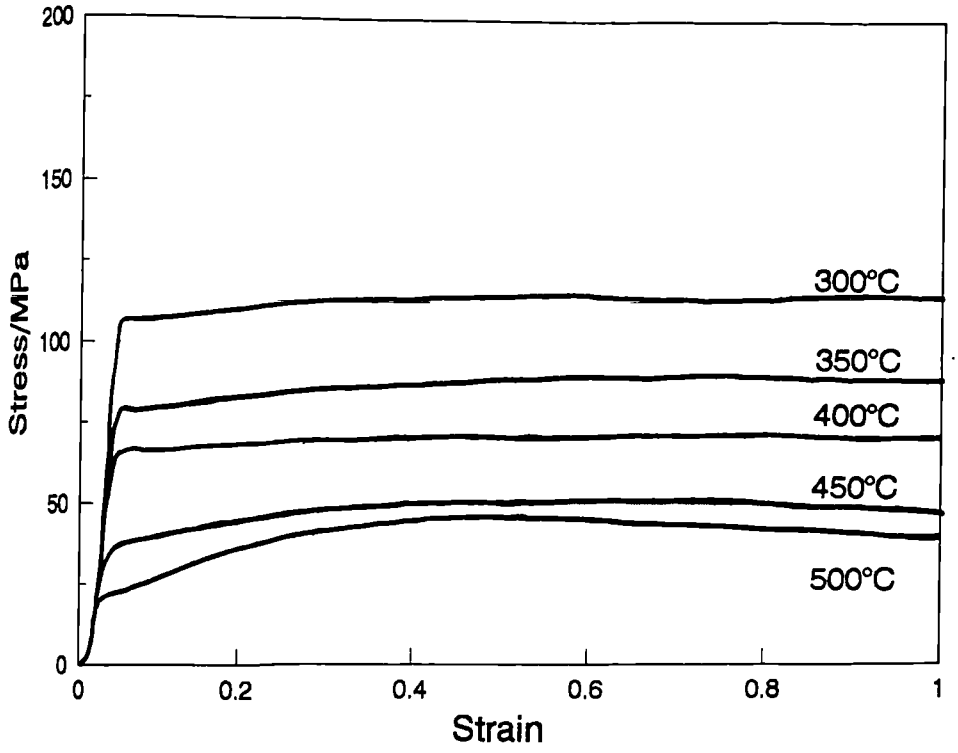

Figure 4.40 MONO series torsion stress-strain curves produced during free end tests. Curves given to a strain of 1.

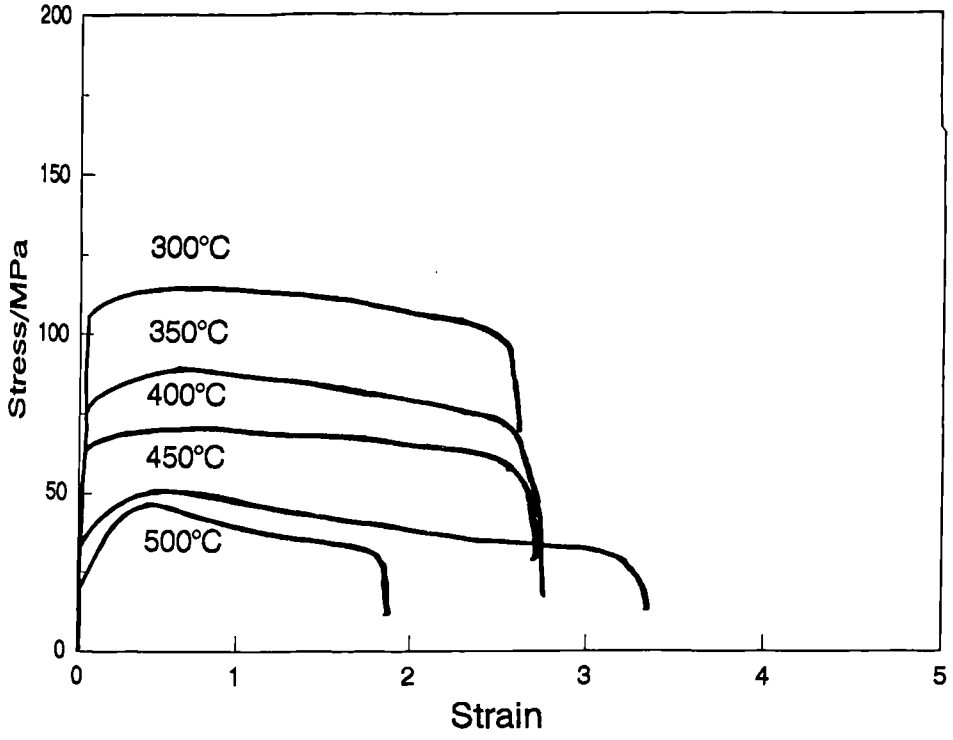

Figure 4.41 MONO series torsion stress-strain curves produced during free end tests. Complete stress-strain curves to failure are shown.

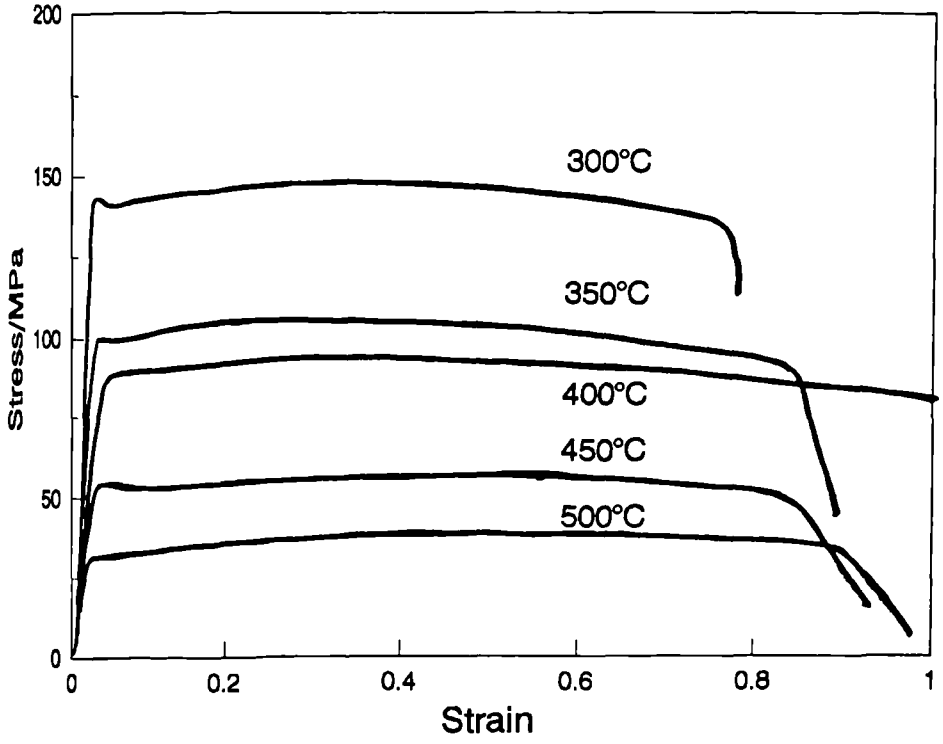

Figure 4.42 MMC series torsion stress-strain curves produced during free end tests. Curves given to a strain of 1.

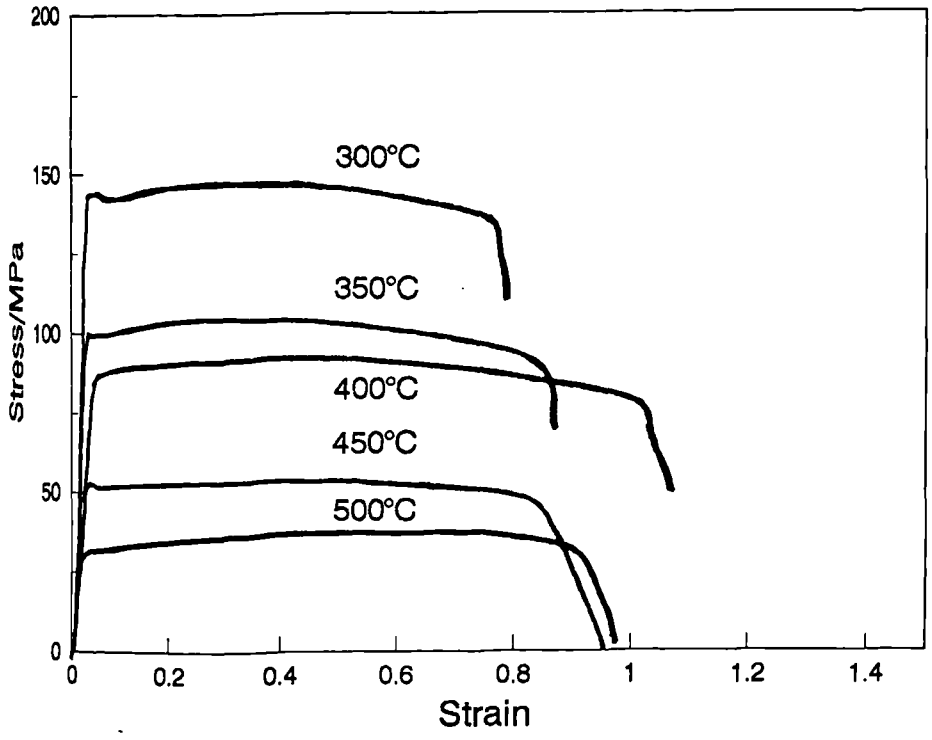

Figure 4.43 MMC series torsion stress-strain curves produced during free end tests. Complete stress-strain curves to failure are shown.

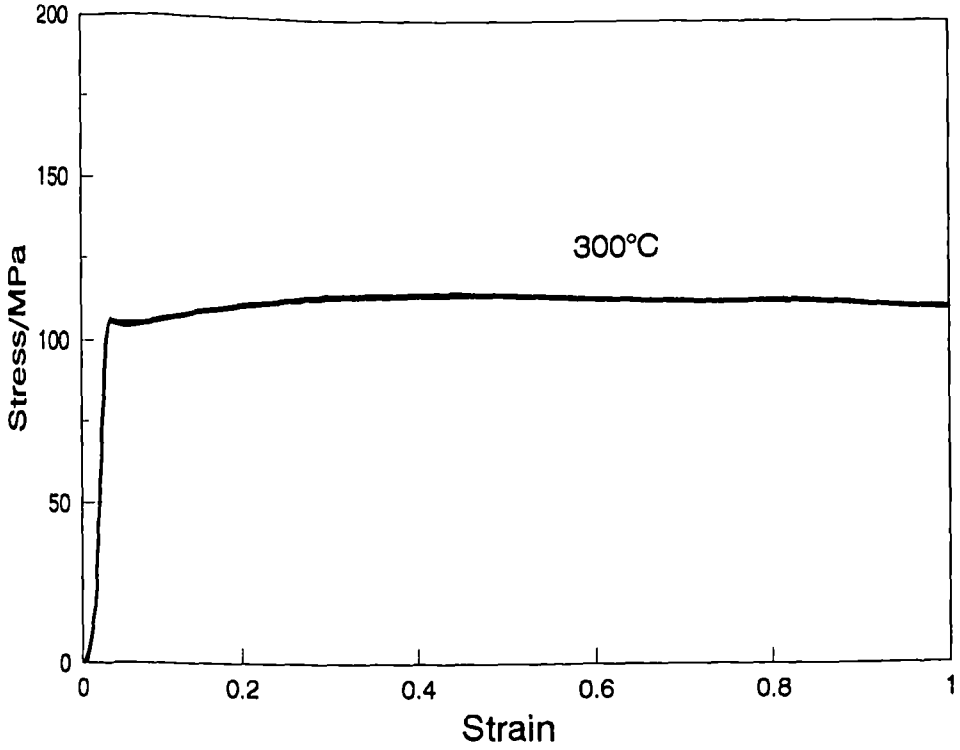

Figure 4.44 MONO series torsion stress-strain curves, produced at the temperature of deformation shown, during fixed end test.

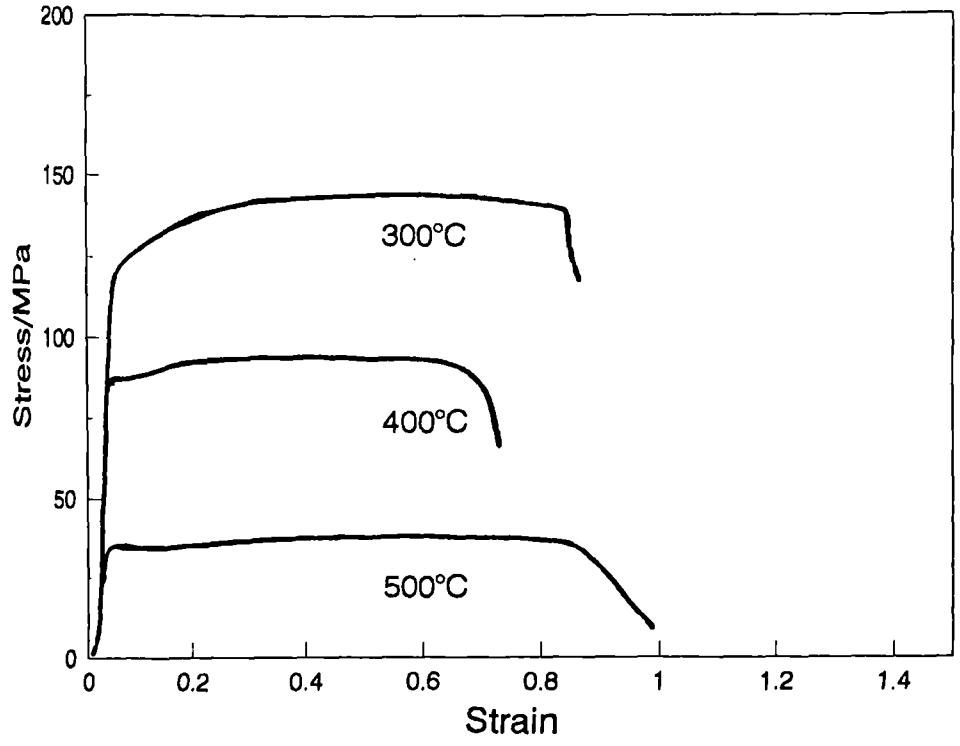

Figure 4.45 MMC series torsion stress-strain curves, produced at the temperature of deformation shown, during fixed end tests.

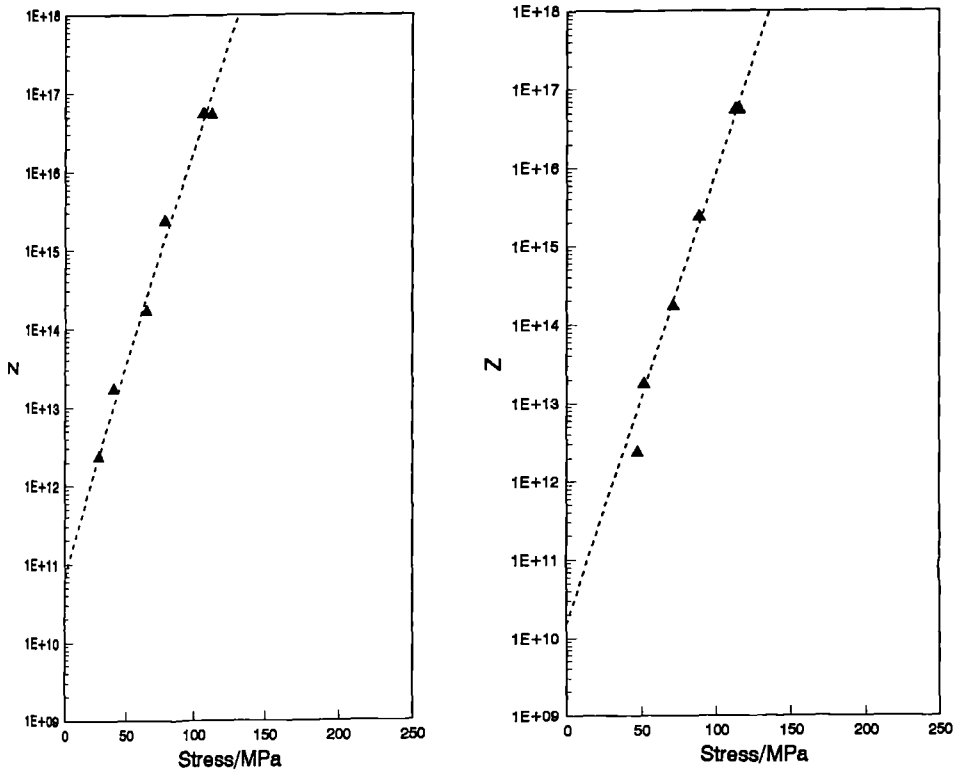

(a) (b)

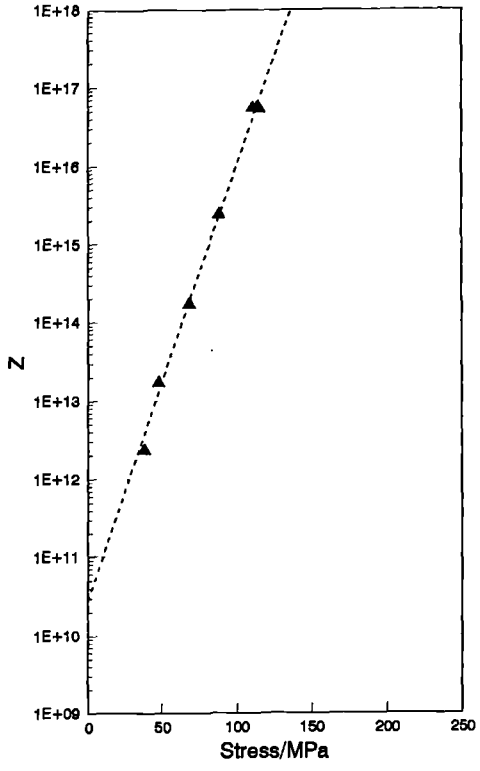

(c)

Figure 4.46 MONO series exponential laws produced from torsion test data at strains of: (a) 0.1 (b) 0.5 (c) 1.0

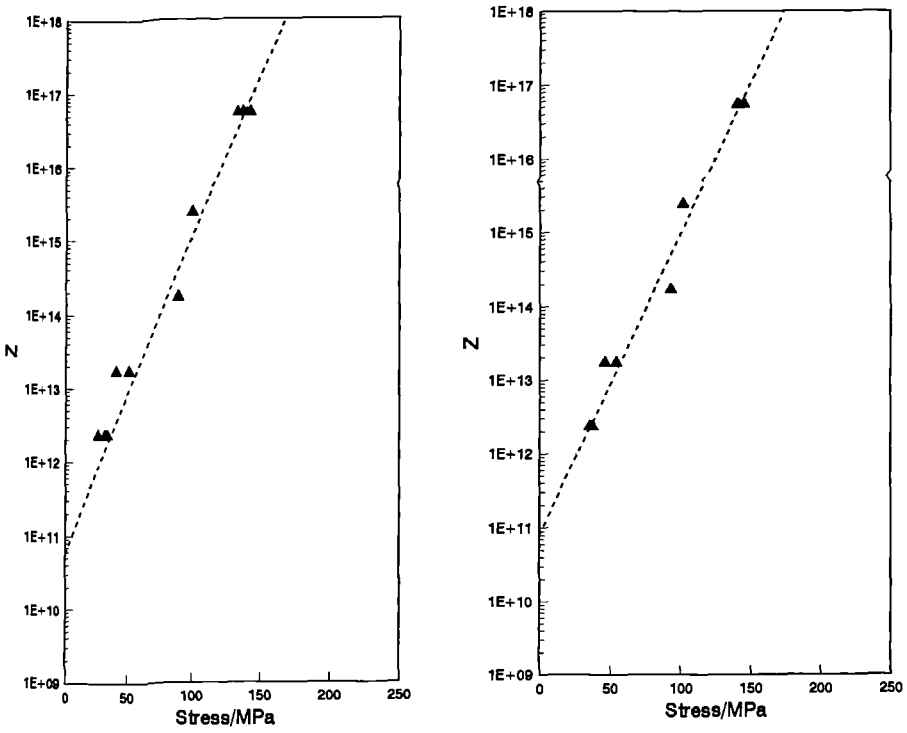

Figure 4.47 MMC series exponential laws produced from torsion test data at strains of: (a) 0.1 (b) 0.5

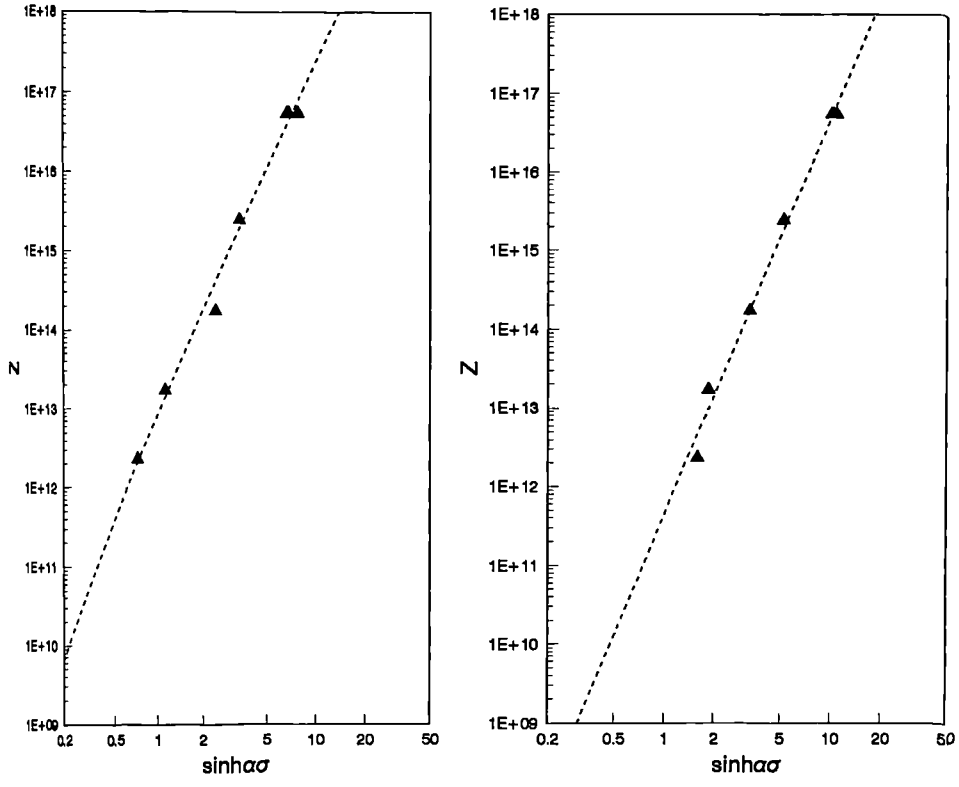

(a) (b)

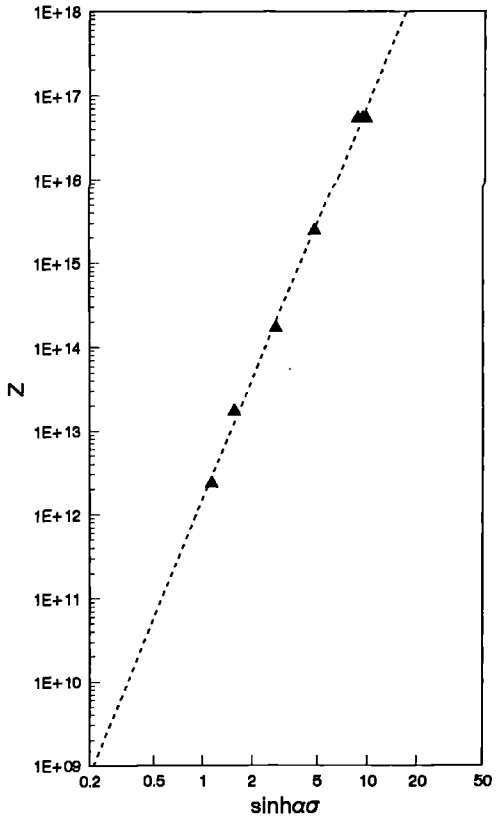

(c)

Figure 4.48 MONO series hyperbolic sine laws produced from torsion test data at strains of: (a) 0.1 (b) 0.5 (c) 1.0

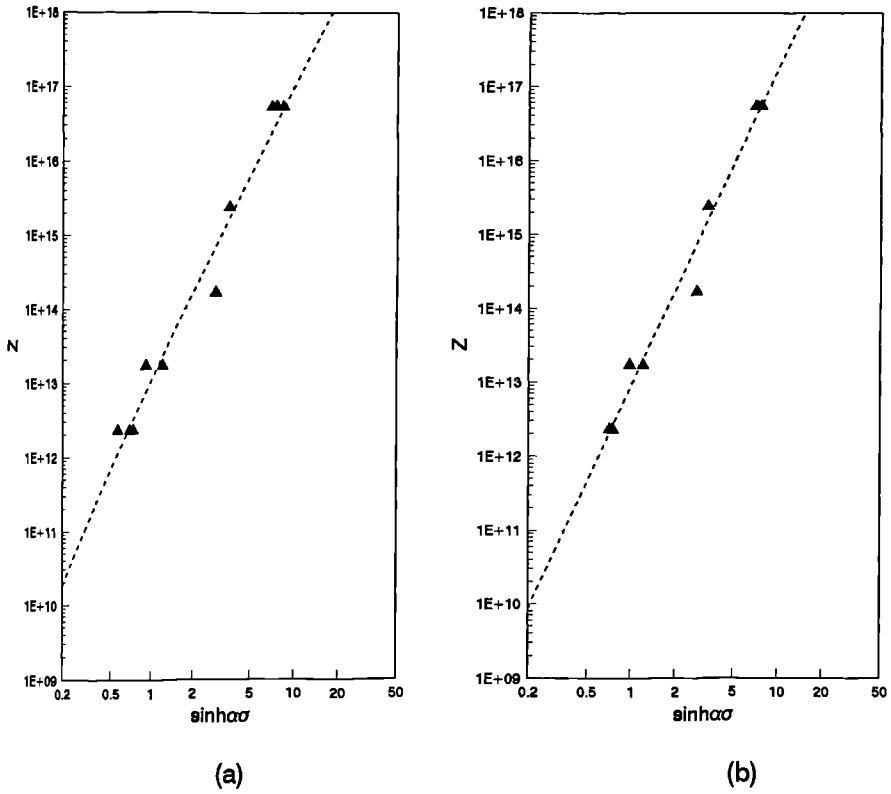

Figure 4.49 MMC series hyperbolic sine laws produced from torsion test data at strains of: (a) 0.1 (b) 0.5

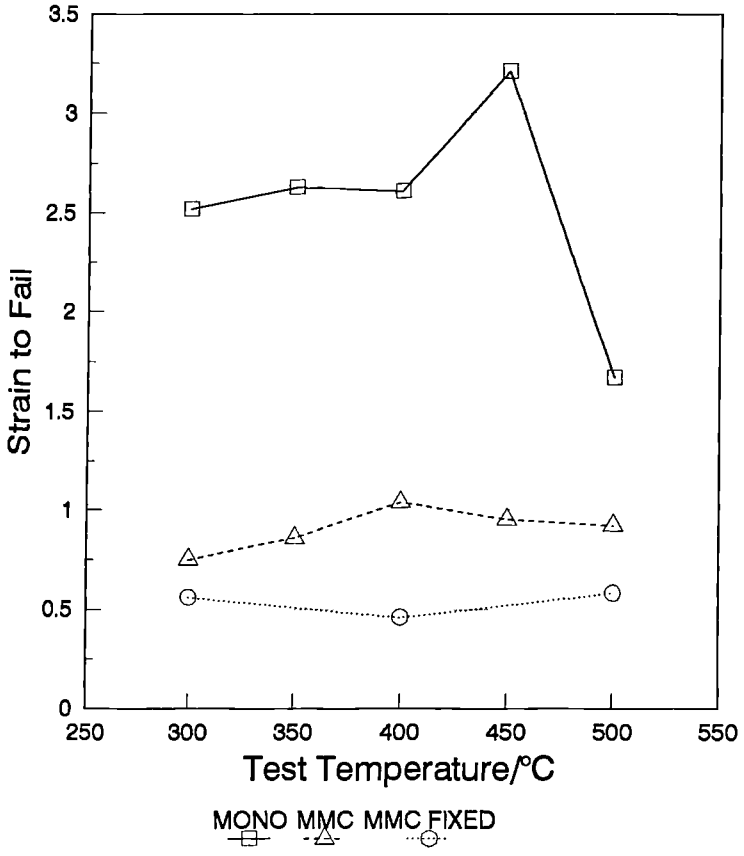

Figure 4.50 Failure strains during torsion testing of MONO and MMC series material.

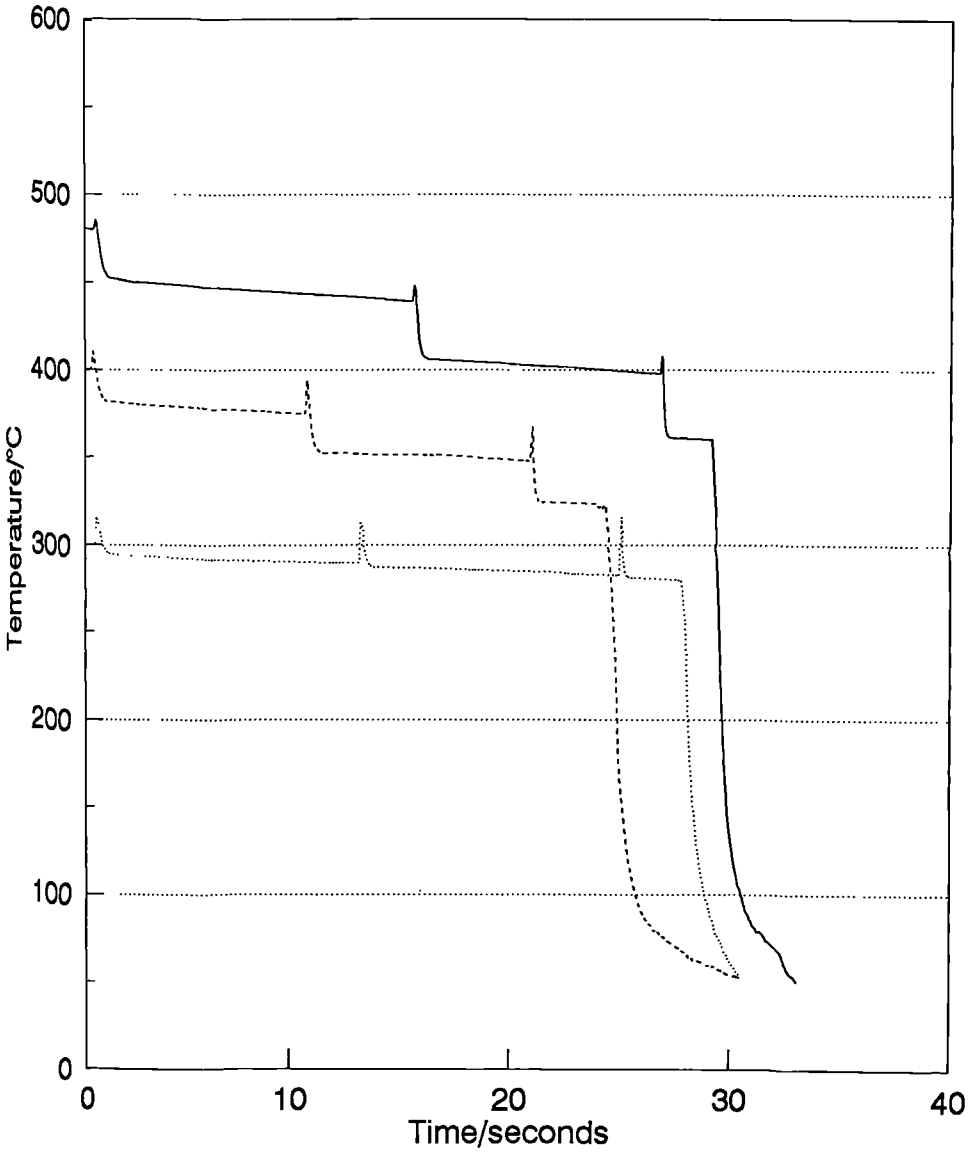

Figure 4.51 Temperature profiles during the rolling of ASC material

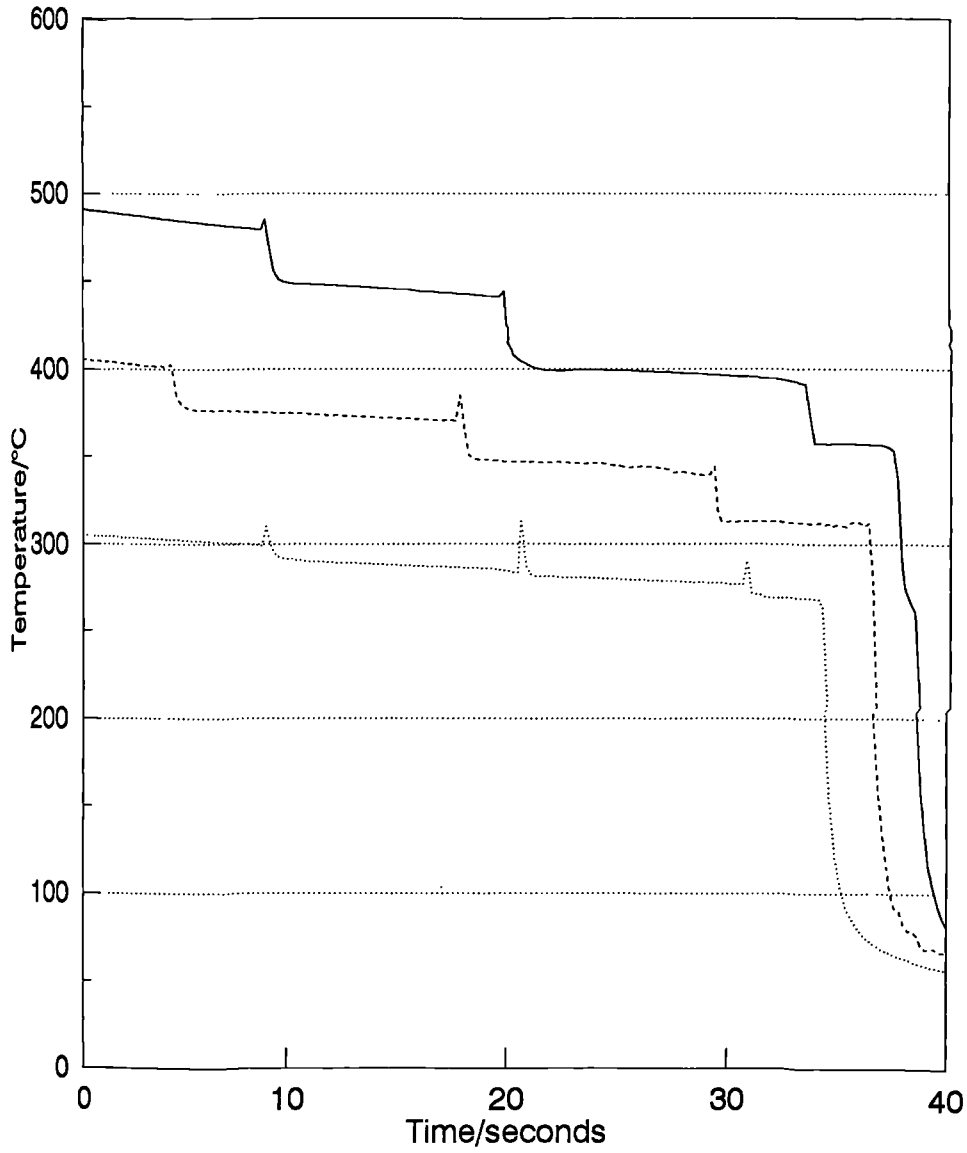

Figure 4.52 Temperature profiles during the rolling of MONO material.

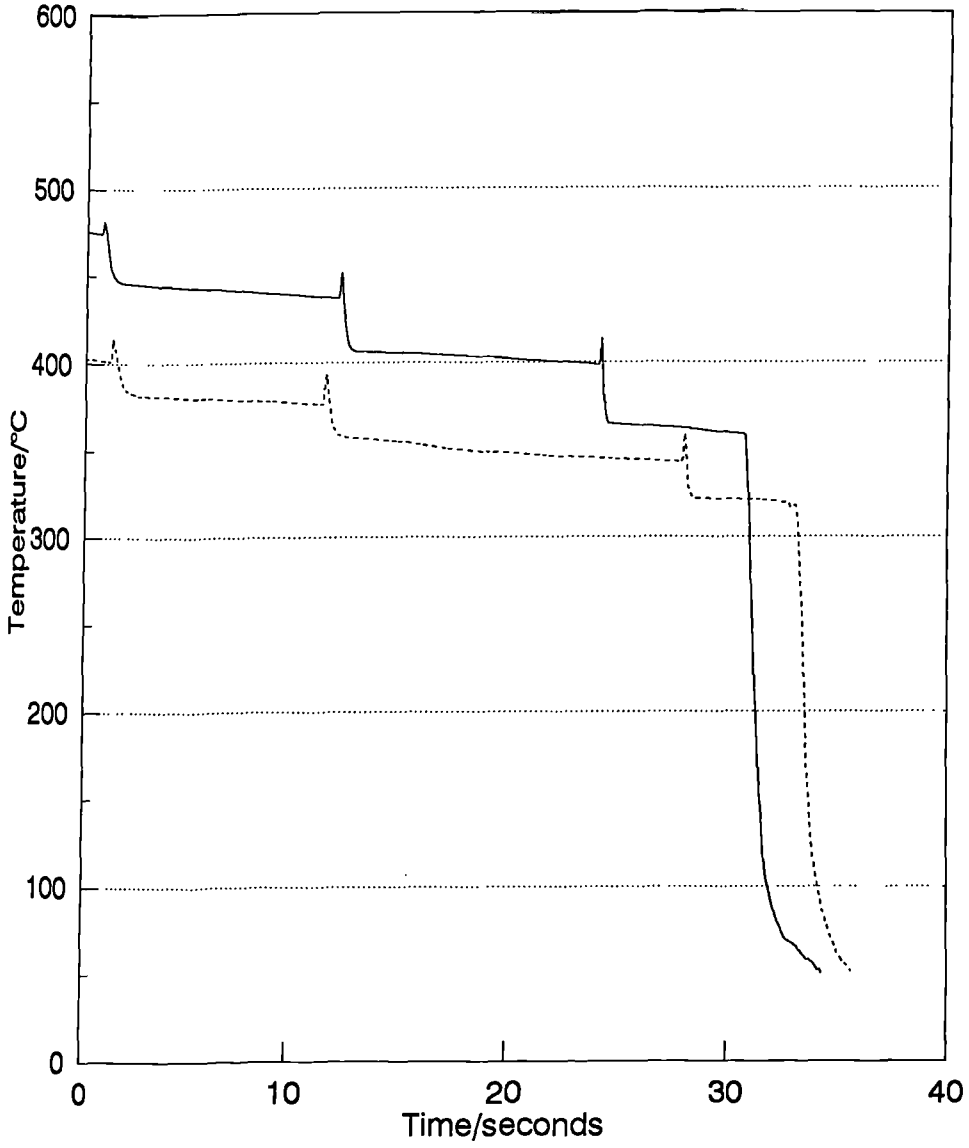

Figure 4.53 Temperature profiles during the rolling of AMMP material.

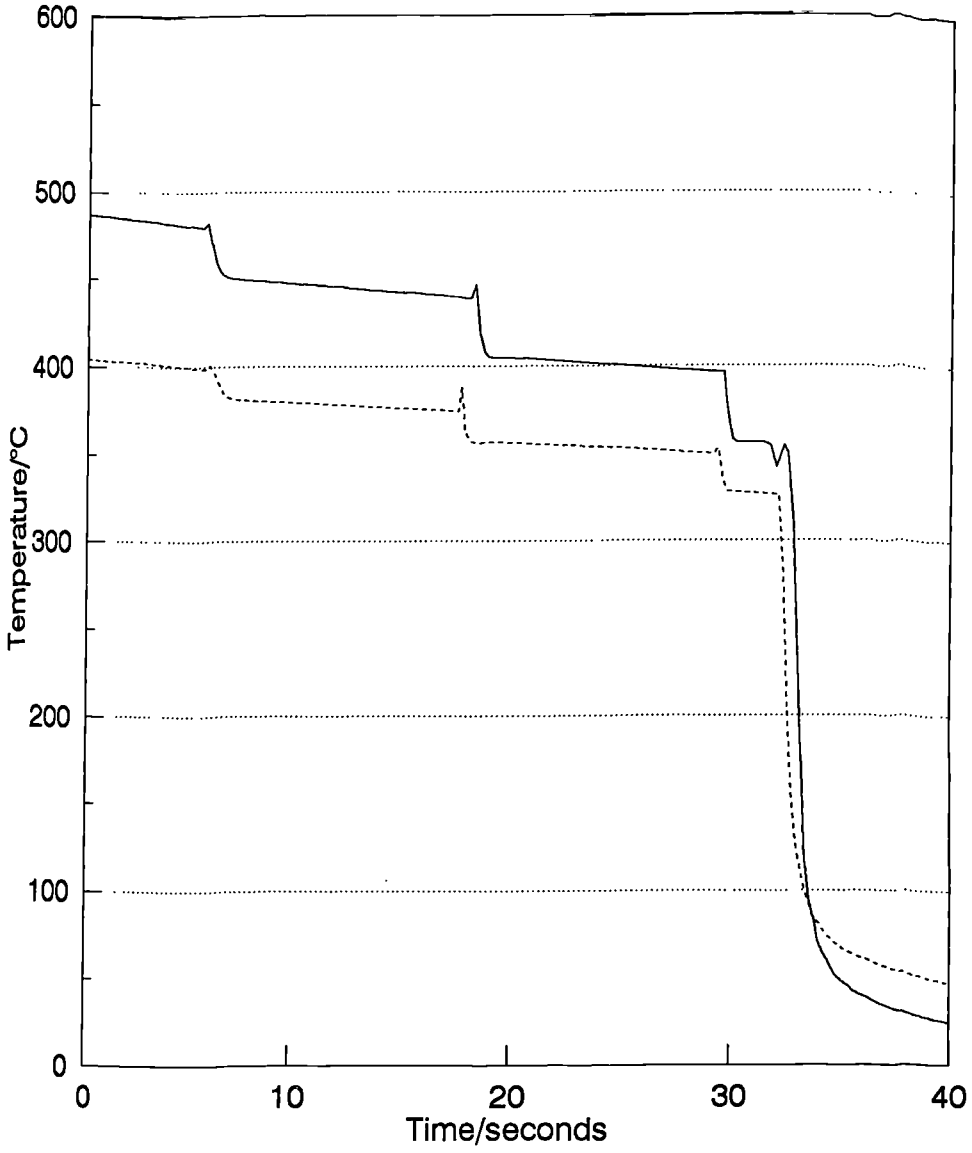

Figure 4.54 Temperature profiles during the rolling of MMC material.

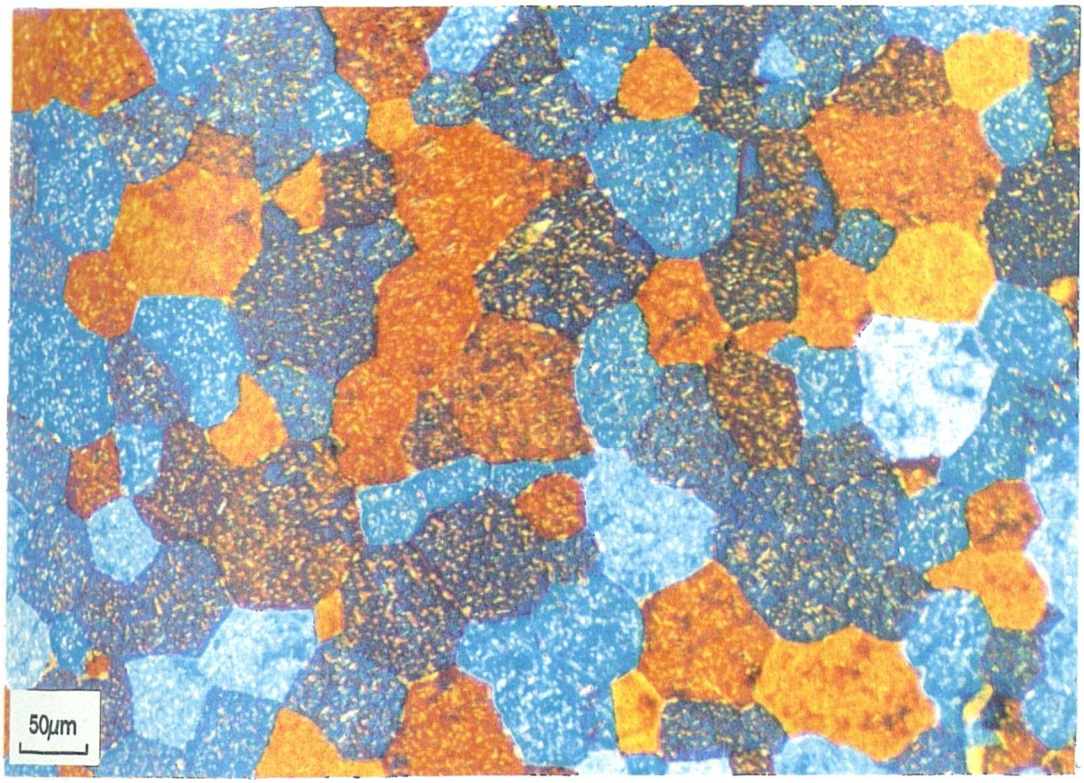

Figure 4.55 Optical micrograph of ASC material, as-supplied.

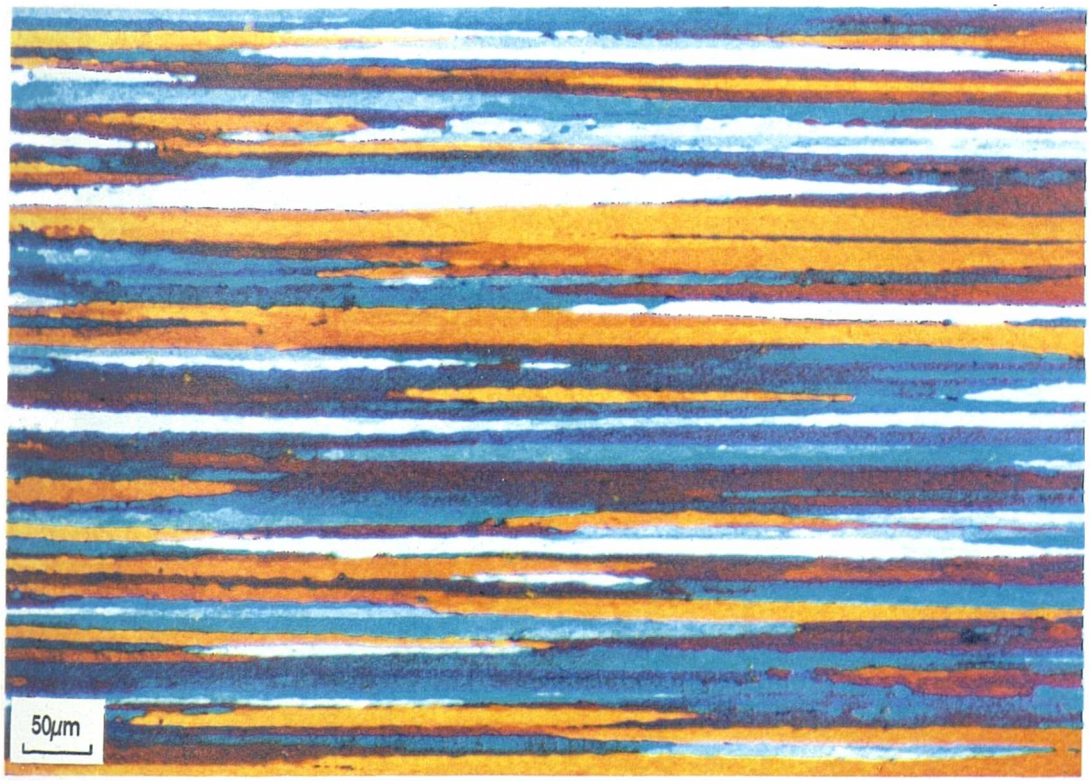

Figure 4.56 Optical micrograph of MONO material, as-supplied.

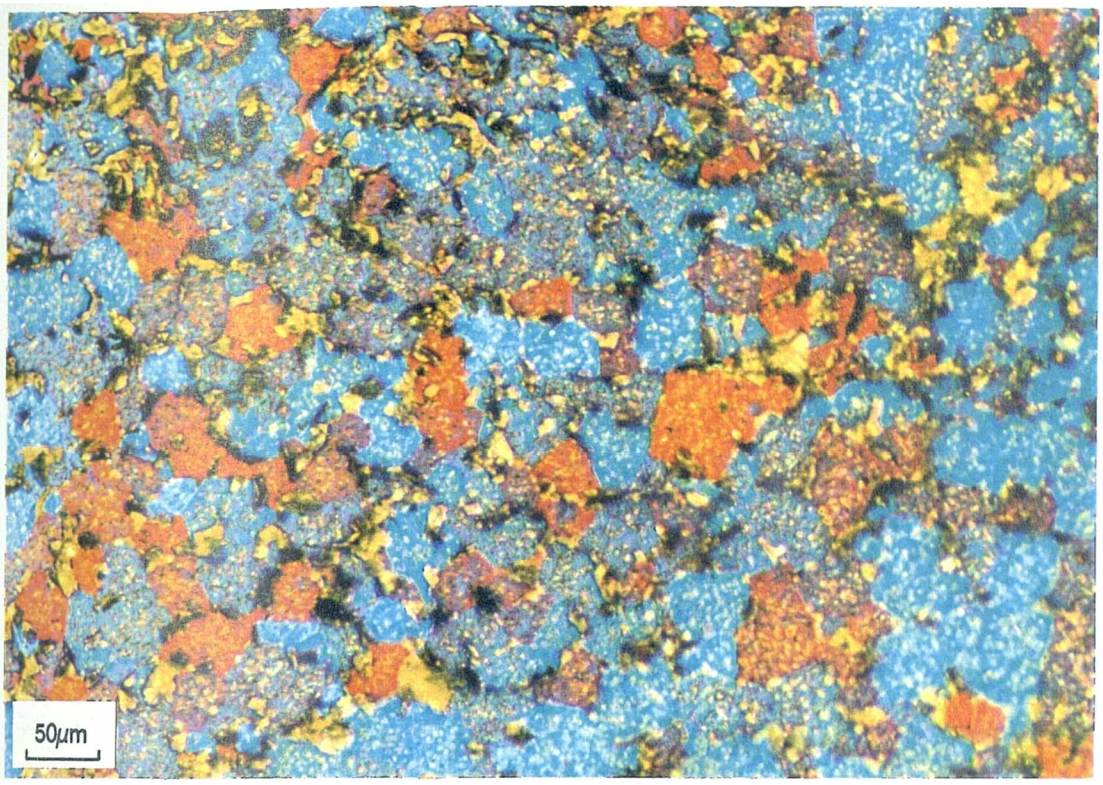

Figure 4.57 Optical micrograph of AMMP material, as-supplied.

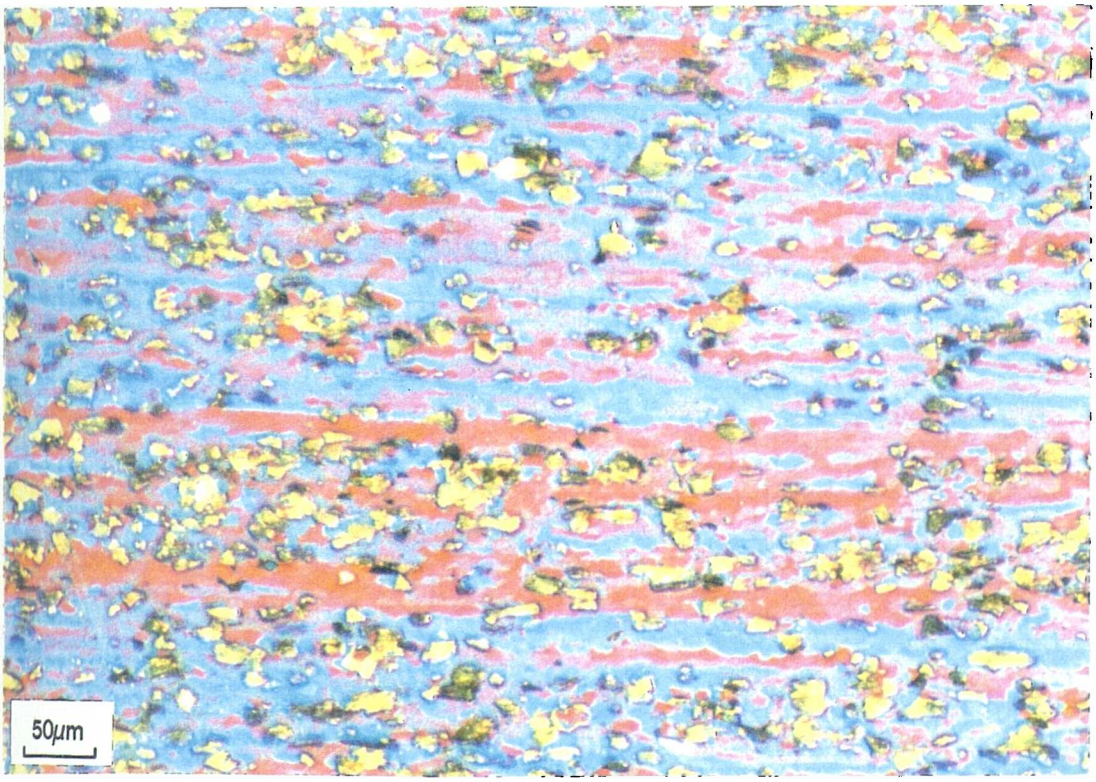

Figure 4.58 Optical micrograph of MMC material, as-supplied.

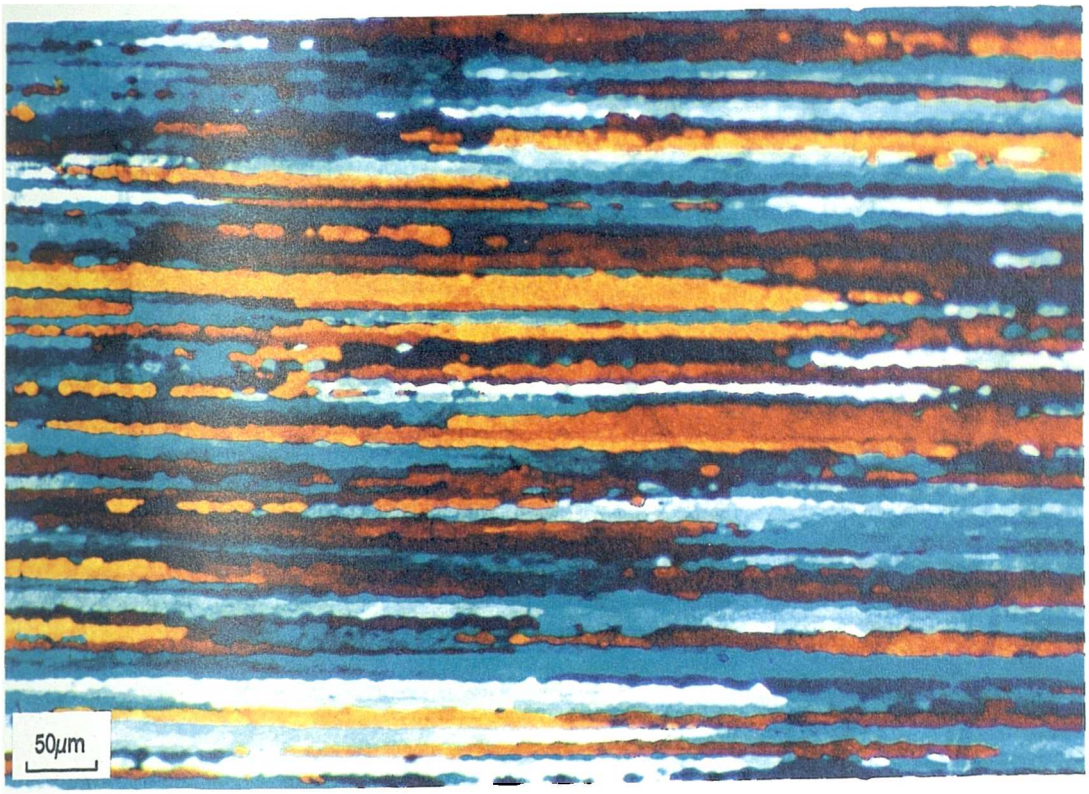

Figure 4.59 Optical micrograph of as-supplied MONO material, solution heat treated for a period equivalent to the rolling reheat

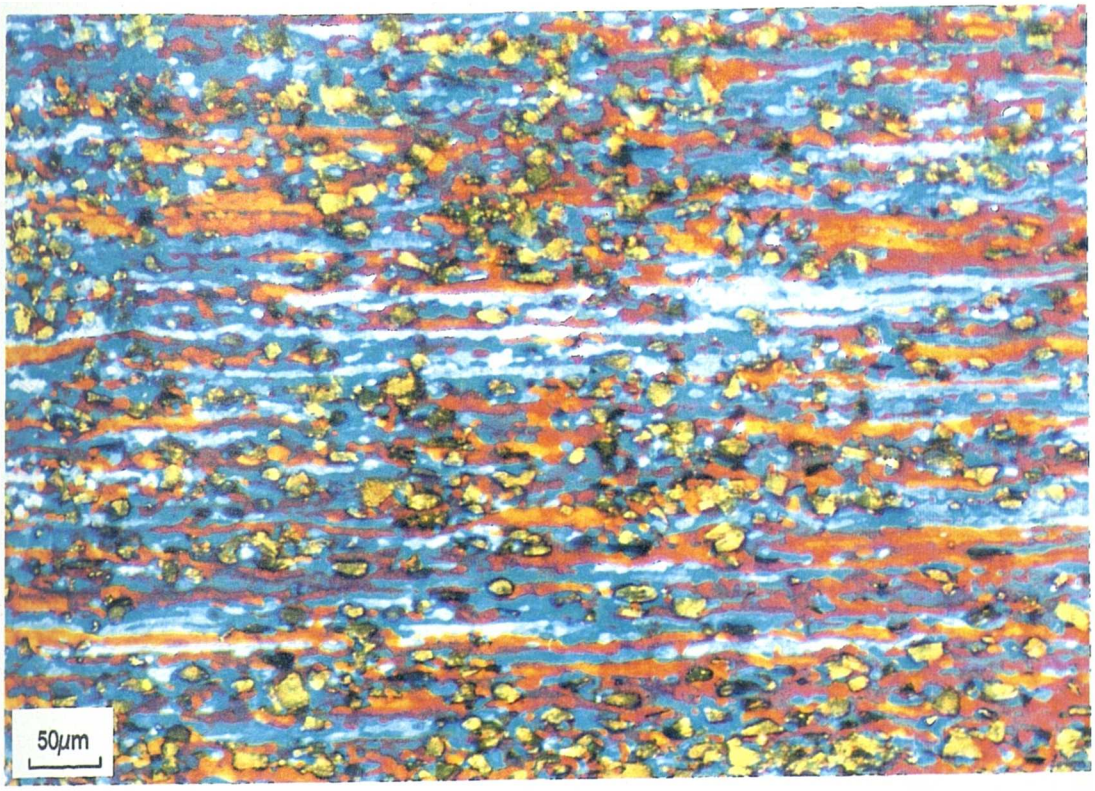

Figure 4.60 Optical micrograph of as-supplied MMC material, solution heat treated for a period equivalent to the rolling reheat.

Figure 4.61(a) Optical micrograph of ASC material, as-rolled at 480°C.

Figure 4.61(b) Optical micrograph of ASC material, rolled at 480°C and subsequently solution heat treated for 1 hour.

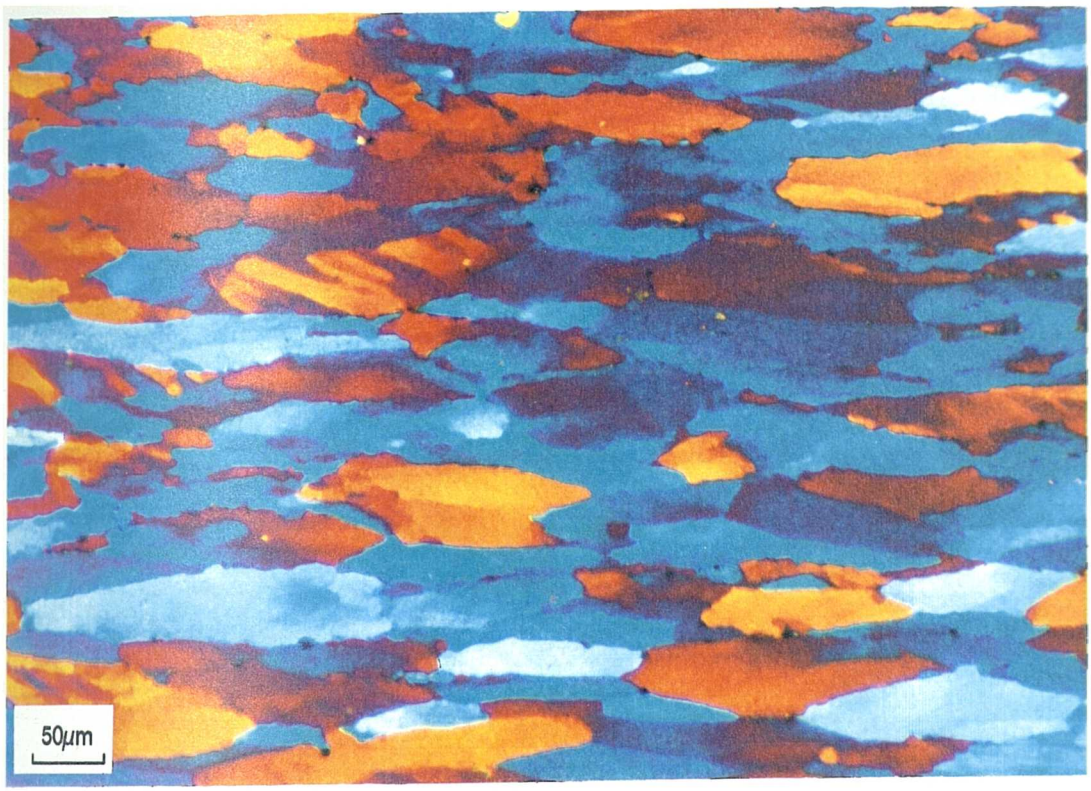

Figure 4.61(c) Optical micrograph of ASC material, rolled at 480°C and subsequently solution heat treated for 24 hours.

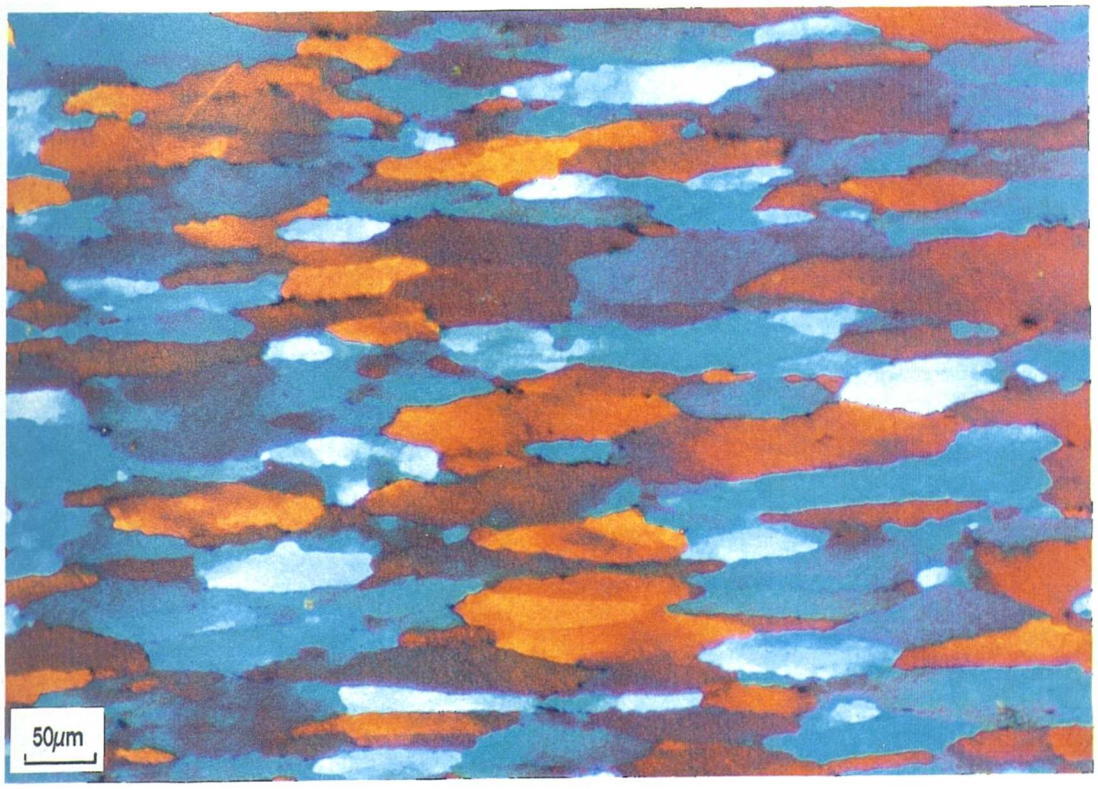

Figure 4.61(d) Optical micrograph of ASC material, rolled at 480°C and subsequently solution heat treated for 48 hours.

Figure 4.61(e) Optical micrograph of ASC material, rolled at 480°C and subsequently solution heat treated for 7 days.

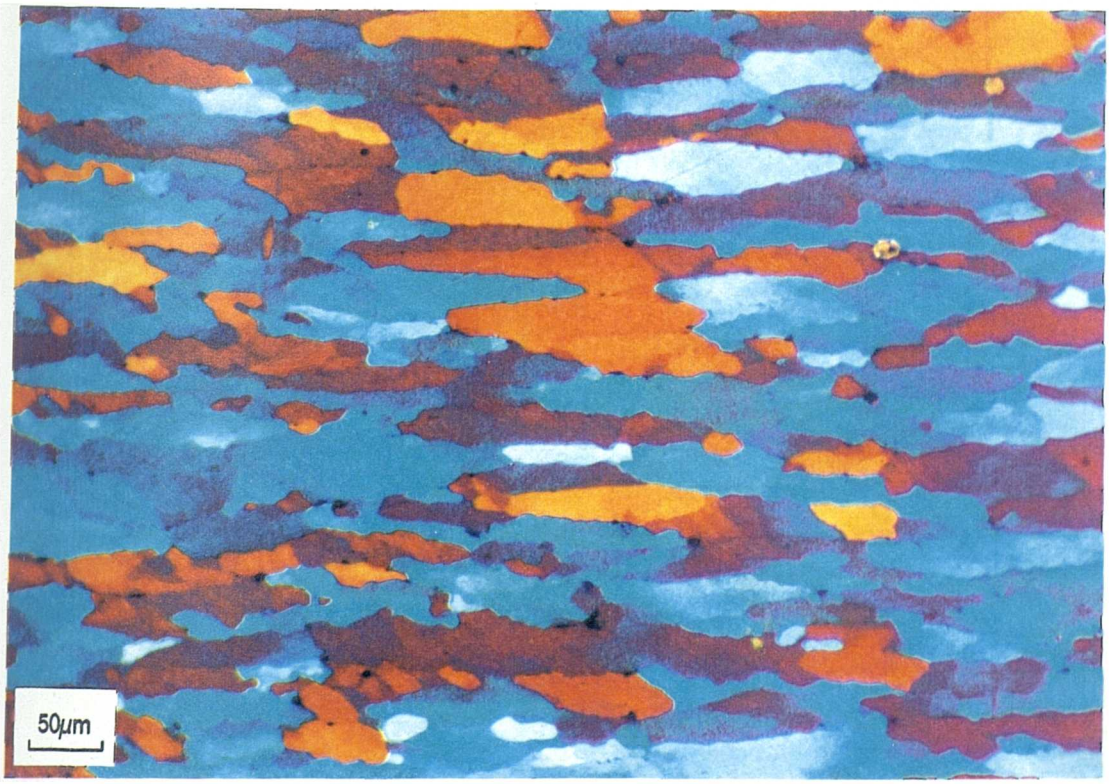

Figure 4.61(f) Optical micrograph of ASC material, rolled at 480°C and subsequently solution heat treated for 14 days.

Figure 4.62(a) Optical micrograph of ASC material, as-rolled at 400°C.

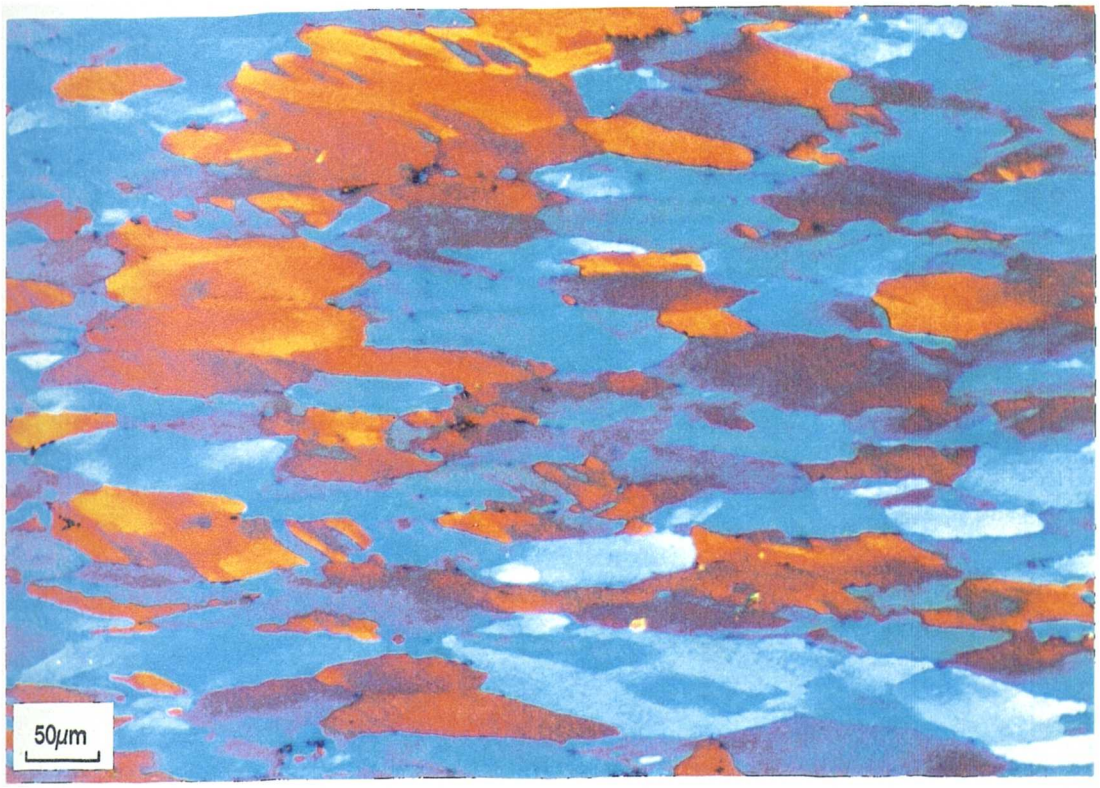

Figure 4.62 (b) Optical micrograph of ASC material, rolled at 400°C and subsequently solution heat treated for 1 hour.

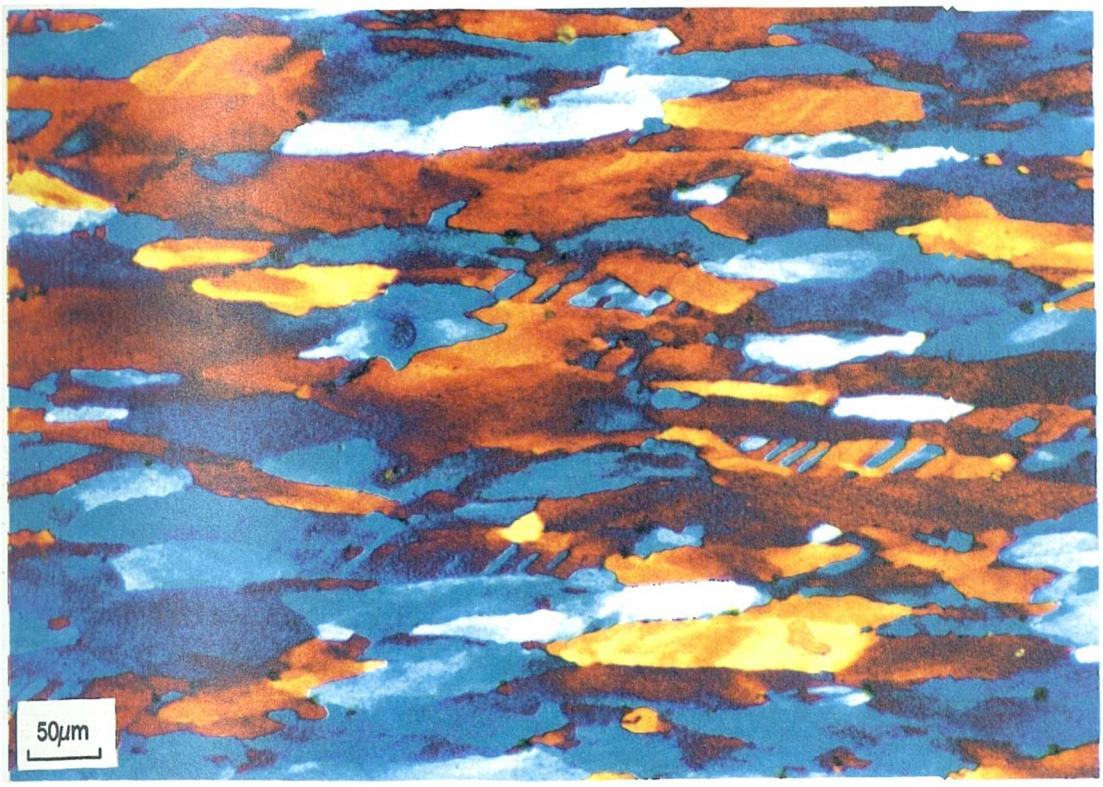

Figure 4.62(c) Optical micrograph of ASC material, rolled at 400°C and subsequently solution heat treated for 24 hours.

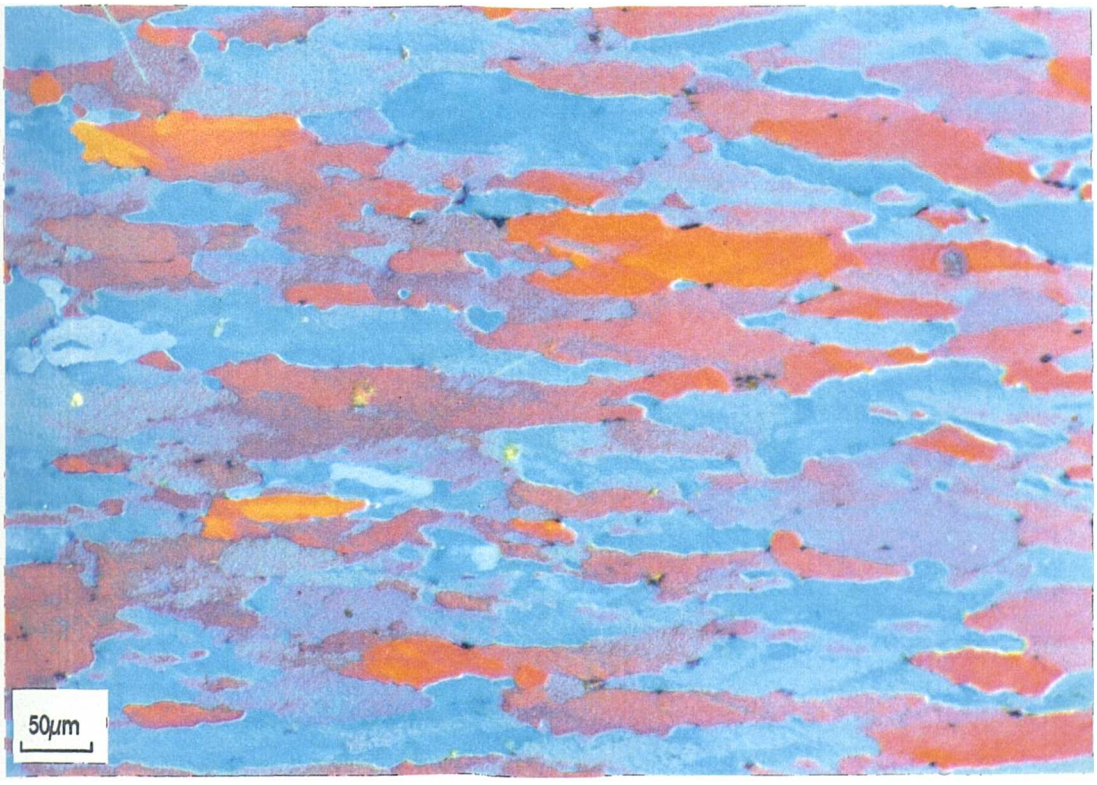

Figure 4.62 (d) Optical micrograph of ASC material, rolled at 400°C and subsequently solution heat treated for 48 hours.

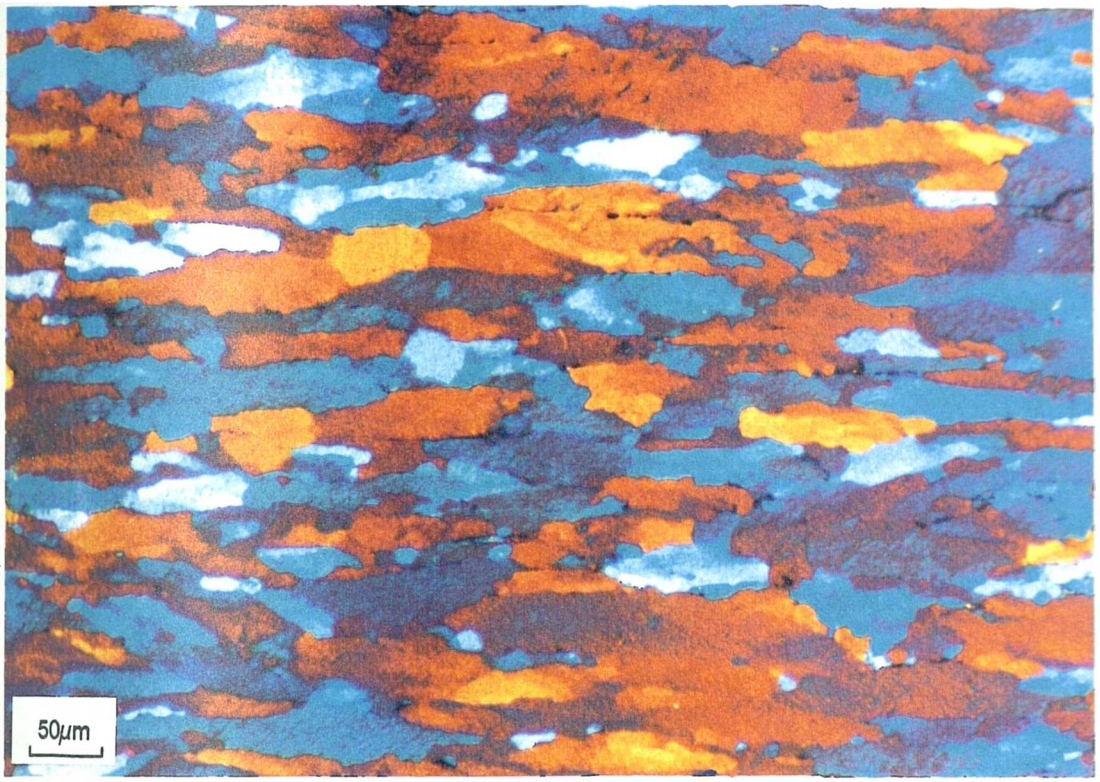

Figure 4.62(e) Optical micrograph of ASC material, rolled at 400°C and subsequently solution heat treated for 7 days.

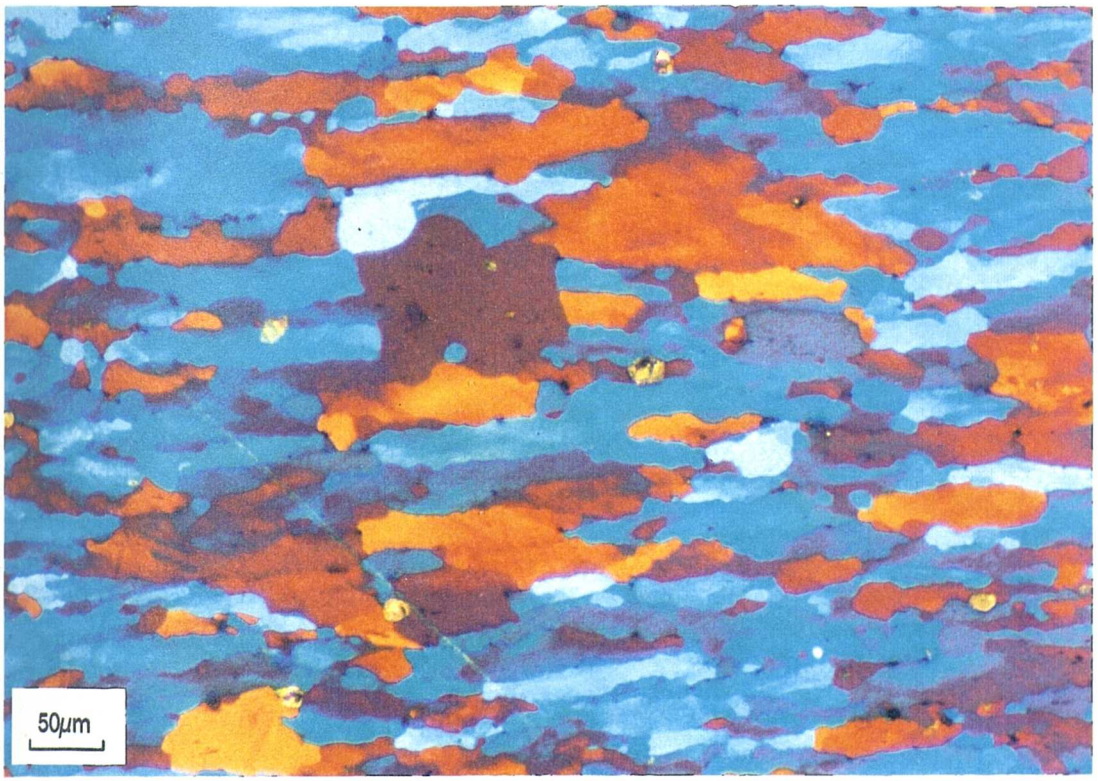

Figure 4.62 (f) Optical micrograph of ASC material, rolled at 400°C and subsequently solution heat treated for 14 days.

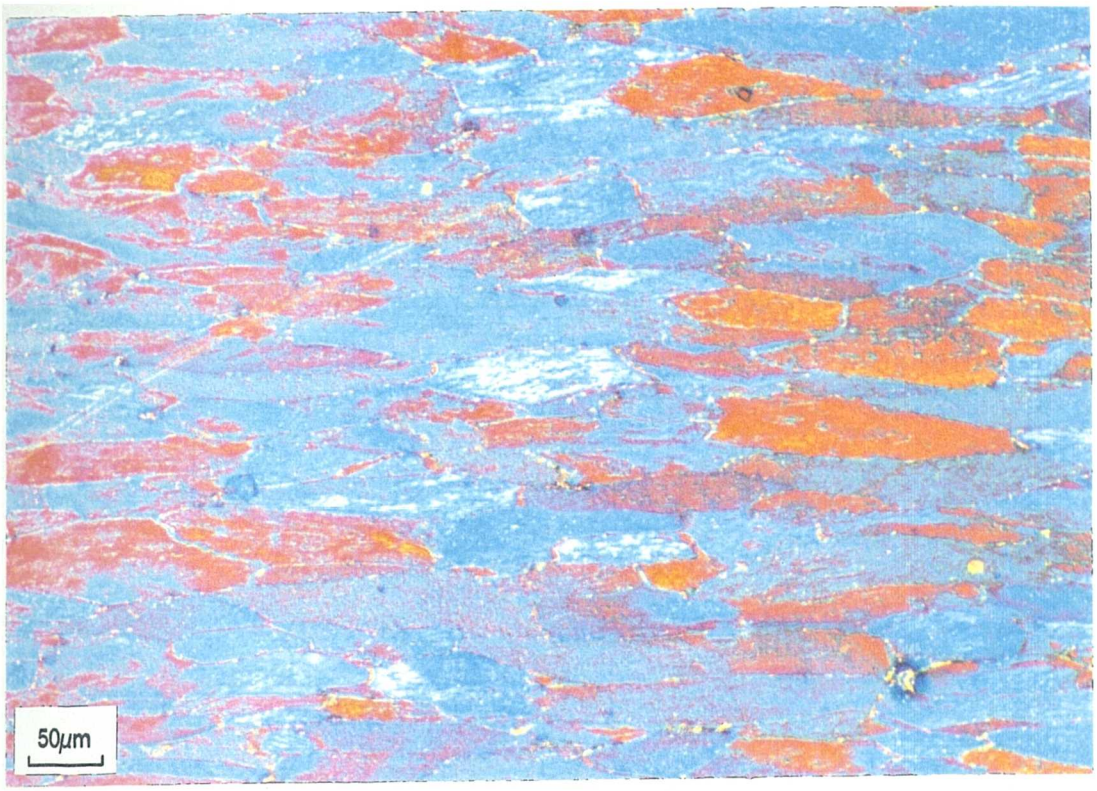

Figure 4.63(a) Optical micrograph of ASC material, as- rolled at 300°C.

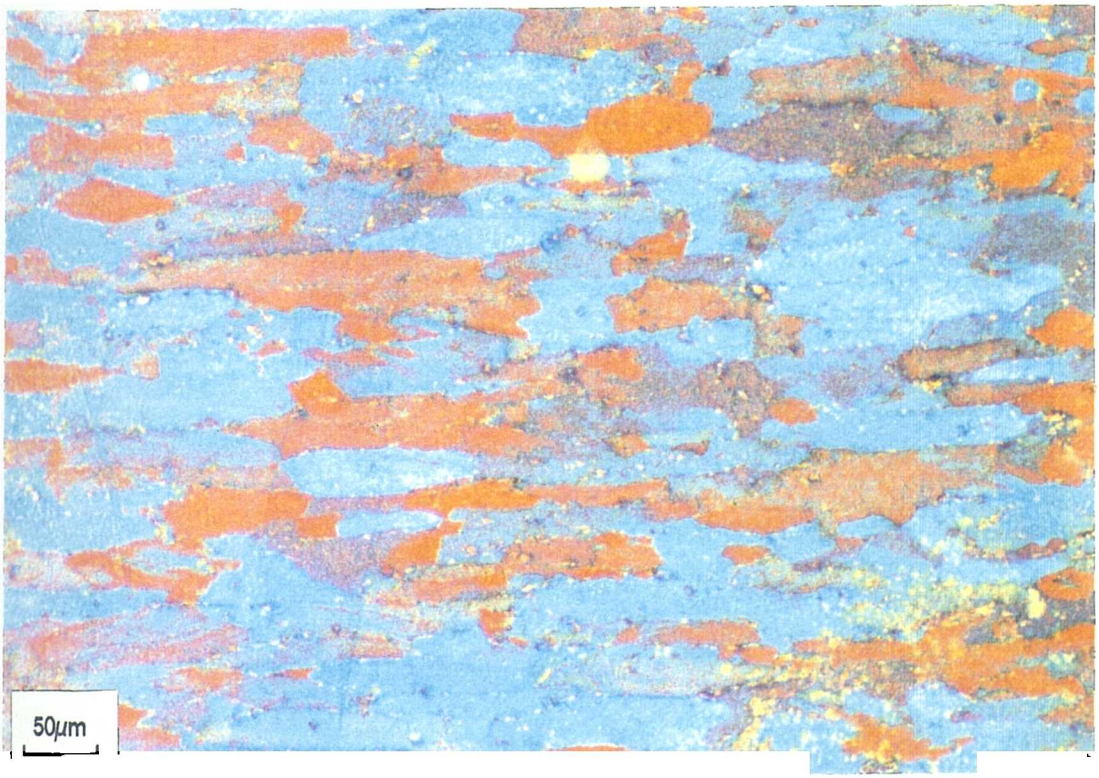

Figure 4.63(b) Optical micrograph of ASC material, rolled at 300°C and subsequently solution heat treated for 5 minutes.

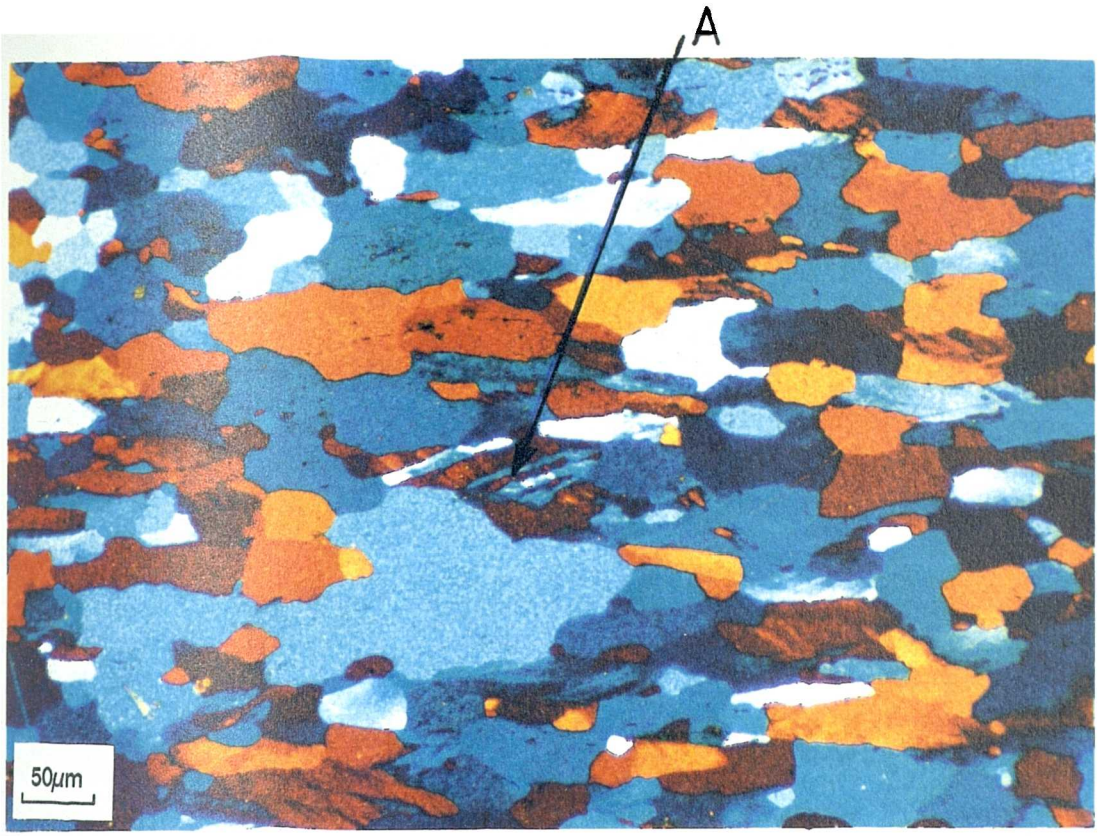

Figure 4.63(c) Optical micrograph of ASC material, rolled at 300°C and subsequently solution heat treated for 10 minutes. Note the new grains forming at "A".

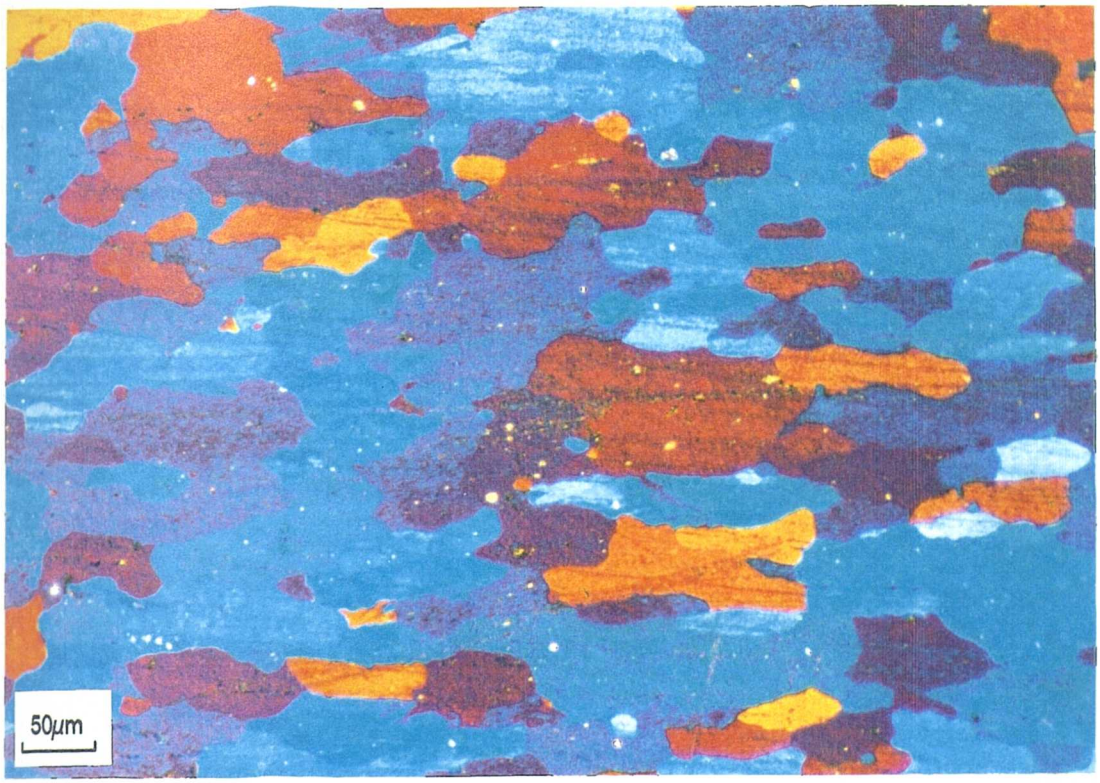

Figure 4.63(d) Optical micrograph of ASC material, rolled at 300°C and subsequently solution heat treated for 20 minutes.

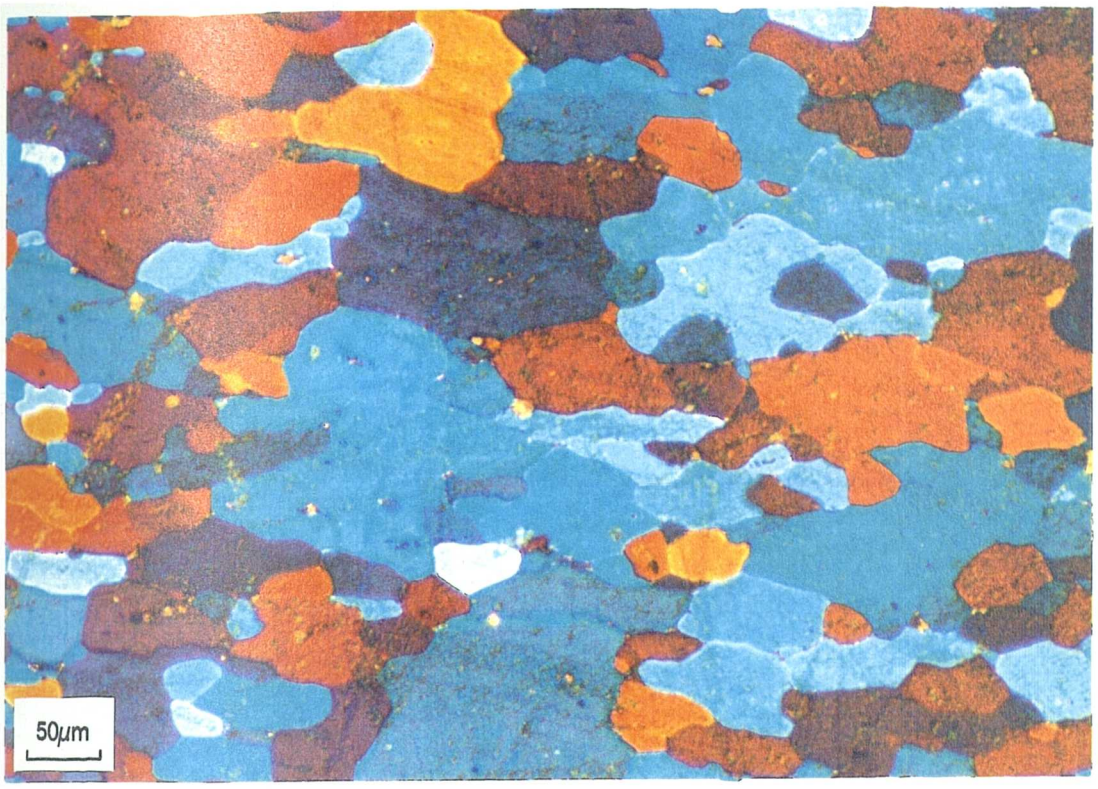

Figure 4.63(e) Optical micrograph of ASC material, rolled at 300°C and subsequently solution heat treated for 30 minutes.

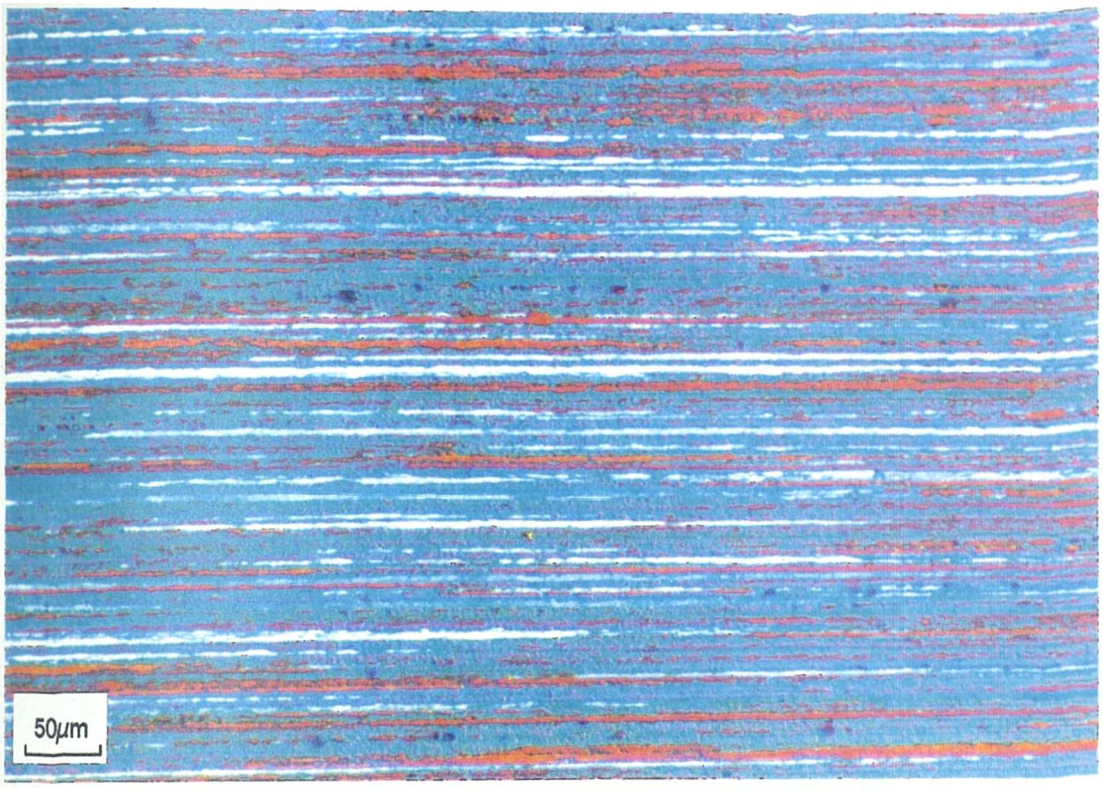

Figure 4.64(a) Optical micrograph of MONO material, as-rolled at 480°C.

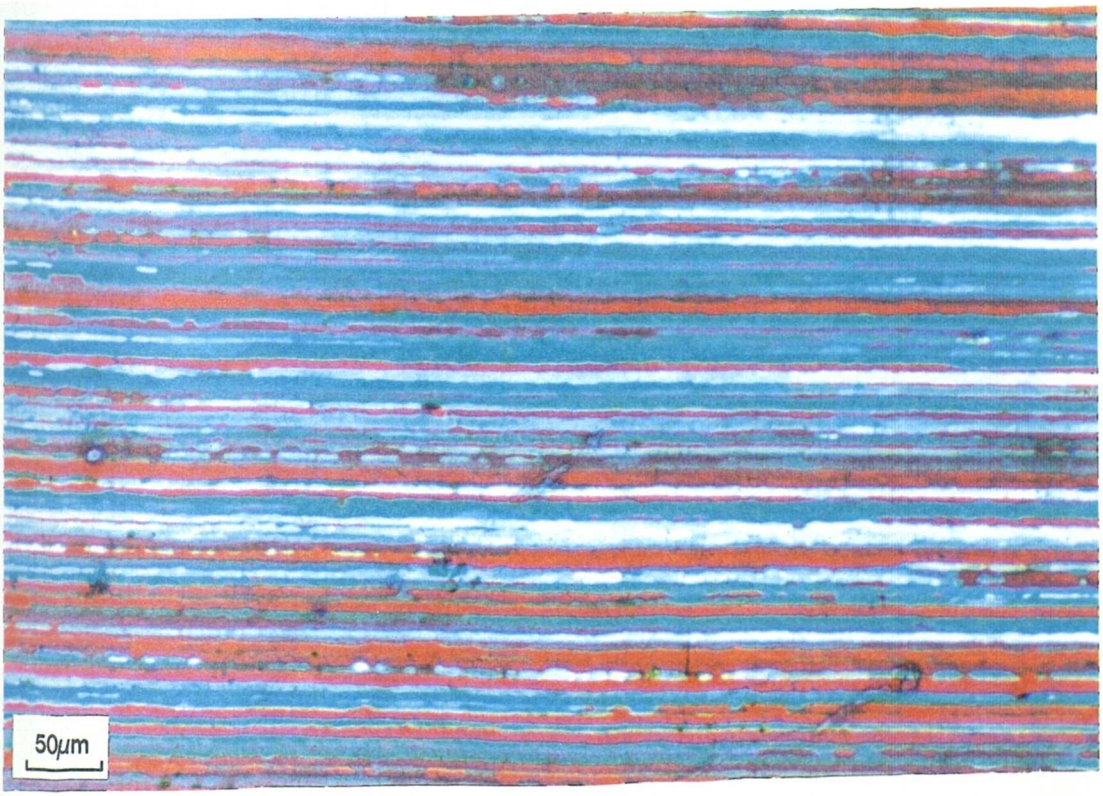

Figure 4.64(b) Optical micrograph of MONO material, rolled at 480°C and subsequently solution heat treated for 1 hour.

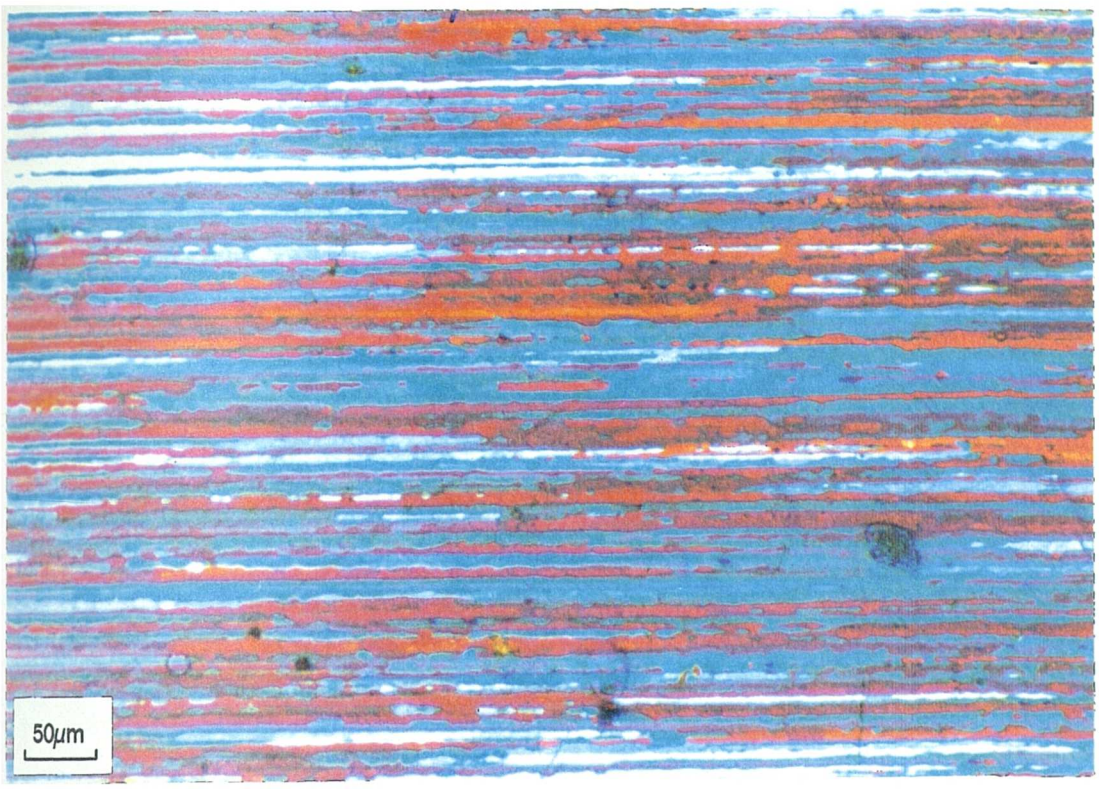

Figure 4.64(c) Optical micrograph of MONO material, rolled at 480°C and subsequently solution heat treated for 4 hours.

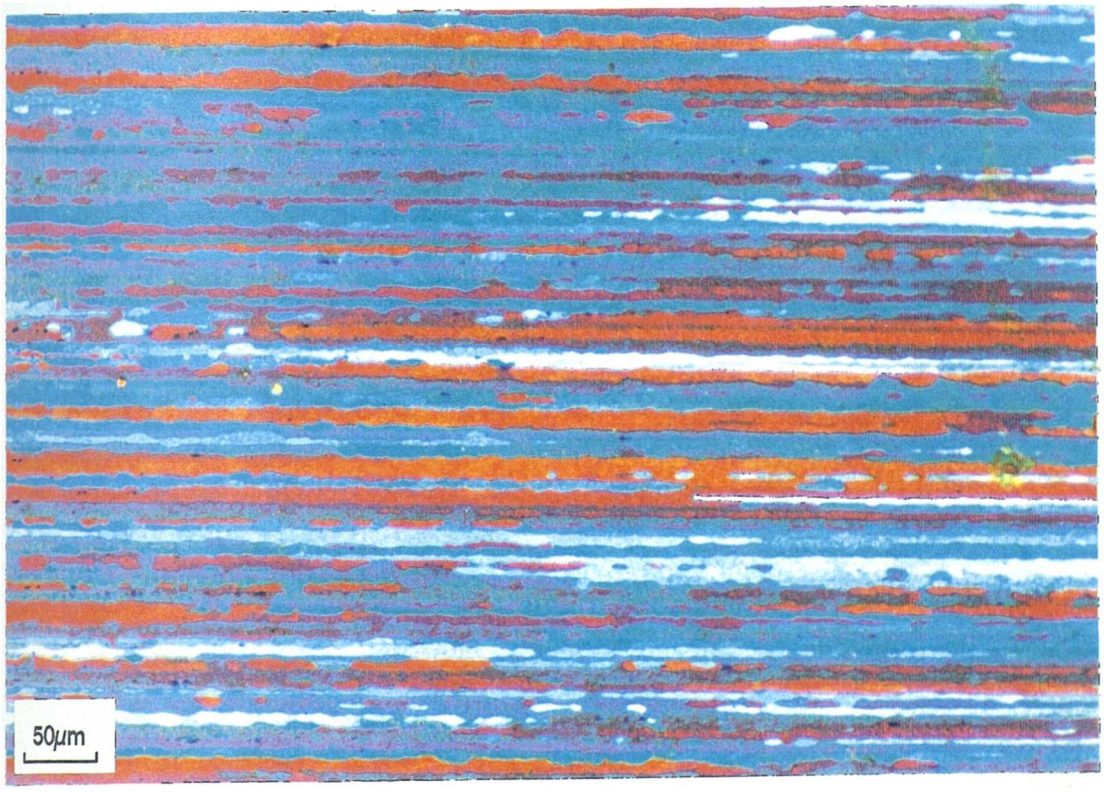

Figure 4.64(d) Optical micrograph of MONO material, rolled at 480°C and subsequently solution heat treated for 48 hours.

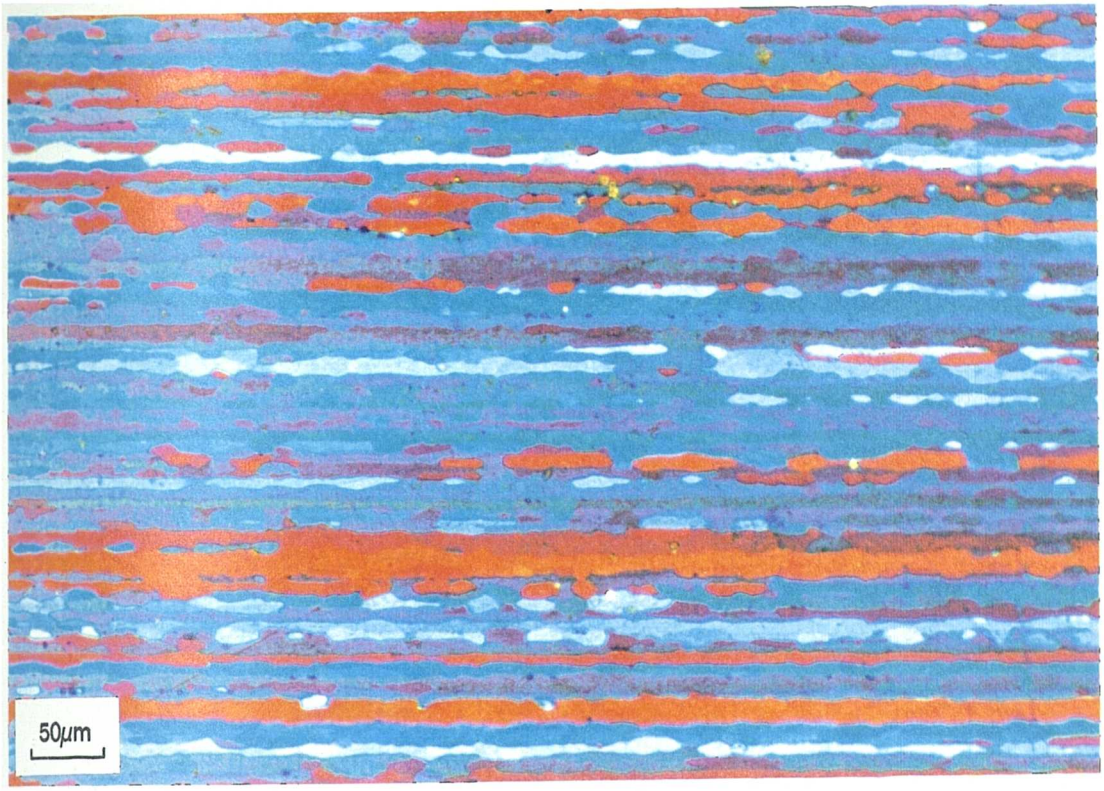

Figure 4.64(e) Optical micrograph of MONO material, rolled at 480°C and subsequently solution heat treated for 14 days.

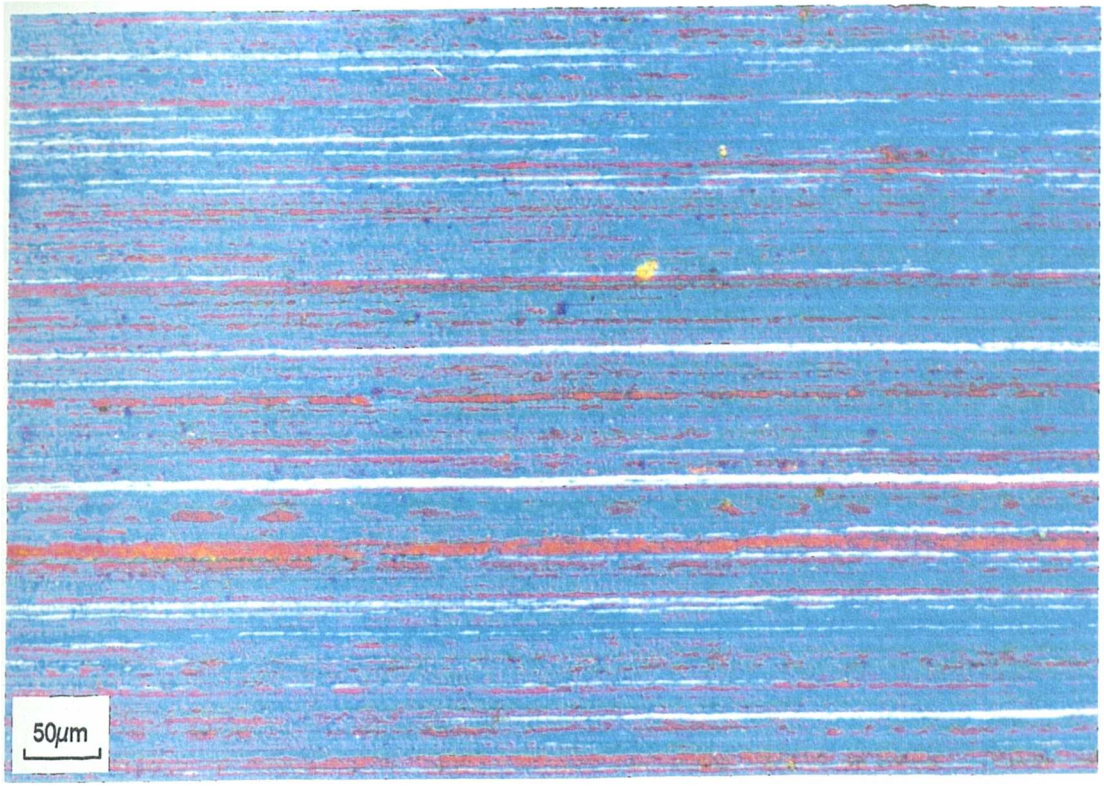

Figure 4.65(a) Optical micrograph of MONO material, as-rolled at 400°C.

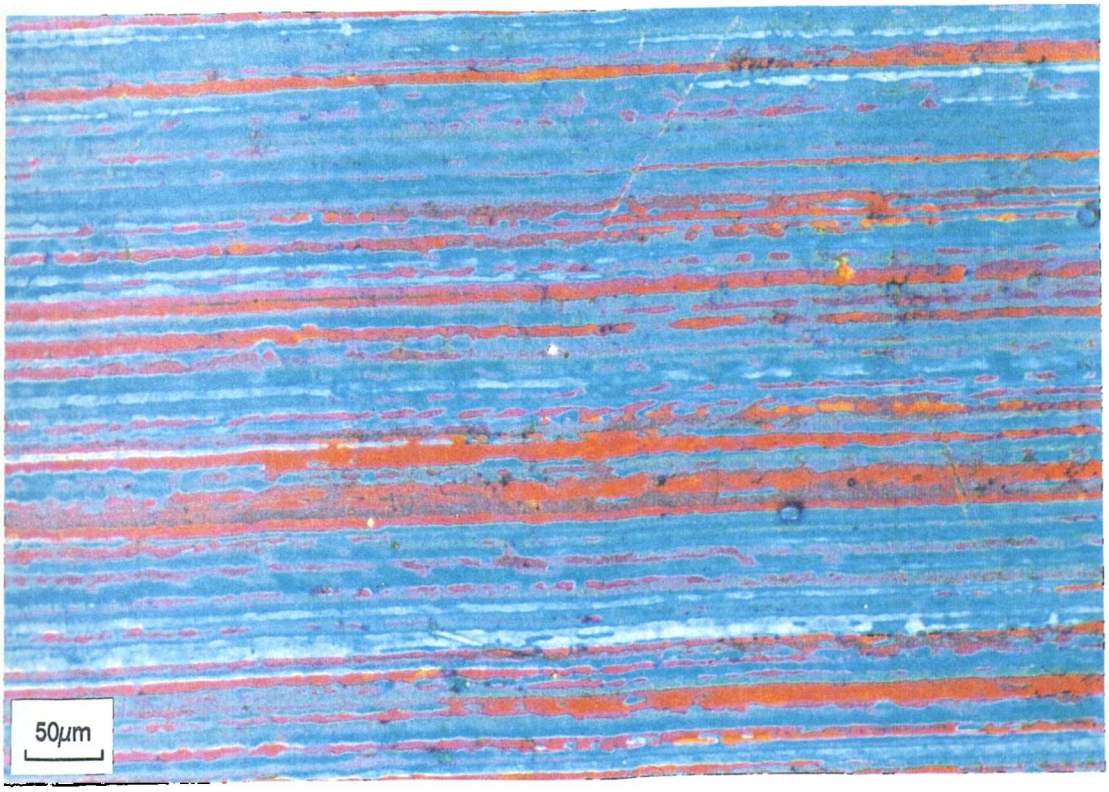

Figure 4.65(b) Optical micrograph of MONO material, rolled at 400°C and subsequently solution heat treated for 1hour.

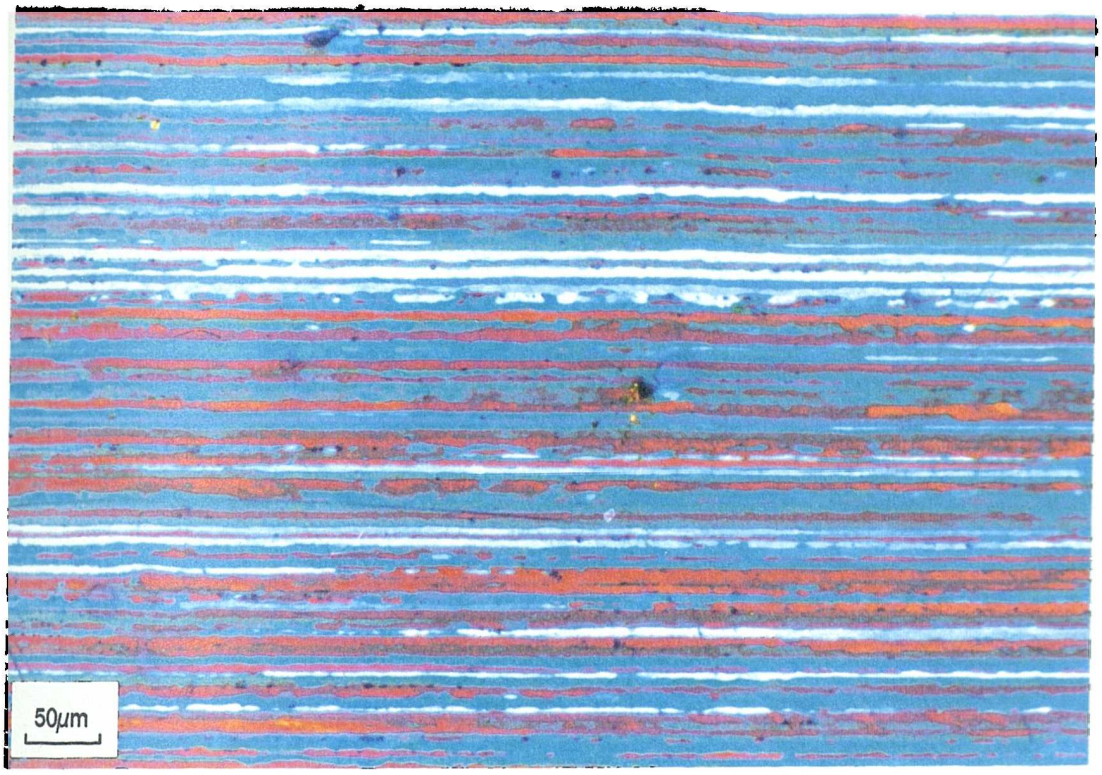

Figure 4.65(c) Optical micrograph of MONO material, rolled at 400°C and subsequently solution heat treated for 4 hours.

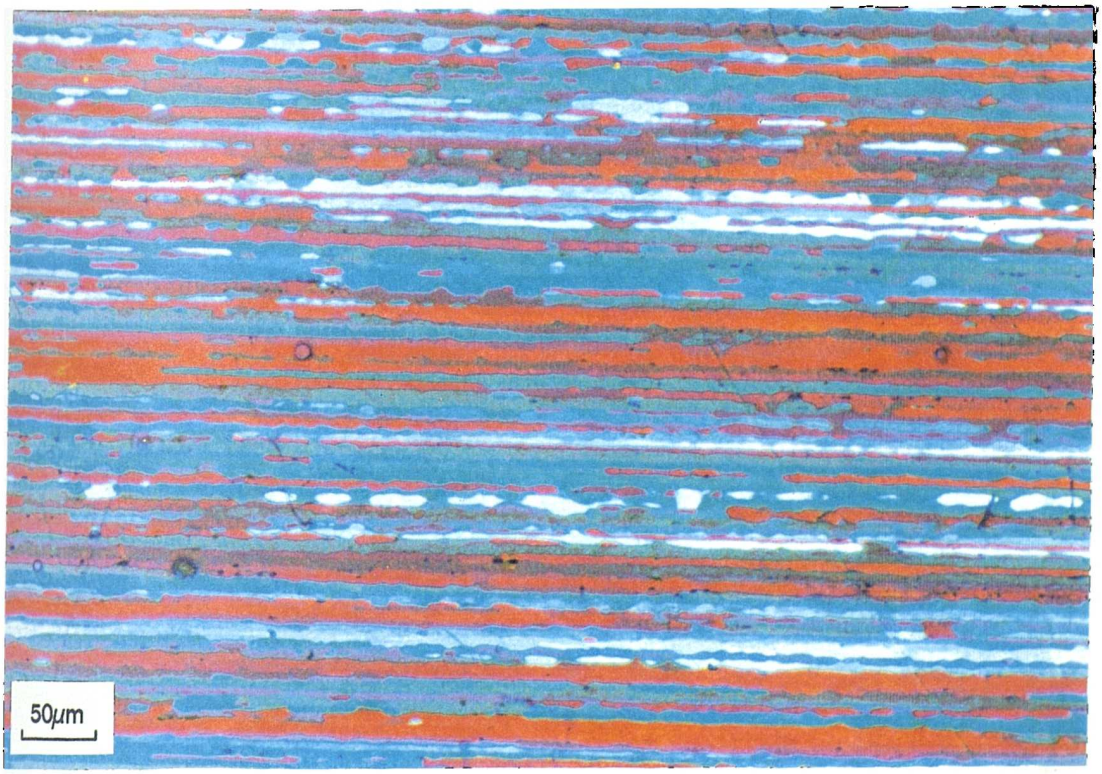

Figure 4.65(d) Optical micrograph of MONO material, rolled at 400°C and subsequently solution heat treated for 48 hours.

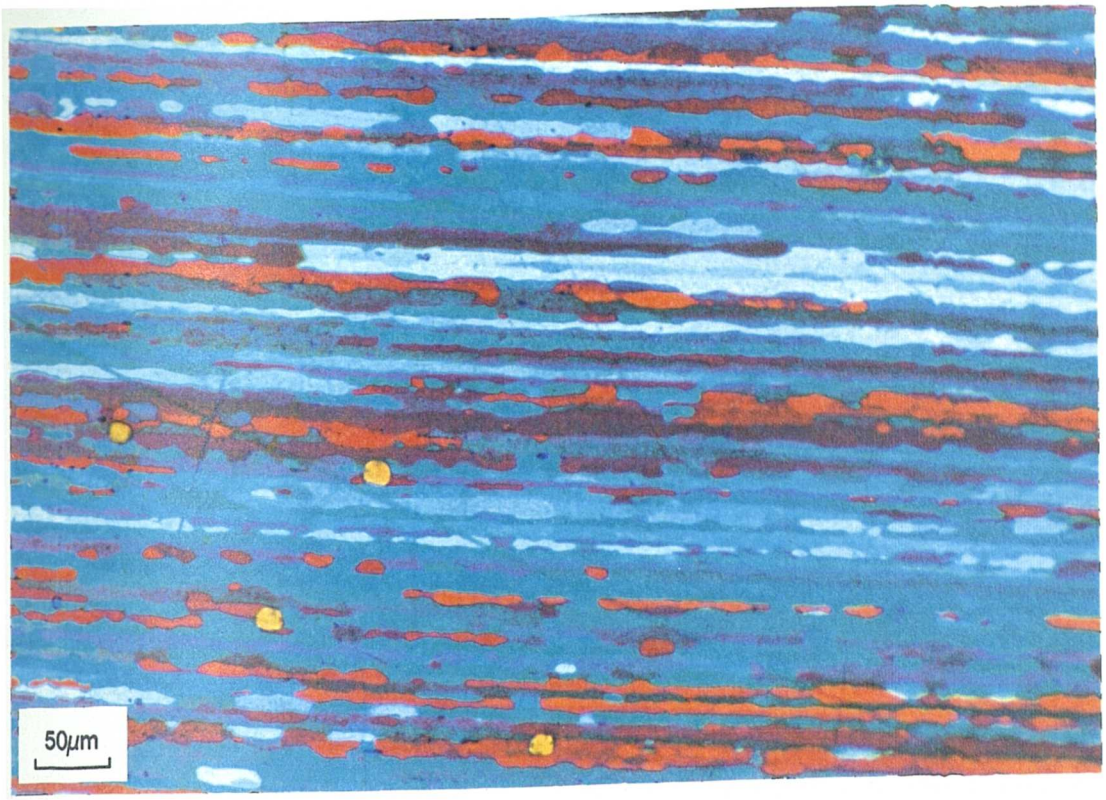

Figure 4.65(e) Optical micrograph of MONO material, rolled at 400°C and subsequently solution heat treated for 14 days.

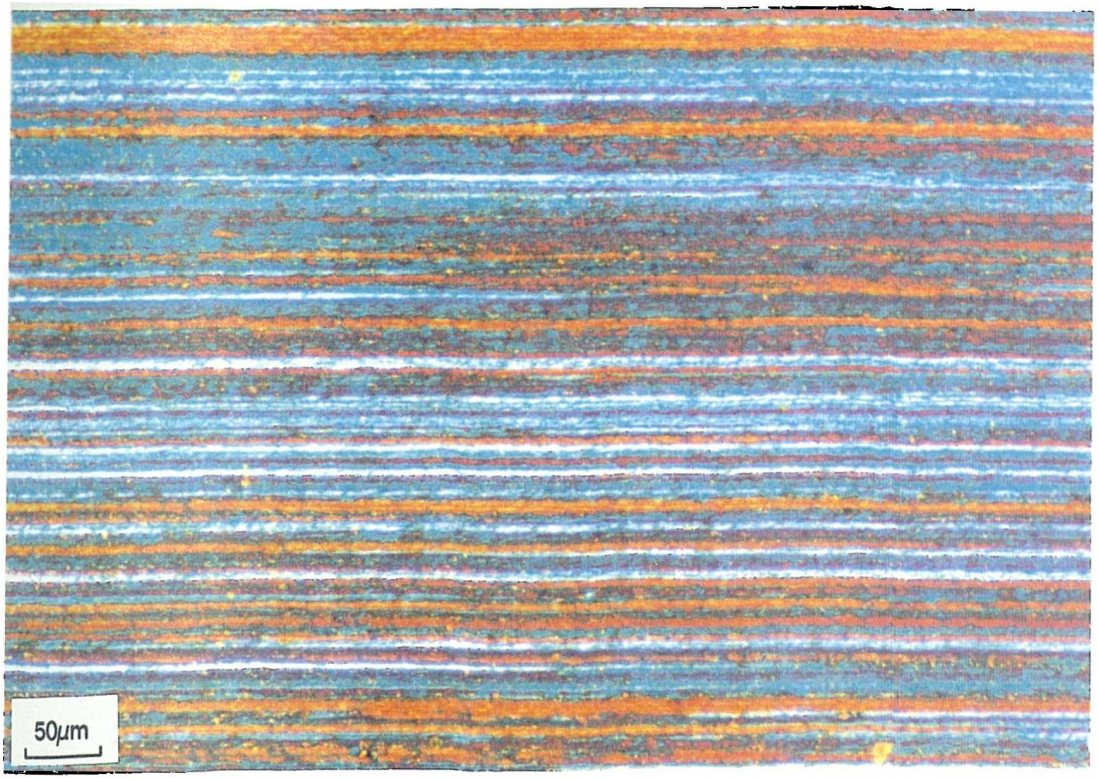

Figure 4.66(a) Optical micrograph of MONO material, as-rolled at 300°C.

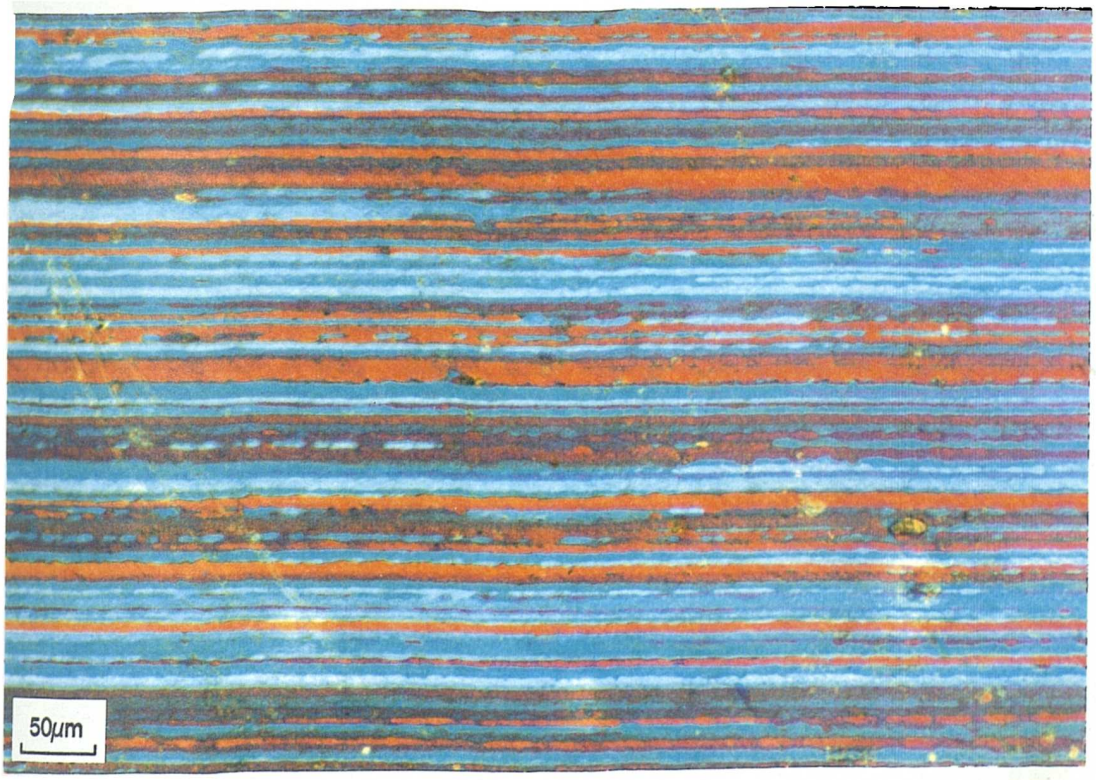

Figure 4.66(b) Optical micrograph of MONO material, rolled at 300°C and subsequently solution heat treated for 1 hour.

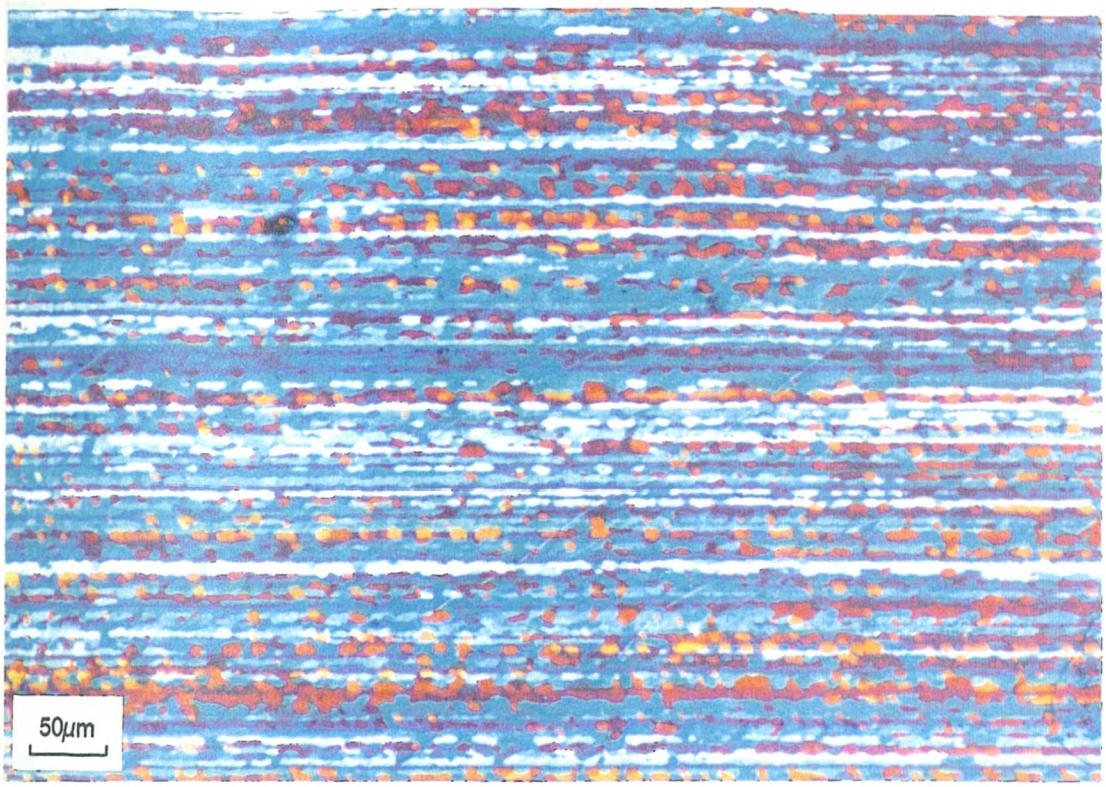

Figure 4.66(c) Optical micrograph of MONO material, rolled at 300°C and subsequently solution heat treated for 4 hours.

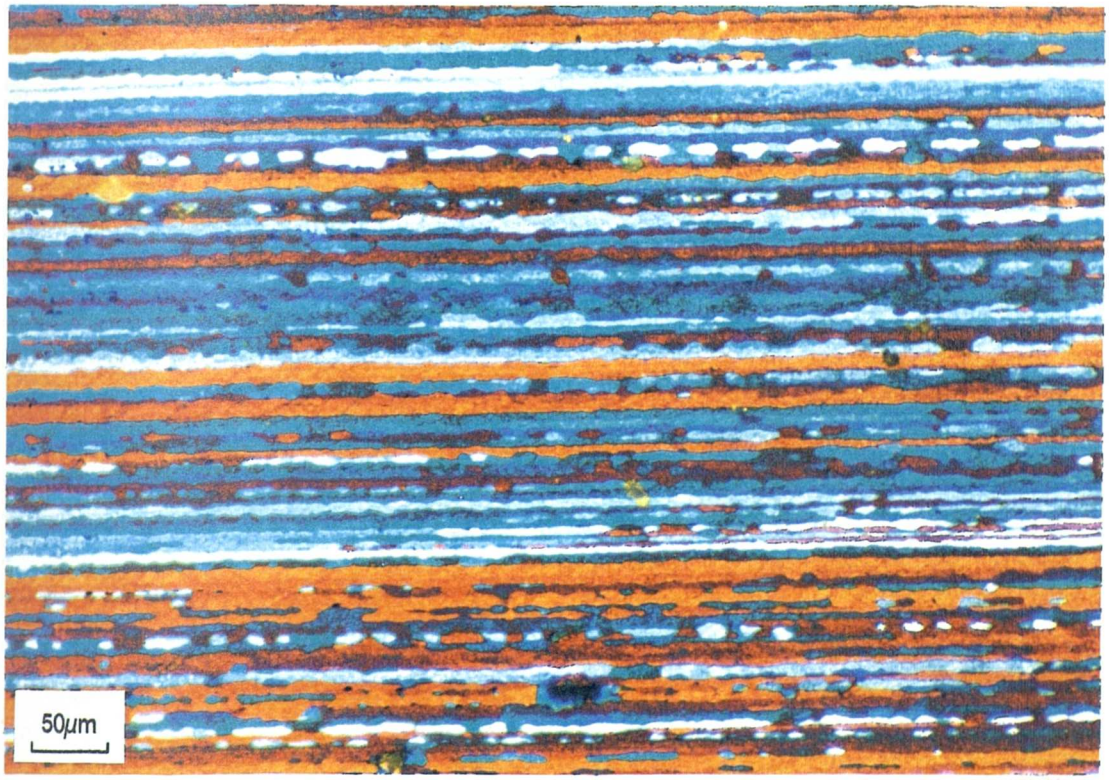

Figure 4.66(d) Optical micrograph of MONO material, rolled at 300°C and subsequently solution heat treated for 48 hours.

Figure 4.66(e) Optical micrograph of MONO material, rolled at 300°C and subsequently solution heat treated for 14 days.

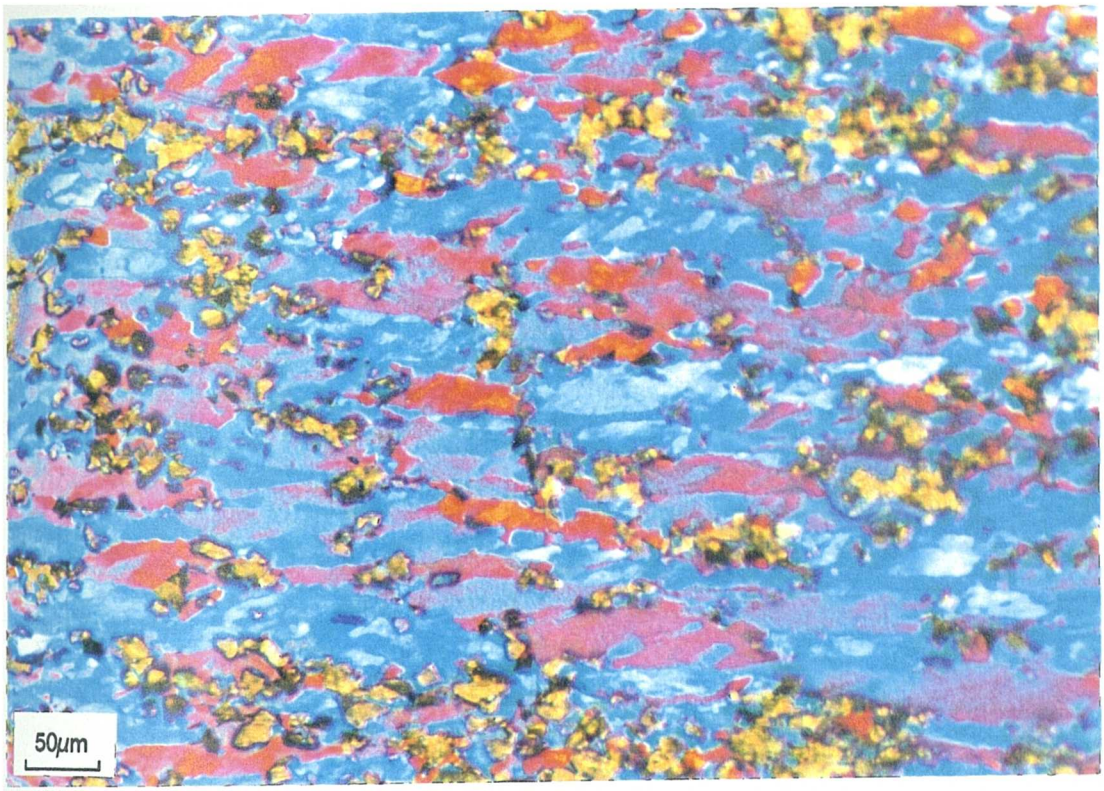

Figure 4.67(a) Optical micrograph of AMMP material, as-rolled at 480°C.

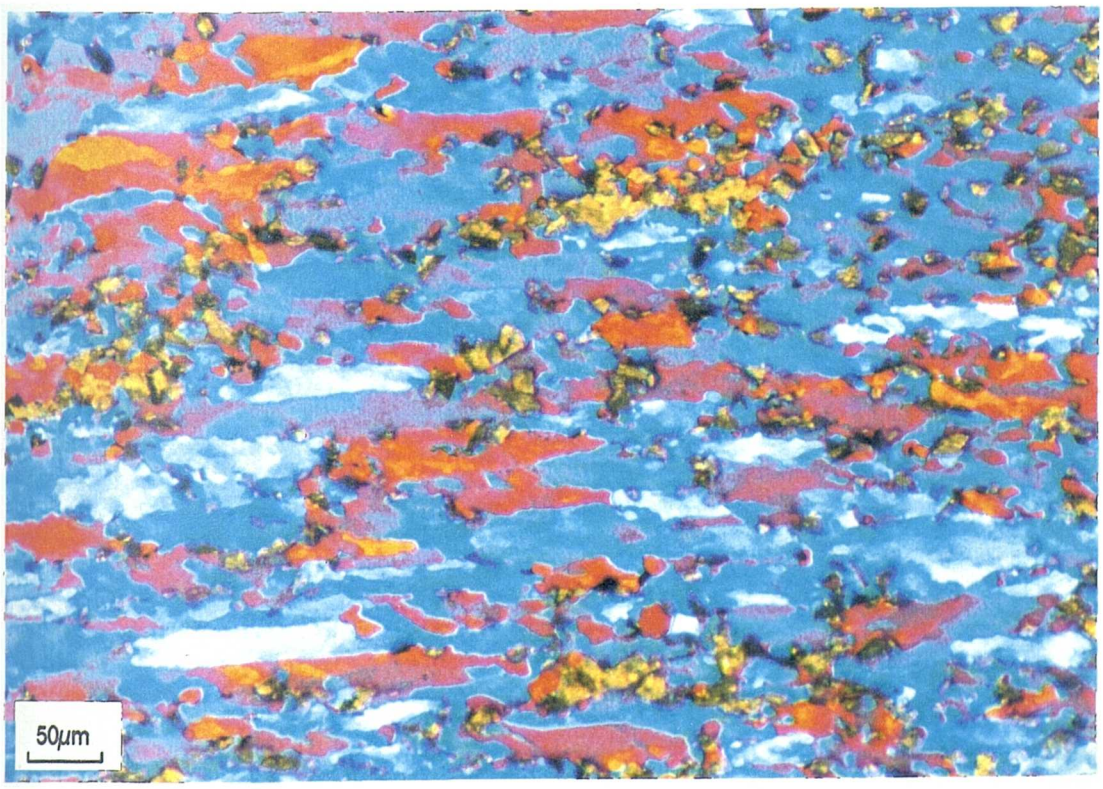

Figure 4.67(b) Optical micrograph of AMMP material, rolled at 480°C and subsequently solution heat treated for 4 hours.

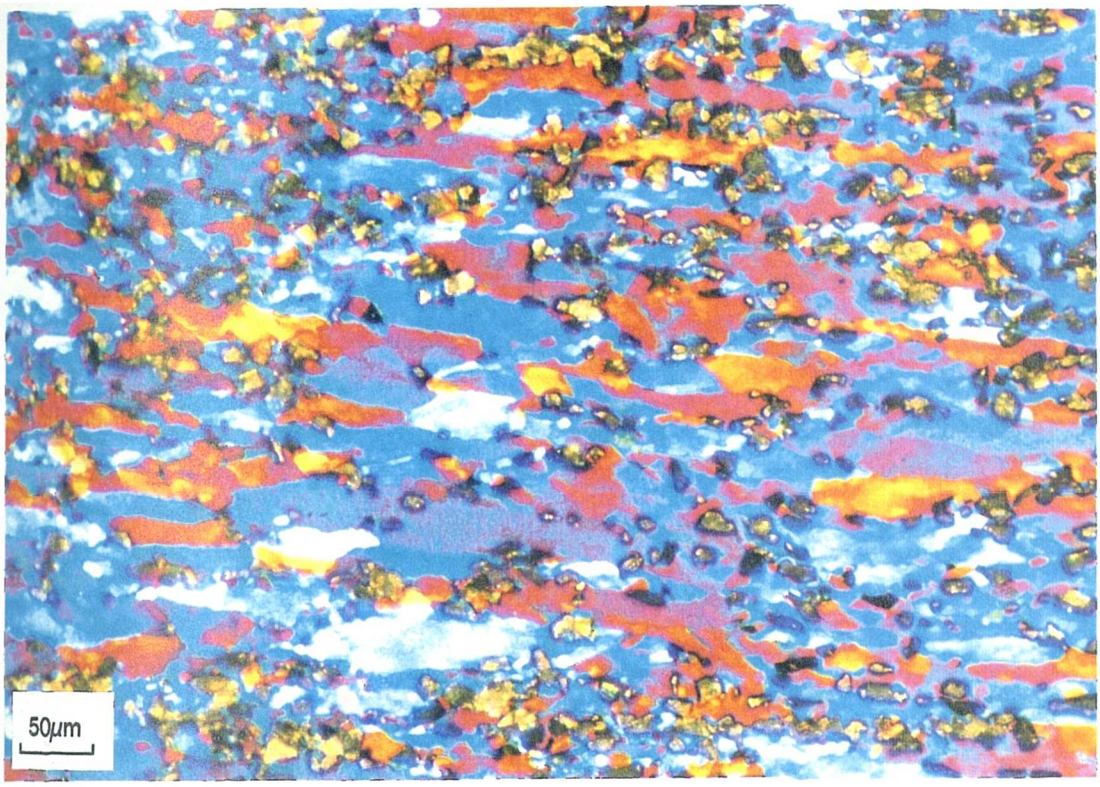

Figure 4.67(c) Optical micrograph of AMMP material, rolled at 480°C and subsequently solution heat treated for 7 hours.

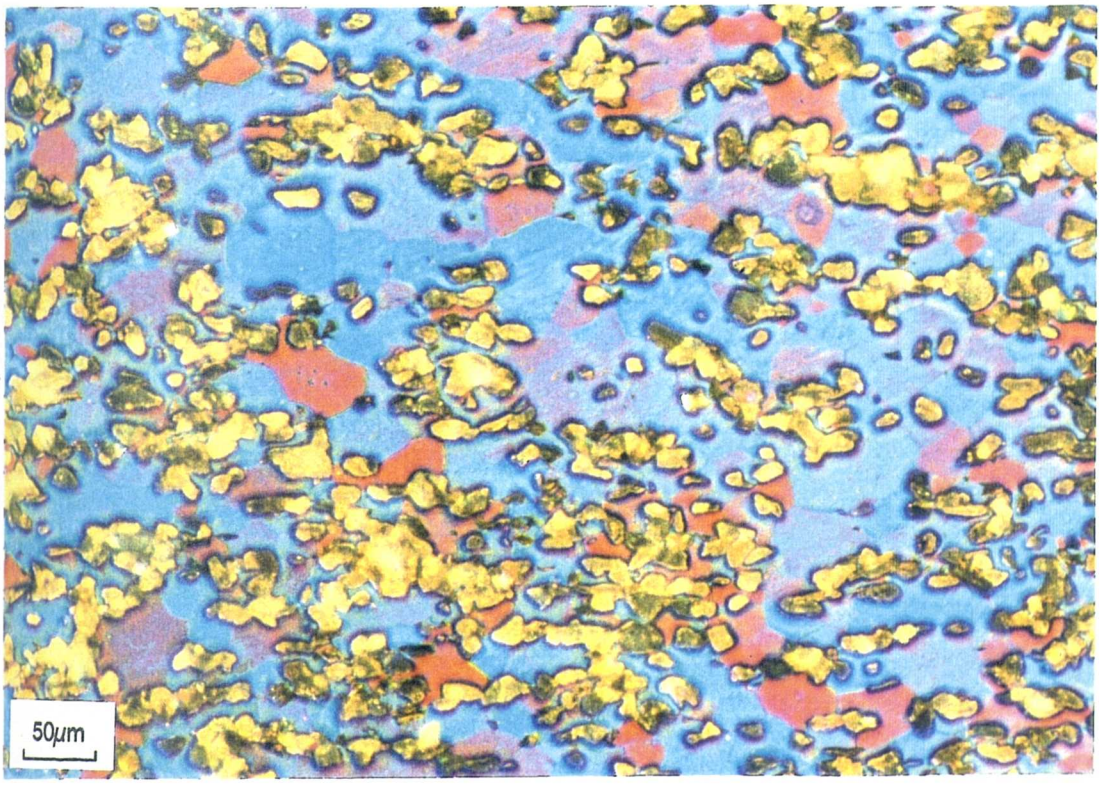

Figure 4.67(d) Optical micrograph of AMMP material, rolled at 480°C and subsequently solution heat treated for 8 hours.

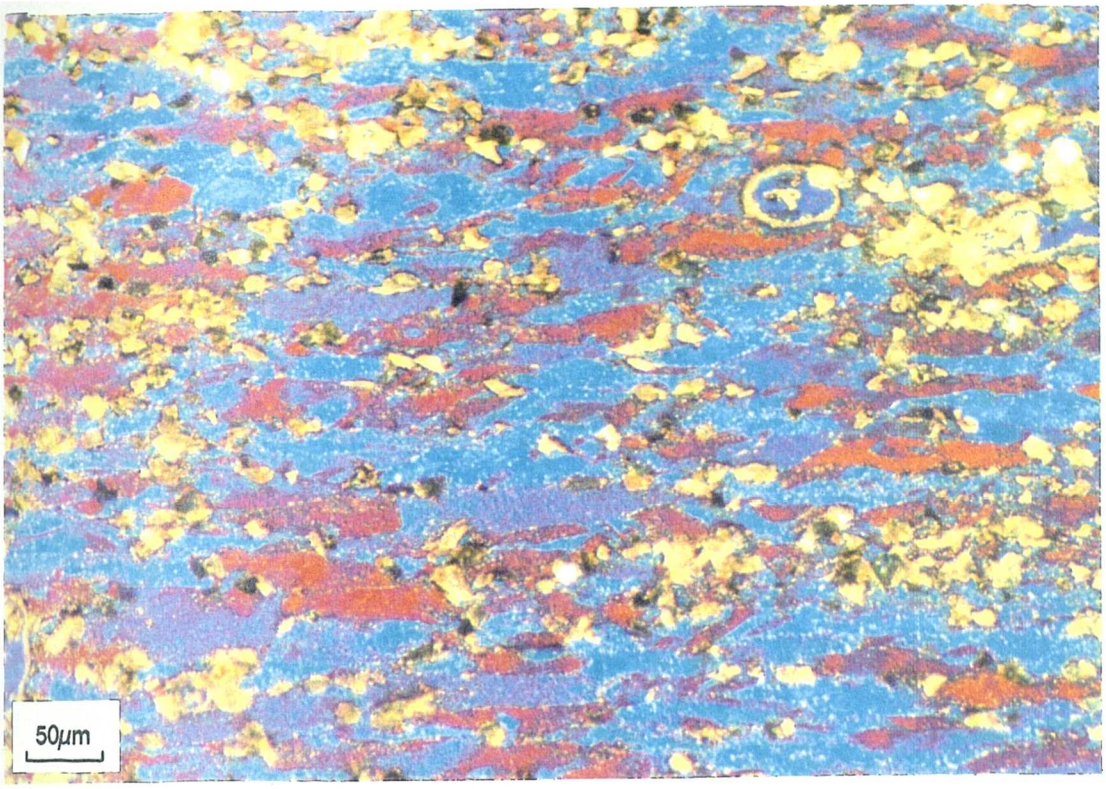

Figure 4.68(a) Optical micrograph of AMMP material, as-rolled at 400°C.

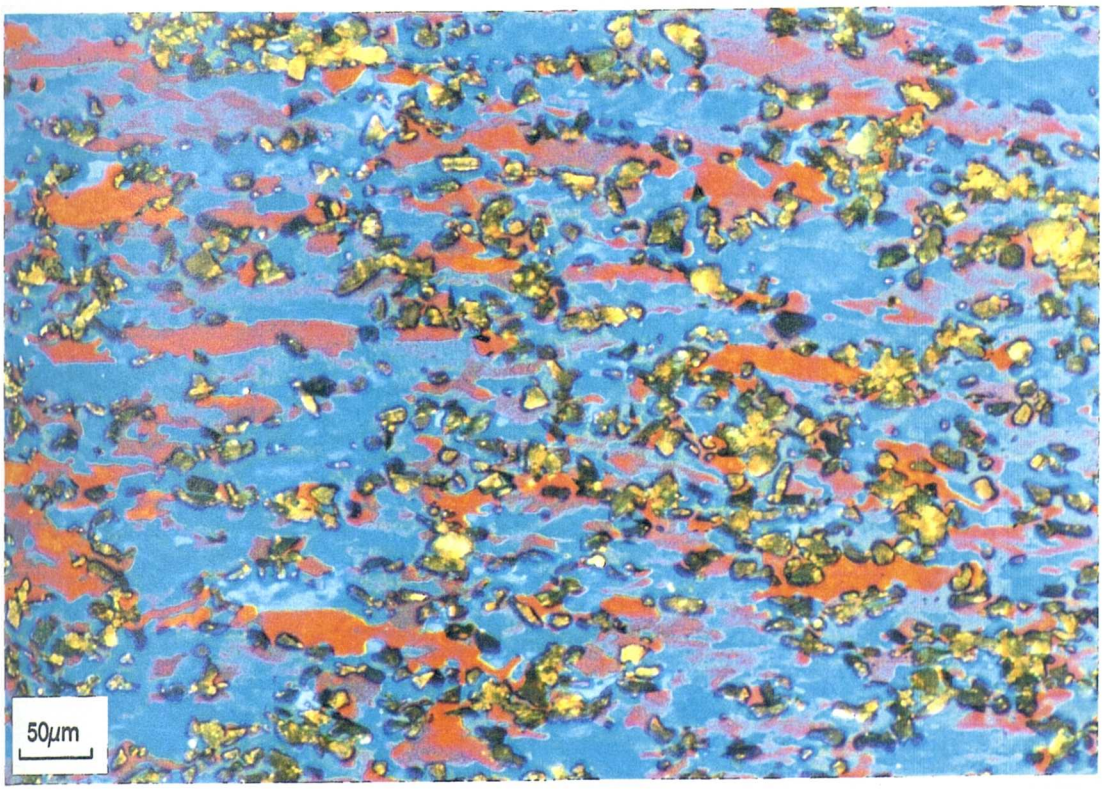

Figure 4.68(b) Optical micrograph of AMMP material, rolled at 400°C and subsequently solution heat treated for 4 hours.

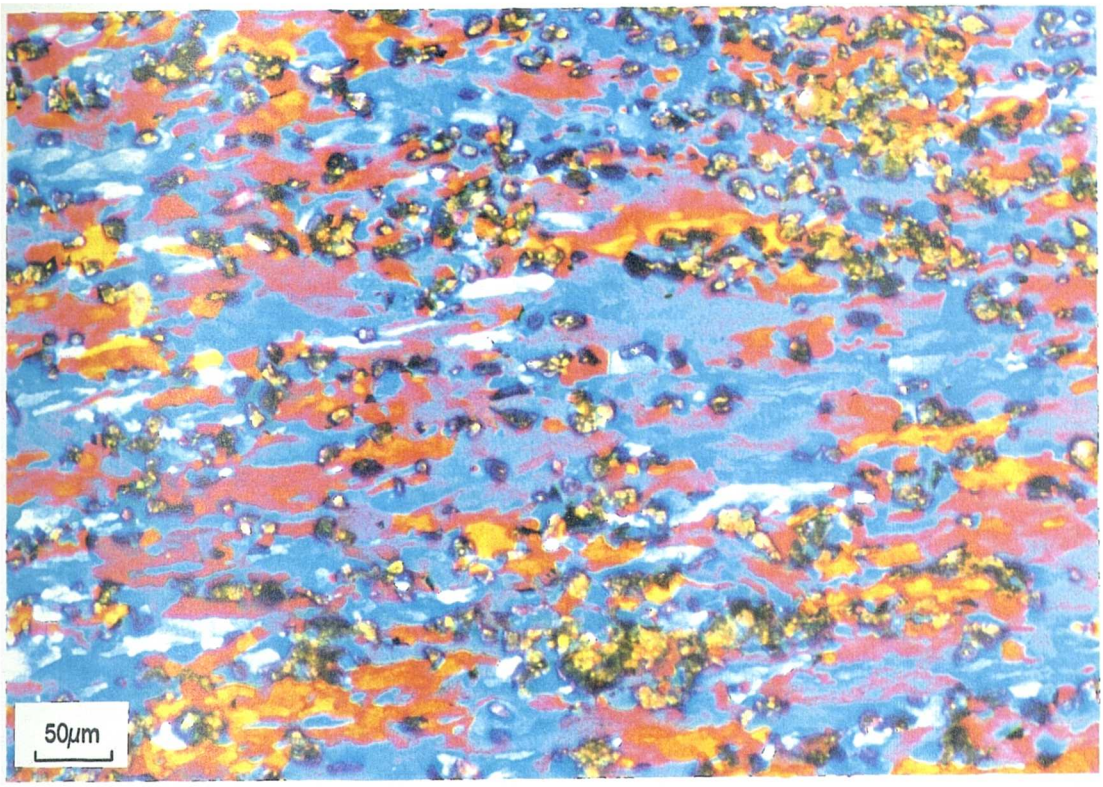

Figure 4.68(c) Optical micrograph of AMMP material, rolled at 400°C and subsequently solution heat treated for 7 hours.

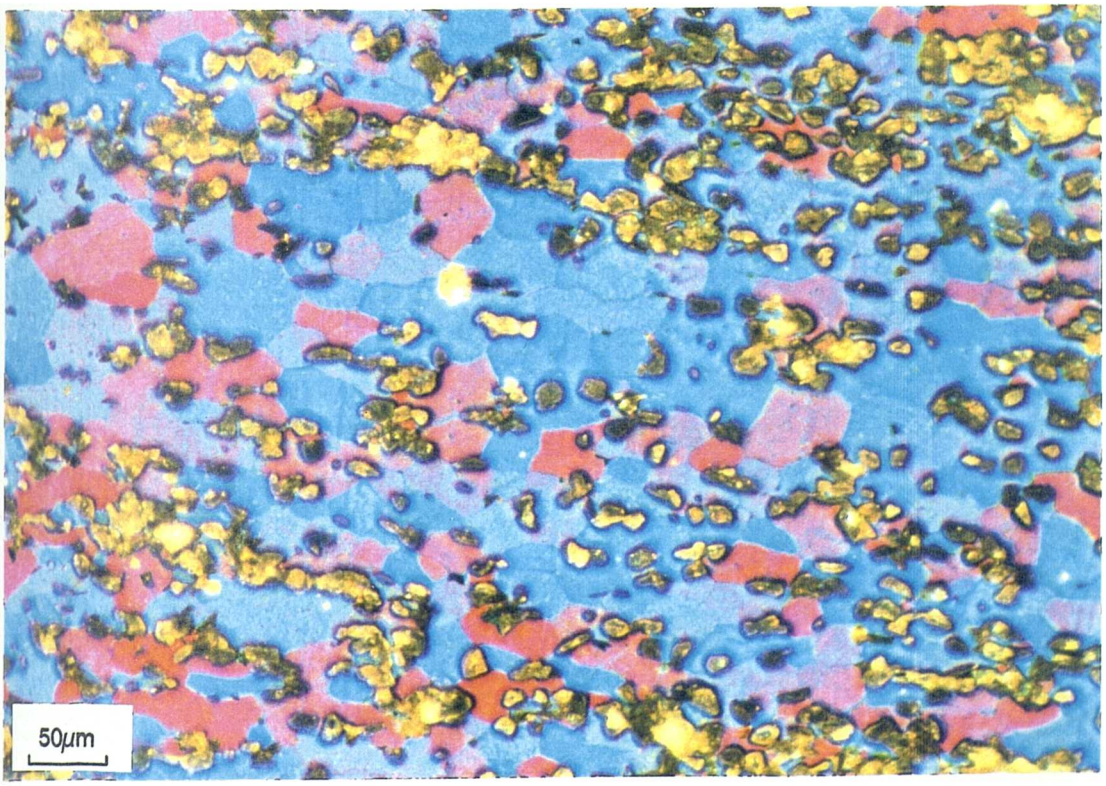

Figure 4.68(d) Optical micrograph of AMMP material, rolled at 400°C and subsequently solution heat treated for 8 hours.

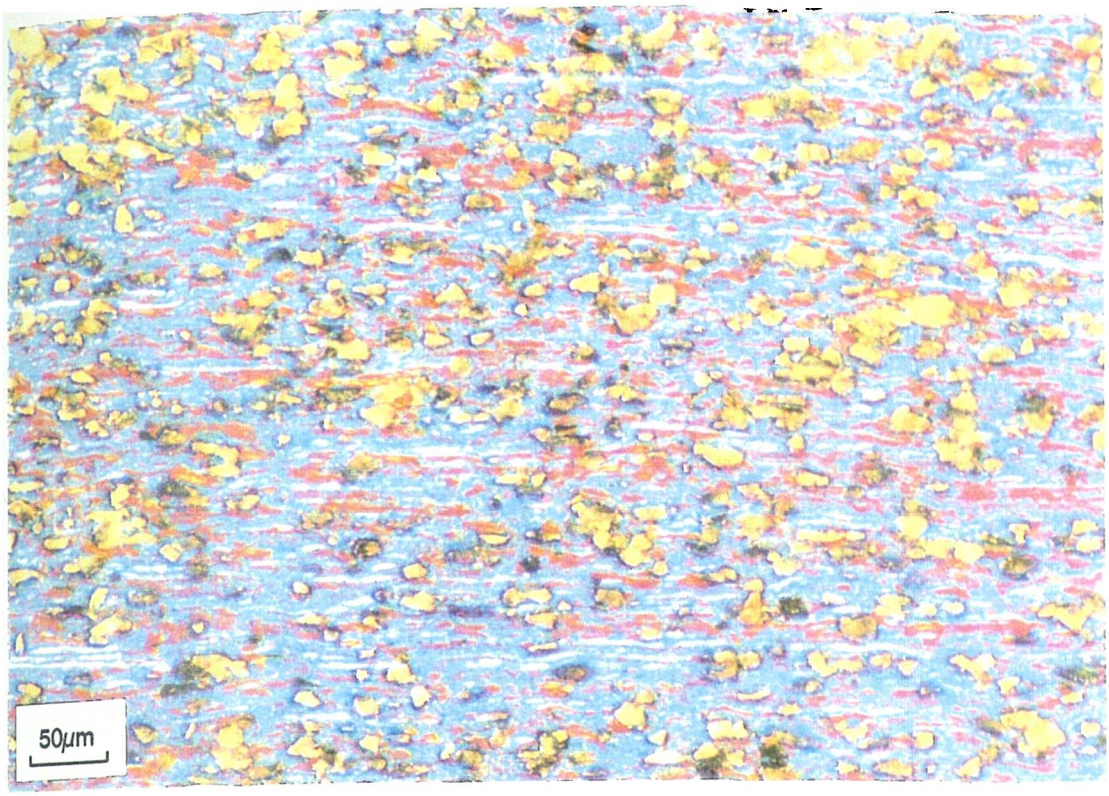

Figure 4.69(a) Optical micrograph of MMC material, as-rolled at 480°C.

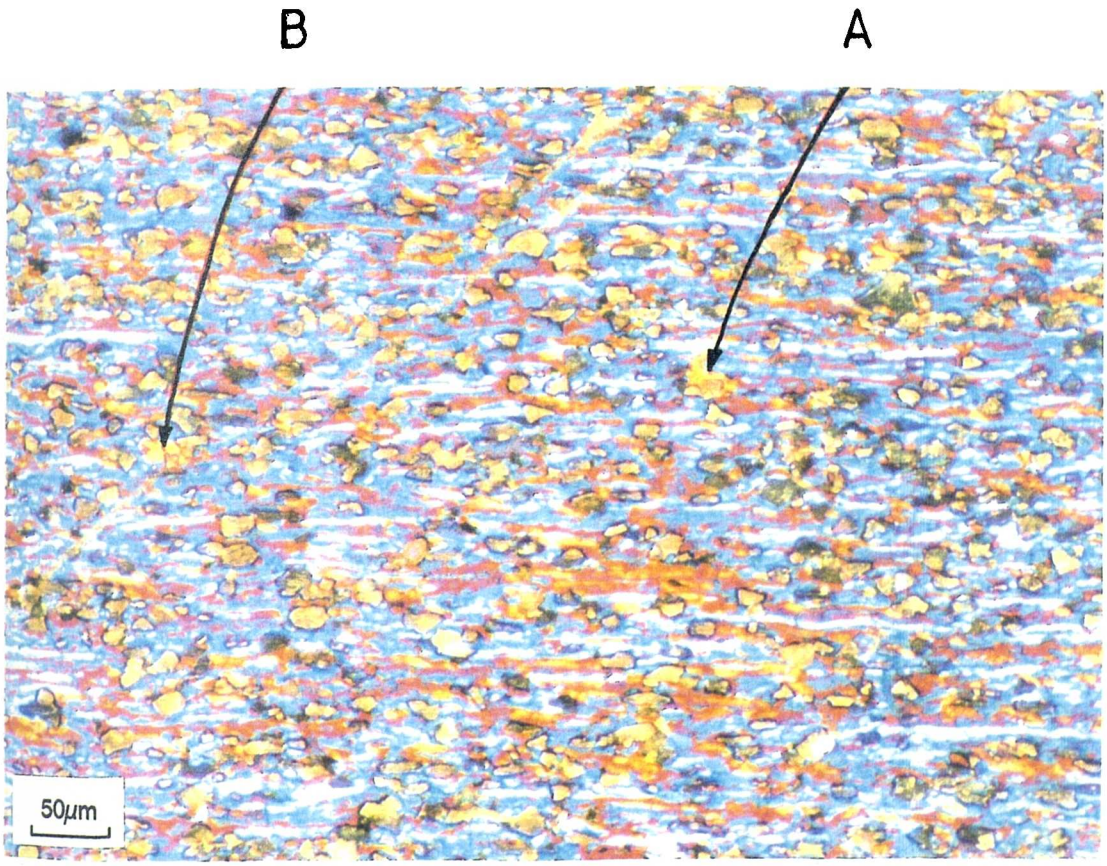

Figure 4.69(b) Optical micrograph of MMC material, rolled at 480°C and subsequently solution heat treated for 1 minute. Note the presence of several larger grains (e.g. "A" and "B").

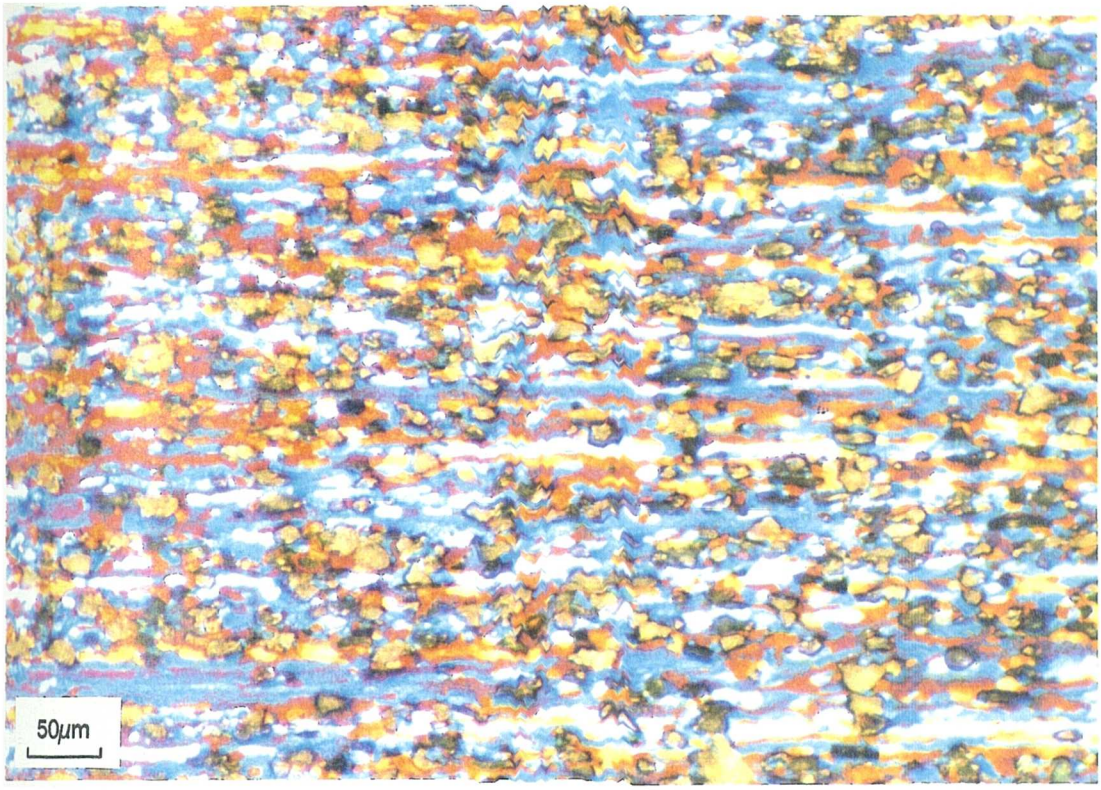

Figure 4.69(c) Optical micrograph of MMC material, rolled at 480°C and subsequently solution heat treated for 2 hours.

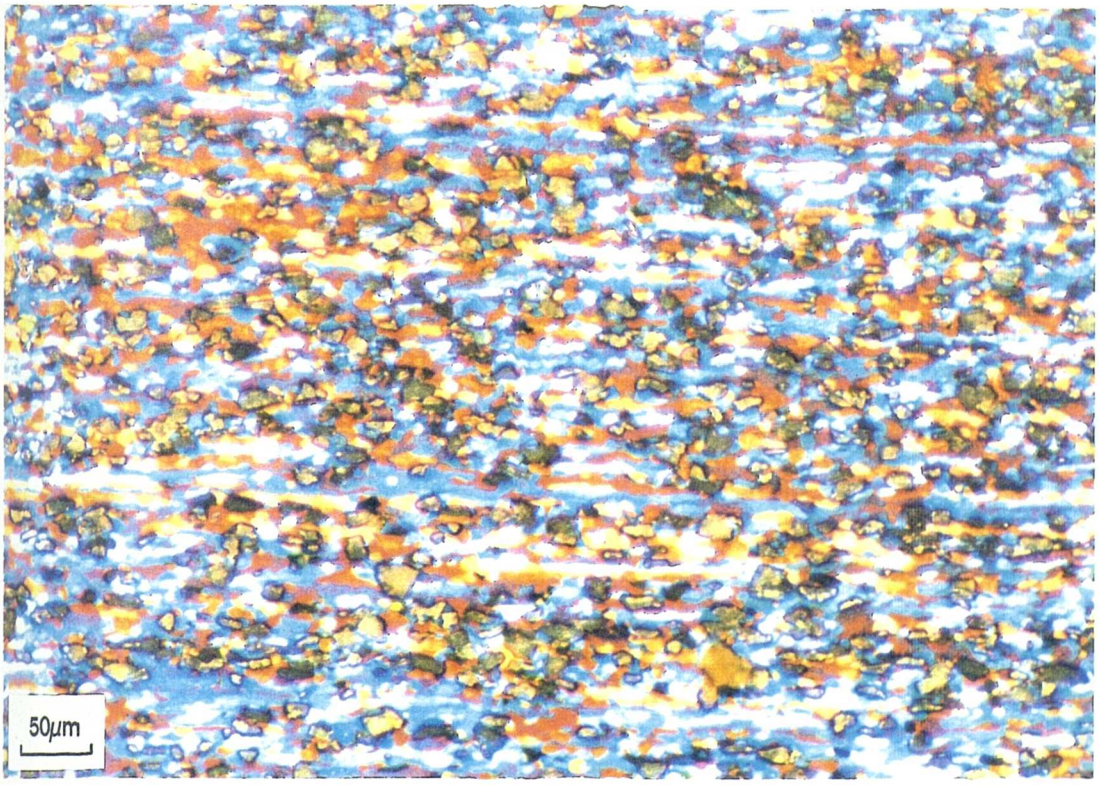

Figure 4.69(d) Optical micrograph of MMC material, rolled at 480°C and subsequently solution heat treated for 4 hours.

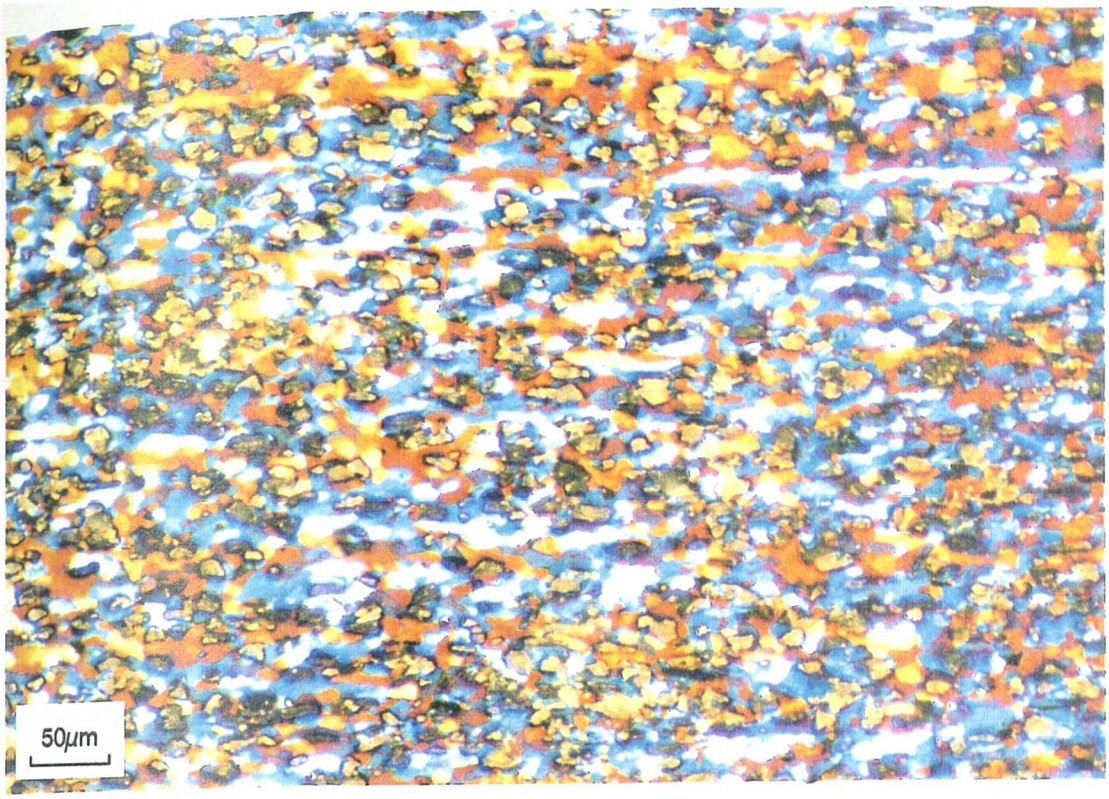

Figure 4.69(e) Optical micrograph of MMC material, rolled at 480°C and subsequently solution heat treated for 8 hours.

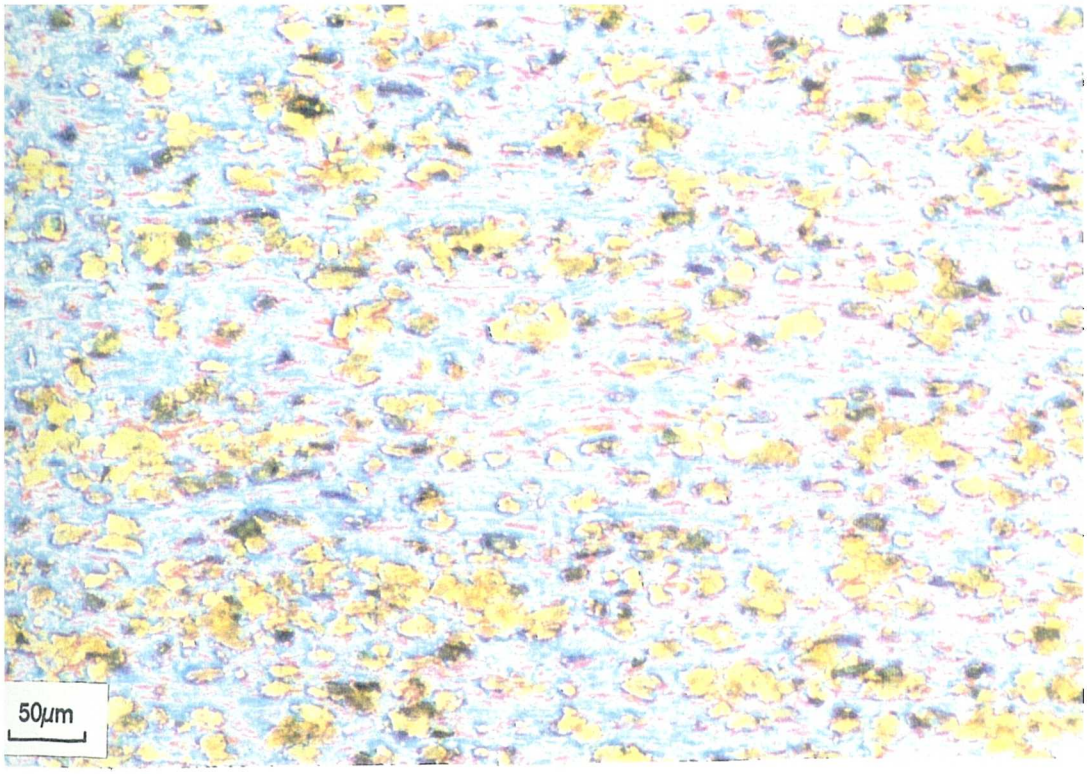

Figure 4.70(a) Optical micrograph of MMC material, as-rolled at 400°C.

Figure 4.70(b) Optical micrograph of MMC material, rolled at 400°C and subsequently solution heat treated for 1 minute.

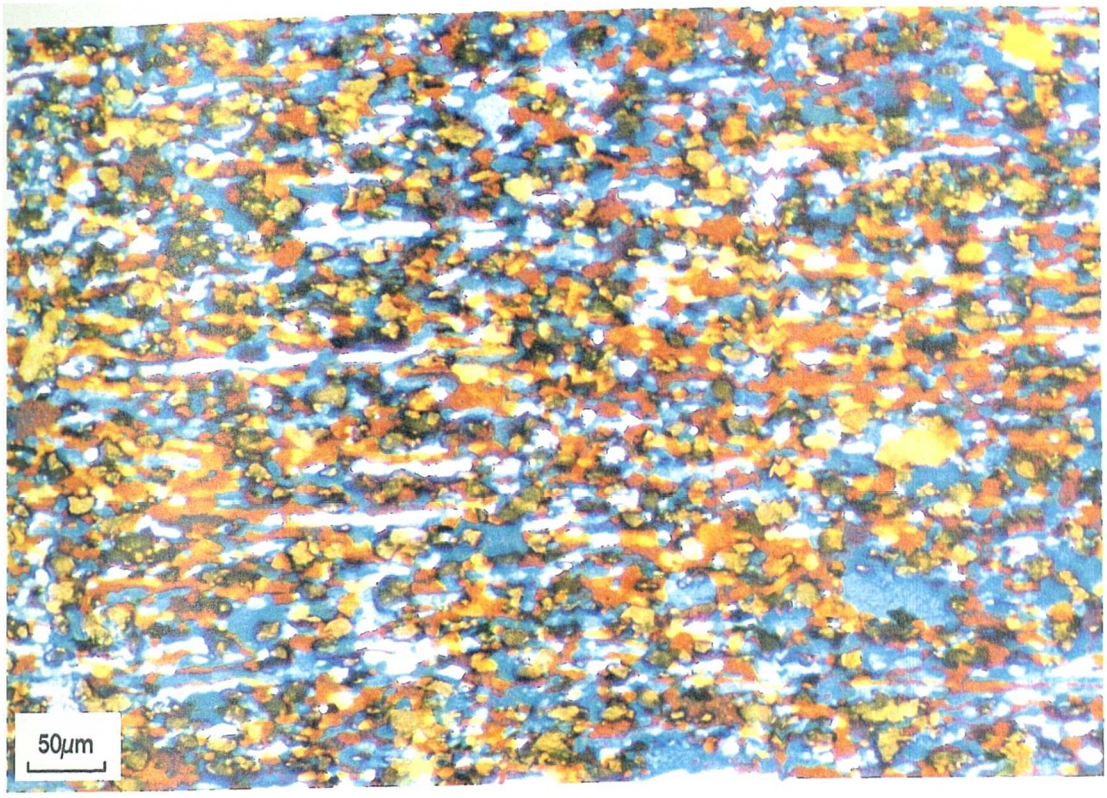

Figure 4.70(c) Optical micrograph of MMC material, rolled at 400°C. and subsequently solution heat treated for 2 hours.

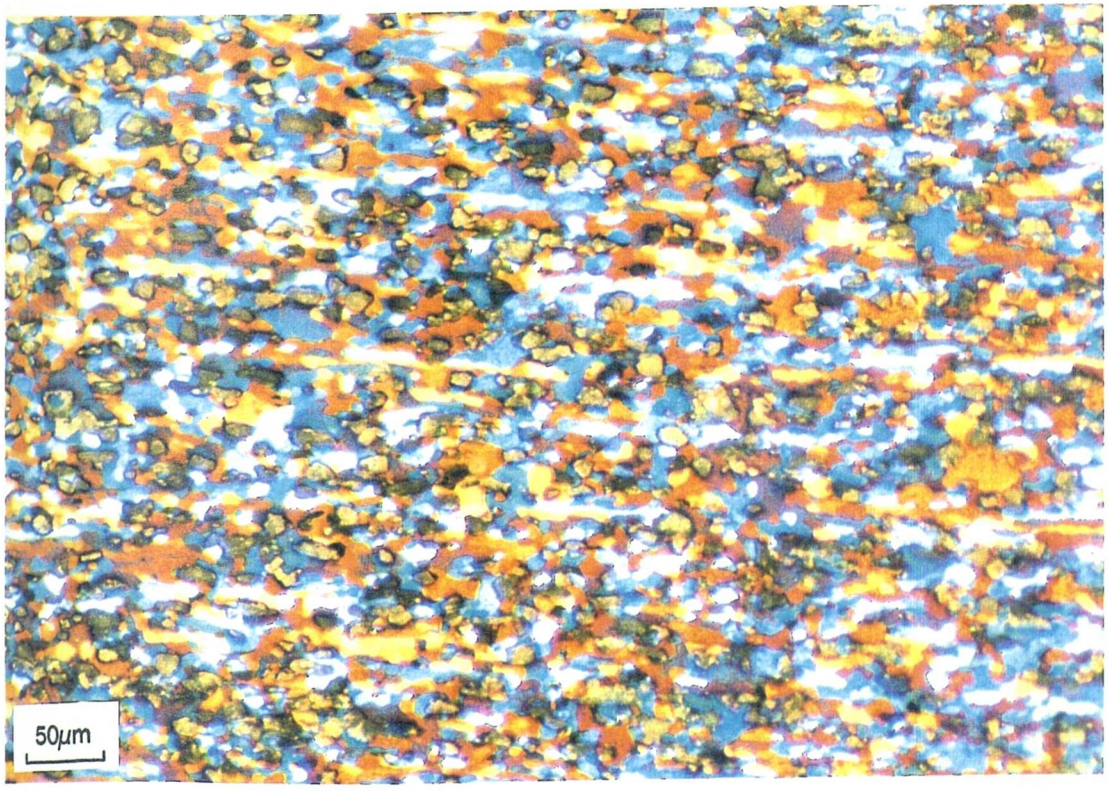

Figure 4.70(d) Optical micrograph of MMC material, rolled at 400°C and subsequently solution heat treated for 4 hours.

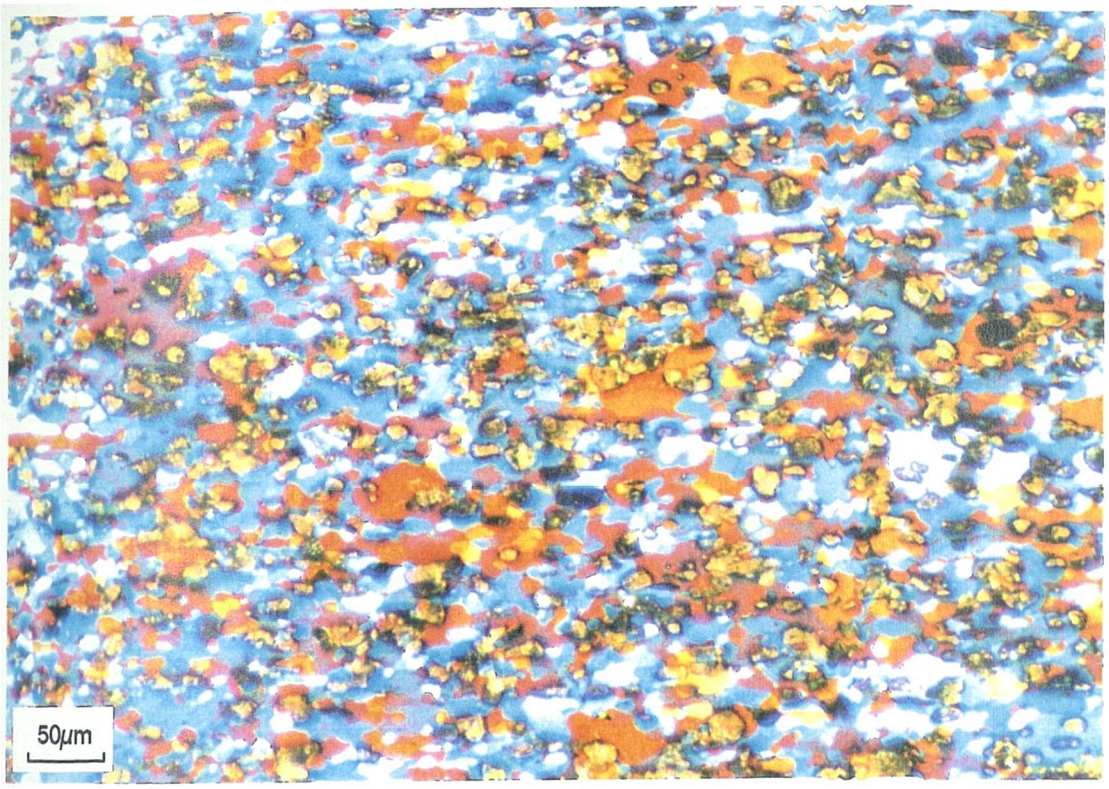

Figure 4.70(e) Optical micrograph of MMC material, rolled at 400°C. and subsequently solution heat treated for 8 hours.

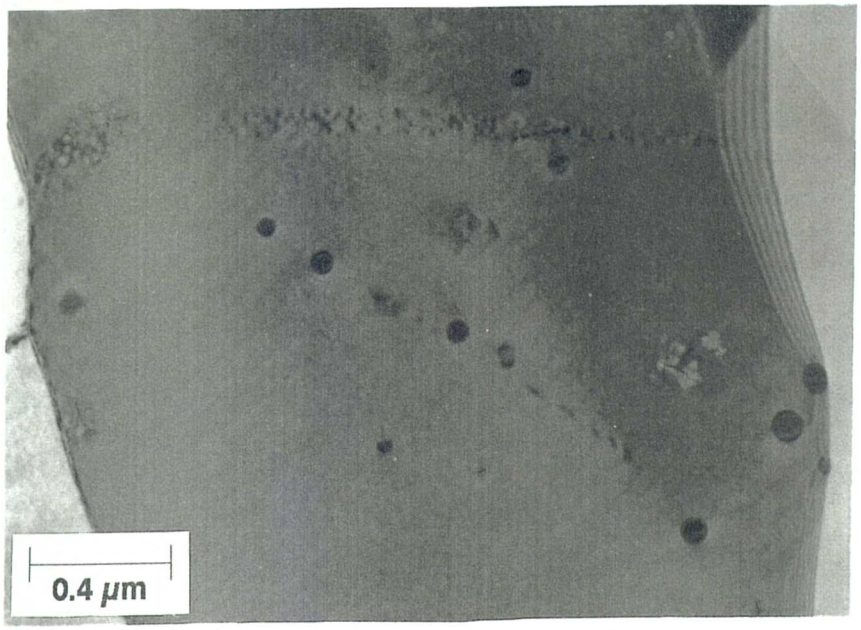

Figure 4.71 TEM micrograph of ASC material, rolled at 400°C and subsequently solution heat treated for 14 days, showing prominent pinning of the boundaries by ß' particles.

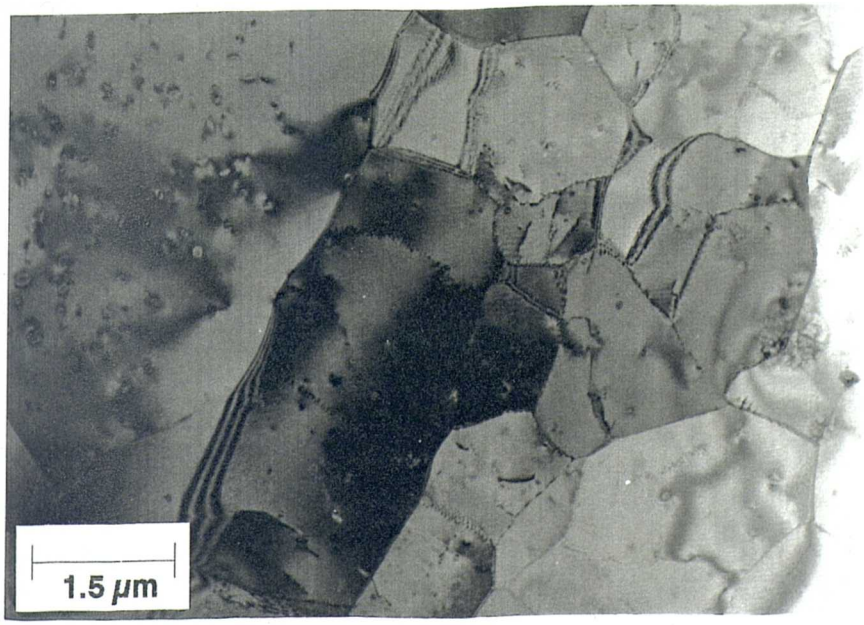

Figure 4.72 TEM micrograph of ASC material, rolled at 400°C and subsequently solution heat treated for 14 days, showing a well recovered substructure.

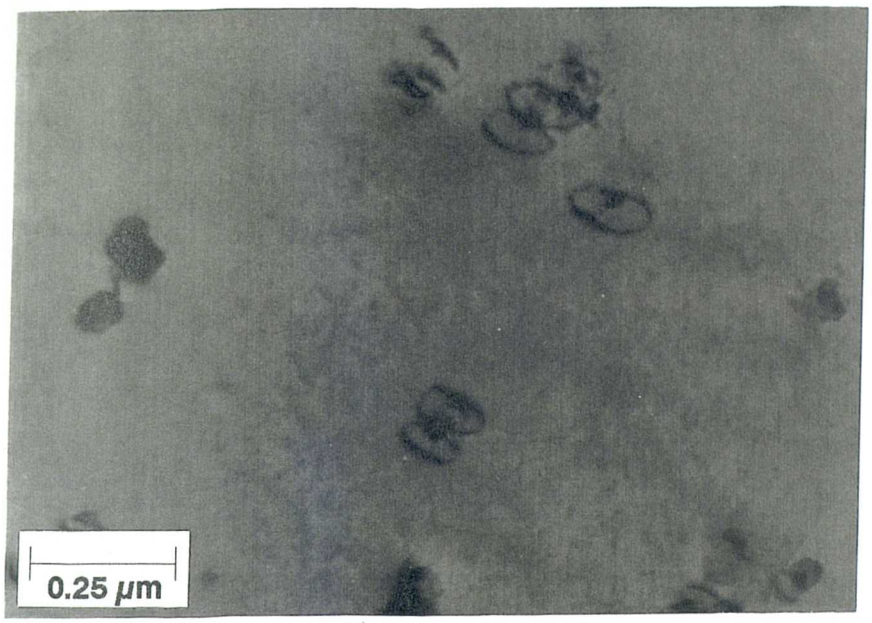

Figure 4.73 TEM micrograph of ASC material, rolled at 300°C and subsequently solution heat treated for 30 minutes. Note extensive looping of dislocations around particles.

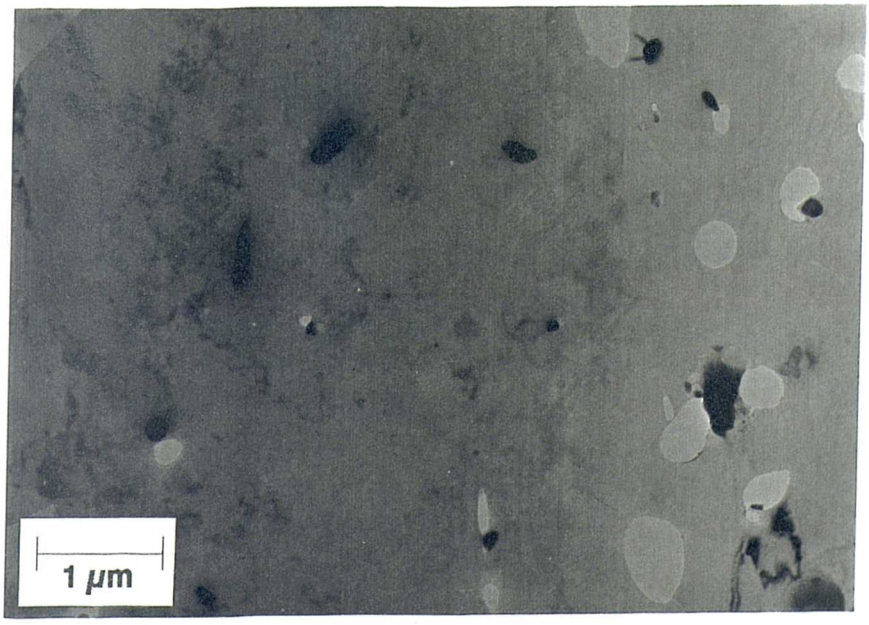

Figure 4.74 TEM micrograph of ASC material, as-rolled at 300°C. "Holes" appear where the foil has preferentially thinned during preparation, possibly as a result of segregation.

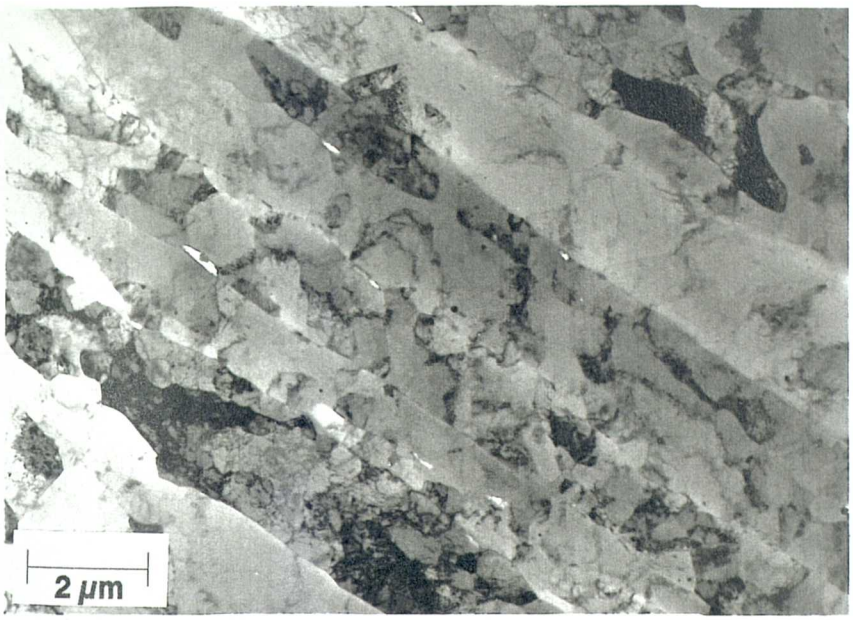

Figure 4.75 TEM micrograph of MONO material, as-rolled at 400°C. Shown are high angle grain boundaries containing a dynamically recovered substructure.

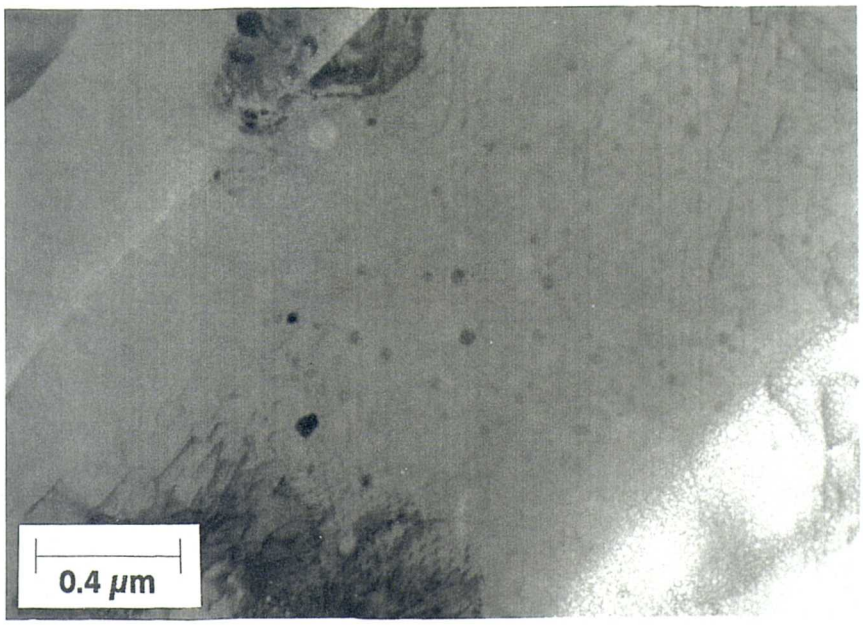

Figure 4.76 TEM micrograph of ASC material, as-rolled at 400°C. A dispersion of ß' particles is shown.

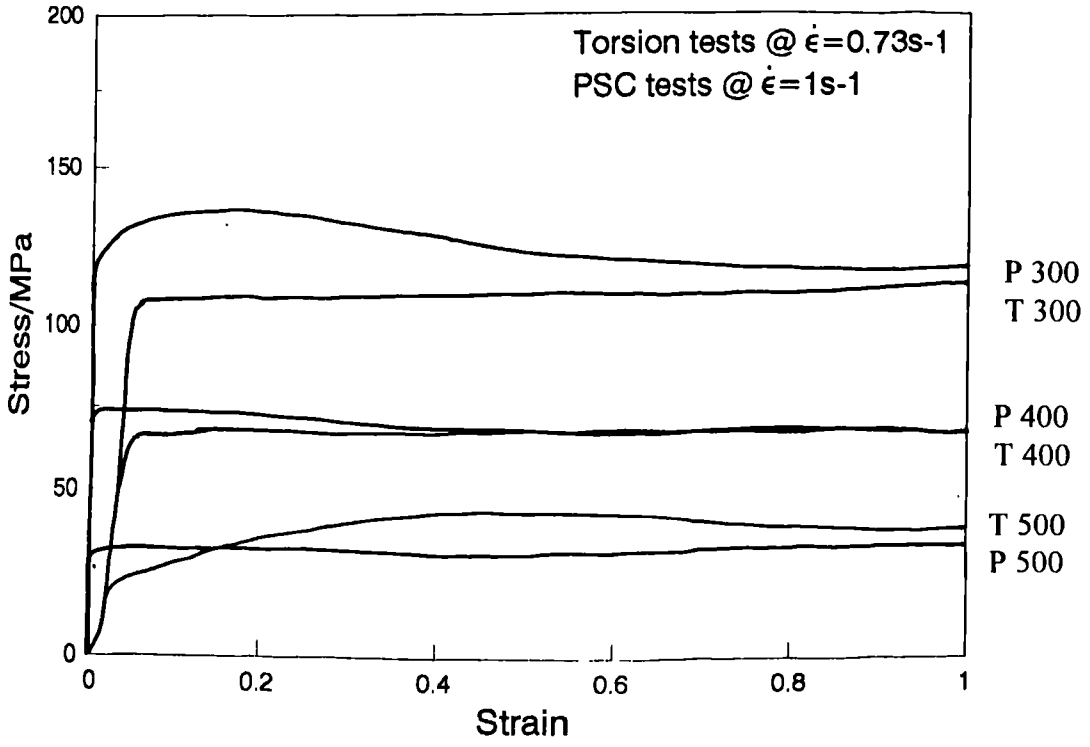

Figure 5.1 Comparison of the stress-strain curves obtained under torsion and PSC test conditions for the MONO series (T = torsion, and P = plane strain compression).

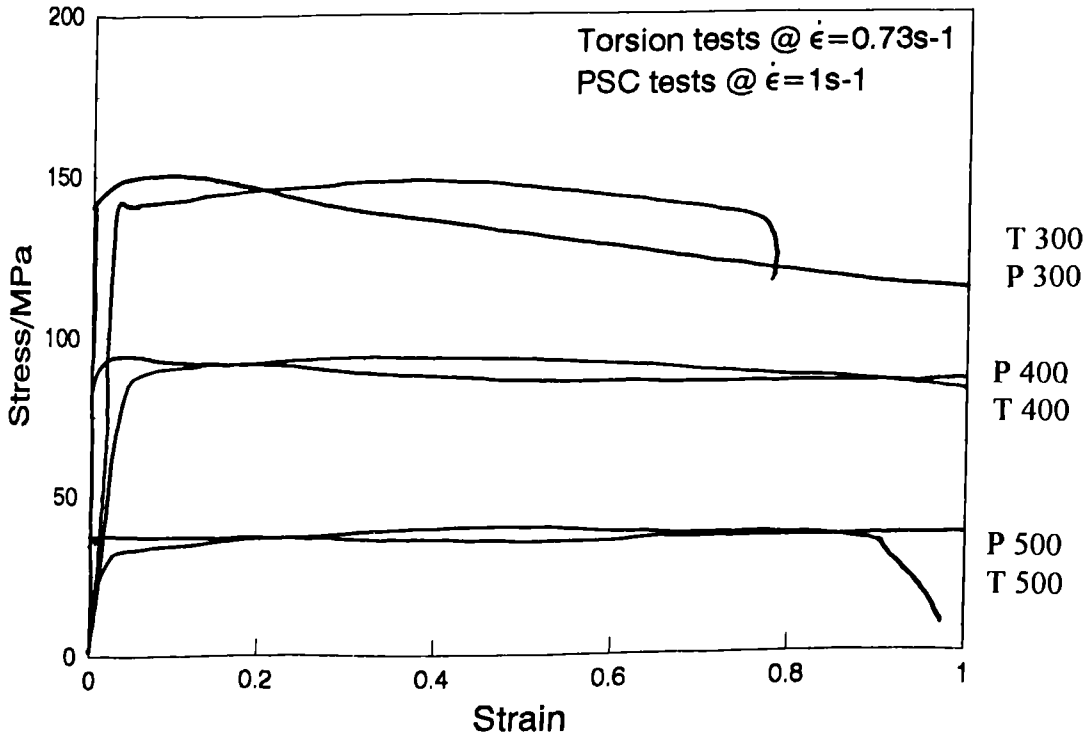

Figure 5.2 Comparison of the stress-strain curves obtained under torsion and PSC test conditions for the MMC series (T = torsion, and P = plane strain compression).

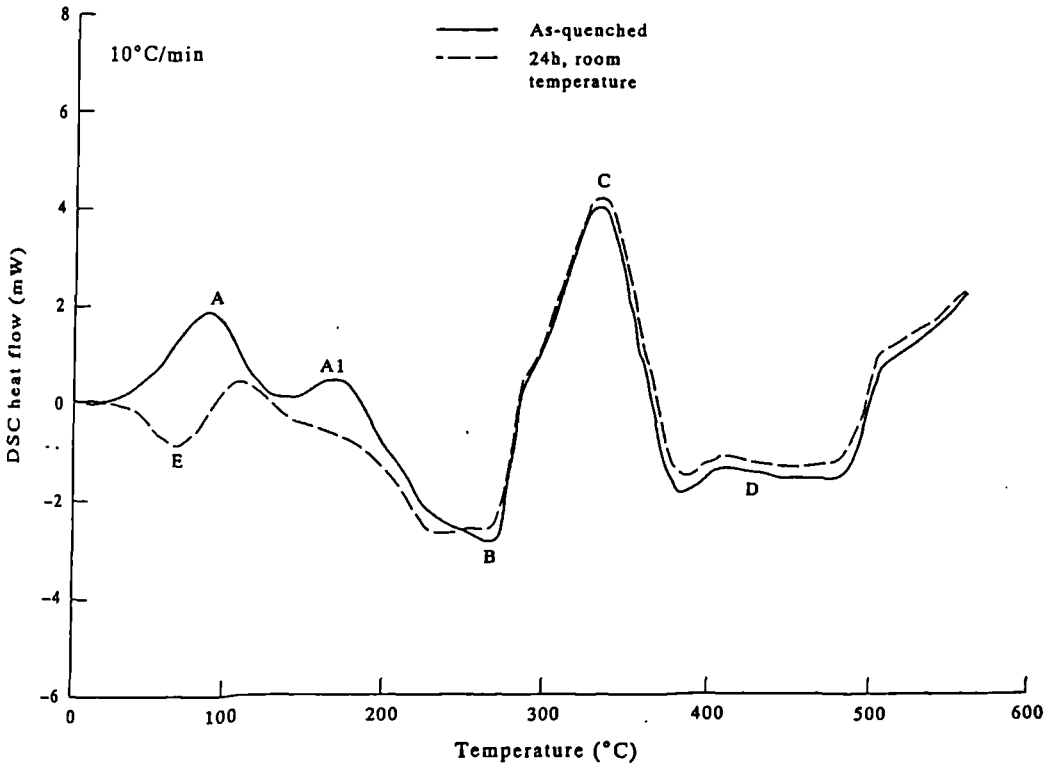

Figure 5.3 DSC thermograms for quenched and R.T. aged 8090 alloy (115). Peak "C" is indicative of the formation of S' phase.

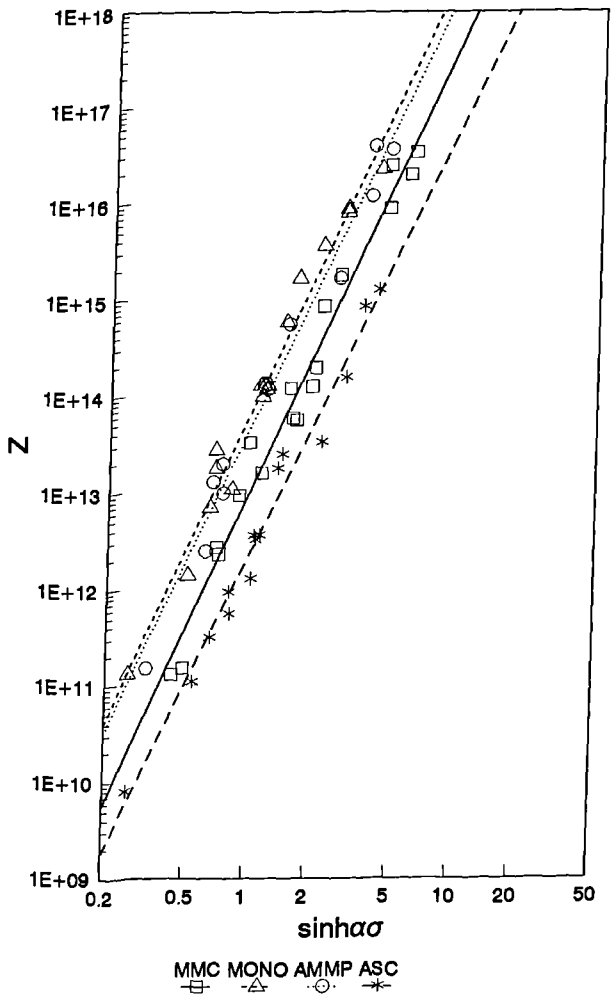

Figure 5.4 Comparison of sinh laws for all materials formulated from PSC test data at ϵ=0.5

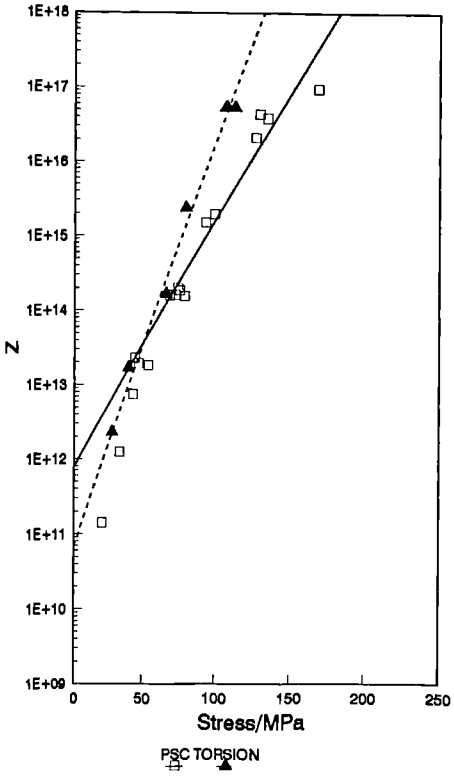

(a)

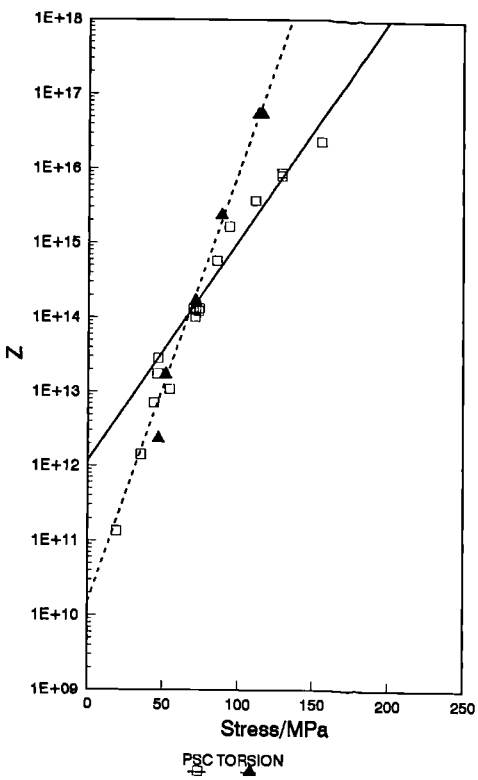

(b)

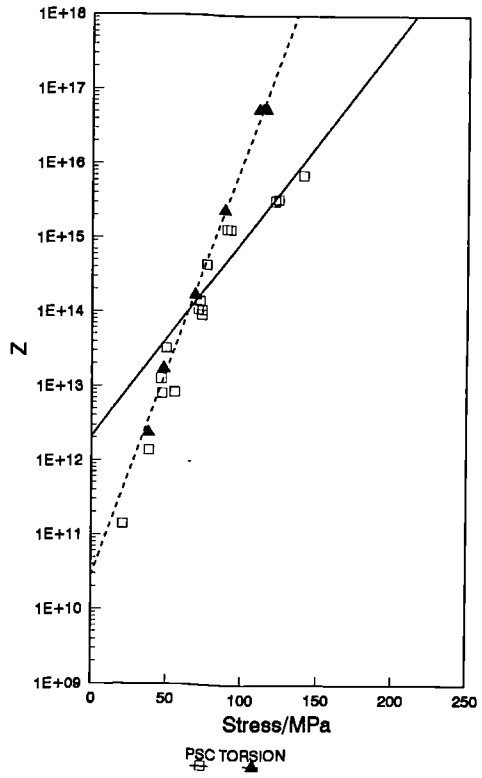

(c)

Figure 5.5 MONO series torsion/PSC comparison of exponential laws at strains of: (a) 0.1 (b) 0.5 (c) 1.0

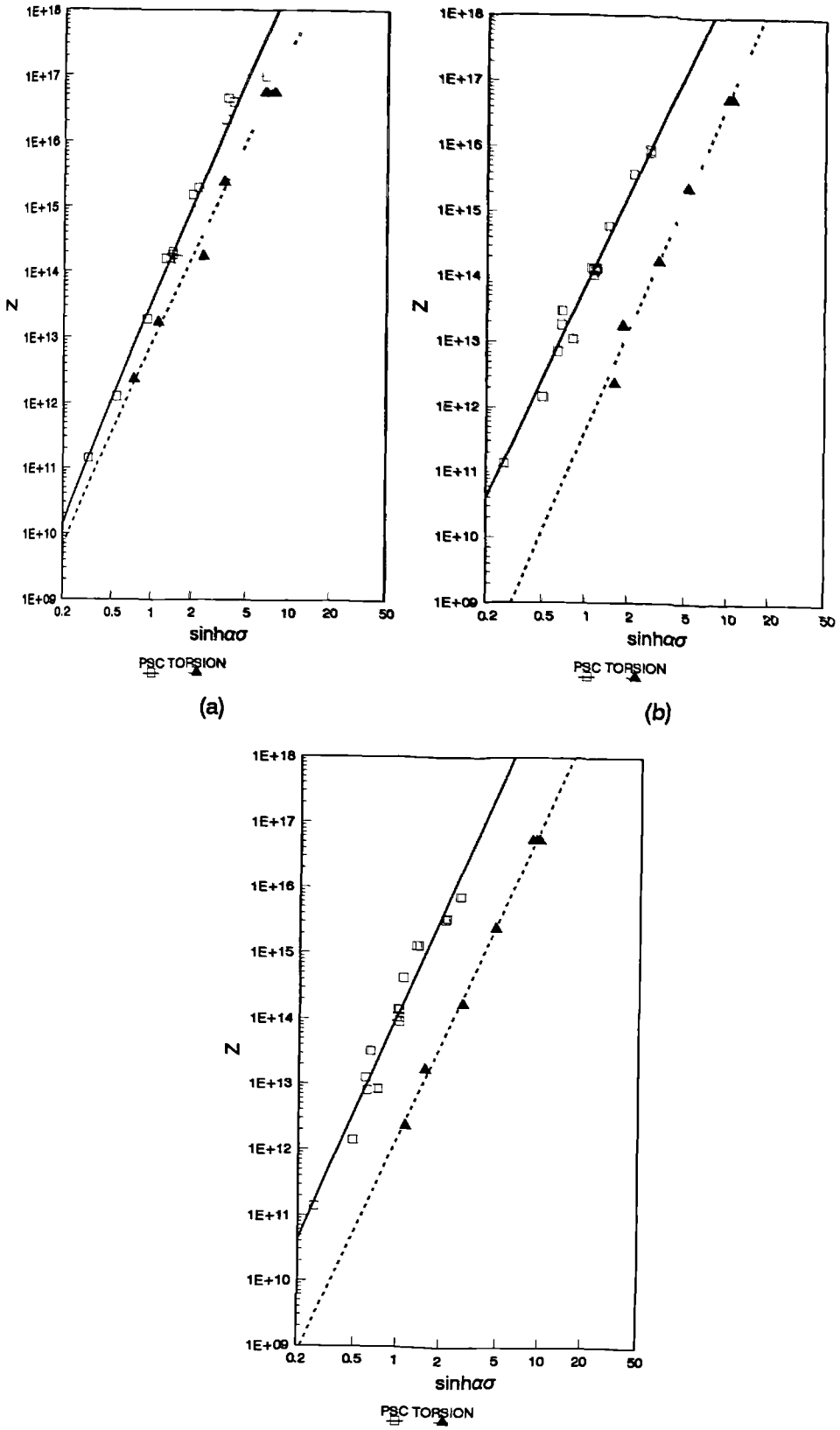

Figure 5.6 MONO series torsion/PSC comparison of hyperbolic sine laws at strains of: (a) 0.1 (b) 0.5 (c) 1.0

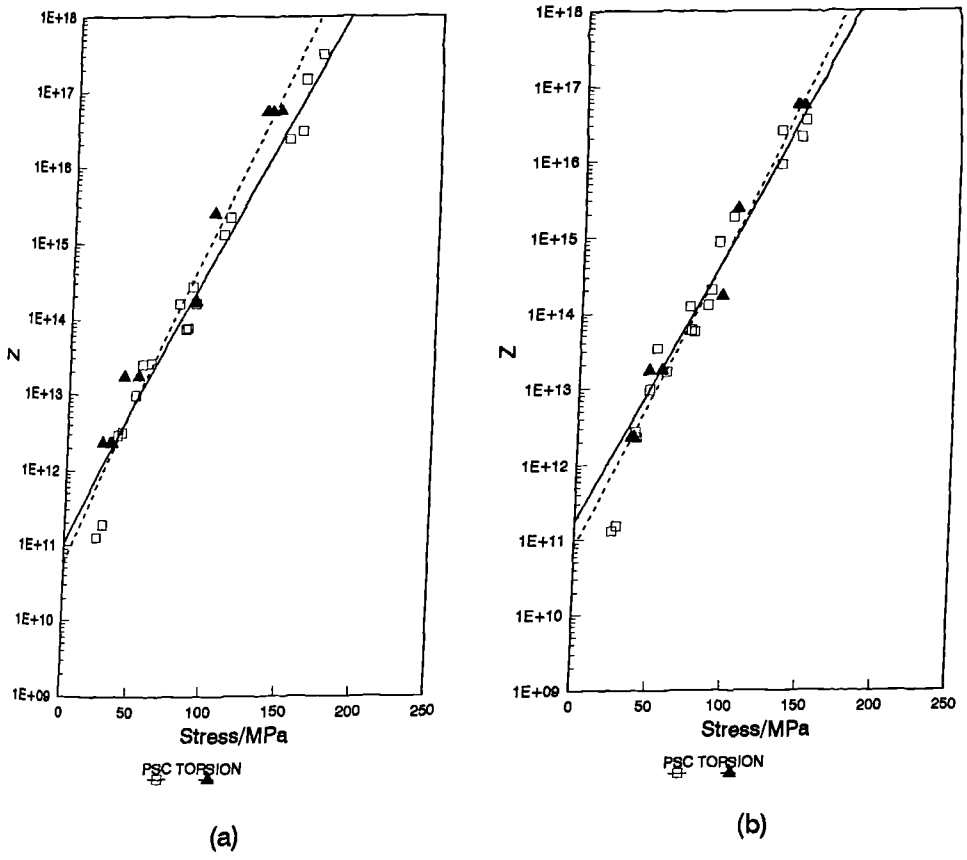

Figure 5.7 MMC series torsion/PSC comparison of exponential laws at strains of: (a) 0.1 and (b) 0.5

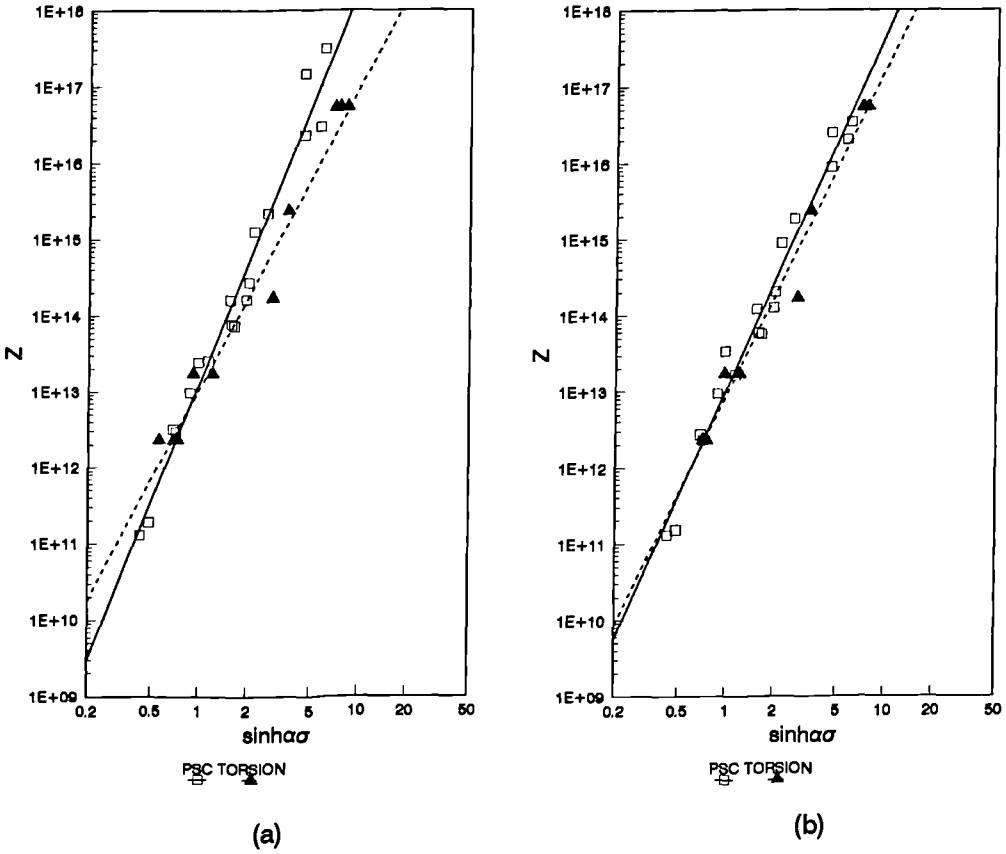

Figure 5.8 MMC series torsion/PSC comparison of hyperbolic sine laws at strains of: (a) 0.1 and (b) 0.5

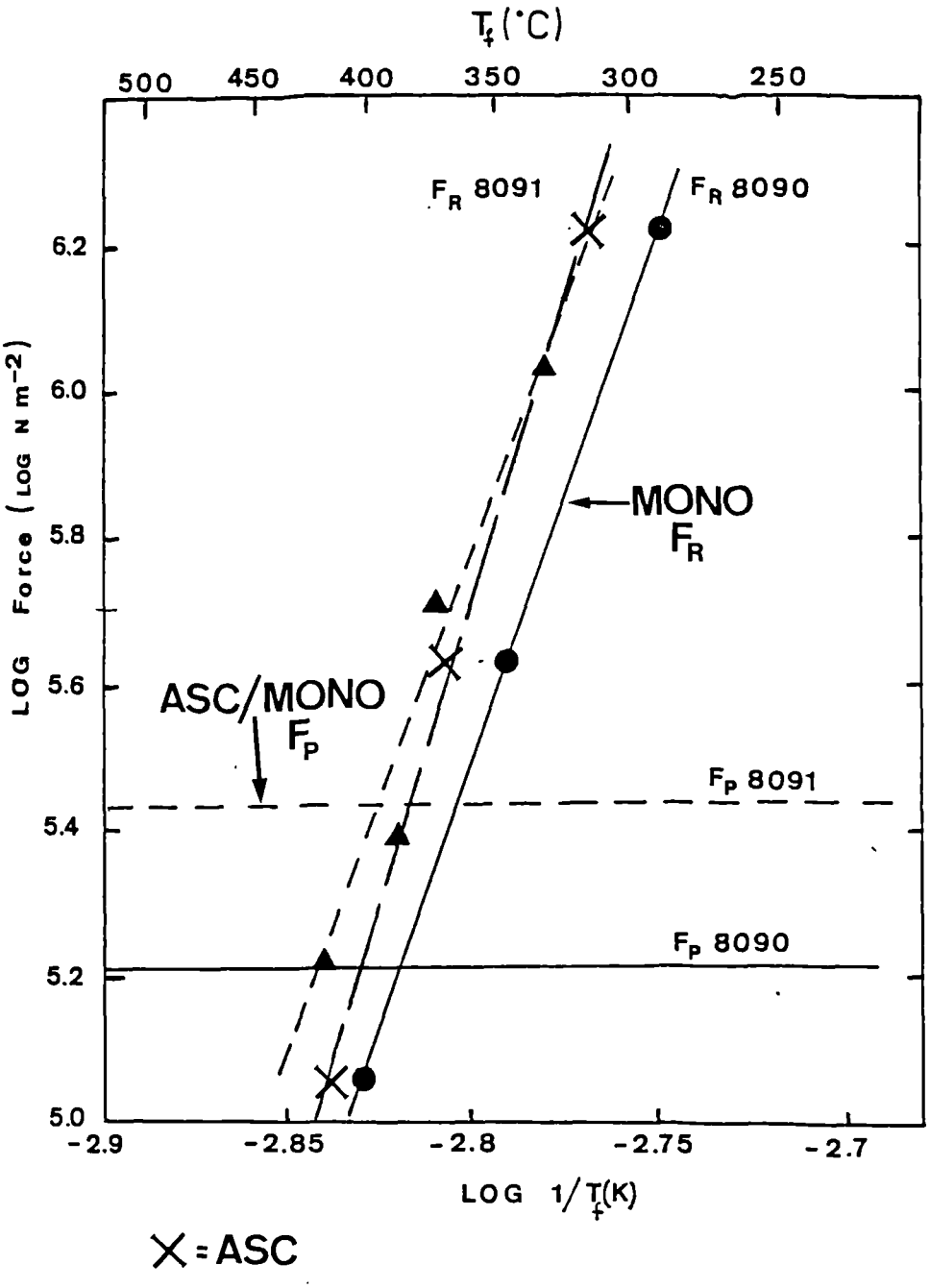

Figure 5.9 Graph of pinning force (F_p) and recrystallisation force (F_R) vs log ($1/T_f$) ,where T_f is the finish rolling temperature (K). (16)
Points from the rolling of ASC and MONO material have been added.

(a)

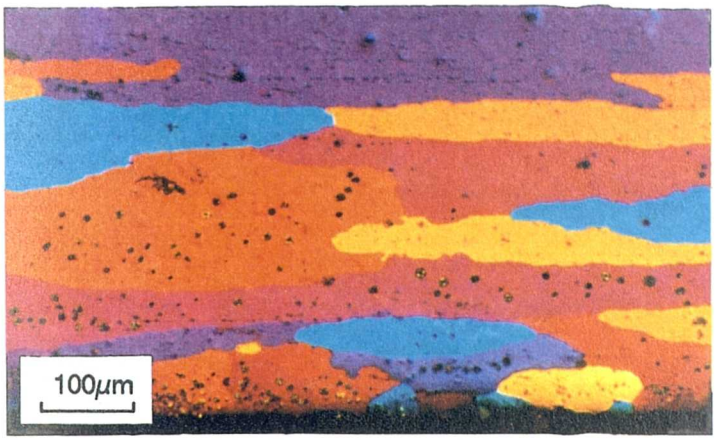

(b)

(c)

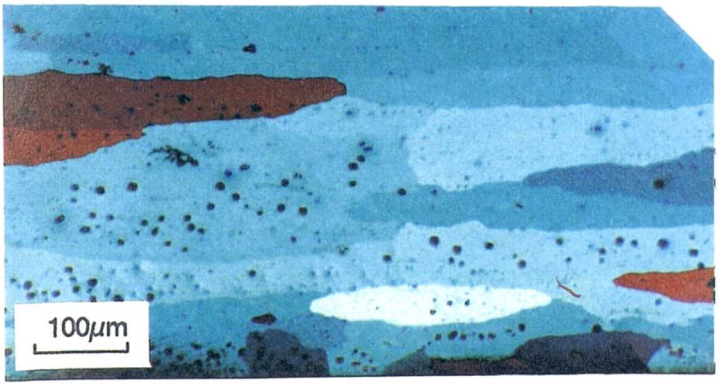

Figure 5.10 The above show the effect of specimen orientation, with respect to the crossed-polars, in revealing the grain structure in anodised aluminium-lithium alloy 8090. The apparent difference in number and shape of grains should be noted.

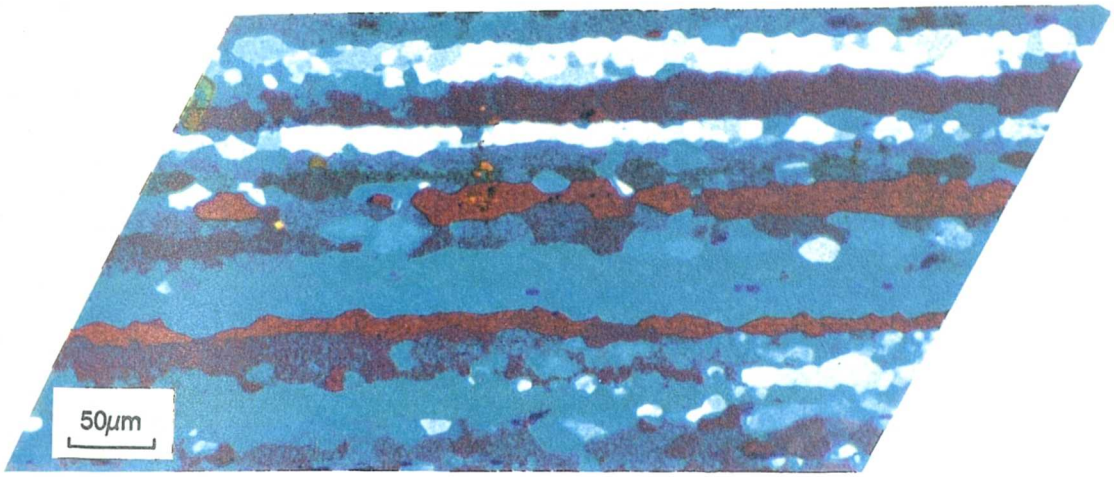

Figure 5.11 The above show the effect of specimen orientation, with respect to the crossed-polars, in revealing the grain structure in the sample ASC, rolled at 300°C and solution heat treated for 14 days. This figure should be directly compared with that in Figure 4.66.

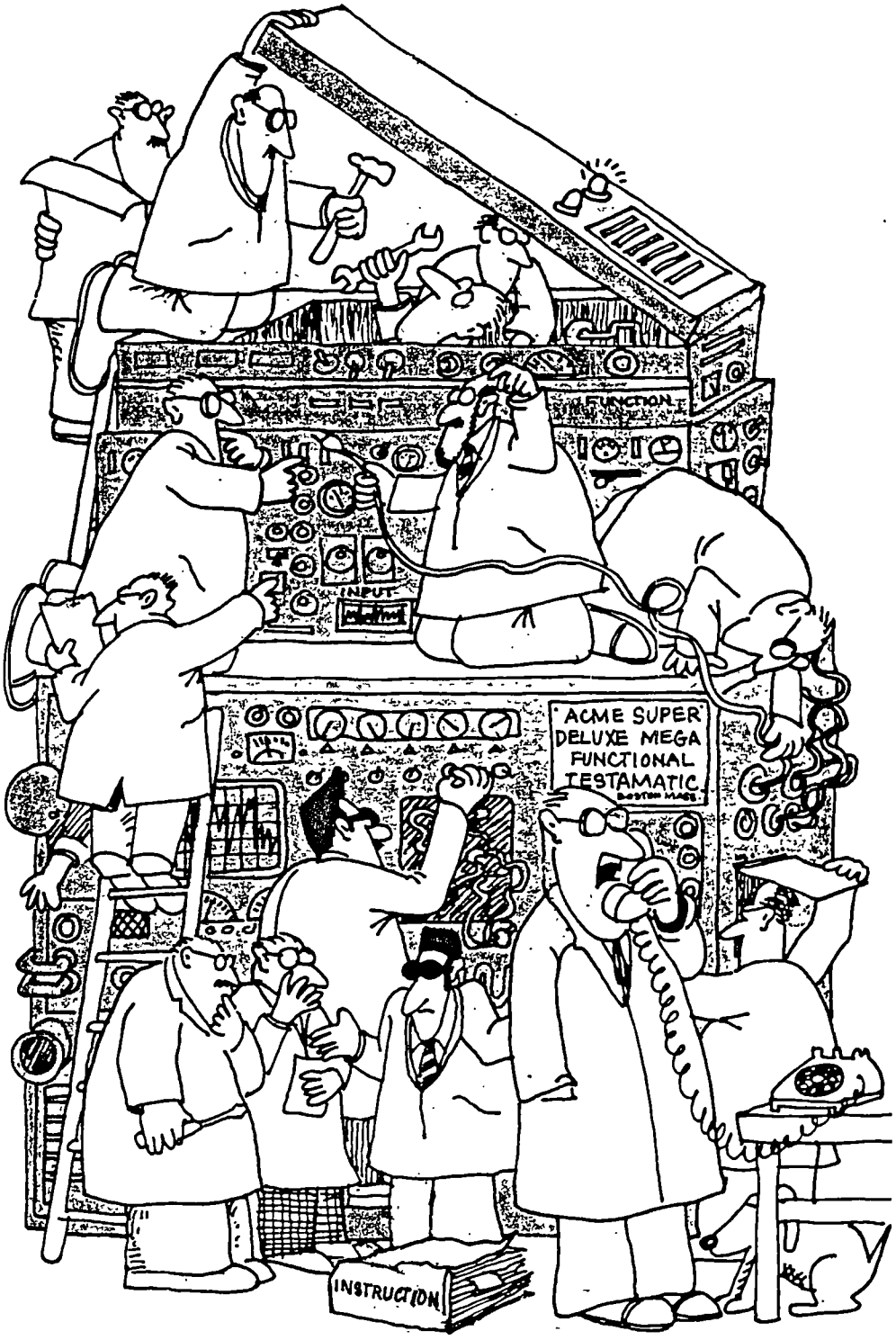

"Sure, sure... no problem, we'll have this baby up and running any day now... yep, just a few more days now... coming right along... heck of a tester... just a few more days more or less... yep, sure... no problem..."